PALEOENVIRONMENTAL EVOLUTION OF ON-SHORE ICE-FREE AREAS AROUND MAXWELL BAY, KING GEORGE ISLAND, SOUTH SHETLAND ISLANDS

Dissertation

Zur Erlangung des akademischen Grades eines

Doktors der Naturwissenschaften

Dr. rer. nat.

am Fachbereich FB05-Geowissenschaften

der Universität Bremen

vorgelegt von Geol. Pablo Alfredo Heredia Barión

geb. In Córdoba, Argentinien

Tag der wissenschaftlichen Aussprache: 7. Juni 2019

Bremen 2019

Erstgutachterin: Professor Dr. Cornelia Spiegel

Zweitgutachter: Professor Dr. Martin Melles

Neji: "¿Porqué tener una batalla inútil tratando de desafiar a tu destino?"

Naruto: "por que me has llamado fracasado...probare que estas equivocado"

-*Naruto*, Masashi Kishimoto-

This Ph. D. thesis was conducted at the Centro de Investigaciones en Ciencias de la Tierra (Research Center on Earth Sciences; CICTERRA), Córdoba, Argentina, an institute that belongs to CONICET- Consejo Nacional de Investigaciones Científicas y Técnicas (National Scientific and Technical Research Council) and the UNC-Universidad Nacional de Cordoba (National University of Cordoba), between April 2013 and January 2017; and the Geosciences Division of the Alfred Wegener Institute, Helmholtz Center for Polar and Marine Research, Bremerhaven, Germany, until its completion. It was carried out in collaboration with the Working Group Geodynamics of the Polar Regions, led by Prof. Dr. Cornelia Spiegel, Bremen University, Department of Geosciences.

This work was financially supported by CONICET, the DNA/IAA in the framework of the Project PICTA, 2011 – 0102, IAA “Geomorfología y Geología Glaciar del Archipiélago James Ross e Islas Shetland del Sur, Sector Norte de la Península Antártica”, the Alfred Wegener Institute (AWI), Helmholtz Center for Polar and Marine Research PACES II (Polar Regions and Coasts in the changing Earth System), as well as by IMCONet (FP7 IRSES, Action no. 318718).

Versicherung an Eides Statt / Affirmation in lieu of an oath

gem. § 5 Abs. 5 der Promotionsordnung vom 18.06.2018 /

according to § 5 (5) of the Doctoral Degree Rules and Regulations of 18 June, 2018

Ich / I, Pablo Alfredo Heredia Barión, Neuelandstraße 72, 27576 Bremerhaven

versichere an Eides Statt durch meine Unterschrift, dass ich die vorliegende Dissertation selbständig und ohne fremde Hilfe angefertigt und alle Stellen, die ich wörtlich dem Sinne nach aus Veröffentlichungen entnommen habe, als solche kenntlich gemacht habe, mich auch keiner anderen als der angegebenen Literatur oder sonstiger Hilfsmittel bedient habe und die zu Prüfungszwecken beigelegte elektronische Version (PDF) der Dissertation mit der abgegebenen gedruckten Version identisch ist. / *With my signature I affirm in lieu of an oath that I prepared the submitted dissertation independently and without illicit assistance from third parties, that I appropriately referenced any text or content from other sources, that I used only literature and resources listed in the dissertation, and that the electronic (PDF) and printed versions of the dissertation are identical.*

Ich versichere an Eides Statt, dass ich die vorgenannten Angaben nach bestem Wissen und Gewissen gemacht habe und dass die Angaben der Wahrheit entsprechen und ich nichts verschwiegen habe. */ I affirm in lieu of an oath that the information provided herein to the best of my knowledge is true and complete.*

Die Strafbarkeit einer falschen eidesstattlichen Versicherung ist mir bekannt, namentlich die Strafandrohung gemäß § 156 StGB bis zu drei Jahren Freiheitsstrafe oder Geldstrafe bei vorsätzlicher Begehung der Tat bzw. gemäß § 161 Abs. 1 StGB bis zu einem Jahr Freiheitsstrafe oder Geldstrafe bei fahrlässiger Begehung. / *I am aware that a false affidavit is a criminal offence which is punishable by law in accordance with § 156 of the German Criminal Code (StGB) with up to three years imprisonment or a fine in case of intention, or in accordance with § 161 (1) of the German Criminal Code with up to one year imprisonment or a fine in case of negligence.*

_____ _____

Ort / Place, Datum / Date Unterschrift / Signature

ABSTRACT

Understanding the Holocene is particularly important for providing the context for recent ice sheet dynamics –i.e. understanding whether current ice sheet dynamics are unusual or part of Holocene natural variability (Bentley et al., 2014). Knowledge on the most recent millennia of Antarctic Ice Sheet history is vital for evaluating the response of the ice sheet to various forcing agents, such as sea-level rise, atmospheric and oceanographic temperature changes, and for constraining grounding-line retreat on Holocene to recent time scales (Bentley et al., 2014). The main objective of this thesis is to add new data to reconstruct the Holocene deglaciation history of King George Island, South Shetland Islands, northwest Antarctic Peninsula, by investigating morpho-sedimentary records of glacigenic and coastal landforms and associated sediments from the on-shore ice-free areas around Maxwell Bay (King George Island), namely Potter Peninsula and Fildes Peninsulas.

In order to accomplish the thesis objectives, I used (i) cosmogenic exposure dating and radiocarbon dating for absolute chronological constraints; (ii) stratigraphy and sedimentology for relative chronological constraints and reconstruction of paleoenvironmental conditions; (iii) geomorphological mapping for spatial distribution of landsystems; (iv) and ground-penetrating radar (GPR) investigations for the study of internal sedimentary architecture of coastal landforms.

Radiocarbon dating results yield new age constraints for the onset of deglaciation on Potter Peninsula, which occurred around at or before 7.8 ka cal BP instead of an earlier accepted age of 9.5 ka cal BP. I provide additional evidence for a short-lived glacier re-advance between 7.2 and 7.0 ka cal BP. This re-advance is likely linked to a glacier re-advance or still-stand documented on South Shetland Islands for that time period. Nevertheless, climatic conditions associated with this glacial re-advance remain unclear. In contrast, on Fildes Peninsula, exposure and radiocarbon dating indicate that glacial oscillations were minimal during the last 7 ka. I applied radiocarbon dating to remnants of mosses preserved in moraines. The moraines were formed close to the present glacier limit between 0.5 and 0.1 ka cal BP, during the last glacier re-advance in South Shetland Islands. This advance is linked to reductions in summer/annual insolation coupled with a shift to more intense Southern Hemisphere westerly winds in the Southern Ocean. Stronger, and possibly more poleward-shifted southern westerly winds produced more precipitation-laden storm fronts passing over the South Shetland Islands and thus, increased ice accumulation.

The data also show that between 1.9 and 1.3 ka cal BP a climatic optimum was reached on Fildes and Potter Peninsula, which lasted until the last glacier readvance. GPR investigations and radiocarbon dating from a gravel spit system on Potter Peninsula document coastal progradation during the late phase of the last glacier re-advance, with a stable relative sea-level. Results also show an interruption of spit progradation that coincides with a proposed onset of accelerated isostatic rebound in reaction to glacier retreat subsequent to the last glacier re-advance. Spit growth resumed in the late 19th century after the rate of isostatic rebound decreased, and continues until today.

The findings of this thesis support both, glacio-isostatic adjustment (GIA) models that show limited and those which show more pronounced ice-load changes on the South Shetland Islands during the late Holocene, suggesting that some GIA model parameters for the South Shetland Islands (e.g.,

lithospheric thickness, mantle viscosity) need to be better constrained. Furthermore, my findings have implications for regional paleoclimatic reconstructions and on ice sheet modeling for the Holocene of the northwest Antarctic Peninsula region.

ZUSAMMENFASSUNG

Das Verständnis über das Holozän ist besonders wichtig, um die gegenwärtige Eisschilddynamik in den richtigen Kontext setzen zu können. So ist z.B. zu klären ob die derzeitige Eisschilddynamik ungewöhnlich ist oder eher als Teil der Holozänen klimatische Schwankungen zu sehen ist (Bentley et al., 2014). Kenntnis über die Entwicklung der antarktischen Eisschilde im letzten Jahrtausend ist dabei sehr wichtig, um das Verhalten dieser Eisschilde gegenüber verschiedenen Faktoren wie z.B. Meerespiegelanstieg, atmosphärische und Schwankungen von Atmosphären und Wassertemperatur abzuschätzen, und um den Rückzug der Aufsetzlinie über Holozäne und rezente Zeitskalen zu bestimmen. Ziel dieser Arbeit ist, neue Daten zur Rekonstruktion der Holozänen Gletscherrückzugsgeschichte auf King George Island, den südlichen Shetland Inseln und der nordwestlichen Antarktischen Halbinsel zu gewinnen. Die Rekonstruktion basiert auf morpho-sedimentären Studien von glazigene und küstennahe Landschaftsformen und ihrer assoziierten Sedimenten der eisfreien Landgebiete in der Maxwell Bay (King George Island), namentlich der Potter und Fildes Halbinsel.

Um die Ziele dieser Arbeit zu erreichen, habe ich folgende Methoden benutzt: (i) kosmogene Expositionsdatierungen und Datierungen mit der Radiokarbon Methode für eine absolute zeitliche Einordnung, (ii) stratigraphische und sedimentologische Methoden für relative Altersabschätzungen und für die Rekonstruktion der paläo-Umweltbedingungen, (iii) Kartieren mit geomorphologischem Schwerpunkt um die räumliche Verteilung der Landschaftssysteme zu erfassen (iv) und Untersuchungen mit dem Bodenradar (Ground Penetrating Radar, GPR) um die interne sedimentäre Struktur der küstennahen Landformen aufzulösen.

Ergebnisse der Radiokarbondatierung geben neue Altershinweise für das Einsetzen des Gletscherrückzugs auf der Potter Halbinsel. Demnach setzte der Gletscherrückzug erst bei oder vor ca. 7,8 ka cal BP ein, anstatt wie bisher angenommenem bei 9,5 ka cal BP. Meine Ergebnisse geben überdies Hinweise auf einen kurzlebigen Gletschervorstoß zwischen 7,2 und 7,0 ka cal BP. Dieser Gletschervorstoß steht wahrscheinlich im Zusammenhang mit einem Gletschervorstoß oder Gletscherstillstand, der auf den ganzen Südlichen Shetland Inseln zu dieser Zeit dokumentiert ist. Nichtdestotrotz bleiben die klimatischen Bedingungen, die mit diesem Gletschervorstoß in Verbindung stehen, weiter unklar. Im Gegensatz dazu zeigen Expositions- und Radiokarbon Alter auf der Fildes Halbinsel, dass glaziale Schwankungen während der letzten 7 ka minimal waren. Überreste von in Moränen erhaltenen Moosen konnten mit der Radiokarbon Methode datiert werden. Die Moränen entstanden in der Nähe der heutigen Gletscherfront zwischen 0,5 und 0,1 ka cal BP, während des letzten Gletschervorstoßes auf den Südlichen Shetland Inseln. Dieser Vorstoß wird im Zusammenhang mit der Verringerung der sommerlichen/jährlich Sonneneinstrahlung, welche an stärkerwerdende Westwinde der Südhemisphäre im Südozean gekoppelt ist, interpretiert: stärkere und womöglich mehr polwärts-verlagerte Westwinde sorgten für niederschlagsreichere Sturmfronten über den Südlichen Shetland Inseln, wodurch es dort zu mehr Eis Akkumulation kam.

Die Daten zeigen außerdem, dass zwischen 1,9 und 1,3 ka cal BP ein klimatisches Optimum auf der Fildes und der Potter Halbinsel erreicht war. Dieses Optimum dauerte bis zum letzten Gletschervorstoß an. Das Vorrücken während der letzten Phase des letzten Gletschervorstoßes bei einem stabilen relativen Meeresspiegel wurde anhand von GPR-Untersuchungen und Radiokarbon Datierungen eines Nehrung-Systems auf der Potter Halbinsel untersucht. Die Ergebnisse zeigen außerdem, dass das Vorrücken der Hakenbildung unterbrochen wurde. Dabei fiel die Unterbrechungsphase mit dem Einsetzen des beschleunigten isostatischen Zurückfederns in Folge

des Gletscherrückzugs nach des letzten Gletschervorstoßes zusammen. Der Haken-Wachstum begann erneut im späten 19th Jahrhundert, nachdem die Rate des isostatischen Zurückfedern nachließ, und setzt sich bis heute fort.

Die Erkenntnisse dieser Arbeit unterstützen sowohl die Modelle der glazial-isostatische Anpassung (GIA) mit beschränkter als auch die mit stärkterer Eismassen-Veränderungen auf den Südlichen Shetland Inseln während des späten Holzäns. Dies legt nahe, dass einige GIA Modellparameter für die Südlichen Shetland Inseln (z.B. Lithosphärenmächtigkeit, Mantelviskosität) besser bestimmt werden müssen. Des Weiteren haben meine Erkenntnisse Auswirkungen auf regionale Paläoklima-Rekonstruktionen und Eisschildmodellierungen für das Holozän der nordwestlichen Antarktischen Halbinsel.

ACKNOWLEDGEMENTS

To begin with, I thank Jorge Strelin who provided me the possibility to go to Antarctica and supervised my thesis during my stay in Córdoba. I also thank Dr. Gerhard Kuhn and Prof. Dr. Cornelia Spiegel who accepted and supervised my thesis as I moved to Bremerhaven. Moreover, I thank Prof. Dr. Martin Melles who agreed to act as external reviewer of the thesis.

I would like to thank all my colleagues and friends at CICTERRA-UNC, AWI and Bremen University, especially Dr. Ricardo Astini, Dr. Mateo Martini, Lucas Oliva, Dr. Santiago Maza, Dr. Julieta Novile, Dr. Johann Philip Klages, Dr. Kurt Martin Stange and Dr. Maximilian Zundel. They all are deeply thanked for their time, backing, and open ears.

Special many thanks go to Dr. Sebastian Lindhorst for moral support and for thoughtful and constructive advices. You shared your deep knowledge with me and supported an important part of my thesis in every aspect and at any time. Without you, the following thesis would not be reality.

I am very glad for the fieldwork assistance by Matias “Turco” Barrionuevo, Dr. Bulat Mavlyudov, Eliseo Flores, Marco “Marquito” Petit and Martin “Tincho” Argota. I am also especially grateful to share the fieldwork with Magnus “Jurgen” Makeschin, in very cold, rainy, snowy and windy conditions during long hours for several months. Special thanks go to the crews of the Uruguayan research station “Artigas”, the Russian Bellingshausen station, the King Sejong Antarctic station and the Argentine research station “Carlini” (former “Jubany”) and the adjoined German Dallmann-Labor (AWI) during the 2014 and 2015 field seasons for their cordial hospitality and invaluable logistical support. They all contributed to make this a memorable adventure.

For their adjuvant assistance with the sample processing and analysis I acknowledge Anke Toltz, Dr. Ruben Rosenkranz, and Susanne Wiebe, Rita Fröhlking and their team of student assistants, and also Christiane Schott and Maximiliano “Pepón” Medina.

Also to mention are Aysel Sorensen, Vera Kolb, Maria Petrogiannis and Leslie Sütterlin for always making things work.

I would also like to thank the Helmholtz Graduate School for Polar and Marine Research (POLMAR) for the opportunity to attend their program, in particular Dr. Claudia Hanfland.

I am grateful to my parents, for letting me always choose to do what I like and give me the chance of doing it. ¡Gracias viejines!

Finally and most importantly, the biggest thanks is reserved for my family: Nancy, who always backed me and never get tired of pushing me forward, and especially our two little daughters, Lara and Luna, who with just a smile transmute any kind of suffering into joy.

A esta tesis de doctorado se la dedico a mi amada Abuela, quien aún me sigue cuidando desde arriba. Que descanses.

Muchas gracias a todos.

Contents

CHAPTER 1: INTRODUCTION

1. AIMS OF THE STUDY

Although a relatively well-known deglaciation history after the Last Glacial Maximum (LGM; 25-20 calibrated age in thousands of years before present, ka cal BP) is now available for the Antarctic Peninsula region (Ó Cofaigh et al. 2014)(Fig. 1A), detailed information is lacking as on how deglaciation continued during the Holocene and on the timing of Neoglacial readvances. Understanding the Holocene is particularly important for providing the context for recent ice sheet change, by revealing whether it is unusual or is a part of Holocene natural variability (Bentley et al., 2014). The most recent millennia of Antarctic Ice Sheet history are important for evaluating the response of the ice sheet to various forcing agents such as sea-level rise, atmospheric and oceanographic temperature changes, for constraining past rates of grounding-line retreat (Bentley et al., 2014), and for the refinement of glacio-isostatic adjustment (GIA) models during this time period. The Holocene ice-unloading history of the northern Antarctic Peninsula region has long been debated (Roberts et al., 2011; Watcham et al., 2011; Whitehouse et al., 2012; Simms et al., 2012; Simms et al., 2018). New field data can help refine GIA models of post-LGM and Holocene deglaciation.

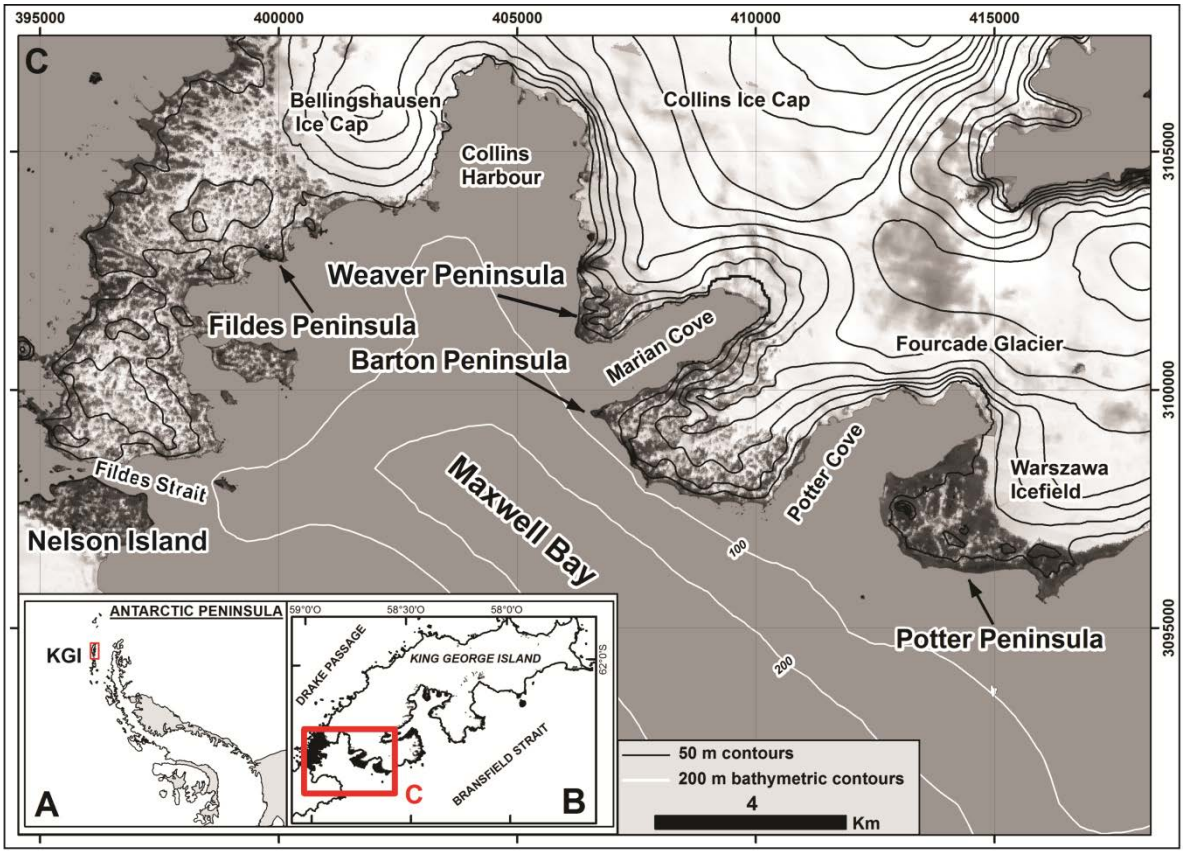

Figure 1. Geographic location of the working area. A) King George Island (KGI) belongs to the South Shetland Islands, wich are on the northwestern tip of Antarctic Peninsula. B) KGI is framed by the Drake Passage and the Bransfield Strait. Box marks the position of the study sites. C) Map of

ice-free areas around Maxwell Bay. Contour lines are from Antarctic Digital Database (http://www.add.scar.org/home/add7), bathymetry from GEBCO (Weatherall et al., 2015)

My research focuses on the Holocene terrestrial glacial chronology and related sea level fluctuations and geomorphological development in King George Island. The main objective of my work is to gain a better understanding of the nature and the timing of the deglaciation and associated climate-controlled processes in the northernmost part of the Western Antarctic Peninsula region. Thus, I am aiming at reconstructing the post-LGM deglaciation history by investigating the terrestrial record of different glacigenic and coastal landforms and associated materials (raised beaches, beach ridges, spit systems, isolation basins, moss banks, glacial erratics, moraines, etc.) from the on-shore ice-free areas around Maxwell Bay. To do so, I used stratigraphy, cosmogenic exposure dating, radiocarbon dating, geomorphological mapping and ground-penetrating radar (GPR) investigations.

2. SETTING

Located 120 km NW off of the Antarctic Peninsula, King George Island (62° 23′ S, 58° 27′ W) is the largest of the South Shetland Islands (SSI), (Fig. 1B). The island group is framed by the Drake Passage towards the NW and the Bransfield Strait towards the SE. At present, approximately 90% of King George Island's surface is covered by the Collins Ice Cap which has a maximum thickness of c. 400 meters (Blindow et al., 2010) (Fig. 1C). King George Island is subject to a maritime climate and regularly hit by cyclonic weather systems that move eastward along the Drake Passage (Kejna et al., 2013). Strength of circumpolar westerly winds increased since the 1970s, especially during the austral summer, accompanied by higher cloudiness and precipitation (van den Broeke, 2000; Turner et al., 2005; Stammerjohn et al., 2008; Montes-Hugo et al., 2009).

The annual mean air temperature on King George Island during the time period 1948 to 2011 CE was -2.5 ºC (Kejna et al., 2013), but temperatures are often above zero during summer. However, the average annual temperature of the South Shetland Islands has increased by almost 3°C since the middle of the last century (Vaughan et al., 2003; Meredith and King, 2005), thus far exceeding average global warming by 1.5-1.8ºC (Sánchez-Lugo et al., 2018). Warming caused rapid glacial retreat (Steig et al., 2009; Osmanoğlu et al., 2013) resulting in the collapse of many permafrost-related and glacigenic landforms (Bockheim et al., 2013). Moreover, ice retreat exposed coastal areas characterized by moraines, raised beaches, isolation basins and bedrock outcrops, leaving fresh exposures for geomorphological and stratigraphic surveys. The ice-free areas are located mainly around the southern bays of King George Island, which are the sites with the greatest concentration of research activities in Antarctica. One of them is Maxwell Bay, where Potter Peninsula and Fildes Peninsula are situated.

2.1 Deglaciation of King George Island after the LGM

The Last Glacial Maximum (LGM) of the Antarctic Peninsula took place between 25-20 ka cal BP, when an ice sheet extended towards the shelf edge (Ó Cofaigh et al., 2014). A smaller ice cap independent from that based on Antarctic Peninsula, positioned at the outer continental shelf 50 km north of its present location covered the South Shetland Islands (John & Sugden, 1971) (Fig. 2). In Maxwell Bay the ice was grounded with a thickness of at least 570 m (Simms et al., 2011). Initial deglaciation of the bay associated with decoupling of the ice sheet from the sea floor occurred between 14.8 and 14.1 ka cal BP (Simms et al. 2011), whereas on-land, deglaciation initiated not earlier than 15.5 ± 2.5 ka BP (Seong et al., 2008). Following the onset of deglaciation, the ice sheet further retreated and became floating with a stable position at 10.1 ka cal BP (Simms et al., 2011).

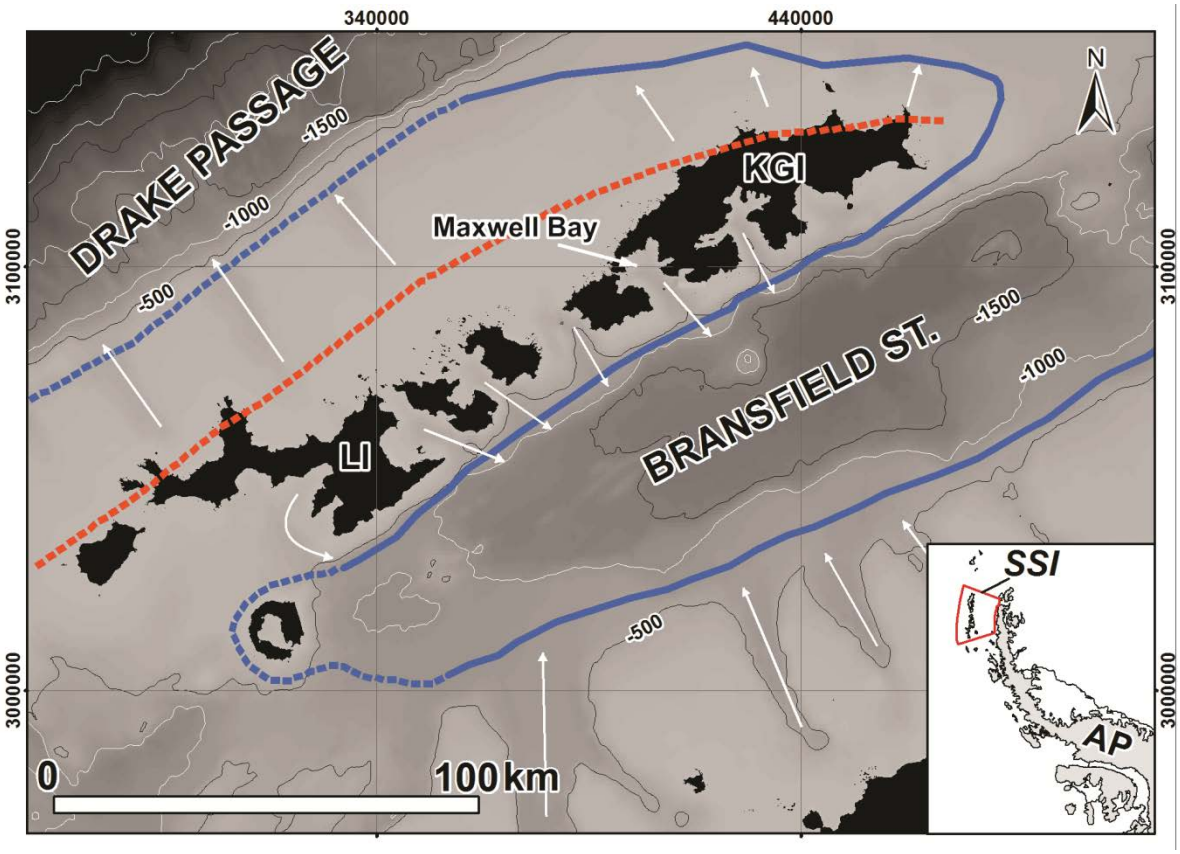

Figure 2. Extension of the LGM ice cap (blue full and dotted line) and its axis (red dotted line). The dashed red line represents the ice cap axis. The white arrows indicate the direction of the ice flow (after Simms te al., 2011). Antartic Peninsula (AP), South Shetland Island (SSI), King George Island (KGI) and Livingston Island (LI). Bathymetric contours every 500 m (Weatherall et al., 2015).

During the early Holocene, rapid glacial retreat took place in Maxwell Bay from 10.1 to 8.2 ka cal BP. The inner bay was ice free by 9.1 ka cal BP, and the entire bay became ice free by 5.9 ka cal BP, except for the tributary fjords, including Potter Cove, which were still filled with ice (Simms et al., 2011). On land, raised beaches across the South Shetland Islands up to elevations of 18 m amsl (John and Sugden, 1971; Fretwell et al., 2010; Hall, 2010) mark the isostatic rebound of

the island chain and surroundings in response to glacial retreat since the LGM (John and Sugden, 1971; Barsch and Mäusbacher, 1986; Bentley et al., 2005, Fretwell et al., 2010; Watcham et al., 2011). The raised beaches have been dated with ages up to c. 6 ka cal BP (Barsch and Mäusbacher, 1986). The progressive ice retreat is associated with the formation of glacial polished surfaces in Barton and Weaver Peninsula (Fig. 1C), and with the onset of lake sedimentation in Fildes and Byers Peninsula, Livingston Island (Fig. 2) between 10 and 8 ka BP (Seong et al., 2008; Watcham et al., 2011; Toro et al., 2013; Oliva et al., 2016; Roberts et al., 2017). Moreover, the first birds started to colonize ice-free areas in Potter Peninsula at c. 7.5 ka cal BP (del Valle et al., 2007).

Deglaciation on land continued during the mid-Holocene Climatic Optimum (3.2-2.7 ka cal BP; Björk et al., 1991a and b), with glaciers retreating to positions landward of their present limits. Formation of peat banks and lakes sediments and establishments of bird colonies continued during that time (del Valle et al., 2002). However, between c. 5.9 and 2.6 ka cal BP, sea surface temperatures decreased and sea-ice cover increased in Maxwell Bay (Milliken et al., 2009). After that, a neoglacial period commenced, with coves still filled with ice. The neoglacial period ended at 1.7 ka cal BP (Simms et al., 2011).

Deglaciation of tributary fjords to Maxwell Bay initiated after 1.7 ka cal BP (Simms et al., 2011; Wölfl et al., 2016). Marine and terrestrial records generally indicate warmer temperatures between 1.4 and 0.55 ka cal BP and a cooler period between 0.55 and 0.05 ka cal BP, tentatively linked to the northern hemisphere Medieval Warm Period and the Little Ice Age (LIA), respectively (Hall, 2007; Hass et al., 2010; Monien et al., 2011; Majewski et al., 2012). The last glacier re-advance on King George Island took place between 0.45 and 0.25 ka cal BP (Yoon et al., 2004; Yoo et al., 2009; Simms et al., 2012). In Maxwell Bay, raised beaches at 7.5 to 4 m masl show a morphogenetic relationship to moraines from former outlet glaciers (John and Sugden, 1971; Sugden and John, 1973). Those beaches, termed “6-m-beaches” by John and Sugden (1971) interfinger with moraines regarded as terminal moraines of the last glacial re-advance (Sugden & John, 1973; Clapperton and Sugden, 1988, Simms et al., 2012). This indicates that such moraines formed coeval with the 6-m-beaches during the last glacial re-advance (John and Sugden, 1971; Sugden and John, 1973; Hall 2010).

2.2 Potter Peninsula

Unlike other ice-free peninsulas around Maxwell Bay, this peninsula is largely covered by till deposits with associated sediments containing datable organic remnants. Therefore, Potter Peninsula is an ideal place to address the objectives of this thesis.

Potter Peninsula is embedded on its S and E coast within Maxwell Bay and borders at its NE side the Fourcade Glacier, an outlet glacier from the Collins Ice Cap, occupying the head of Potter Cove (Fig. 1C). On the other hand, the Warszawa Icefield limits the eastern border of the ice-free area of Potter Peninsula. As elsewhere in King George Island, Potter Peninsula is generally ice-free during summer times although snow and ice patches are commonly present. The Three Brothers Hill (196 m) is the most prominent morphological feature, being an andesitic plug with columnar jointing, which marks the final stage of activity of a Paleogene stratovolcano. This volcano erupted lava flows and pyroclastic rocks, and its related pyroclastic rocks and hypabyssal intrusions are mainly responsible for the lithology of Potter Peninsula (Kraus and del Valle, 2008). The landscape of Potter Peninsula is characterized by glacial landforms, mainly moraines surrounded by a coastal environment with active, Holocene (Lindhorst and Shutter 2014, Heredia Barión et al., accepted, Chapter 2; Heredia Barión et al., reviewed, Chapter 3) and probably older raised marine features (John and Sugden, 1971).

2.3 Fildes Peninsula

Better resolved GIA models are needed to examine the impact of future Antarctic Peninsula ice-melt on rates of regional-global sea-level rise (Lindow et al., 2014). Such models rely on well-dated geomorphological features and lake records from a limited number of ice-free areas in Antarctica such as Fildes Peninsula in the southwest of King George Island to test their performance (Watcham et al., 2011)(Fig. 1). Fildes Peninsula is the most prominent ice-free area of King George Island (Fig. 1B and C). The peninsula is a tableland composed of raised marine platforms at an altitude up to 180 m (John and Sugden 1971), shaped on Late Cretaceous to Paleogene basic volcanic rocks (Barton 1965). Fildes Strait separates Fildes Peninsula from Nelson Island, with Maxwell Bay to the east, and the open waters of the Drake Passage on its W coast (Fig. 1). The coastline has an indented shape with coves and is characterized by sea cliffs and stacks (Hall, 2003).

The Bellingshausen Ice Cap occupies the N of Fildes Peninsula (Fig. 1C). The ice is bounded by prominent moraines (Shetland I moraines; Hall, 2007) exposing lake, marine and fluvial sediments detached and transported presumably during the most extended glacier advance of the last 7 ka, after 1.3 ka cal BP (Hall, 2007; Heredia Barión et al., in prep; Chapter 4). On the NW coast of the peninsula a prominent marine platform exists at c. 35-40 masl, which cuts into volcanic bedrock, and which is <7 km long and as much as 1 km wide (John and Sugden, 1971). This feature is flat to gently undulating and seaward sloping (Hall, 2003). On its surface it is possible to find granitic erratic blocks (Barsch and Mäusbacher, 1986; Hall, 2003), whereas most of other erratics on King George Island are composed of basic, quartz-free lithologies. I surveyed and classified all of the limited number of large (>50 cm diameter) boulders on the NW glacial foreland and sampled granitic erratics (Heredia Barión et al., in prep., Chapter 4) Another

characteristic of the area is the presence of several lakes filling over-deepened glacial basins. Radiocarbon ages obtained from marine-terrestrial transition sediments from lakes and raised beaches have been used to reconstruct past changes in local RSL at several sites across the South Shetland Islands, having a highstand at 18-15 m amsl during 8.0-7.0 ka cal BP (Watcham et al., 2011).

3. OUTLINE OF THESIS

This thesis is subdivided into five chapters.

Chapter 1 introduces the overall aims and regional setting of this study, including its deglaciation history after the LGM.

Chapter 2 shows the sedimentary architecture of a gravel spit based on GPR data, and a new concept for the development of polar gravel spits and the interplay of glacier retreat, glacio-isostatic adjustment and coastal progradation is presented, allowing for the prediction of future coastal developments in comparable polar settings. Chapter 3 focuses on the geomorphological evolution and radiocarbon chronology of glacial fluctuations in Potter Peninsula. The presented data show that the deglaciation phase on Potter Peninsula started several hundreds of years before the generally accepted age and lasts until the present. Furthermore, it is likely that during the Holocene, the glacier limit advanced towards the outer Potter Cove several times, while occupying a bigger proportion of the peninsula than today. Chapter 4 is based on sediment core studies, radiocarbon and surface exposure dating chronology. This chapter shows evidence for a phase of relatively fast mid-Holocene glacier retreat on Fildes Peninsula, after 7 ky cal BP onwards. I also show that Fildes Peninsula only experienced one glacier readvance during the Holocene. This last glacier re-advance most likely occurred several centuries ago.

Chapter 5 presents the conclusions of this thesis.

Chapter 2 is based on a manuscript accepted by “Earth Surface Processes and Landforms”. Chapter 3 was sent to “The Holocene” and reviewed with minor revisions, whereas chapter 4 is based on a manuscript in preparation for publication in Nature´s “Scientific Reports”.

4. OVERVIEW OF SELECTED METHODS

4.1 Ground-penetrating radar (GPR)

Ground-penetrating radar (GPR) is based on the transmission of high-frequency electromagnetic pulses that are partly reflected at electromagnetic discontinuities in the subsurface. The amplitude of the reflected signal is recorded as a function of

the two-way-travel time (TWT). GPR always images an interference pattern caused by the thickness of individual electromagnetically uniform sediment packages and the wavelengths present in the GPR signal. GPR data from the spit-system described in chapter 2 were acquired by means of a GSSI (Geophysical Survey Systems Inc.) SIR-3000 GPR with a 200 MHz antenna; operated in discrete mode (trace increment 0.05 m). Post-processing of GPR data using the software ReflexW (Sandmeier Geo) comprises data editing, subtraction of low-frequency signal components (dewow), frequency filtering, gain adjustment, topographic migration and correction for along-profile topography. A mean subsurface radar-wave velocity of 0.08 m ns-1 was determined based on the analysis of diffraction hyperbolas. Interpretation of GPR data is based on migrated as well as non-migrated data, the latter being essential for a correct tracing of ringing multiples and diffraction hyperbolas. Only non-migrated data are shown in this work. Data interpretation follows the approach of radar-facies interpretation (Gawthorpe et al., 1993; Bristow, 1995). Analogous to the concepts of seismic interpretation introduced by Mitchum et al. (1977), the term 'radar facies' describes a two or three-dimensional set of reflections with similar characteristics, bordered by 'radar surfaces' (Bristow, 1995). Consequently, the interpretation of unconformities in this thesis is based on the tracing of reflection terminations and abrupt changes of the radar facies.

4.2 Cosmogenic exposure dating

I used cosmogenic isotope analysis to produce exposure ages for erratic boulders remnants of glacial retreat. The cosmogenic isotope concentration in a rock is proportional to the length of time that it has been exposed on, or close to the earth's surface (Balco, 2011). The production rate (amount of cosmogenic isotopes produced each year per gram of the relevant mineral) of cosmogenic isotopes varies both spatially and in time, typically due to atmospheric depth and magnetic field effects.

For sample processing I remove the upper few centimetres of sub-horizontal exposed erratic surfaces with a hammer and chisel. We assume that the rock surface has been completely shielded until its first exposure by glacial retreat. The shapes, sizes and positions of the sampled boulders suggest recent overturning is very unlikely. We measured the skyline of each sample with a clinometer and compass for topographic shielding, determined using the online geometric shielding calculator, v. 1.1 (Balco et al., 2008). We minimized the possibility of burial by snow by sampling at well-exposed localities with flat and snow-free ground and collected samples from positions away from slopes or cliffs to minimize the probability of post-depositional movement. With the support of a GPS Trimble Pathfinder ProXH we performed differential GPS (dGPS) surveys of the locations of erratic boulders sampled for exposure dating. As geodetic reference, we used the landmark DALL 66019M002 (S62°14′16.335″, W58°39′52.364″, ellipsoidal height 39.376 m) located on the Argentine Carlini base, up to 17 km away from the

sampled erratics. Post-processed uncertainties for the samples were less than 0.1 m in the altitudinal as well as in the horizontal. All coordinates are based on the WGS84 ellipsoid.

Cosmogenic exposure dating is a powerful chronological tool for reconstructing glacier and ice sheet extent and thickness. It has not been widely applied on South Shetland Islands, mainly because quartz-rich (mainly granitic) bedrock and erratics required for Berylium-10 (^{10}Be) isotope analysis are largely absent from the basaltic-andesitic volcanic-arc environment of the islands. Elsewhere in the Antarctic Peninsula region, where granitic erratics are more prevalent, ^{10}Be exposure dating has proved successful in establishing the timing and rate of deglaciation from Last Glacial Maximum limits (Johnson et al., 2012; Davies et al., 2017; Johnson et al., 2017). Such dating is particularly useful in areas with few sedimentary deposits, insufficient organic material for radiocarbon dating or where large marine reservoir effects prevent accurate radiocarbon dating (Seong et al., 2008; Balco and Schaefer, 2013; Glasser et al., 2014; Ó Cofaigh et al., 2014). I obtained ^{10}Be exposure ages from the limited number granitic erratics, remnants of Bellingshausen Ice Cap retreat following the LGM (chapter 4). These erratics were most likely transported from the Peninsula area at the LGM when the South Shetland Islands and Antarctic Peninsula ice sheets coalesced. For cosmogenic isotope dating, ^{10}Be is most commonly used as it has the best determined production rate and can be measured at low concentrations (Balco, 2011).

Purified quartz separates were prepared from the rock samples at Bremen University cosmogenic nuclide laboratory. We used standard physical rock preparation, using a jaw crusher, sieves (125 µm–1000 µm) and Frantz magnetic separation up to 1.5 A. We further cleared the non-magnetic fraction of unwanted phases such as feldspar and carbonates through chemical purification with a 30% HCl + 0.03% H_2O_2 leaching. The resulting, almost pure quartz and feldspar sample was further cleaned of meteoric beryllium by 3 steps of weak 2% HNO_3 + 2% HF leaching. We weighed the mass before and after, to keep track of how much mass had been lost.

Separation of beryllium from the quartz separates was carried out at the Institute for Geology und Mineralogy, University of Cologne, Germany. Quartz purity was determined prior to dissolution by ICP-OES. The samples were spiked with ~300 micrograms of commercially available Be carrier (Scharlab, 1000 microgram/l Berylium ICP standard solution, batch number 14569501). After digestion in HF acid, remaining insoluble fluoride salts were heated several times in the presence of aqua regia and aliquot of the sample was taken for an ICP-OES measurement before the sample underwent column separation using the single-step column procedure (Binnie et al., 2015). The separated $Be(OH)_2$ was co-precipitated alongside Ag (Stone et al., 2004) with a respective mass ratio of around 1:5, before being pressed into Cu targets for measurement on Cologne AMS, Institute of

Nuclear Physics, University of Cologne (Dewald et al., 2013). $^{10}Be/^{9}Be$ AMS measurements were normalised to the standards of Nishiizumi using the nominal values reported in Nishiizumi et al. (2007). A blank was prepared in tandem with the samples and ^{10}Be concentrations are reported following subtraction of the ^{10}Be atoms measured in the blank. Though sample concentrations are relatively low the maximum blank subtraction was <6%. Analytical uncertainties for the ^{10}Be concentrations were derived by summing in quadrature the uncertainty in the mass of Be added during sample processing (estimated to be 1% at 1 sigma) and the AMS measurement uncertainties of both the samples and blank.

^{10}Be exposures ages were calculated using CRONUS-Earth online calculator version 3 (http://hess.ess.washington.edu/math/v3/v3_age_in.html; see Balco et al. 2008). As is normal in the Antarctic Peninsula region, we used the Antarctic ("Ant") pressure flag and the scaling scheme "LSDn" (Lifton et al., 2014). We employed the scaling model "LSDn" because it is physically based, scaling neutrons, protons and muons independently (Johnson et al., 2017). For sites in Antarctica, using the LSDn scaling yields smaller systematic biases compared with the scaling scheme "Lm" (Lal, 1991; Stone, 2000; Balco et al., 2008; Johnson et al., 2017). No snow cover or erosion correction was applied following the assumptions given by in the region (Johnson et al., 2012; Lindow et al., 2014; Glasser et al., 2014; Ó Cofaigh et al., 2014; Johnson et al., 2017). We applied a quartz density of 2.7 g cm-3 for the samples and no erosion was considered in the age calculations because we did not find clear evidence on the surfaces sampled and the lithologies are not prone to substantial erosion.

I chose to measure cosmogenic ^{3}He in basaltic boulders surrounding the Three Brothers Hill because this nuclide accumulates in pyroxene and olivine crystals, which are present as phenocrysts in Potter Peninsula basalts (chapter 3). The basalts of the peninsula have been K-Ar dated at 49 ± 1 to 42 ± 1 Ma (cf. Smellie et al., 1984). Cosmogenic ^{3}He is stable, and therefore accumulates within a rock, recording the total time of exposure to cosmic rays that it has experienced.

I used four samples of 1 kg weight each from basaltic boulders. Some of them showed striated surfaces. To confirm the mineralogy and rock type of the samples, we made thin sections at CICTERRA, Córdoba, Argentina. The thin section analysis showed olivine and clinopyroxene phenocrysts, which represented 5-10 % of the total sample mass, with a modal grain size of ca. 200-500 µm.

To process the samples, we used standard physical rock preparation, using a jaw crusher, sieves (125 µm-1000 µm) and Frantz magnetic separation up to 1.5 A at Bremen University, Germany. We used as a first step a low amperage (ca. 0.10-0.20 A) to get magnetic grains separated from the olivine and pyroxene. The olivine and pyroxene represented the non-magnetic fraction. We mainly used a

slope on the machine of up to 24°. After that, we ran the non-magnetic fraction again, this time using 0.20-0.30 A. This left the nonmagnetic fraction with concentrated olivine and pyroxene, plus any other non-magnetic fractions. If those included feldspars, we ran the non-magnetic fraction again, this time using 1.5 A. The pyroxene and olivine went to the magnetic side, the feldspar to the non-magnetic. Using di-iodomethane (DIM, ρ = 3.3 g cm^{-3}) we concentrated the olivines and pyroxenes further. If the olivine and pyroxene concentrate had matrix still attached, even after magnetic or heavy-liquid separation, we treated them with dilute 5% HNO_3 to clean them. This was done in a bottle or beaker, in an ultrasonic bath, for c. 30 minutes. We weighed the masses before and after, to keep track of how much mass was lost. We obtained pure pyroxene ± olivine separates for each sample. Those samples were examined under a binocular microscope and back-picked for purity. Unfortunately, of the five samples, the mass of the separate of one sample was too small. Consequently, just four samples were further analysed.

The remaining steps of sample analyses were performed at the noble gas laboratory of GFZ Potsdam, Germany. Pyroxene separates were squeezed between two hard-metal plates in an ultrahigh vacuum crusher in an attempt to determine the trapped $^3He/^4He$. After crushing, pulverized samples were sieved to >100 µm before heating in order to minimize the contribution of atmospheric He irreversibly adsorbed to the grains (Protin et al., 2016). They were subsequently wrapped in Al foil and loaded to the sample carrousel above the resistance-heated extraction furnace, which was baked at 100°C for one week. Noble gases were extracted in two heating steps at 900 and 1750°C (with an initial 600°C step for sample 02-Potter), purified in two Ti sponge and foil getters and two SAES (ZrAl) getters, and measured in a Helix SFT mass spectrometer using procedures similar to those reported by Niedermann et al. (1997). ^4He blank values were (2-10) $\times$ 10^{-12} cm^3 STP for crushing extractions, (4-5) $\times$ 10^{-12} cm^3 STP for 600 and 900°C heating steps and (18-40) $\times$ 10^{-12} cm^3 STP for 1750°C steps. He concentrations were calculated by peak-height comparison with our in-house noble gas standard, an artificial mixture of the five noble gases in nitrogen with a $^3He/^4He$ ratio of (21.66 ± 0.24) $\times$ 10^{-6} (Blard et al., 2015). Two aliquots of the CRONUS-P pyroxene standard material were measured alongside the samples and gave ^3He concentrations of 4.86 ± 0.10 $\times$ 10^9 and 4.79 ± 0.10 $\times$ 10^9 at g^{-1}, which agree within 2σ uncertainties with the global mean value of 5.02 ± 0.12 $\times$ 10^9 at g^{-1} (Blard et al., 2015).

To calculate ^3He exposure ages, the ^3He concentrations specifically produced by cosmic ray irradiation ($^3He_{cosmo}$) must be determined. Ideally, He in phenocrysts is a mixture of only magmatic and cosmogenic components. If so, the concentration of cosmogenic ^3He is calculated using the following equation (Niedermann, 2002):

$$^3He_{cosmo} = {}^4He_{heat} \times (^3He/^4He_{heat} - {}^3He/^4He_{crush})$$

$^4He_{heat}$ is the ^4He concentration and $^3He/^4He_{heat}$ the isotope ratio determined during stepwise heating, while $^3He/^4He_{crush}$ is the isotope ratio determined by crushing the mineral separates in vacuo. The latter method selectively releases gases trapped in fluid and melt inclusions. In contrast, heating also releases gases from the crystal lattice, such as cosmogenic He. The cosmogenic component is thus calculated by subtracting trapped ^3He from the total ^3He that is released by heating of the sample powders in vacuo. However, in our samples $^3He/^4He_{crush}$ ratios were systematically higher than $^3He/^4He_{heat}$, so exposure ages calculated according to the equation above are negative. This is because in old basalts such as those analyzed here, radiogenic 4He produced by decay of U and Th (either in the phenocrysts or implanted form the basalt matrix; Williams et al., 2005) and ^3He generated by the thermal neutron capture reaction $^6Li(n, \alpha)^3H \rightarrow ^3He$ (Dunai et al., 2007) may be present as well. Indeed, the $^3He/^4He_{crush}$ values were lower than expected for typical magmatic He (Table SM 2), indicating that radiogenic He dominates over magmatic He and is even extracted by crushing. Therefore, instead of using $^3He/^4He_{crush}$ in the equation above, we assumed that magmatic He is negligible and thus non-cosmogenic He is essentially represented by radiogenic He with a typical $^3He/^4He$ ratio of 0.028×10^{-6} (0.02 Ra, where Ra is the atmospheric $^3He/^4He$ ratio). To be conservative, a 100% uncertainty was assigned to that value. Because of the dominance of radiogenic He, which prevented a determination of the magmatic $^3He/^4He$ ratio as some radiogenic He was even released by crushing, a mere correction for radiogenic ^4He based on U and Th contents (Blard and Farley, 2008) is not feasible for these samples.

The exposures ages were calculated using the CRONUScalc calculator (Version 2.0; Marrero et al., 2016) with the time-dependent Lal (1991)/Stone (2000) scaling model (Lm) for altitude at Antarctic pressure conditions and the primary calibration data set for ^3He in pyroxene (Borchers et al., 2016), which yields a long term sea-level high latitude (SLHL) scaled production rate of 122 ± 13 at g^{-1} yr^{-1} (Borchers et al., 2016). External age uncertainties in Supplemental Table S2 include production rate uncertainties. Using other scaling models (eg. Lifton-Sato-Dunai, Lifton et al., 2014), the exposure ages change by up to c. 6%. We report both internal and external uncertainties, but following Balco et al. (2008) we use external uncertainties because we compare the obtained exposure ages with calibrated AMS radiocarbon ages from the excavated sedimentary sequences on the peninsula and other radiocarbon and cosmogenic exposure ages at the South Shetland Islands.

4.3 Radiocarbon dating

Absolute age data were obtained by AMS radiocarbon dating of mosses, seaweed, marine mollusk shells, bird and seal bones penguin bone. To reduce the risk of contamination with modern material, all samples for dating were taken from fresh outcrops, at least 0.3 m below the surface, packed in zip-lock bags and stored at 4 °C. Sample preparation for samples was undertaken at the Alfred Wegener

Institute Helmholtz Centre for Polar and Marine Research and the British Antarctic Survey. Sample measurements and corrections for $^{13}C/^{12}C$ ratio and calculation of Conventional Radiocarbon Ages were undertaken by ETH Zürich and Beta Analytical Inc., USA. Local reservoir corrections (ΔR) for marine samples as reported for the SSI are in a broad range of about 700 to 1100 years (Curl, 1980; Björck et al., 1991; Berkman and Forman, 1996; Milliken et al., 2009; Hall et al., 2010; Hass et al., 2010; Watcham et al., 2011). Hall et al. (2010), based on paired radiocarbon and uranium–thorium dates of Antarctic solitary corals, proposed a ΔR of 791 ±121 years. This local reservoir age is further supported by results of Simms et al. (2012) who used optical-stimulated luminescence dating of cobble surfaces to investigate the depositional ages of beach ridges on KGI. Due to the verification with two independent dating methods, the local reservoir correction proposed by Hall et al. (2010) was used in this study. Calibration of conventional radiocarbon ages was done using the software Calib (v7.0.4, Stuiver and Reimer, 1993) and the calibration curve Marine13 (Reimer et al., 2013). Calibrated ages are rounded to the next decade and provided as median of the probability distribution with 2σ error range (95.4 % probability).

4.4 Stratigraphical logging

Trough satellite and aerial imagery I located recently ice-free areas of the island, with potential stratigraphic outcrops. Once in the field I tested the selected points to be surveyed to find suitable outcrops for stratigraphical logging. I made stratigraphic logs from pit dugs, and I characterized them using textural criteria, fabric, composition, sedimentary structures and the stratigraphic relationships existing between different depositional units (chapter 3 and 4). For a better facies interpretation I collected samples for textural studies (chapter 3). I digitalized the stratigraphical profiles with the software SedLog 3.0 (Zervas et al. 2009).

4.5 Geomorphological mapping

Geomorphological mapping is essential for accurately locating and interpreting potential outcrops and landforms to be surveyed. I carried out geomorphological mapping of Potter Peninsula and Fildes Peninsula (chapter 2-4) through interpretation of geomorphological features in the field combined with the study of satellite images and orthorectified panchromatic aerial images. Then, I used the software ArcMap to digitalize and georeferenciate the mapped landforms from the surveyed localities.

5. STATEMENT OF CONTRIBUTION FROM AUTHOR AND CO-AUTHORS

Three scientific manuscripts have been prepared that are presented in chapters 2-4.

Contributions to chapter 2/ Heredia Barión P., Lindhorst S, Schutter I, Falk U, Kuhn G. 2018. Reaction of a polar gravel spit system to atmospheric warming and glacier retreat as reflected by morphology and internal sediment geometries (South Shetland Islands, Antarctica). Earth Surface Processes and Landforms: doi:10.1002/esp.4565.

The PhD candidate together with Lindhorst S. wrote and prepared the manuscript, interpreted GPR data, and did radiocarbon dating. The PhD candidate also designed and conceived the figures. Furthermore, Lindhorst S. as well as Schutter I. undertook GPR fieldwork and data processing. Falk U. processed data on wind speed and direction. Kuhn G. reviewed and edited the manuscript.

Contributions to chapter 3/ Heredia Barión P A, Strelin J A, Spiegel C, Wacker L, Niedermann S, Kuhn G. (submitted to The Holocene, reviewed with minor revisions). Holocene glacial dynamics and geomorphology of Potter Peninsula, King George Island (NW Antarctic Peninsula).

The PhD candidate conceived and wrote the manuscript. He also designed the figures and undertook sampling for radiocarbon dating and ^{3}He exposure dating, and processed the samples together with Strelin J A. Spiegel C. edited the manuscript as well as provided laboratory facilities for physical sample processing prior to ^{3}He exposure dating. Wacker L. and Niedermann S. did radiocarbon dating and analyzed noble gases for ^{3}He exposure dating respectively. Kuhn G. reviewed and edited the manuscript.

Contributions to chapter 4/ Heredia Barión P, Roberts S J, Spiegel C, Binnie S A, Wacker L, Davies J, Gabriel I, Jones V, Blockley S, Pearson E, Juggins S, Foster L, Kuhn G. (in prep. for publication in Nature´s Scientific Reports). Mid–late Holocene deglaciation of northern Fildes Peninsula, King George Island, NW Antarctic Peninsula.

The PhD candidate designed the research, undertook fieldwork, sample collection and conducted cosmogenic nuclide dating laboratory analyses together with Binnie S A. and interpreted the results. The PhD candidate also conceived and wrote the manuscript, figures and tables along with Roberts S J, Davies J. and Gabriel I. Spiegel C. provided laboratory facilities for rock processing prior to ^{10}Be exposure dating, while Wacker L. and Kuhn G. undertook radiocarbon dating. Roberts S J. and Pearson E. collected, dated and analysed data from the Kiteschee core with Davies J, Jones V. (diatom analysis) and Gabriel I, Blockley S. (tephra counting, tephrochronology and geochemical identification of tephra layers). Roberts S J, Pearson E, Juggins S, and Foster L. re-evaluated GDGT-based temperature calibrations and GDGT-MSAT temperature reconstructions for the Yanou Lake record. Juggins S, Spiegel C, Binnie S A, Kuhn G, Pearson E. and Juggins S. edited the manuscript and all authors commented on it.

CHAPTER 2: REACTION OF A POLAR GRAVEL-SPIT SYSTEM TO ATMOSPHERIC WARMING AND GLACIER RETREAT AS REFLECTED BY MORPHOLOGY AND INTERNAL SEDIMENT GEOMETRIES (SOUTH SHETLAND ISLANDS, ANTARCTICA)

Pablo Heredia Barión[1,2*], Sebastian Lindhorst[3], Ilona Schutter[3], Ulrike Falk[1], Gerhard Kuhn[1]

[1] Alfred Wegener Institute, Helmholtz Center for Polar and Marine Research, Geosciences Division, Am Alten Hafen 26, 27568 Bremerhaven, Germany, pablo.heredia@awi.de

[2] University of Bremen, Department of Geosciences, Klagenfurterstr. 2-4, 28359 Bremen, Germany

[3] University of Hamburg, Institute for Geology, Bundesstr. 55, 20146 Hamburg, Germany

ABSTRACT

Sedimentary architecture and morphogenetic evolution of a polar bay-mouth gravel-spit system are revealed based on topographic mapping, sedimentological data, radiocarbon dating and ground-penetrating radar investigations. Data document variable rates of spit progradation in reaction to atmospheric warming synchronous to the termination of the last glacial re-advance (LGR, 0.45-0.25 ka BP), the southern hemisphere equivalent of the Little Ice Age cooling period. Results show an interruption of spit progradation that coincides with the proposed onset of accelerated isostatic rebound in reaction to glacier retreat. Spit growth resumed in the late 19th century after the rate of isostatic rebound decreased, and continues until today. The direction of modern spit progradation, however, is rotated northwards compared to the growth axis of the early post-LGR spit. This is interpreted to reflect the shift and strengthening in the regional wind field during the last century. A new concept for the interplay of polar gravel-spit progradation and glacio-isostatic adjustment is presented, allowing for the prediction of future coastal evolution in comparable polar settings.

KEYWORDS

Ground-penetrating radar; polar gravel beaches; glacio-isostatic adjustment; deglaciation; Antarctic Peninsula

1. INTRODUCTION

A spit is a wave-built sediment body attached to a headland on one end and terminating in open waters on the other (Evans, 1942). Gravel spits prograde by arcuate-shaped accretion of gravel ridges (Bluck et al., 2001). Among other morphologies of barrier coasts, they are typical for comparable sheltered coastal

environments and tend to be best developed in areas where short-period waves approach the coast at a high angle (Otvos, 2012; Cooper et al., 2015). In high latitudes, spits often consist of cobbles and boulders derived from moraines in upstream direction. Periglacial and polar beach systems are subjected to glacio-isostatic movements and consequently varying relative sea level. This results in a complex sedimentary architecture due to shifts in sediment supply and depocenters (Orford et al., 2002), as well as, the accommodation space, i.e. the space which is available for sedimentation. Polar beach systems are valuable archives of sea level, past sea-ice conditions as well as the wave- and storm climate (Baroni and Orombelli, 1991; Møller et al., 2002; Hall and Perry, 2004; Santana and Dumont, 2007; Mason 2010; St-Hilaire-Gravel et al., 2010, 2015; Lindhorst and Schutter, 2014; Simkins et al., 2015; Nielsen et al., 2017).

Morphodynamics of gravel spit formation in mid-latitude settings is well understood (Forbes and Taylor, 1987; Forbes et al., 1995; Tamura, 2012; Bujalesky and Gonzalez Bonorino, 2015; Burningham 2015). The same is valid for the involved main controlling factors: coast-oblique incident waves that cause a significant longshore drift, the availability of a sediment source in the up-drift direction, and wave refraction around the growing tip of the spit leading to a reduction in alongshore-transport capacity and, as such, triggering sedimentation (Bluck et al., 2001; Nielsen and Johannessen, 2009). However, only few studies have focused on the dynamics of gravel beaches in polar regions (St-Hilaire-Gravel et al. 2012, 2015; Lindhorst and Schutter, 2014; Strzelecki et al., 2015, 2018) and there still is a gap in knowledge on the evolution, the sedimentary dynamics and the resulting internal architecture of gravel-spit systems developed under the circumstances of rapid atmospheric warming and associated changes of wind climate and relative sea level. This study aims at filling this gap by revealing the genesis of, and by providing a concept for, the evolution of polar gravel-spit systems that developed during a phase of accelerated deglaciation and subsequent crustal isostatic adjustment.

1.1 Regional setting

Study site

The studied spit is about 350 m wide and 280 m long, and located at the mouth of Potter Cove, a tributary fjord of Maxwell Bay situated in the SW of King George Island (Figures 1-3). King George Island (KGI, 62° 23′ S, 58° 27′ W) is the largest of the South Shetland Islands (SSI), located 120 km NW of the Antarctic Peninsula (AP). The Drake Passage towards the NW and the Bransfield Strait towards the SE frame the island group. About 90 % of the island is covered by the Collins Ice Cap, which elevates to 700 m above present mean sea level (amsl) (Rückamp et al., 2011; Osmanoğlu et al., 2013). Outcropping bedrock and moraines, and active and raised beaches characterize the ice-free areas on KGI. The Potter Cove spit system stands exemplarily for similar systems along the coasts of the SSI and elsewhere (Figure 4).

Potter Cove is about 4 km long and 2.5 km wide with a recently stranded tide-water glacier located at the head of the cove. Water depths in the inner cove are up to 50 m and exceed 100 m in the outer cove (Schloss et al., 2012). In the surroundings

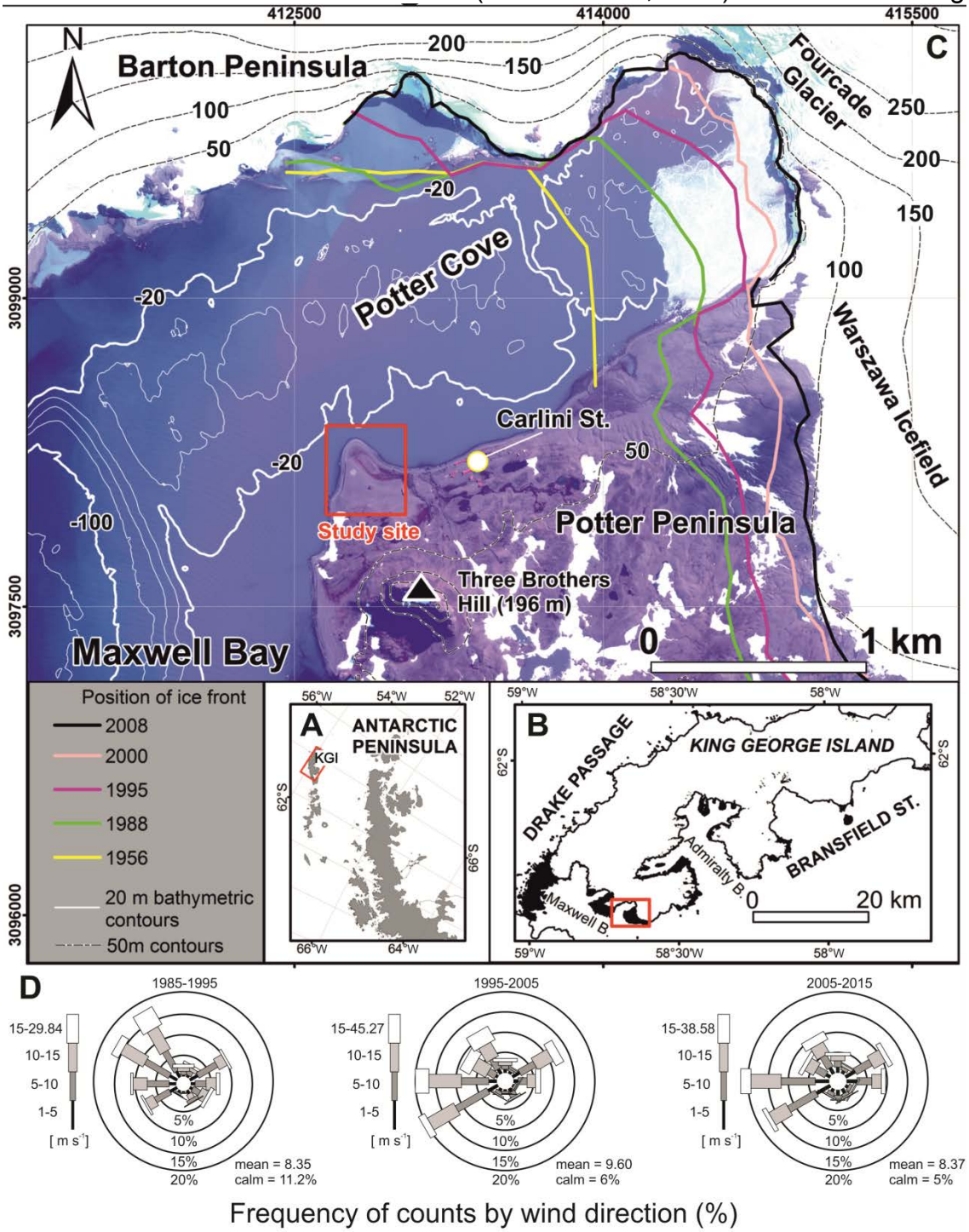

Figure 1. Location of studied spit system. A) King George Island (KGI) belongs to the South Shetland Islands, W of the Antarctic Peninsula. B) KGI is framed by the Drake Passage and the Bransfield Strait. Ice-free areas (black) are limited to the coastal zone, whereas the inland is glaciated (white); box marks the position of Potter Peninsula; C) Satellite image of Potter Peninsula with location of the Potter Cove spit system (box). Past ice front positions are from Rückamp et al.

(2011); bathymetric data from Deregibus et al. (2015). D) Wind data for the 1985-2015 CE observational period.

of the spit, water depths reach 20 m (Deregibus et al., 2015; Figure 1C). The tidal range is about 1.2 m during neap and 1.5 m during spring tide (Schoene et al., 1998).

Atmospheric and marine climate

Average sea-surface temperature in Potter Cove reaches 1 ºC during the summer months, and has increased by 0.36 ºC per decade during the past two decades (Schloss et al. 2012). Maxwell Bay and Potter Cove are generally free of sea ice from November/December to April/May; open waters in the Bransfield Strait last from December to April (Griffith and Anderson, 1989; Yoon et al., 1997; Schloss et al., 2012). The wind field in the study area is W-E bi-directional, with predominant winds from SW to NW and from NE to SE; average wind speed is about 15 m s^{-1} (Braun et al. 2001; Bañón et al., 2013; Schloss et al., 2014; Falk and Sala 2015; SMN, 2016; Figure 1D). SW to NW winds are more common during the austral summer, whereas NE to E winds are weaker and less common. However, local scale wind patterns, especially in fjords and coves, are strongly influenced by the surrounding topography (Braun et al., 2004; Navarro et al., 2013; Falk and Sala).

The southern and western coasts of Potter Peninsula including the western coast of the spit are exposed to oceanic waves coming from the Bransfield Strait (Figures 1 and 3A). During open-water seasons, the predominant direction of incident waves is oblique to the coast from S to SW creating a northward-flowing longshore current (Lim et al., 2013). Waves are refracted at the entrance of Potter Cove and bend around the spit into the cove, where wave energy decreases. During westerly storms, waves at the entrance of the cove reach a height of up to 1.7 m, whereas waves in the inner cove are 50-40 % lower (Lim et al., 2013). The wave climate of Potter Cove is strongly influenced by local wind conditions and only subjected to 1948 to 2011 CE was -2.5 ºC (Kejna et al., 2013), but temperatures are often above zero during summer. Average annual air temperatures above the AP have increased rapidly by up to 3°C in the second half of the last century, causing an accelerated glacier retreat (Meredith and King, 2005; Cook et al., 2005; Vaughan, 2006).

2015).

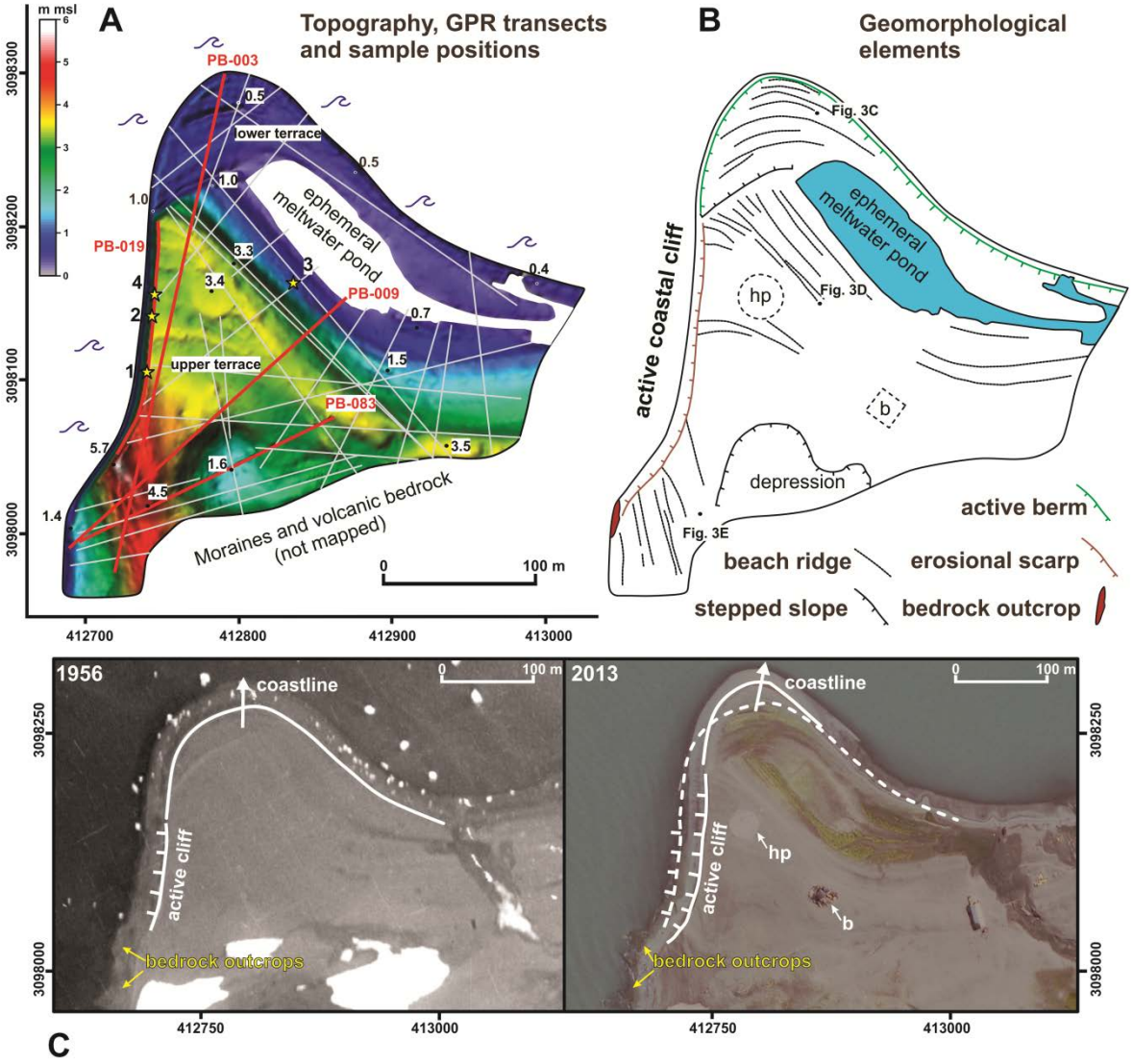

Figure 2. Topography and geomorphology of Potter Cove spit system. A) Digital terrain model based on dGPS measurements (numbers refer to elevation in m above mean sea level). Note upper and the lower terrace, and the position of GPR transects (lines presented in the text are marked in red); yellow stars mark sample positions for radiocarbon dating. B) Geomorphological elements of the spit system. Figure numbers refer to surface photographs; hp: heliport; b: building. C) Aerial and satellite imagery of the spit system, taken in 1956 and 2013 respectively. White arrows indicate the direction of spit progradation.

minimal swell energy (Lim et al., 2013). Fetch inside Potter Cove is very limited and, as a result, even strong easterly winds cannot create significant wave heights.

KGI is subjected to a maritime climate and regularly hit by cyclonic weather systems moving eastward along the Drake Passage (Kejna et al., 2013). The strength of circumpolar westerly winds has increased since the 1970s, especially during the austral summer, accompanied by higher cloudiness and precipitation (van den Broeke, 2000; Turner et al., 2005; Stammerjohn et al., 2008; Montes-Hugo et al., 2009). The annual mean air temperature on KGI during the time period

Holocene deglaciation and sea-level history

The deglaciation of Potter Cove initiated somewhat after 1.6 ka cal BP (Wölfl et al., 2016). Along the coasts of the SSI, Holocene raised beaches occur up to elevations of 18 m amsl (John and Sugden, 1971; Fretwell et al., 2010; Hall, 2010; Simms et al., 2012). Beach uplift on the SSI results from crustal relaxation in reaction to decreasing ice load following the Last Glacial Maximum (John and Sugden, 1971; Bentley et al., 2005, Fretwell et al., 2010; Watcham et al., 2011; Ó Cofaigh et al., 2014). Raised beaches along the coasts of Maxwell Bay, located at 7.5 to 4 m amsl (locally termed "6-m-beaches"), interfinger with terminal moraines of the last glacial-readvance (LGR), which occurred between 0.45 and 0.25 ka cal BP (John and Sugden, 1971; Sugden and John, 1973; Clapperton and Sugden, 1988; Yoon et al., 2004; Yoo et al., 2009; Simms et al., 2012). It is therefore likely that these beaches developed during the LGR (John and Sugden, 1971; Sugden and John, 1973; Hall 2010).

Recent uplift of KGI was 0.4 mm a^{-1} during the last decade (Rülke et al., 2015). Average uplift during the entire Holocene, however, is 2.8 to 3 mm a^{-1} (Bentley et al., 2005; Fretwell et al., 2010). Fall of relative sea level on KGI accelerated during the last 500 years (Bentley et al., 2005, Hall, 2010; Watcham et al., 2011). This was most likely the result of a short-term acceleration in glacio-isostatic rebound after the LGR, with a modeled peak uplift rate of 12.5 mm a^{-1} between 1700 and 1840 CE (Simms et al., 2012).

There are numerous sea-level curves for the SSI, derived from dating of raised beaches, marine abrasion terraces, and isolation basins (Pallàs et al., 1997; Bentley et al., 2005; Hall, 2010; Watcham et al., 2011). However, Holocene ice retreat and resulting fall of relative sea level was not a continuous process (Simms et al., 2011). Bentley et al. (2005) show that an initial post-glacial sea-level fall was interrupted by a mid-Holocene highstand at about 14.5 to 16 m amsl from 5.8 to 3.0 ka cal BP. In contrast, data presented by Hall (2010) show a continuous sea-level fall, which becomes accelerated between 1.5 and 0.5 ka cal BP. Watcham et al. (2011) presented a sea-level curve based on data from isolation basins and raised beaches. This curve shows two mid-Holocene sea-level highstands for KGI at about 8.0 and 7.0 ka cal BP, and a subsequent sea-level fall due to long-term glacio-isostatic rebound. Simms et al. (2012) mentioned that most sea-level curves for the SSI indicate an accelerated fall over the past 2.0 ka cal BP, whereas sea-level records from regions along the western AP reflect a decrease in uplift rate over time.

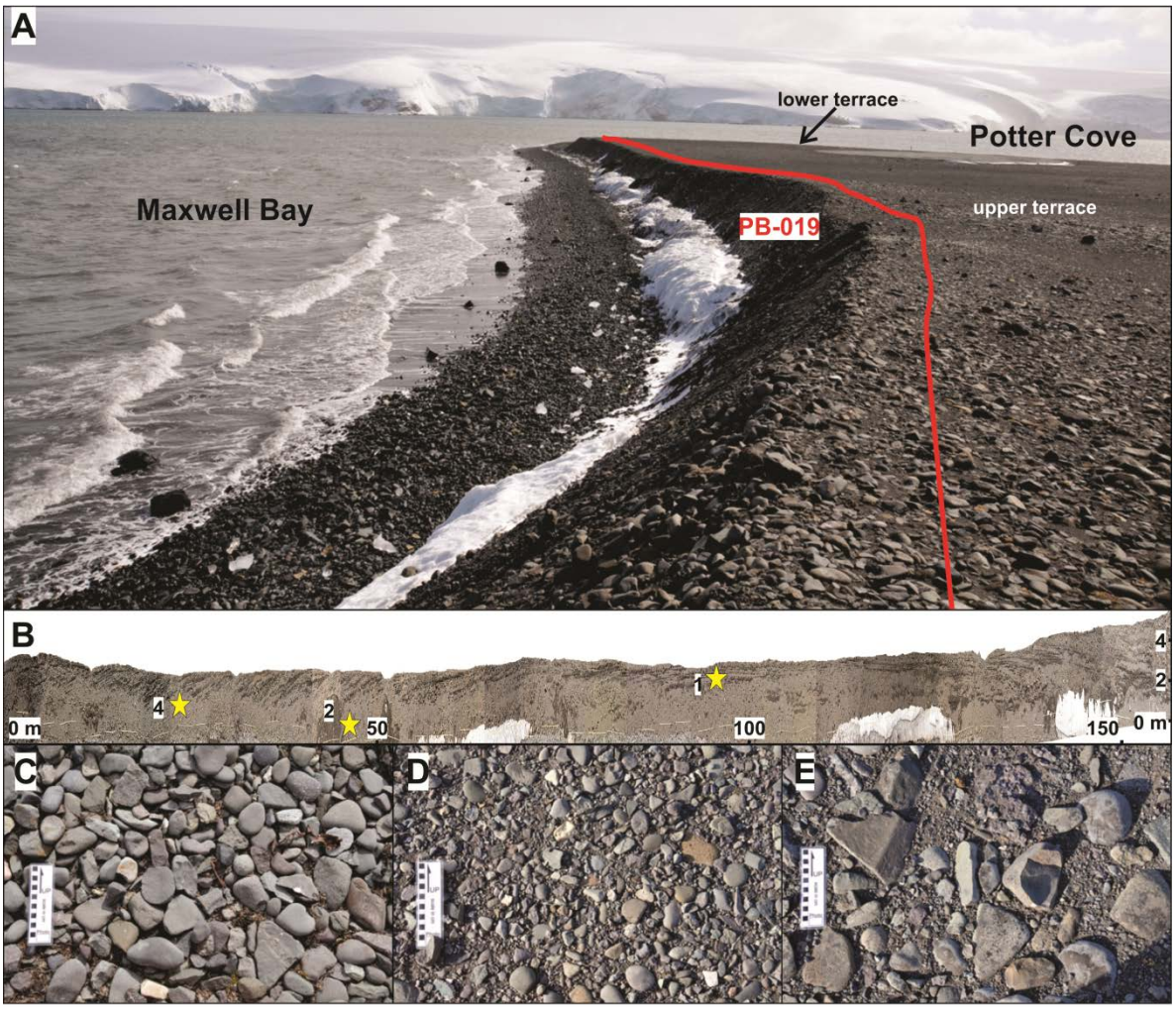

Figure 3. A) View along the west coast of the spit looking north. Height of cliff is up to 5 m. Positions of GPR transect PB-019 and the lower and upper terrace are shown. B) Panorama of cliff section showing internal sedimentary bedding and position of dated samples. Elevations are in m amsl. C, D, E) Images of surface sediment texture; see Figure 2 for locations.

2. METHODS

2.1 Topographic mapping

Data on ridge- and terrace elevations, required for spit-system mapping and for the topographic correction of ground-penetrating radar data, were collected using a Leica GS09 differential GPS (dGPS) in either RTK rapid static or RTK kinematic mode (3D-accuracy of better 2 cm). As geodetic reference, the point DALL 66019M002 (S62°14′16.335″/W58°39′52.364″/ ellipsoidal height 39.376 m) located on Carlini (formerly Jubany) Station was used. All UTM coordinates refer to zone 21E and are based on the WGS84 ellipsoid. No fixed tidal datum exists for the working area due to the lack of long-term water-level observations. Measured WGS84 ellipsoid heights were therefore corrected for the geoid undulation of -22.00 m ± 0.10 m using the data of the EGM96 (Lemoine et al., 1998). A geoid height of zero is taken as local vertical datum and referred to as present mean sea level (msl).

2.2 Ground-penetrating radar

Ground-penetrating radar (GPR) is based on the transmission of high-frequency electromagnetic pulses that are partly reflected at electromagnetic discontinuities in the subsurface. The amplitude of the reflected signal is recorded as a function of the two-way-travel time (TWT). GPR always images an interference pattern caused by the thickness of individual electromagnetically uniform sediment packages and the wavelengths present in the GPR signal (Lindhorst and Schutter, 2014). GPR data for this study were acquired by means of a GSSI (Geophysical Survey Systems Inc.) SIR-3000 GPR with a 200 MHz antenna; operated in discrete mode (trace increment 0.05 m). Post-processing of GPR data using the software ReflexW (Sandmeier Geo) comprises data editing, subtraction of low-frequency signal components (dewow), frequency filtering, gain adjustment, topographic migration and correction for along-profile topography. A mean subsurface radar-wave velocity of 0.08 m ns^{-1} was determined based on the analysis of diffraction

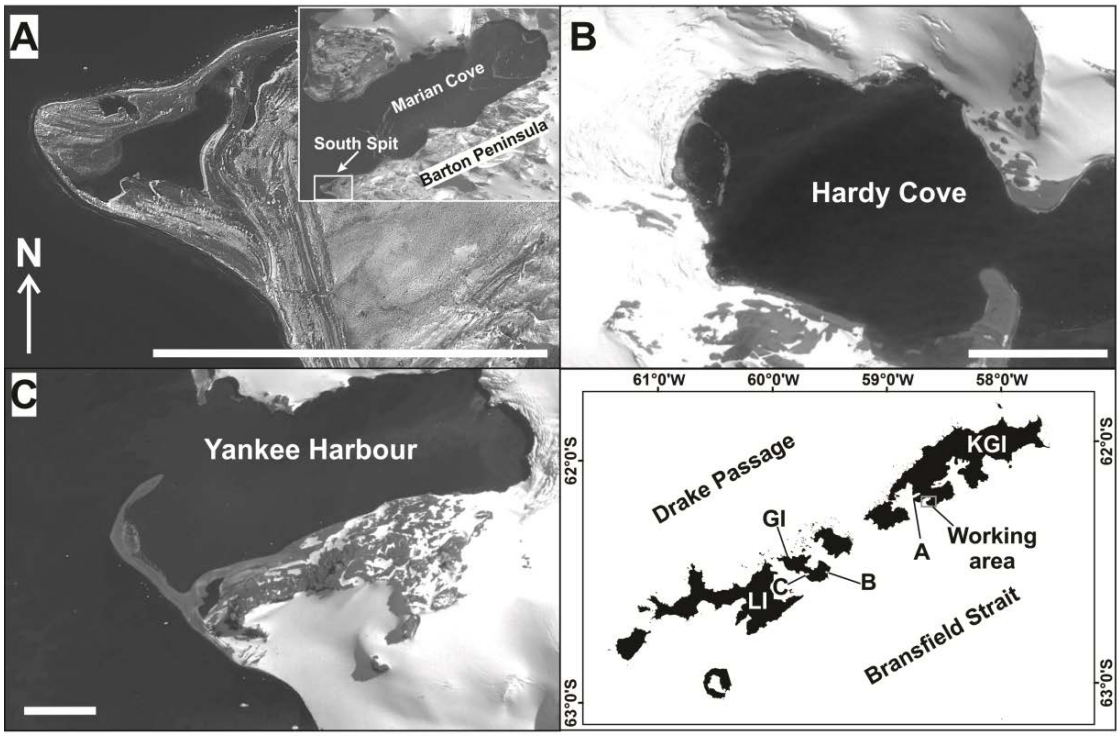

Area/name	Dimension (km^2)	Coordinates		Reference
		Geographic		
		Latitude (ºS)	Longitude (ºW)	
A. South Spit, Barton Peninsula	0.08	62.224297	58.795571	John and Sugden, 1971; Sugden and John, 1973; Curl 1980; Hall 2010
B. Hardy Cove	0.04	62.522512	59.582713	-
C. Spit Point, Yankee Harbour	0.16	62.533880	59.781206	Sugden and John 1971

Figure 4. Selection of other gravel spits of the South Shetland Islands, comparable to the Potter Cove System. GI: Greenwich Island; LI: Livingston Island. Scale bars represent 500 m in each picture. Satellite images (Google Earth) are from 2011 (A, B), and from 2010 (C).

hyperbolas. Interpretation of GPR data is based on migrated as well as non-migrated data, the latter being essential for a correct tracing of ringing multiples and diffraction hyperbolas. Only non-migrated data are shown in this work. Data

interpretation follows the approach of radar-facies interpretation (Gawthorpe et al., 1993; Bristow, 1995) as applied by Lindhorst et al. (2008) to spit sediments of lower latitudes. Analogous to the concepts of seismic interpretation introduced by Mitchum et al. (1977), the term 'radar facies' describes a two or three- dimensional set of reflections with similar characteristics, bordered by 'radar surfaces' (Bristow, 1995). Consequently, the interpretation of unconformities is based on the tracing of reflection terminations and abrupt changes of the radar facies.

2.3 Absolute age determination

Absolute age data were obtained by AMS radiocarbon dating of seaweed and a penguin bone. To reduce the risk of contamination with modern material, all samples for dating were taken from fresh outcrops, at least 0.3 m below the surface, packed in zip-lock bags and stored at 4 °C. Sample preparation and measurement as well as correction for carbon isotope fractionation and calculation of conventional radiocarbon ages (CRA) were performed by Beta Analytic Inc., USA. Local reservoir corrections (ΔR) for marine samples as reported for the SSI are in a broad range of about 700 to 1100 years (Curl, 1980; Björck et al., 1991a; Berkman and Forman, 1996; Milliken et al., 2009; Hall et al., 2010; Hass et al., 2010; Watcham et al., 2011). Hall et al. (2010), based on paired radiocarbon and uranium–thorium dates of Antarctic solitary corals, proposed a ΔR of 791 ±121 years. This local reservoir age is further supported by results of Simms et al. (2012) who used optical-stimulated luminescence dating of cobble surfaces to investigate the depositional ages of beach ridges on KGI. Due to the verification with two independent dating methods, the local reservoir correction proposed by Hall et al. (2010) was used in this study. Calibration of conventional radiocarbon ages was done using the software Calib (v7.0.4, Stuiver and Reimer, 1993) and the calibration curve Marine13 (Reimer et al., 2013). Calibrated ages are rounded to the next decade and provided as median of the probability distribution with 2σ error range (95.4 % probability).

2.4 Historical aerial imagery

To reconstruct coastal evolution through time, an orthorectified panchromatic aerial image (Falkland Island Dependency Aerial Survey Expedition, FIDASE; image ID X26FID0039076; pixel resolution 0.9 m; acquired 1956/12/20) and a satellite scenery (WorldView2, DigitalWorld; scene ID: 103001001F612100; pixel resolution 0.5 m; acquired 2013/03/07) were georeferenced and compared with regard to coastline position as marked by the location of the active berm. The berm was chosen as local reference to minimize errors potentially induced by tidal water-level oscillations.

2.5 Data on wind speed and direction

Carlini Station (National Meteorological Service of Argentina) is located at 15 m amsl and 600 m away from the spit system (Figure 1). Continuous meteorological observations are available since May 1985. They encompass three-hourly measurements of surface air temperature, wind direction and velocity, barometric sea-level pressure and cloudiness (SMN, 2016). The data are available from SCAR READER (Turner et al., 2004). Data on wind direction and velocity are

analyzed for sea-ice free months (November- April) with respect to decadal summaries of wind statistics (Figure 1D).

3. RESULTS

3.1 Morphology

The Potter Cove spit is attached to a headland composed of volcanic rocks and glacial moraines (Figures 1 and 2A). Two terrace levels are present, here termed lower and upper terrace, connected by a slope facing north. This slope is characterized by superimposed ridges that create a stairways morphology (overall slope 5°; Figure 2A, B). Towards Maxwell Bay, there is an up to 5 m high active cliff, whereas an active gravel berm ridge frames the modern beach towards the interior of Potter Cove (Figure 2B). From W to E, the height of the berm ridge decreases from 1 to 0.4 m amsl.

The upper terrace (situated at 3 to 5.7 m amsl) exhibits a series of curved, NNW-SSE to NW-SE striking, morphological ridges, towards the W truncated by the cliff (Figure 3A). The height difference between swales and adjacent ridge crests is less than 0.6 m in the SW and less than 0.2 m on the rest of the terrace. The upper terrace slightly descends towards the NE with an overall slope of 0.6º.

The lower terrace is located at and below 0.8 m amsl. Ridge crests on this terrace are located at 0.4 to 0.8 m amsl and ridges are curved with their convex side facing N (Figure 2B). Ridge elevations are less than 0.2 m. The landward, S-slope of the lower terrace, measured over all the ridges is 0.2º, with a maximum of 0.6º.

3.2 Sedimentology

Grain sizes along the modern beach and on the spit range from sand to gravel. Sediments are in general poorly sorted (Figures 3C-E). However, well sorted gravel sheets occur in the modern swash zone. Ridges of the lower terrace are composed of rounded to well-rounded (according to the classification scheme by Tucker, 1996) cobbles, with a maximum grain size of 12 cm and an almost matrix-free texture (Figure 3C). Sediments of the upper terrace coarsen from the NE to the SW (increase in maximum grain size from 5 to 20 cm), accompanied by a trend towards better rounding and less matrix content. Most gravels at the surface and in the uppermost part of the sediment column are gelifracted with sharp angular edges (Figure 3E).

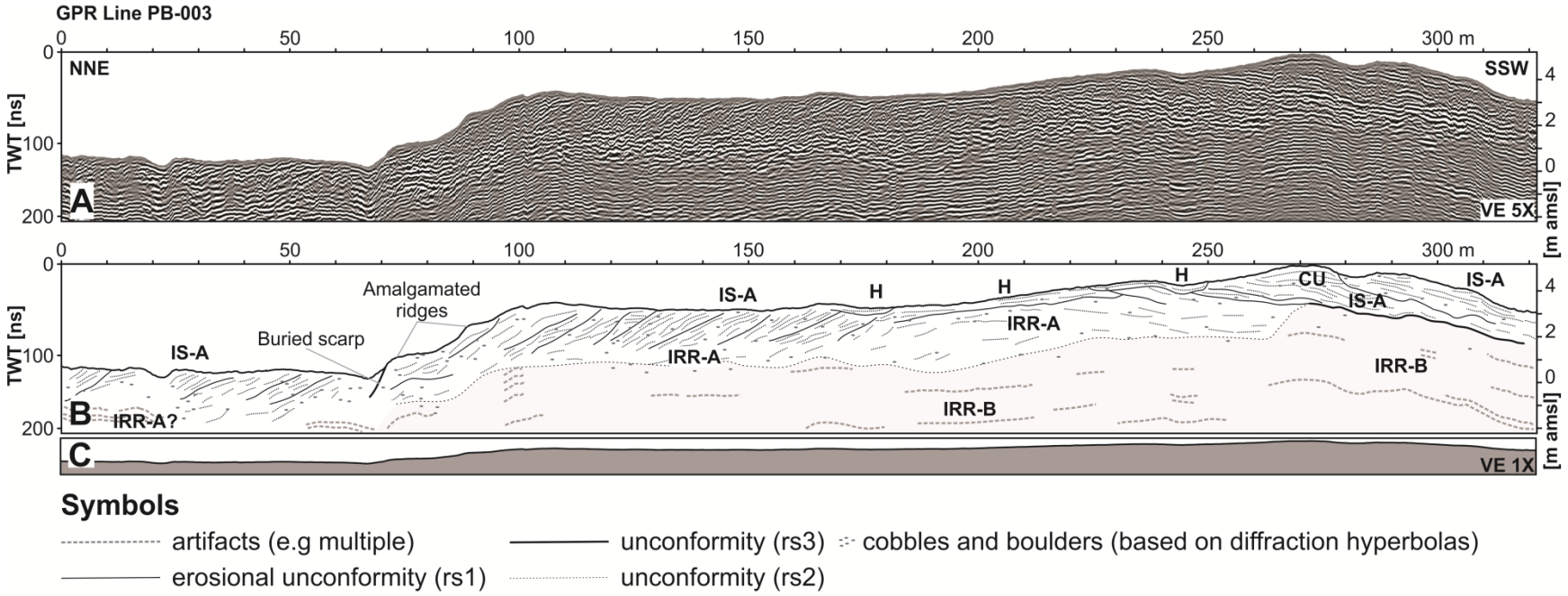

Figure 5. A) GPR line PB-003 showing the internal architecture of the lower and upper terrace of the spit system. For location see Figure 2. B) Interpretation of A. For a detailed discussion of radar facies and sediment geometries see text and Table I. C) Along-transect topography without vertical exaggeration (VE).

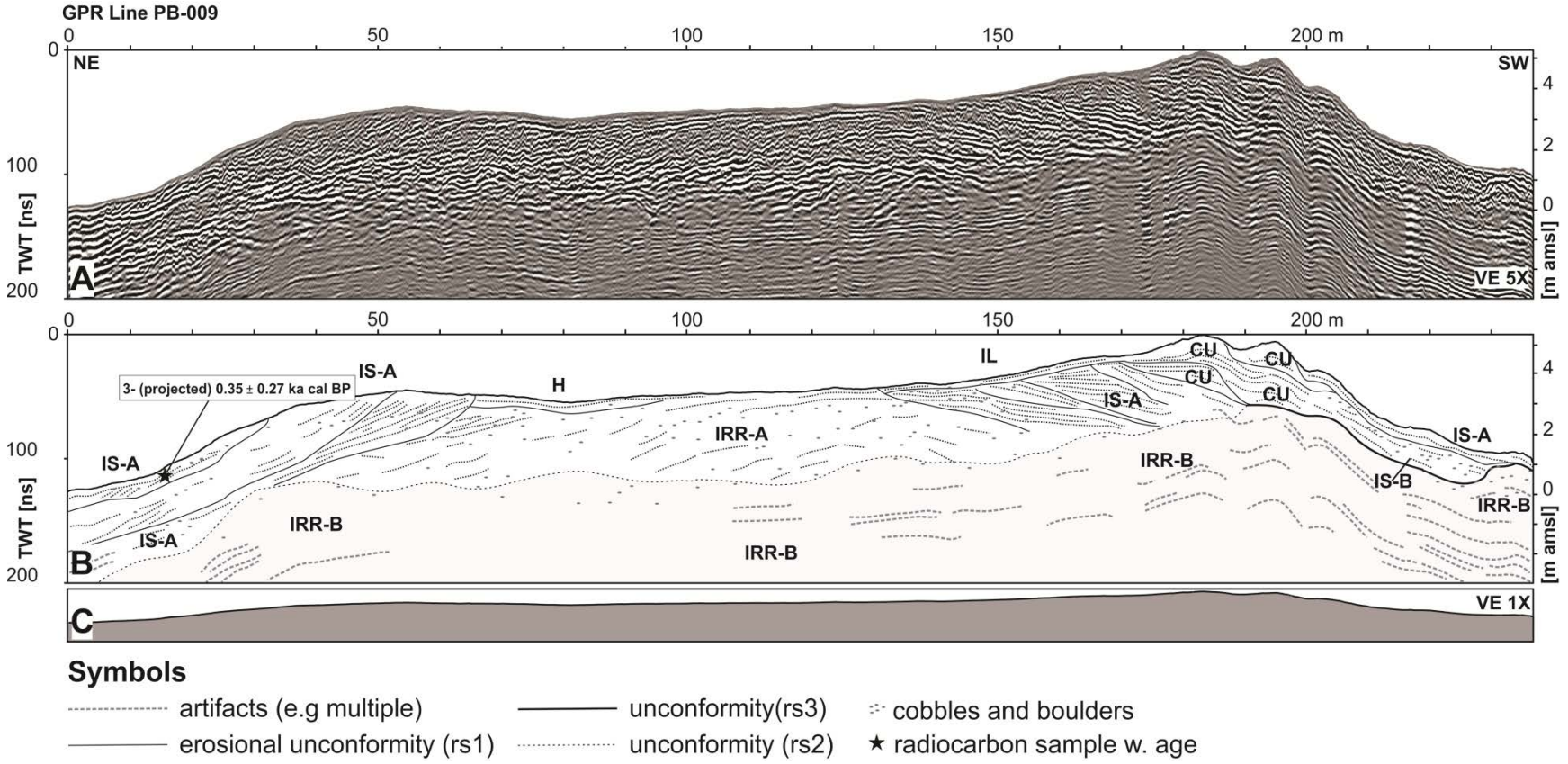

Figure 6. A) GPR line PB-009. For location see Figure 2. B) Interpretation of A. For a detailed discussion of radar facies and sediment geometries see text and Table I. C) Along-transect topography without vertical exaggeration.

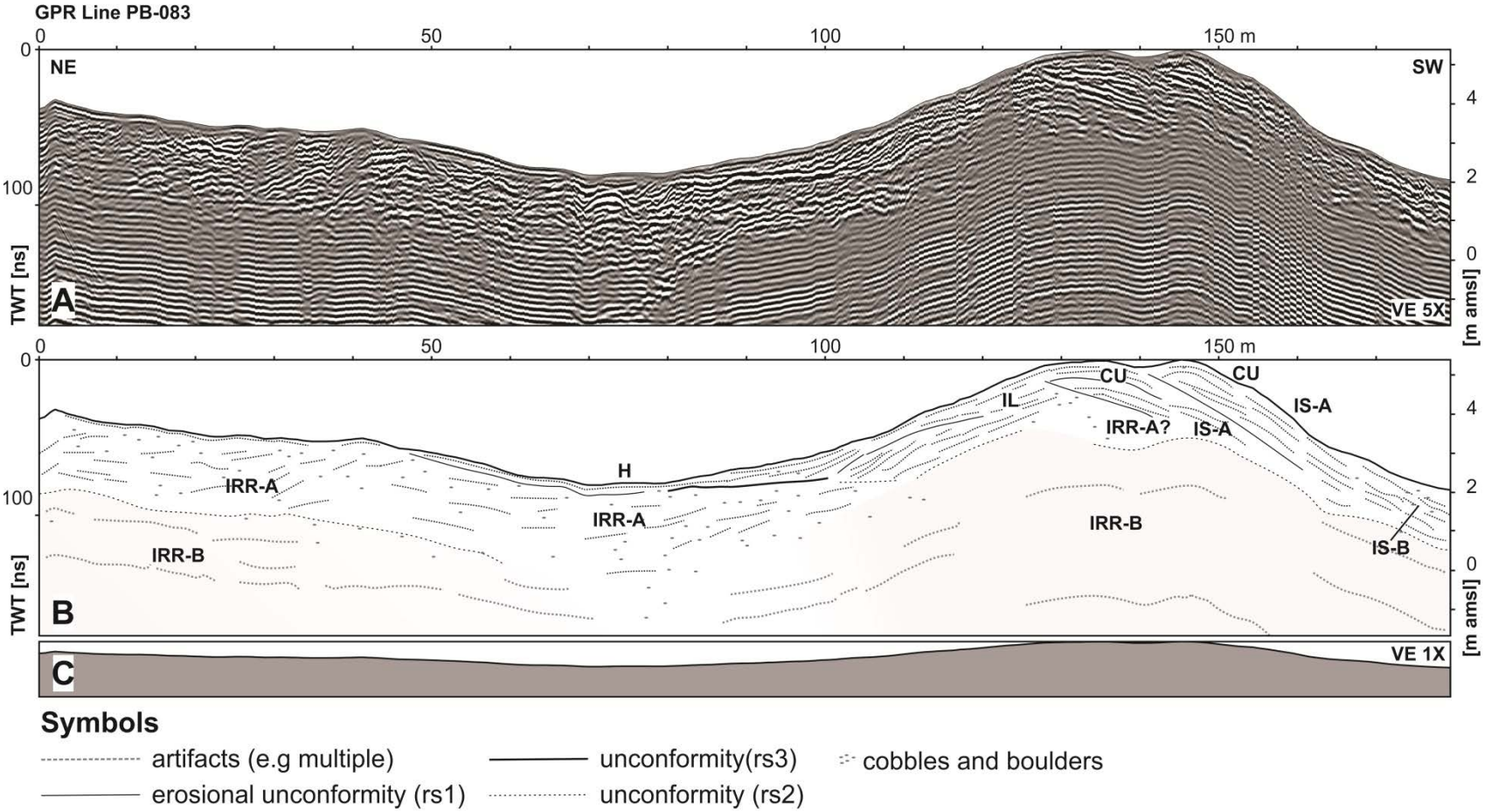

Figure 7. A) GPR line PB-083. For location see Figure 2. B) Interpretation of A. For a detailed discussion of radar facies and sediment geometries see text and Table I. C) Along-transect topography without vertical exaggeration.

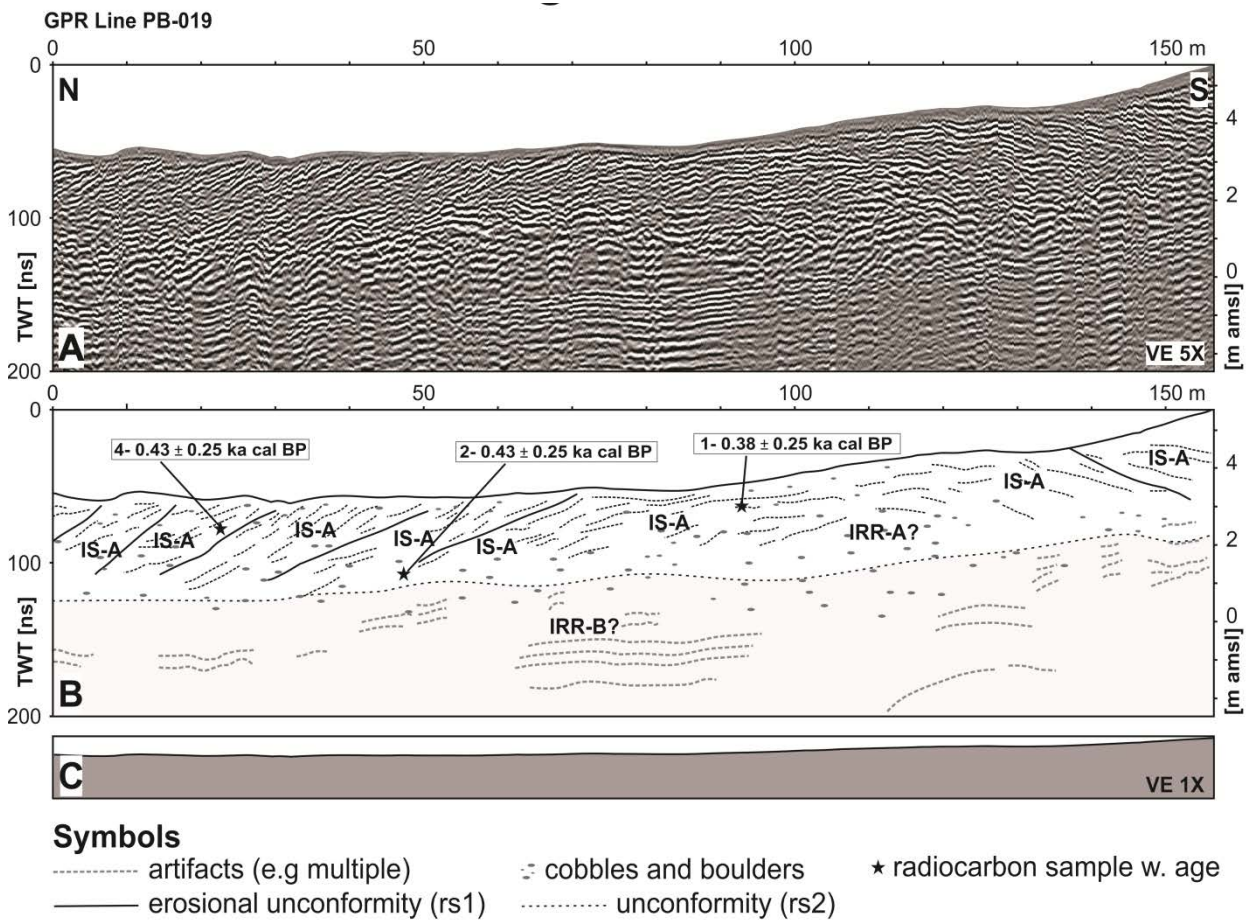

Figure 8. A) GPR line PB-019 imaging the internal architecture of the upper terrace along the active coastal cliff. For location see Figures 2, 3. B) Interpretation of A. For a detailed discussion of radar facies and sediment geometries see text and Table I. C) Along-transect topography without vertical exaggeration.

3.3 Spit-internal sediment geometries

Out of 29 GPR lines, 4 were selected to document the internal architecture of the spit system (Figures 2A and 5-8). Seven radar facies (rf) and three radar surfaces (rs) were defined to classify the radar-reflection patterns and to deduce the sedimentary geometries (Table I). The spit system comprises two distinct units. The upper unit, Unit 1, is characterized by clear GPR reflections and unconformably overlies the lower Unit 2, which shows irregular reflections (rf IRR-B), diffraction hyperbolas, and pronounced ringing multiples. Units are seen to represent the sediments of the spit overlying the basement respectively. The contact between the two units elevates towards the SSW. In the GPR data, this contact is irregular and poorly defined with the exception of the southwestern part of the study area, where a clear contact (rs3) is imaged (Figures 5 and 6).

Sediments of the spit (Unit 1) have a thickness of 1 to 3.5 m, with lower values in the central part of the spit and higher values in the SW, where morphological ridges are superimposed on the upper terrace. Internally, tabular, continuous reflections (rf IS-A) predominate, dipping radially from the presumed spit axis towards the shores (Figures 5 and 6). These reflections are bundled into packages by erosional unconformities, characterized by the truncation of underlying reflections (rs1; Figures 5, 6 and 8). Morphological ridges of the upper terrace show convex curved reflections of low to high amplitude (rf CU), bounded by seaward-dipping unconformities (rs1) as well as tabular to slightly convex reflections of medium to high amplitude (rf IL), bounded by landward-dipping unconformities (Figures 6 and 7). The central part of the spit system is dominated by irregular, low- to high-amplitude reflections with numerous diffraction hyperbolas (rf IRR-A). Near the surface, slightly concave, low- to medium-amplitude reflections occur (rf H; Figures 5-7).

3.4 Historical coastline development and wind-field evolution

Historical aerial and satellite imagery shows that the active cliff on the W side of the spit system retreated by 20 m in the time period 1956 to 2013 CE. Simultaneously, the northern coastline prograded by 25 m towards the NNE (linearly averaged rate of progradation is 0.44 m a^{-1}; Figure 2C). In the year 1956 the front of the Potter Cove tide-water glacier was located 1200 m away from the gravel spit inside the cove (Figure 1C). Since then the glacier front has experienced a net retreat of more than 1000 m along the flow line and has stepped back onto land in the year 2016 (Jerosch et al., 2018).

Radar facies		Characteristics	Interpretation
Inclined			
IS-A	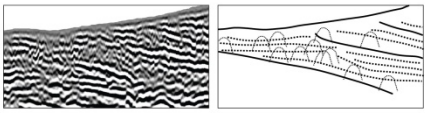	Medium to high amplitude, tabular to slightly convex/concave, moderately continuous. Diffraction hyperbolas. Dip of beds: 2-11º	Planar beds of prograding beach face
IS-B	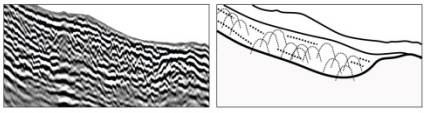	Medium to high amplitude, discontinuous. Diffraction hyperbolas, partly aligned. Dip of beds: up to 7°	Intertidal gravel sheets
IL	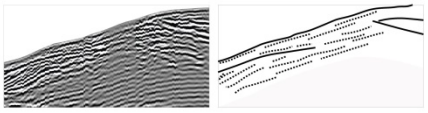	Medium to high amplitude, tabular to slightly convex, moderately continuous. Landward dip: < 12º	Washover beds
Curved			
CU	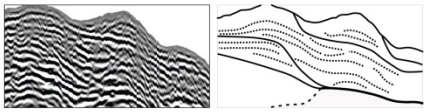	Low to high amplitude, convex curved, moderately continuous. Landward/seaward dip: < 3.5°	Aggrading storm beds resulting from wave overtopping
Horizontal planar			
H	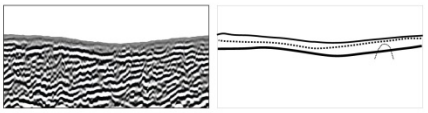	Low to medium amplitude, planar to slightly concave, moderately to highly continuous.	Backbarrier beds, deposited by meltwater or wind transport
Irregular			
IRR-A	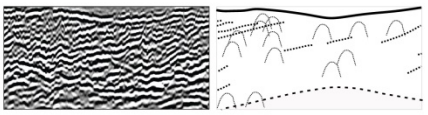	Low to high amplitude, irregular, slightly tabular, numerous diffraction hyperbolas	Poorly sorted glacial till with cobble to boulder size components
IRR-B	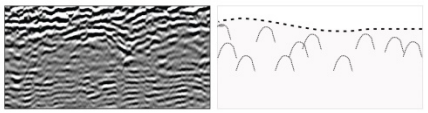	Very low amplitude to transparent, irregular, numerous diffraction hyperbolas in uppermost part	Volcanic bedrock. Diffraction hyperbolas are caused by fractures and the sharp, irregular surface of the rock.
Radar surfaces			
rs1	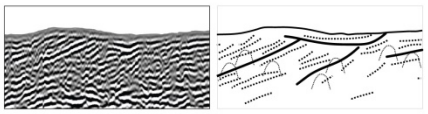	Medium amplitude, moderately continuous, in parts truncation of reflections	Erosional unconformity
rs2	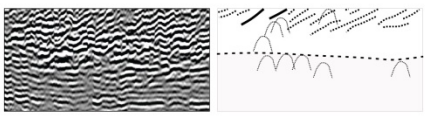	Distinct change of radar facies	Unconformity
rs3	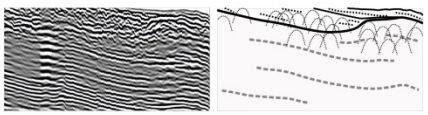	Medium reflection, moderately continuos, numerous diffraction hyperbolas	Contact of beach sediments and substratum (volcanic bedrock or till)

Table I. Radar facies and radar surfaces defined for the interpretation of the GPR data

The direction of predominant winds in the Potter Cove area changed from NW to W-SW over the last 30 years (Figure 1D). Moreover, the study site became stormier, with >20% of W-SW winds exceeding 15 m s^{-1} and a general increase in maximum wind speed in more recent times (c. 30 m s^{-1} in the time period 1985-1995, and 38-45 m s^{-1} in the subsequent decade 1995-2015).

4. DISCUSSION

Bay-mouth spit systems like the Potter Cove spit, are common morphological features along the periglacial coasts of the SSI, where they developed at the entrances of coves and embayments (Figure 4). These entire systems exhibit superimposed beach ridges, and most comprise several terrace levels, separated by slopes or truncated by erosional scarps (John and Sugden, 1971; Sugden and John, 1973; Curl, 1980; Hall 2010). Data on the internal architecture of these systems is missing. Similarities in overall morphology, i.e. the existence of several terrace levels connected by steep slopes, however, suggest that bay-mouth spit development is not only controlled by local factors like wave-climate, nearshore bathymetry and sediment availability, but may reflect regional patterns of relative sea-level changes and climate development.

4.1 Sedimentary architecture of Potter Cove gravel spit system

The Potter Cove spit comprises two terrace levels, located around 3.5 m and 0.8 m amsl, respectively (Figure 9). Both terraces are characterized by a shallow ridge and swale morphology and are connected by a north-facing slope with superimposed ridges (Figure 2). Morphologically, these terraces form a spit southward-attached to moraines and the volcanic rocks of Potter Peninsula (Figures 1 and 2). In such a coastal configuration, moraines act as both headland anchor and source of sediment which is distributed along the coast by alongshore currents (Hayes et al., 2010). The western coast of the spit, facing Maxwell Bay, is under erosion and an active coastal cliff developed, documenting ongoing cannibalization and reorganization of the spit system (Figures 2 and 3).

GPR data document that both terrace levels are composed of well-stratified gravel deposits (Figures 3B, 5 and 8; Table I). The 1 to 3.5 m thick beach sediments unconformably overlie a basement characterized by irregular GPR reflections and diffraction hyperbolas or appearing transparent in the GPR data (Figures 5 and 6). Whereas transparent parts are interpreted as volcanic bedrock based on outcrop evidence 70 m E to the GPR line PB-009 (Figure 2B), diffraction hyperbolas point to the presence of large boulders and cobbles as this is common in the moraines that crop out immediately S of the upper terrace. The contact between spit sediments and underlying moraine deposits remains unclear in the GPR data, most likely due to the similar lithology of both depositional units.

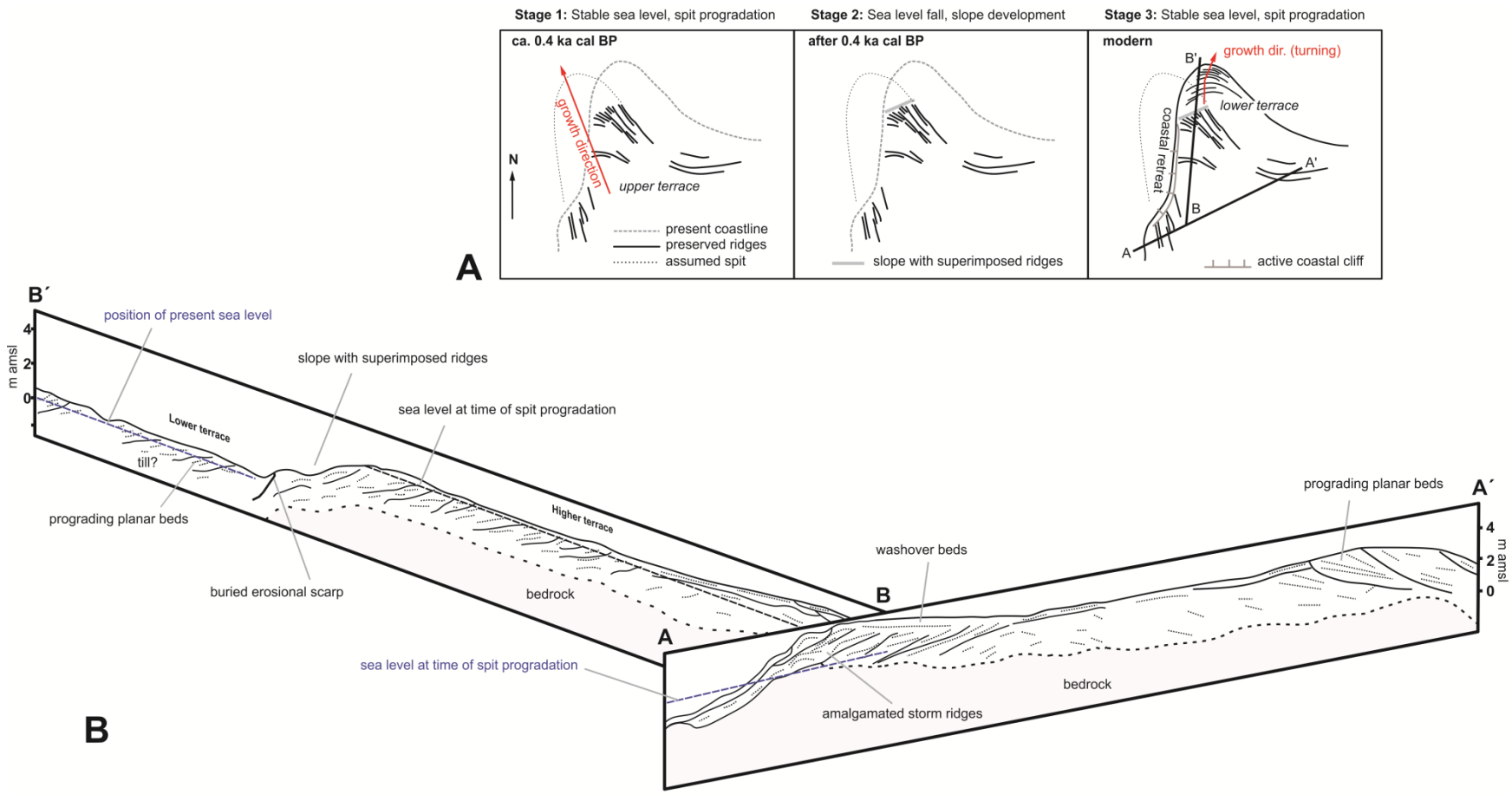

Figure 9. A) Simplified genetic model for the Potter Cove gravel-spit system through time. Note rotation of the axis of spit progradation from stage 1 to 3. B) Fence diagram summarizing the main architectural elements of the spit system based on the GPR data. For orientation of cross sections see A.

The main sedimentary architectural elements of the upper terrace are packages of divergent seaward-dipping gravelly beds delimited by erosional unconformities (Figures 5-8). Sedimentary beds dip with up to 11º towards the modern shore and are seen as the result of swash sedimentation at the beach face. Superimposed on the prograding beach sediments of the upper terrace, there are morphological ridges composed of gravel-size sediments (Figures 2B, 3C-E). These ridges are interpreted as beach ridges built by waves with run-up heights lower than the ridge crests, according to architectural similarities with gravel beach ridges described from elsewhere in KGI (Lindhorst and Schutter, 2014).

Gravel ridges towards the SW, facing Maxwell Bay, are coarser grained and composed of rounded cobbles (Figure 3E). These ridges are amalgamated and superimposed on the SW slope of the upper terrace (Figures 5-7 and Figure 9, stage 1). Ridge internal sediment geometries comprise of convex-aggradational and landward-dipping beds and are interpreted to reflect waves of higher energy that were able to overwash the ridge crests and to transport material to the landward side of the ridge (Lindhorst and Schutter, 2014) (Figure 7). Differences in ridge-internal geometries between the northern and the western slope of the spit are attributed to the higher-energetic wave-climate at the coast facing Maxwell Bay compared to the sheltered coast inside Potter Cove (Figures 1 and 3).

The lower terrace consists of up to 2 m thick, seaward-dipping gravelly beds, bound into packages by seaward-dipping erosional unconformities. Several arcuate morphological ridges, composed of gravels to cobbles, are superimposed onto the prograding beach deposits of the lower terrace (Figure 2). Seaward-dipping internal beds, as imaged by the GPR, indicate swash deposition with low wave run-up heights even during storms as expected for the comparable sheltered environment inside Potter Cove (Figure 5).

Based on the internal sediment geometries, which predominantly comprise seaward-dipping beds, both terrace levels are interpreted to result from spit progradation (Figure 9). For the upper terrace, striking of beach ridges and internal sediment geometries indicate a NW-SE oriented axis of spit progradation (Figure 9, stage 1). This is slightly different from the lower terrace that started to grow in a northerly direction and subsequently experienced a shift of the direction of progradation towards the NNE over the last decades (Figure 2C and Figure 9, stage 3). Even little changes in storm intensity or the predominant angle of wave impact have been shown elsewhere to alter the pattern of spit progradation (Allard et al., 2008; Ashton et al., 2016). Consequently, the still ongoing rotation of the axis of spit progradation is proposed to reflect either a strengthening of westerly storms or the reaction of the system to the observed change of the predominant wind direction during the last decades and a subordinate shift in the direction of (storm-) wave impact onto the coast. Increased storm frequency or -intensity would both result in higher sediment redistribution from the western coast of the spit towards the interior of Potter Cove, due to intensification of the alongshore transport. With the available local meteorological data it remains unclear as to whether the

observed shift in the direction of spit progradation is part of a long-term trend or caused by more recent changes in the wind field. On a more regional scale, however, there is evidence that the strength of circumpolar westerly winds increased since the 1970s, especially during the austral summer (van den Broeke, 2000; Turner et al., 2005; Stammerjohn et al., 2008; Montes-Hugo et al., 2009). This is attributed to the poleward movement of the Southern Annular Mode during the last decades, which caused a strengthening of atmospheric low pressure systems around the AP (Marshall et al., 2006). In this context, the observed change in the progradational direction of the spit is likely to reflect larger scale changes in the wind system during the last decades.

4.2 Timing of spit evolution

Radiocarbon ages are regarded as similar within the sigma-2 error range (Table II; Figure 2). Seaweed ages from beach sediments, in general, can be regarded as maximum ages, while penguin bones, due to the potential of multiple relocations prior to final burial, represent minimum ages (Watcham et al., 2011). It is therefore assumed that the upper terrace formed not before 0.65 ka cal BP, with a median of the probability distribution around 0.4 ka cal BP (Figure 9, stage 1). Age estimates for the upper terrace fit well with dating results from beach systems at similar elevation in the proximity of the study site (Hall et al., 2010; Simms et al., 2012; Lindhorst and Schutter, 2014). The very recent age of the lower terrace, by contrast, does not allow for absolute age determination using the radiocarbon method. However, given a linearly averaged rate of progradation of 0.44 m yr^{-1} as inferred from historical aerial imagery (Figure 2C), the growth of the lower terrace is expected to have started around 1880 CE (0.07 ka BP; Figure 9, stage 3).

4.3 Reaction of spit system to accelerated glacier retreat

Based on the direct comparison of radiocarbon ages and dates obtained by means of optical stimulated luminescence, Simms et al. (2012) concluded that the formation of beaches now elevated to 7.5-4 m amsl is linked to the last glacial readvance (LGR; 0.45-0.25 ka cal BP; Yoon et al., 2004; Yoo et al., 2009; Simms et al., 2012). These beaches are generally seen as transgressive features, deposited under the circumstances of a relative sea-level rise and increasing storminess during the late stage of the LGR (John and Sugden, 1971; Simms et al., 2012). The internal architecture of the Potter Cove spit system, however, contradicts this general interpretation and draws a more differentiated picture comprising subsequent phases of coastal progradation interrupted by a rapid fall of relative sea level (Figure 10).

The very gentle seaward slope of the upper terrace (0.6°) is indicative of either rapid spit growth in a very short time period or slow spit growth under a stable relative sea level, i.e. a very low rate of glacio-isostatic adjustment. Due to the large error bars, the radiocarbon ages do not allow for a determination of the duration of the older phase of coastal progradation during which the upper terrace formed. However, given that the progradation rate of the lower terrace (0.44 m yr^{-1}) is representative of this setting, sediments of the upper terrace are expected to have been deposited within 200 to 300 years. In combination with the tilt of the

upper terrace (c. 0.3 m over a preserved distance of ca. 90 m along the former axis of spit progradation) this results in a minimum estimate for the rate of relative sea level fall of 1 to 1.5 mm a^{-1} during the time of early post-LGR spit progradation. This rate is far below the long-term average uplift of the study area during the entire Holocene, which is estimated at 2.8 to 3 mm a^{-1} (Bentley et al., 2005; Fretwell et al., 2010). The recent uplift rate, by contrast, is close to zero (Simms et al., 2012; Rülke et al., 2015). This latter is also corroborated by the almost non-existing dip of the lower terrace that indicates no significant uplift since onset of spit progradation, i.e. during the last 100 to 150 years.

The upper terrace is nowadays located at c. 3.5 m amsl, whereas the lower terrace is situated at 0.8 m amsl. Both are connected by a north-facing slope (5° angle) with superimposed beach ridges (Figure 5 and Figure 9, Stage 2). The similarity of internal sediment geometries of the upper and lower terrace indicates comparable elevations with regard to mean sea level during both phases of coastal progradation (Figure 9). The connecting slope is consequently interpreted to have formed during a period of accelerated sea-level fall which amounts to about 2.7 m in total (Figure 9, stage 2). Such a period of accelerated fall of relative sea level is expected to result in a reduction of accommodation space and sediment supply, as indicated by a down-stepping of coastal sediments and the amalgamation of wave-formed ridges on the slope (Figures 5, 9 and 10). Formation of this slope as the result of increased coastal erosion or a longer period of sediment starvation under constant isostatic uplift can be excluded, as amalgamated ridges represent constructive sedimentary features. Comparable morphologies are described from beach-ridge systems of Varanger Peninsula and interpreted as the product of a sudden drop in sea level (Fletcher et al., 1993). Based on modeling results, increased glacio-isostatic uplift in reaction to glacier retreat is assumed for the time following the maximal glacier advance of the LGR, i.e. after around 0.35 ka BP (1600 CE, Simms et al., 2012). The results of these rebound models further show that a reduction of 16 to 22 % in ice volume is sufficient to explain about 2.5 m of uplift within 250 years until the mid-19th century.

Summarizing, progradation of polar gravel spits as exemplarily observed in the Potter Cove spit system, is bound to phases of comparable low rates of glacio-isostatic uplift and a resulting stable relative sea level. The morphology of the Potter Cove spit system, with two terrace levels connected by a steep slope with superimposed amalgamated beach ridges, is seen to archive two phases of coastal progradation separated by an abrupt increase in the rate of local glacio-isostatic uplift in reaction to deglaciation after the last glacial re-advance. Based on

No	Sample ID	Lab ID	Dated material	Coordinates		Altitude	$^{12}C/^{13}C$ ratio [o/oo]	^{14}C age [a BP]	Calibrated age (ΔR 791 ± 121 a)			
				WGS84 UTM 21E		m amsl			cal BP (2 σ ranges, 95.4% probability)			
				X	Y				Rel. area u. distribution	Range [a]		Median of prob. [ka]
1	PB-3000-2	Beta-297365	seaweed	412739	3098106	2.7	-23.8	1540 ± 30	1.00	110	610	0.38 ± 0.25
2	PB-3006-1	Beta-304147	seaweed	412742	3098145	1.1	-24.1	1600 ± 30	0.005	150	160	0.43 ± 0.25
									0.009	190	220	
									0.98	220	650	
3	PB-PC1.0	Beta-338478	seaweed	412839	3098163	0.6	-21.3	1510 ± 30	0.001	1	4	0.35 ± 0.27
									0.99	60	550	
4	Po-23	Beta-431963	penguin bone	412761	3098081	2.3	-22	1600 ± 30	0.005	150	160	0.43 ± 0.25
									0.009	190	220	
									0.98	220	650	

Table II. Results of radiocarbon dating

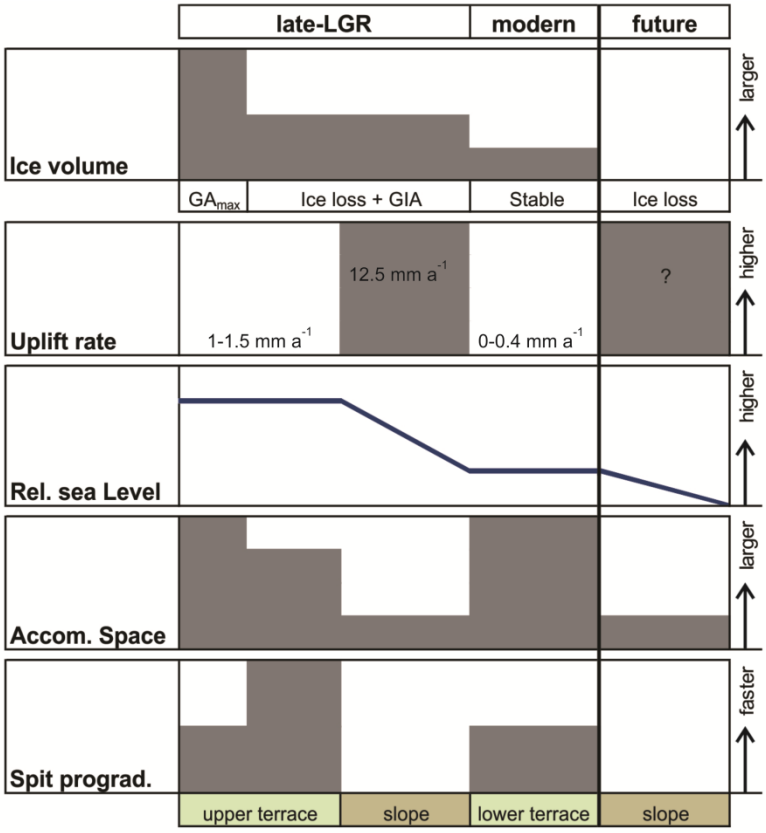

Figure 10. Concept for the interplay of ice volume, glacio-isostatic adjustment (GIA), relative sea-level change, and spit progradation. Note the predicted future development of the system. LGR: last glacial re-advance; GA_{max}: maximum glacier extent during the LGR.

these findings, a concept for the interplay of ice volume, glacio-isostatic adjustment, relative sea level, and spit progradation is presented (Figure 10). This concept not only explains the morphological and sedimentological characteristics of the Potter Cove system, but also allows predicting future developments of comparable systems elsewhere.

5. CONCLUSIONS

Sedimentary architecture and development of a polar gravel-spit system have been revealed based on ground-penetrating radar- and topographical data, historical aerial imagery and radiocarbon ages. Morphology and internal sediment geometries document changes in the rate of glacio-isostatic uplift between 1-1.5 mm and 12.5 mm a^{-1} on multi-decadal to centennial time scales. Based on the proposed interplay of fast changes in the rate of crustal relaxation and modes of beach sedimentation, a concept for the interaction of isostatic coastal uplift and spit development has been presented. This concept does not only explain the observed architecture of the spit system but bears implications for the expected future development of similar beach systems in KGI and elsewhere in comparable settings. Accelerated glacier retreat and reduction in ice volume of inland ice shields during the last decades is expected to cause a significant increase in the

rate of isostatic uplift and therefore relative sea level fall during the next decades. The current phase of coastal progradation is expected to terminate in the near future and to be replaced by the development of steep slopes with superimposed amalgamated ridges due to the reduction in accommodation space.

ACKNOWLEDGEMENTS

We acknowledge funding by the German Research Foundation (DFG project Li2005/1-1 to SL) in the framework of the DFG-priority program 1158 “Antarctic Research with comparative investigations in Arctic ice areas” and support by the Alfred Wegener Institute (AWI), Helmholtz Centre PACES II (Polar Regions and Coasts in the changing Earth System). PHB, UF and GK were funded as well by IMCONet (FP7 IRSES, action no. 319718). SL and IS thank the crews of the Argentine research station “Carlini” and the adjoined German Dallmann-Labor (AWI) during the 2010 and 2011 field seasons for their cordial hospitality and invaluable logistical support. We also thank KM Stange for his comments, which improved an early version of this manuscript. The manuscript has been significantly improved by the detailed and thorough reviews made by two anonymous reviewers.

Supplementary data

Ground-penetrating radar data obtained in the framework of this study are available from the data depository PANGAEA (Lindhorst and Schutter, 2013).

CHAPTER 3: HOLOCENE GLACIAL DYNAMICS AND GEOMORPHOLOGY OF POTTER PENINSULA, KING GEORGE ISLAND (NW ANTARCTIC PENINSULA)

Heredia Barión, P. A.[1,2], Strelin, J. A.[3,4], Spiegel, C.[1], Wacker, L.[5], Niedermann, S.[6], Kuhn, G.[2]

[1] University of Bremen, Department of Geosciences, Klagenfurterstr. 2-4, 28359 Bremen, Germany.

[2] Alfred Wegener Institute, Helmholtz Center for Polar and Marine Research, Geosciences Division, Am Alten Hafen 26, 27568 Bremerhaven, Germany.

[3] Centro de Investigaciones en Ciencias de la Tierra (CONICET-UNC), Vélez Sársfield 1611, X5016GCA, Córdoba, Argentina.

[4] Instituto Antártico Argentino, Convenio MREC - Universidad Nacional de Córdoba, Vélez Sársfield 1611, X5016GCA, Córdoba, Argentina.

[5] ETH Zürich, Laboratory of Ion Beam Physics, Schafmattstr. 20, 8093 Zürich, Switzerland.

[6] Deutsches GeoForschungsZentrum GFZ, Telegrafenberg, 14473 Potsdam, Germany.

ABSTRACT

Despite comprehensive post- Last Glacial Maximum reconstructions of the Antarctic Peninsula ice sheet, detailed information is still missing on how deglaciation continued during the Holocene. Because its key stratigraphic exposures and geomorphology, Potter Peninsula on King George Island, is an ideal place to answer those questions. This study contributes to unraveling glacial oscillations and landscape development of Potter Peninsula by adding chronostratigraphic data and detailed geomorphological mapping. Our data show that the deglaciation phase on Potter Peninsula started at ≥7.8 ka cal BP, instead of the generally accepted minimum age of 9.5 ka cal BP. Moreover, we suggest that the study area experienced several cycles of reglaciation and glacial retreat during the Holocene. During these cycles, the glacial front reached positions similar to the present day, or was positioned further landward as compared to today. Regarding the warming of the last decades, our results indicate that periglacial and paraglacial processes are actively modifying the glacier foreland. Our findings also have implications on regional paleoclimate reconstructions and on ice sheet modeling for the Holocene of the northwest Antarctic Peninsula region.

KEYWORDS:

Deglaciation; geomorphological mapping; radiocarbon dating; South Shetland Islands

1. INTRODUCTION

The Antarctic Peninsula (AP) Ice Sheet is affected by environmental changes caused by the climate warming especially since 1992 (Vaughan et al., 2013). For predictions of the future and for assessments of sea-level variations during deglaciation and periods of warming, more data and the refinement of existing models is needed (Spada et al., 2013). One of the key locations to study the impact of the recent warming is King George Island (KGI), the largest of the South Shetland Islands (SSI), situated northwest of the AP (Fig. 1A). KGI stands as an example of those changes responding to climate warming in the AP region and a test-bed for predicting future responses to climate change (Kennicutt, 2009).

The average annual temperature of the SSI has increased by almost 3°C since the middle of the last century (Vaughan et al., 2003; Meredith and King, 2005), thus far exceeding average global warming by 1.5-1.8ºC (Sánchez-Lugo et al., 2018). The warming caused rapid glacial retreat (Steig et al., 2009; Osmanoğlu et al., 2013) resulting in the collapse of many permafrost-related and glacigenic landforms (Bockheim et al., 2013). Moreover, the ice retreat exposed coastal areas leaving fresh exposures for geomorphological and stratigraphic surveys. They are located mainly around the southern bays of KGI, which are the sites with the greatest concentration of research activities in Antarctica. One of them is Maxwell Bay, where Potter Peninsula is situated (Fig. 1C).

Although a comparably well-known deglaciation history after the Last Glacial Maximum (LGM; 25-20 calibrated age in thousands of years before present, ka cal BP) is now available for the AP region (Ó Cofaigh et al. 2014), detailed information is still missing for the Holocene in more local ice cap model reconstructions (Bentley et al., 2014) such as on KGI. Moreover, detailed age data of geomorphological features from this ice-free area can help refine existing ice-models for the AP and establish whether post-LGM retreat was a continuous process or interrupted by glacial re-advances during the Holocene. Understanding the Holocene is particularly important for providing the context for recent ice-sheet change, in order to assess whether it is unusual or a part of a normal Holocene variability (Bentley et al., 2014). The most recent millennia of Antarctic Ice Sheet history are important for evaluating the response of the ice sheet to various forcing agents such as sea-level rise, atmospheric and oceanographic temperature influences, and for constraining past rates of grounding-line retreat (Bentley et al., 2014).

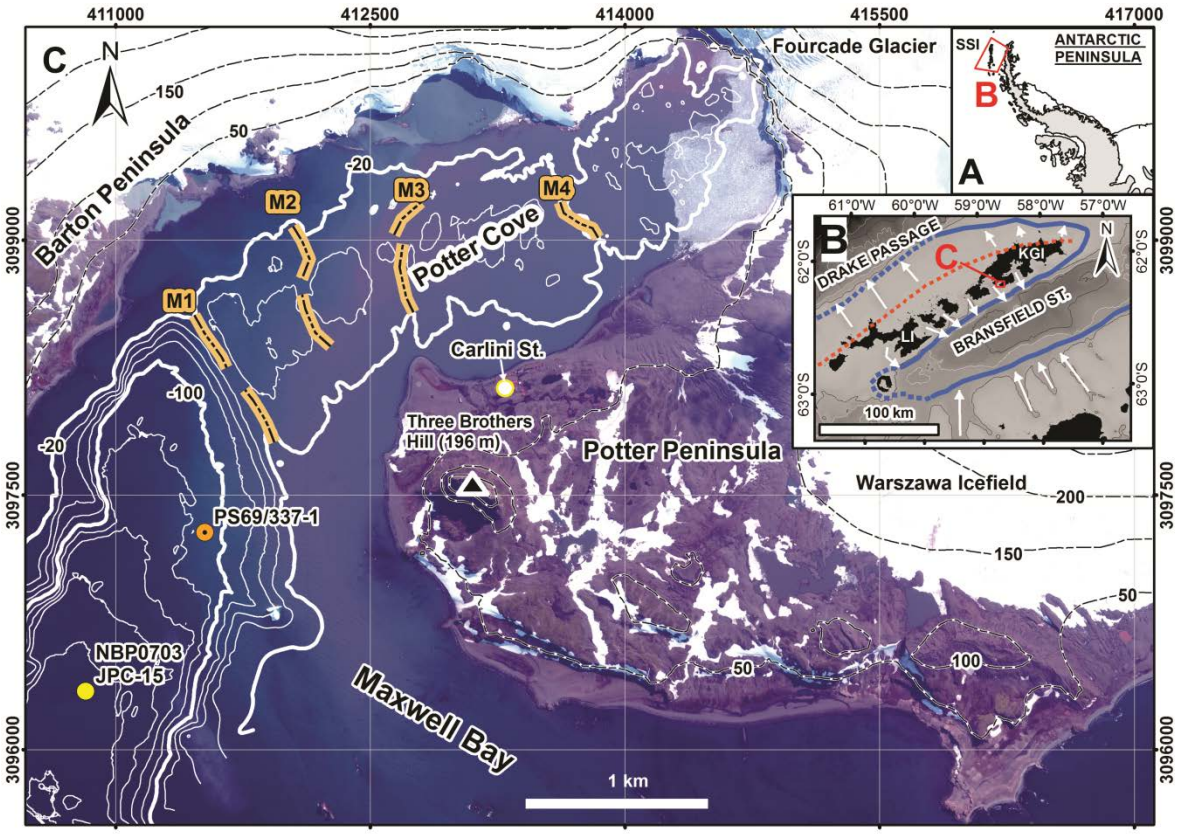

Figure 1. Geographic context of the study area. A) Location of the South Shetland Islands (SSI) and B) King George Island (KGI) and Livingston Island (LI). Bathymetric contours every 500 m (Weatherall et al., 2015). Note the extension of the LGM ice cap (blue full and dotted line) and its axis (red dotted line; after Simms et al., 2011). C) Location and topography of Potter Peninsula and bathymetry of Potter Cove (Deregibus et al., 2015). Note also the position of sedimentary cores and the position of moraine complexes (NBP0703_JPC-15, Majewski et al., 2012; PS69/337-1, Wölfl et al., 2016). Moraine complex M4 represents the position of Fourcade Glacier in 1956 (Wölfl et al., 2016); see Fig 2 and 3 for ice front position in 1956.

Potter Peninsula is an ideal place to unravel those questions. Unlike other ice-free peninsulas around Maxwell Bay, this peninsula is largely covered by till deposits with associated sediments containing datable organic remnants. Based on the study of one key exposure on Potter Peninsula, Sugden and John (1973) proposed a minimum age for the onset of the deglaciation on Potter Peninsula at 9670 ± 230 ^{14}C years before present (9.5 cal ka BP). This age was determined at the base of a 2.5 m thick stratigraphic section, the "Potter Cove section" (see Fig. 2). This section is composed of marine sands with remnants of algae and bivalves deposited in an ice-free environment, which are capped by till, representing a subsequent glacial re-advance. del Valle et al. (2007) studied a similar stratigraphic profile situated 60 m away to the west, named "Pingfo II". Fourcade (1960), González-Ferrán and Katsui (1970), John and Sugden (1971) and Sugden and John (1973), published sketch maps of Potter Peninsula, and Birkenmajer (1998) tried a reconstruction of the Quaternary glacial history of the peninsula based on previous works. This study aims to discuss the paleoenvironmental evolution of

Potter Peninsula after the LGM through the use of detailed geomorphological mapping and also by adding new chronological constraints. To do so, we re-excavated a profile in a similar location to the one made by del Valle et al. (2007), but went deeper to find a similar minimum age for the deglaciation or even an older age. In addition; we also studied an additional stratigraphic profile in the glacier foreland, next to the present ice limit.

2. REGIONAL SETTING

2.1 Study area

Potter Peninsula is adjacent to Maxwell Bay and borders the Fourcade Glacier at its northeastern side. The Fourcade Glacier is an outlet glacier from the Collins Ice Cap, occupying the head of Potter Cove (Fig. 1C). On the other side, the Warszawa Icefield limits the eastern border of the ice-free area of Potter Peninsula. As elsewhere on KGI, the peninsula is generally ice-free during summer times although snow and ice patches are commonly present. The Three Brothers Hill (196 m) is the most prominent morphological feature, being an andesitic neck with columnar jointing, related to the final stage of activity of a Paleogene stratovolcano. This volcano erupted lava flows and pyroclastic rocks. These rock types, along with related hypabyssal intrusives are the main lithologies exposed on Potter Peninsula (Kraus and del Valle, 2008a). The landscape of Potter Peninsula is characterized by glacial landforms, mainly moraines surrounded by a coastal environment with active, Holocene (Lindhorst and Schutter 2014, Heredia Barión et al., in review) and probably older raised marine features (John and Sugden, 1971).

2.2 Glaciological and climate setting

During the LGM an ice sheet extended towards the shelf edge of the AP (Ó Cofaigh et al., 2014). A second, smaller ice cap reaching the outer continental shelf 50 km north of its present location covered the SSI (John and Sugden, 1971) (Fig. 1B). Initial deglaciation of Maxwell Bay associated with decoupling of the ice sheet from the sea floor, occurred between 14.8 and 14.1 ka cal BP (Simms et al., 2011), whereas further inland, the age of deglaciation was determined as 15.5 ± 2.5 ka BP, based on cosmogenic nuclide dating (Seong et al., 2008).

Today, approximately 90% of the surface of KGI is covered by the Collins Ice Cap reaching a maximum thickness of about 400 meters (Blindow et al., 2010). The Equilibrium Line Altitude (ELA) of the ice cap and discharge glaciers increased from c. 150 in the 1980s (Curl et al., 1980) to c. 260 meters above mean sea level (m amsl) in 2015 CE (Falk et al., 2018).

KGI has a maritime climate and is regularly hit by cyclonic weather systems moving eastward along the Drake Passage (Kejna et al., 2013). The annual mean air temperature on KGI between 1948 and 2011 CE was -2.5 ºC (Kejna et al.,

2013), but temperatures are often above zero during summer. The warming trend over the past decades has currently come to a halt, and between 1999 and 2015 CE a slight cooling occurred (Oliva et al., 2017a). Together with an increase of precipitation on the western AP during the last 5 decades (Thomas et al., 2008; Goodwin et al., 2016), this resulted in a slightly positive glacier mass balance on the islands peripheral to the northern AP, such as the SSI (Oliva et al., 2017a).

3. METHODS

We used geomorphological mapping, radiocarbon and cosmogenic ^{3}He exposure dating in our methodology. The obtained ^{3}He exposure ages, however, show very scattered values, presumably due to nuclide inheritance, and thus we do not consider them for our interpretation. For the interested reader we documented the results in the Supplemental Material.

3.1 Geomorphological mapping

Geomorphological mapping is essential for accurately locating and interpreting potential outcrops, landforms and landsystems to be surveyed. We carried out geomorphological mapping of Potter Peninsula through interpretation of geomorphological features in the field combined with the study of a satellite image (WorldView2, DigitalWorld; scene ID: 103001001F612100; pixel resolution 0.5 m; acquired 2013/03/07). We also take into account an orthorectified panchromatic aerial image of 1956 (Falkland Island Dependency Aerial Survey Expedition, FIDASE; image ID X26FID0039076; pixel resolution 0.9 m; acquired 1956/12/20) to infer the area deglaciated over the last decades.

We based our topography on a digital elevation model from the peninsula with a spatial resolution of 3 m pixel^{-1} (Kraus and del Valle, 2008b). Then, we digitalized and georeferenced the mapped landforms from the surveyed localities.

3.2 Stratigraphic profiles

Since we excavated one of our profiles in a similar location to “Pingfo II” (del Valle et al., 2007), we named it “new Pingfo II” section. We also excavated another section in glacial deposits next to the present glacier limit, named as “Inland outcrop”.

We characterized the stratigraphic sections by describing their facies, using textural criteria, fabric, composition, sedimentary structures and the stratigraphic relationships existing between the different depositional units. The profiles were excavated by using shovel and pick-axe. For the measurement of the profile depths we employed measuring tape and hand level.

For a better sedimentary facies interpretation of the new Pingfo II section we carried out sediment textural studies (see Supplemental Material, available online). We digitized the stratigraphic profiles with the software SedLog 3.0 (Zervas et al., 2009).

3.3 Radiocarbon dating

Absolute age data were obtained by AMS radiocarbon dating of seaweed, marine mollusk shells, penguin and undetermined bones, and remnants of mosses embedded in sediments. To reduce the risk of contamination with modern material, all samples for radiocarbon dating were taken from fresh and previously cleaned outcrops and stored in zip-lock plastic bags at 4ºC. We did the sample preparation at the Alfred Wegener Institute Helmholtz Centre for Polar and Marine Research. Sample measurements as well as correction for $^{13}C/^{12}C$ ratio and calculation of Conventional Radiocarbon Ages were done by ETH Zürich and Beta Analytics INC., USA (Table II). We used the ΔR value of 791 ± 121 years (Hall et al., 2010). For further explanation on the chosen ΔR value, please see the Supplemental Material, available online. Calibration of conventional radiocarbon ages was done using the software Calib (v7.0.4, Stuiver and Reimer, 1993) and the calibration curve Marine13 (Reimer et al., 2013) and SHCal13 for Southern Hemisphere (Hogg et al., 2013) for marine and moss samples respectively.

Calibrated ages in thousands of years before present (ka cal BP) are rounded to the next decade and provided as median of the probability distribution with 2σ error range (95.4% probability). A Bayesian age-depth model for the Potter Cove sedimentary sequence was built using the Bacon R package (Blaauw and Christen, 2011).

4. RESULTS

4.1 Geomorphological setting

Our field observations showed that the contact between the Warszawa Icefield and the ice-free area is gentle. On the other hand, the contact between the Fourcade Glacier and the sea creates a steep ice front (Fig. 1C).

The Warszawa Icefield and the Fourcade Glacier markedly retreated from 1956 to 2013, as evident from satellite image analysis (Fig. 3). About 40 % of the present-day deglaciated area of Potter Peninsula became ice-free since 1956. However, due to the extended snow cover (see Fig. 3A), detecting a glacier border is difficult and retreat values are thus viewed as maximum values.

Except for the Three Brothers Hill, Potter Peninsula is roughly divided in two sub environments, a lower environment situated between 0 and 15 m, and a higher-

elevated environment covering altitudes between 50 and 100 m, showing a staircase morphology. The low areas comprise Holocene and active beaches. The higher-elevated area includes vegetated cryogenized bedrock plateaus and glacial deposits/till.

We subdivided the study area into five local geomorphological units (Fig. 2A, B and Table I), following the classification proposed by Oliva and Ruiz-Fernández (2017) in similar settings of the SSI. From the glacier to the coast, the following units are identified:

Unit 1: Recently deglaciated/proglacial area

This area has no vegetation cover and borders the Warszawa Icefield. Towards the north and southeast it is bordered by the sea. It covers an altitude range from sea-level (in the north) up to 80 m amsl towards inland (southeast). The area next to the current glacial front is in many cases waterlogged. Moreover, many lakes developed in the last decades as the glacier front retreated (Fig. 3B). The northeastward retreat of the Warszawa Icefield over the last six decades exposed about 2.7 km2, corresponding to 37% of the present ice free area of the peninsula.

Periglacial processes as frost cracking and freeze thaw in cobbles and boulders of coarse-grained pyroclastic lithologies is active (Fig. 3D) On the other hand, blocks of metric sizes of those lithologies are more resistant to such processes and remain intensely polished and striated. Basaltic lithologies stand more resistant to such periglacial processes.

Fluted glacial deposits or flutings are widespread in Unit 1 (Fig. 2, 4E and F). In the northern part, the flutes are oriented NW-SE whereas west of Superior Lake they are oriented NNE-SSW and towards Stranger Point, they are oriented N-S and NW-SE. Flutes formed parallel to the ice-flow and are the product of combined erosional and depositional processes of subglacial origin in a water-saturated –warm-based– bed of deformable till (Glasser and Benett, 2004; Benn and Evans, 2010).

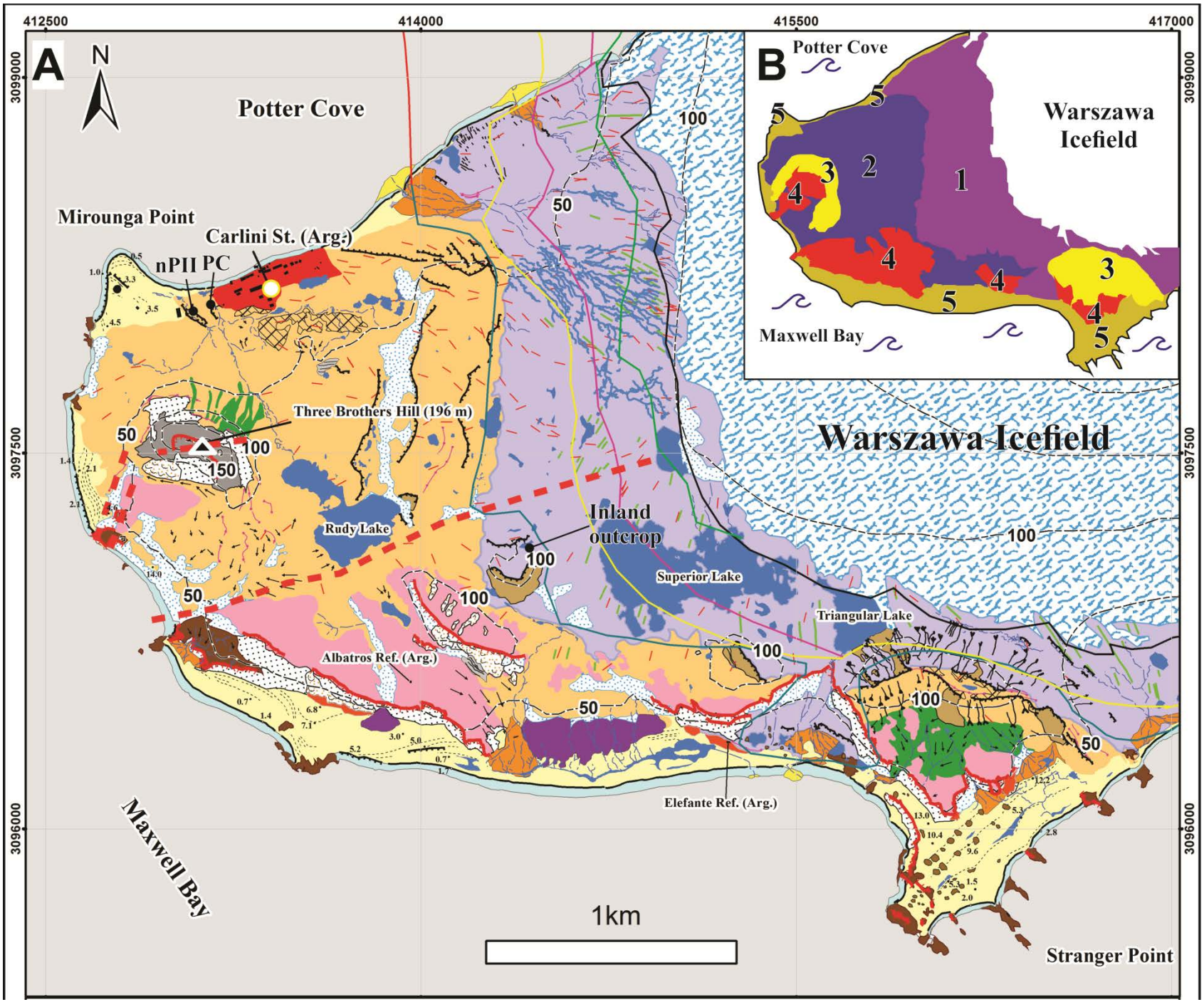
A
N
Potter Cove
Mirounga Point
Carlini St. (Arg.)
nPII PC
Three Brothers Hill (196 m)
Rudy Lake
Inland outcrop
Superior Lake
Triangular Lake
Albatros Ref. (Arg.)
Elefante Ref. (Arg.)
Maxwell Bay
Warszawa Icefield
Stranger Point
1km
412500
414000
415500
417000
3099000
3097500
3096000
B
Potter Cove
Warszawa Icefield
Maxwell Bay

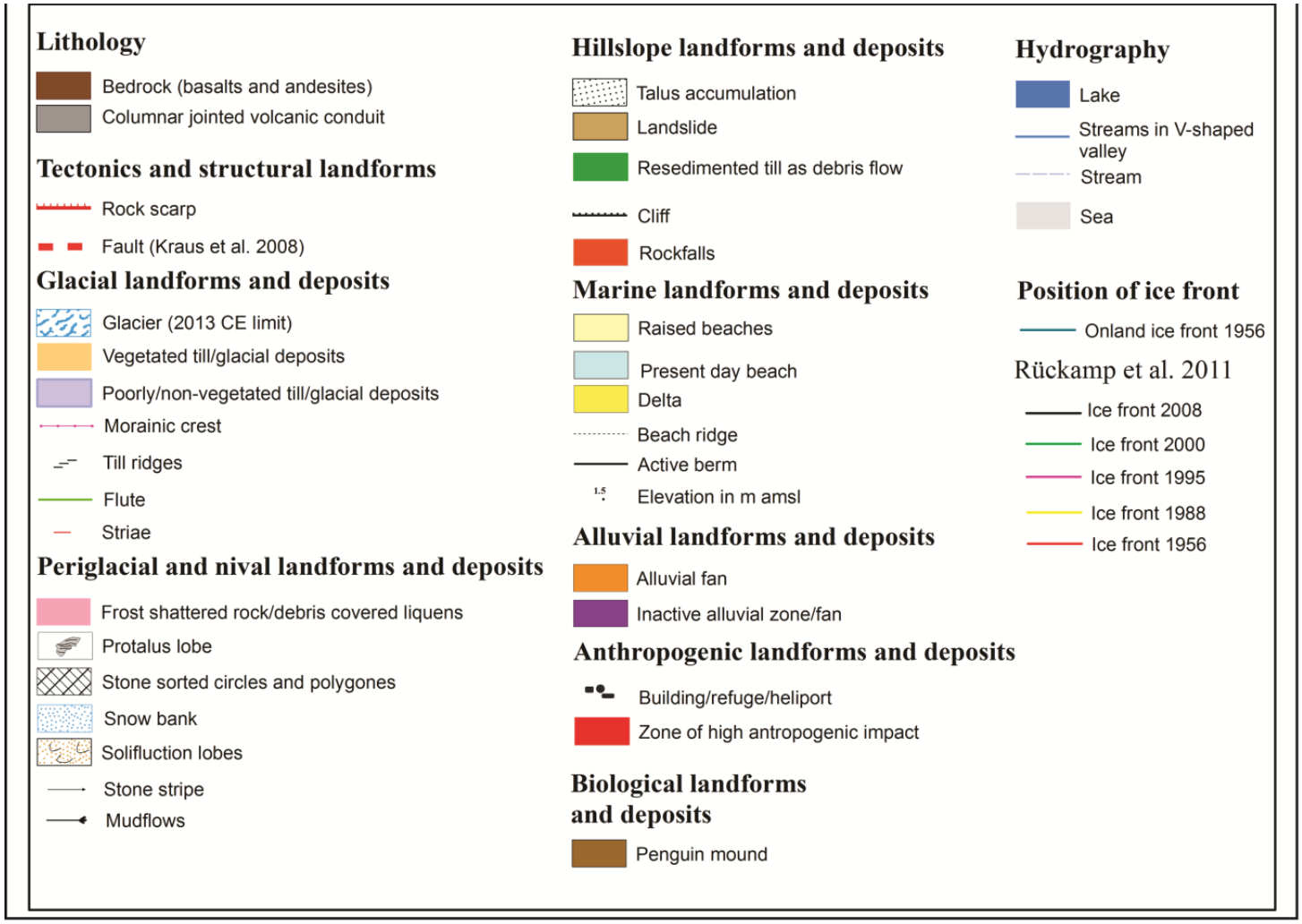

Figure 2. A) Landforms and geomorphological map of Potter Peninsula. PC: Potter Cove section (Sugden and John, 1973); nPII: new Pingfo II section (this study); B) Mapped geomorphological units (1 to 5) described in the text and in Table I.

Local geomorphological units	Landform	Characteristics, distribution, dimensions
Unit 1: Proglacial area (recently deglaciated)	Polished and striated blocks	Linear and continuous glacial scratches and polish on boulder surfaces. Distributed in different volcanic lithologies.
	Till ridges (squeeze-crevasse-ridges)	Aligned longitudinal diamictitic ridges. 0.3 m high,15-60 m long
	Fluted feautures/Flutings	Streamlined, attenuated, lineal hills, associated or not with bedrock obstacles and boulders. Lenght:Width=from 20:1 to 10:1
	Moraine ridges	Linear and curvilinear ridges with gentle lee-flanks and steep stoss-flanks.
	Deltas	Fan-shaped features resulting from the discharge of proglacial streams carrying sediments to the sea. 70 m long and 200 m wide.
	Lakes	Semi-permanent intra-moraine water bodies. Triangular Lake has an outflow towards the south. There are also some filling hollows and the water source is from snow packs, thawing of permafrost/ice core and from seasonal proglacial streams.
	Alluvial fans	Fan-shaped deposits of decametric dimensions. Built up from sediment discharge of proglacial streams. Are connected to deltas downstream.
	Landslides	Erosive scars and convex accumulation of debris triggered by water saturation of the active layer resting on permafrost. 225 m wide, 70 m long.
Unit 2: Older deglaciated area	Lakes	Intra-moraine water bodies. There are also some filling hollows and the water source is from snow packs and rest of water from mass movements after the degradation of moraines
	Stone sorted-circles/polygons	Features on gentle surfaces (3-6º) with thick-grained (i.e. cobbles) sediments towards the periphery. Mainly developed in water saturated areas along streams.
	Stone stripes	Features with classified sediments of several centimeters width and several meters lenght. Developed in slopes up to 10º. They are between 20 and 50 m amsl.
	Inactive protalus lobe	Feature with tongue-like form, conformed of angular boulders. 75 m long, 70 m width. Vegetation on it suggests inactivity of the landform. Located at 30 m amsl.
	Landslides	Erosive scars and shallow convex accumulation of debris triggered by water saturation of the active layer of permafrost.
	Striated and polished blocks and bedrock	Lineal and continuous glacial polish and scratches on some bedrock outrops and principally on boulder surfaces. It represents by mostly basaltic and andesitic lithologies
Unit 3: Moraine systems	Kettle-lakes	Water filled hollow created by water of seasonal snow packs and fusion of ice-core or active table.
	Polished and striated blocks	Linear and continuous glacial scratches and polishing on boulder surfaces.
	Stone sorted-circles/polygons	Features on gentle surfaces (3-6º) with thick-grained (ie. cobbles) sediments towards the periphery. Located at 90 m amsl.
	Landslides	Accumulation of debris triggered by water saturation of the active layer resting on permafrost and possibly on ice core. Distributed on the slopes of the moraine. 20/80 m width, 120/180 m lenght.

	Stone stripes	Features with classified sediments of several centimeters width and several meters lenght. Developed on slopes up to 10º. Located between 20 and 70 m amsl.
	Mudflows/slumps	Rapid mass movements in fine grained sediments transport material down-valley on the Stranger Point moraine system. The sliding surface corresponds to the limit of the active layer in contact with the permafrost table. More abundant on the northern slope of the moraine. Variable size
	Resedimented till as debris flows	Degraded moraines surrounding Three Brothers Hill with slopes of 22-27º reworked into several channelized shallow debris flows. On moraines slopes of 12º the debris flows are not channelized and are wider with stone stripes developed on top.
Unit 4:Bedrock plateaus and Three Brothers Hilll	Polished bedrock (striae)	Linear and continuous scratches and polish of glacial origin on bedrock surfaces.
	Talus accumulations	Accumulations of coarse sediments at the foot of rock cliffs intensely affected by frost shattering. Poorly lichenized sediments suggest active dynamics. An exception is around the Three Brothers Hill. Situated from next to sea-level up to 100 m amsl.
	Solifluction lobes	Appear as step-like landforms at Three Brothers Hill, often with concentration of clasts in the risers. Risers varying from 30 cm up to 1 m in lobes. Developed at south facing talus slopes of the hill. At Three Brothers Hill, appear as tongue-like features with ca. 6 m width in slopes of up to 20º. The lobes are densely covered by vegetation. Located between 80 and 40 m amsl on the bedrock plateaus. There they have not vegetation cover. Their width varies depending if they are associated with rock scarps or located on the plateau itself.
	Rock falls	Accumulation of large blocks fallen from the margin of bedrock outcrops. They are next to sea-level up to 14 m amsl.
	Stone stripes	Features with classified sediments of several centimeters width and several meters lenght. Developed on slopes up to 10º
	Frost shattered rock/debris covered w/ lichens	Highly gelifracted and vegetated bedrock plateaus. Situated between 45 and 90 m amsl.
	Protalus lobes	Feature with tongue-like form, conformed of angular boulders. C. 120 m long, 50 m wide. Absence of vegetation indicates activity of the landform. Located at 50 m amsl.
Unit 5: Raised beaches and present-day beach	Raised beaches	The highest beaches are found at Stranger Point (ca. 14 m amsl). Their elevation and their surface grain-size decreases along the south coast of the Peninsula in direction to Potter Cove, where just present-day beach levels exist east of Carlini Station. Beach ridges are well developed on each raised beach. The raised beaches are poorly vegetated with exception of areas next to inactive lagoons and those at Stranger Point at 6 m amsl and higher levels.
	Present-day beach (PDB)	Surrounds the Peninsula. The active berm mean elevation ranges from 2.4 m amsl at Stranger Point to up to 1 m amsl at Mirounga Point (Lindhorst and Schutter, 2014; Heredia Barión et al., 2018, submitted for publication). Significant biological activity (penguins, sea lions, elephant seals and stranded algae).
	Deltas	Features resulting from the discharge of fluvial sediments in the sea. Up to 50 m long and 70 m wide.

	Alluvial fans	Fan-shaped deposits of decametric dimensions. Built up from moraine material, basically through debris flow and sediments transported by snow-melting streams.
	Inactive alluvial zone/fans	Deposits of debris of alluvial origin no longer active. They cover raised beaches.
	Penguin mounds	Approximately circular, dome-shaped features. The biggest are 20-25 m in diameter and 3 m height. Principally distributed in raised beaches of Stranger Point and next to the PDB along the southeast coast.
	Lake/lagoon	Permanent water body distributed in flat areas present between series of raised beaches and the active berm.

Table I. Landforms and local geomorphological units identified on Potter Peninsula.

Meltwater channels coming from the glacier front cut steep interfluves up to 4 m high into the fluted glacial deposits (Fig. 4E). The meltwater channels run parallel to the axes of the flutes and discharge into the cove forming two alluvial fans and deltas (Fig. 2).

Several till ridges are located along the north coast of Unit 1, between the alluvial fans. These ridges resemble crevasse-squeeze ridges formed by pressing of saturated basal till during stagnation phases transverse to glacial flow (Benn and Evans, 2010), especially on inter-ice stream ridges (Klages et al., 2013). Moreover, morainic ridges of 80 m length are located southeast of the ridges.

Unit 2: Older deglaciated area

This area is ice-free at least since 1956. It is composed of glacial deposits and occupies mostly the western sector of the peninsula. It is mostly situated at 60 to 75 m amsl, but also reaches down to sea level. In contrast to the proglacial area, the glacial deposits and other landforms of Unit 2 are covered to a high percentage by mosses and lichens (Fig. 3C). Polished and striated andesitic and basaltic blocks are common (Fig. 4C), but there are no pyroclastic rocks with such characteristics. Apart from preserved glacial deposits and these erosional features, other glacial landforms are absent in this unit.

Periglacial landforms like sorted polygons and stone stripes are widespread. A small-sized protalus lobe at 30 m amsl is found several hundred meters away southeast of Carlini Station (Fig. 2).

Several lakes developed in this unit. The largest is Rudy Lake, with an effluent running towards Potter Cove. At its east side debris flows developed on the interface between the active layer and permafrost (Fig. 4A). Note that we could not find kame terraces described by Birkenmajer (1998) around Rudy Lake and southeast and north of it.

Unit 3: Stranger Point and Three Brothers Hill moraine systems

The Stranger Point moraine system is located north of Stranger Point. It is situated up to 105 m amsl and stretches over 1.25 km. The moraine is elevated 40 m above the adjacent bedrock plateau and 25 m above the raised beaches of Stranger Point,

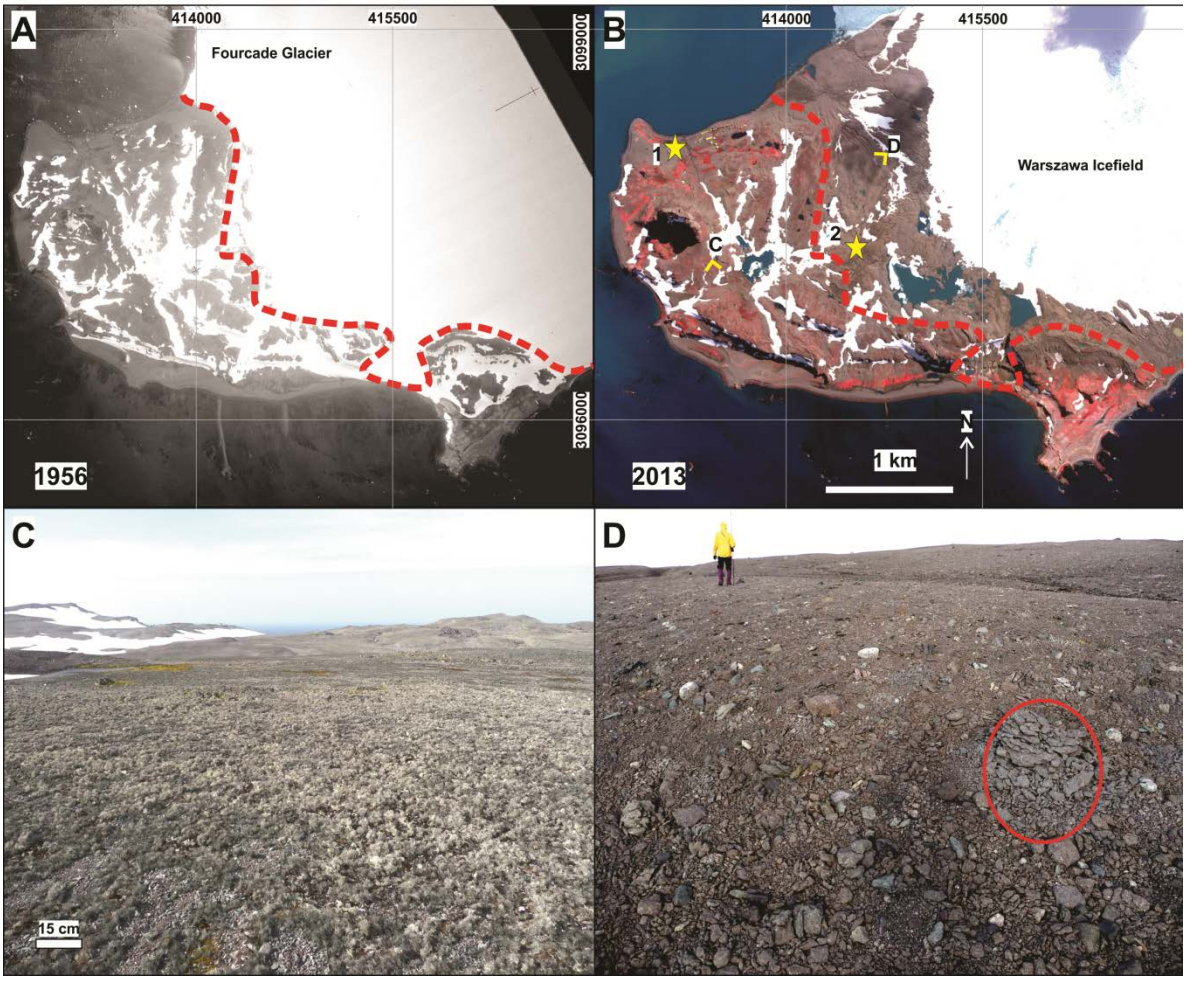

Figure 3. Comparison between the positions of the tide-water Fourcade and inland Warszawa glaciers in (A)1956 CE and (B) 2013 CE; B is a composite satellite image (NIR-G-B) reflecting in red tones the vegetation cover (mostly lichens) on the Peninsula. Stars labeled 1 and 2 indicate the position of the stratigraphic sections, new Pingfo II and inland glacial deposits respectively; see Figs. 5 and 7 for their stratigraphy. (C) and (D) are field photos from vegetated and recently deglaciated glacial deposits (geomorphological Units 2 and 1, respectively). Note the action of freeze-thaw processes causing laminated cracking in pyroclastic lithologies (circle). The directions of the points of view of C and D are indicated in B.

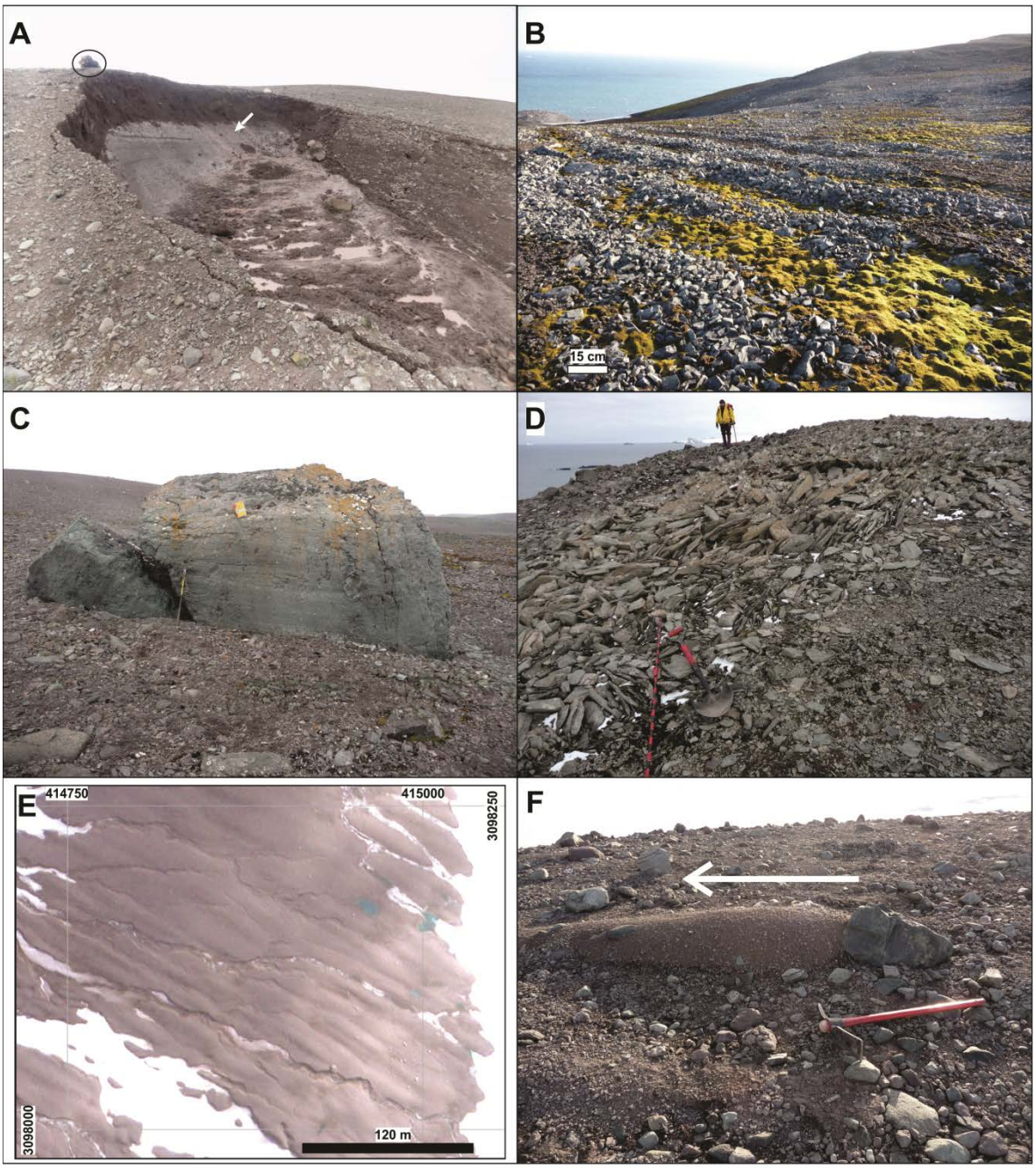

Figure 4. Some of the most widespread landforms observed on Potter Peninsula: (A) slump on glacial deposits showing the permafrost (white arrow); bag on top as scale, (B) stone stripes, (C) polished and striated block, (D) frost shattered bedrock covered in some extent with lichens, (E) flutings in recently deglaciated glacial deposits, being eroded by fluvioglacial activity; and (F) flutes in a smaller scale with indication of former ice movement direction.

where this moraine rests on preserved raised beaches located at 6 m amsl and higher, up to ~12 m amsl. The eastern flank of the moraine descends smoothly towards the present-day beach, while on the western side, the moraine descends to 60 m amsl bordering the Triangular Lake. On its northern flank the moraine

borders the proglacial area of Unit 1. This moraine is likely to sit directly on the bedrock plateau, which is exposed towards the south. Since the moraine is degraded through slumps and debris flows, only discontinuous and relatively few morainic crests are preserved on it.

The moraine consists of unconsolidated basaltic and andesitic gravels and boulders in a sandy to silty matrix. In some cases the boulders show signs of glacial abrasion, namely striae and polished surfaces. Cobbles and boulders of coarse-grained volcanics (i.e. pyroclastics) are generally intensely cracked. Those cracked sediments are reworked by cryoturbation processes, generating stone sorted polygons and stone stripes of metric sizes (Fig. 4B).

The northern, ice facing slope of the moraine declines towards the glacier with about 20º, while the southern slope declines with a similar value towards the south. However, because the northern slope has a higher insolation than the southern slope, the snow does not accumulate for long time and the active layer thaws deeper and faster. Thus, periglacial mass movements such as mudflows and landslides are reworking the unconsolidated sediments of the northern side faster than those of the southern slope. Mudflows and landslides are likely generated at the contact between the permafrost and the active layer. For the mudflows, the permafrost table acts as the sliding surface for the downslope mobilization of the water-saturated overlying sediments (Oliva and Ruiz-Fernández, 2017). Landslides are likely triggered by water saturation of the active layer of permafrost. Furthermore, re-deposited till (as a product of the moraine degradation) is reworked by solifluction on inclined surfaces, creating stone stripes.

The Three Brothers Hill moraine system is partly vegetated and surrounds the homonym hill. It covers an altitude between about 100 and 10 m amsl and it is composed of basaltic and andesitic blocks embedded in an unconsolidated sandy-silty matrix. Morainic ridges surround the hill in a stepped fashion around its northern flank reaching up to 40º slope inclination, while along the south-eastern flank the morainic ridges occur at the foot of the neck, on a slope that incline about 5º, and also the ridges are wider spaced. The northern morainic ridges are highly degraded by debris flows which redeposit unconsolidated moraine sediments downslope. Also talus accumulations coming from the weathering of Three Brothers Hill as well as rock falls coming from steeped walls of the hill partially cover preserved morainic crests (Fig. 2). Centimeter-sized stone stripes are formed on the surface of the southern sector of the moraine.

Unit 4: Bedrock plateaus and Three Brothers Hill

Bedrock exposures form two tilted plateaus and a nearly horizontal plateau, landward of the south coast and of Stranger Point respectively. The heights of the tilted plateaus range from 40 m up to 95 m landwards. The plateau surfaces are

intensely cryogenized (Fig. 4D). In some parts, however, the bedrock is still relatively fresh and exhibits polished surfaces and striae. One of the tilted plateaus has a slope of 10º and solifluction processes evacuate the debris resulting from frost shattering in form of stone stripes and solifluction lobes. Protalus lobes and talus accumulations are developed at 50 m amsl at the foot of rock scarps of this plateau (Fig. 2). Talus accumulations also reach the south coast.

The quasi-horizontal plateau landward of Stranger Point is located at 45-50 m amsl. It is also affected by frost shattering and is intensely vegetated. All the plateaus show rockfall activity. As in the tilted plateaus, several sorted talus accumulations at the foot of their cliffs descend to the raised beaches towards the coast of Stranger Point.

As we mention earlier, the Three Brothers Hill is a Paleogene andesitic neck with columnar jointing. Its weathering by frost action caused talus accumulations and rockfalls in its surroundings. Moreover, vegetated solifluction lobes are located on the south side of the hill, protected from sun radiation.

Unit 5: Raised beaches and modern beach environment.

The southern and west coast of the peninsula is occupied by a series of raised beaches composed of gravel beach-ridge systems developed on top of a prograding strand plain (Lindhorst and Schutter, 2014). The northern coast exhibits modern gravel ridges up to 2 m amsl gently sloping seawards. The rest of the coastline is composed of beach ridge-systems clustering around 11.5, 9.5, 7.5 and ≥ 5.5 m amsl (Lindhorst and Schutter, 2014). Furthermore, a well-developed spit system occurs at the mouth of Potter Cove, at Mirounga Point (Heredia Barión et al., 2018, in review) (Fig. 2). At Stranger Point, numerous abandoned as well as populated penguin rookeries are situated on top of the ridges (Fretwell et al., 2010). They are up to 35 m in diameter and rise up to 2 m above the underlying ridges (Lindhorst and Schutter, 2014). The present-day beach has elevations up to ca. 2 m depending on whether the coast is sheltered or exposed to the predominant waves (Lindhorst and Schutter, 2014).

Deposits of clast-supported, rounded and subrounded cobbles are facing the northern flank of the Three Brothers Hill at 110 m amsl. The cobbles have diameters up to 30 cm, and the deposits are protected from falling scree by an overhang of a cliff of Three Brothers Hill. These cobbles were interpreted as pockets of in situ beach material deposited by marine action in a former (Pleistocene) non-glacial interval and subsequently overridden by ice (“residual beaches”, John and Sugden, 1971). Actually, they are possibly kame terraces deposits and may have early Holocene exposure ages (Watcham, 2010).

Several alluvial fans resting on Unit 5 are a product of the discharge of moraine sediments from debris flows and sediments transported by snow-melting streams on raised beaches. The discharge of Triangular Lake to the sea produces an alluvial fan and also a small delta. Inactive alluvial fans cover raised beaches and they terminate against a lagoon at the south coast of the peninsula, next to Elefante Refugee (Fig. 2).

4.2 Chronostratigraphy

The top of the new Pingfo II section is located at 6 m amsl and in this section, we dated twenty one samples with AMS radiocarbon dating (Fig. 5 and Table II; Supplemental Figure S1, available online). Samples included remains of seaweed, Laternula elliptica shells and rest of bones, likely from birds and seals (cf. del Valle et al., 2007). It is important to note that all the radiocarbon ages from different organisms are in agreement, suggesting that their reservoir effect has the same value and thus, it is not an issue for radiocarbon dating in this section. The chronological model for the marine sediments from the section is illustrated in Fig. 6. The obtained sedimentation rate of 10 mm a^{-1} is quite homogenous throughout the section. The modeled ages cluster between 7.8 and 7.5 ka cal BP.

As indicated by the till deposited on top and the coarsening upward trend of the profile, a glacier re-advance took place over relative distal glaciomarine sediments and deformed the overlying glacio-proximal sediments (Fig. 5). Moreover, we found several escape structures made by Laternula elliptica, dissecting debris flow beds deposited between the glaciomarine sediments (Fig. 5). Such escape structures together with the presence of debris flow beds may indicate a high sedimentation rate related to the proximity of a glacier, forcing the bivalves to go up and try to escape towards the surface through the sediments deposited on top of them, as described by del Valle et al. (2007).

A second stratigraphic section 2.3 m thick was excavated in recently deglaciated inland glacial deposits, 700 m away from the present (2013 CE) limit of the glacier. The section contains two tills (Fig. 7). There, we obtained two radiocarbon dates

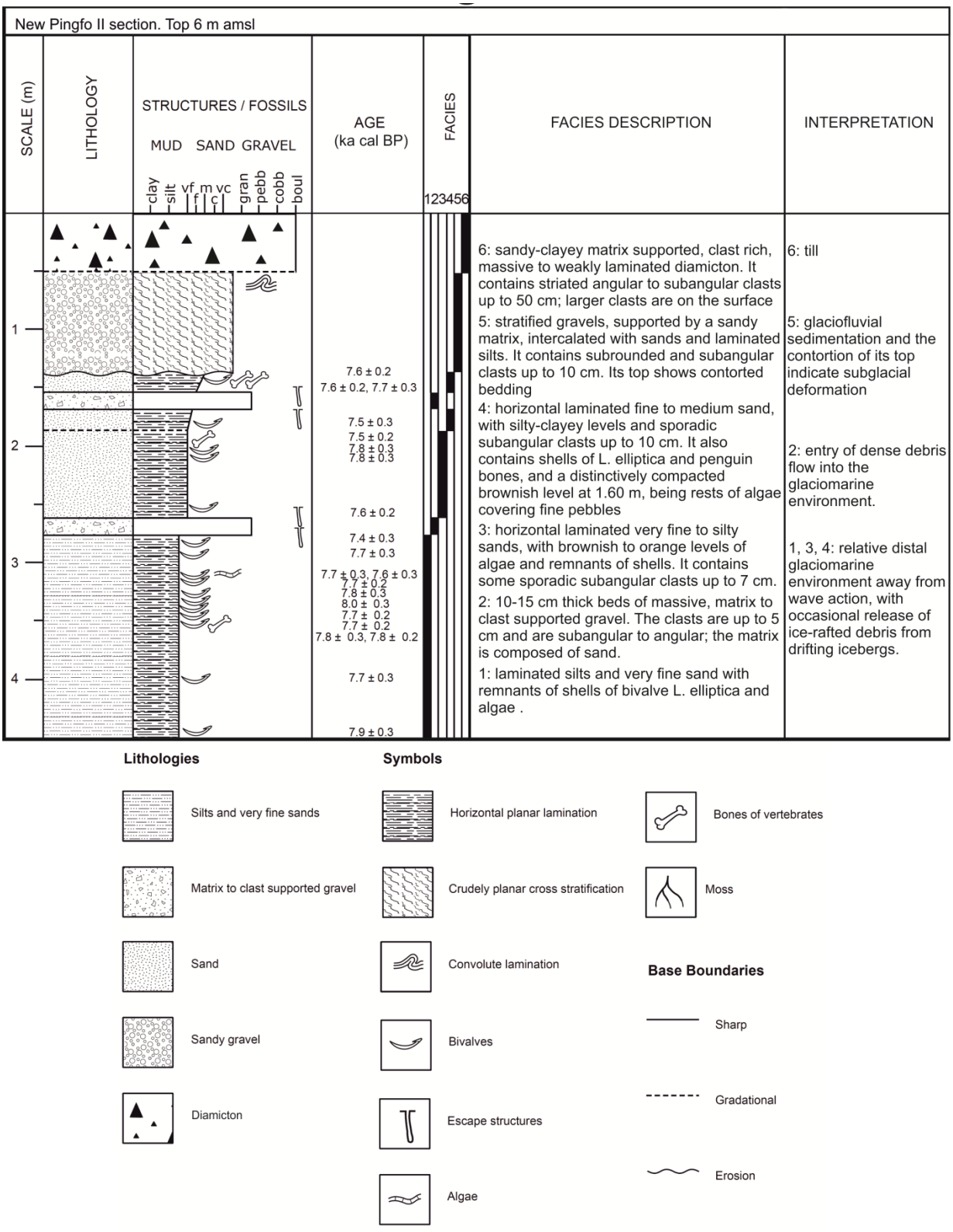

Figure 5. Stratigraphic profile of new Pingfo II section (see Fig. 2 and location 1 in Fig. 3; see also Supplemental Figure S1, available online). See Table I for radiocarbon dating details. The legend shows the lithologies and symbols used in this profile and the one in Fig. 7.

No	Lab ID	Dated material	Depth m below top outcrop	Facies	$\delta^{13}C$ (‰)	^{14}C age [a BP]	Calibrated age (ΔR 791 ± 121 a) cal BP (2σ ranges, 95.4% probability)			
							median of prob. [a]	rounded median [ka]	2σ error [a]	rounded error [ka]
1	Beta-441402	Bone (penguin)	1.50	4	-21.6	7860 ± 40	7555	7.6	240	0.2
2	Beta-441403	Bone (penguin)	1.55	4	-22.2	7890 ± 40	7582	7.6	240	0.2
3	ETH-67269	Bivalve shell	1.60	4	-1.6	8010 ± 85	7695	7.7	267	0.3
4	ETH-67267	Bivalve shell	1.70	4	0.0	7805 ± 85	7507	7.5	275.5	0.3
5	Beta - 431964	Bone (penguin)	1.85	3 - 4	-23.1	7780 ± 30	7485	7.5	226.5	0.2
6	ETH-67270	Bivalve shell	2.05	3	-1.3	8170 ± 85	7840	7.8	287	0.3
7	ETH-67272	Bivalve shell	2.10	3	-13.4	8115 ± 80	7789	7.8	281.5	0.3
8	ETH-71994	Bivalve shell	2.56	3	2.0	7920 ± 20	7609	7.6	226.5	0.2
9	ETH-67268	Bivalve shell	2.70	3	-13.6	7705 ± 80	7418	7.4	267.5	0.3
10	ETH-67273	Bivalve shell	2.95	1	-4.4	8005 ± 85	7691	7.7	266	0.3
11	ETH-67275	Bivalve shell	3.05	1	-12.1	7950 ± 70	7639	7.6	273.5	0.3
12	ETH-67274	Seaweed	3.05	1	-2.3	8020 ± 90	7705	7.7	254	0.3
13	ETH-67276	Bivalve shell	3.10	1	-10.5	8145 ± 70	7816	7.8	273	0.3
14	ETH-72000	Bivalve shell	3.11	1	1.3	8015 ± 20	7698	7.7	227.5	0.2
15	ETH-67277	Bivalve shell	3.30	1	-1.0	8300 ± 75	7973	8.0	296	0.3
16	ETH-71996	Bivalve shell	3.41	1	2.9	8005 ± 20	7688	7.7	226.5	0.2
17	ETH-71997	Bivalve shell	3.46	1	0.8	7995 ± 20	7679	7.7	227	0.2
18	Beta - 441404	Bone (indeterminate)	3.50	1	-23.8	8100 ± 40	7774	7.8	240	0.2
19	ETH-67278	bivalve shell	3.50	1	-9.0	8090 ± 75	7766	7.8	270.5	0.3
20	ETH-72001	Bivalve shell	4.00	1	2.1	7995 ± 65	7681	7.7	248.5	0.3
21	ETH-71995	Bivalve shell	4.47	1	8.0	8195 ± 25	7862	7.9	251	0.3
22	Beta-441400	Moss	2.20	1	-20.9	1880 ± 30	1778	1.8	79	0.1
23	Beta-441401	Moss	2.20	1	-22.1	1850 ± 30	1741	1.7	104.5	0.1

Table II. Results of radiocarbon dating. Samples 1-21 belong to the new Pingfo II section, whereas 22 and 23 belong to the inland outcrop. Samples Coordinates: 62.2389ºS, 58.6729ºW; UTM -21: 413071, 3098082 (Samples 1-21); 62.2473 ºS; 58.6466 ºW; 414461,3097178 (Samples 22 and 23)

from the base of the section (1.7 and 1.8 ka cal BP; Fig. 7 and Samples 22 and 23, Table II), containing fragments of mosses embedded in the glacial deposits. Deposits of this section record a glacier re-advance.

5. DISCUSSION

Based on the chronological data and geomorphological mapping, we propose the following Holocene landscape evolution for Potter Peninsula.

Early Holocene

There are different opinions about the environmental development on the SSI during the early Holocene, based on evidence of regional warming and an extensive glacial retreat after the LGM, but also on indications for a glacier still-stand and even a re-advance.

The chronostratigraphy of the new Pingfo II section reflects the transition from a relative distal glaciomarine environment between 7.8 and 7.5 ka cal BP to a subsequent proximal glaciomarine and glacier front environment, as the Fourcade glacier re-advanced over the previously deposited sediments (Fig. 5), reaching the mouth of Potter Cove. The re-advance bulldozed over the marine sediments, leaving algae as a compacted seaweed layer. Our interpretation of the changes in the sedimentary environment is in agreement with previous studies of Sugden and John (1973) and del Valle et al. (2007). On the other hand, our chronology differs from the one obtained by Sugden and John (1973). They propose that the onset of the deglaciation on Potter Peninsula was at or before 9.5 ka cal BP. Although our profile is deeper than the section from these authors, our detailed chronostratigraphy could not replicate or even find such an older age. Other authors obtained similar results (Strelin et al., 2014). Instead our oldest modeled age is 7.8 ka cal BP, and oldest radiocarbon date was 8.0 ka cal BP. Furthermore, our new radiocarbon data are more consistent, detailed and reliable than previously available data. The oldest age obtained by Sugden and John (1973) seems to be an outlier in comparison to our age model (Fig. 6). Thus, we propose to place the minimum age for the onset of the deglaciation phase on Potter Peninsula at 7.8 ka cal BP. Moreover, while the marine sediments were deposited at 7.8 to 7.5 ka cal BP, the relative sea level was up to 14 m above present mean sea level at Potter Peninsula, based on calculated isostatic uplift values for this area (Fretwell et al., 2010). Sediment cores retrieved from inner Maxwell Bay, suggest that the bay was ice free by 9.1 ka cal BP (Simms et al., 2011) and the glacier retreat increased around 8.0 ka cal BP, when the warmest Holocene conditions are recorded in the AP (Bentley et al., 2009, Milliken et al., 2009). Ice retreat is also evidenced by the existence of ice-free areas further inland around Maxwell Bay. There, glacially polished bedrock surfaces dated with cosmogenic nuclides at Barton and Weaver Peninsulas as well as the onset of lake sedimentation at Barton and Fildes Peninsulas between 11.0 and c. 8.0 ka cal BP (Seong et al., 2008; Watcham et al., 2011; Oliva et al., 2016a) evidence the start of

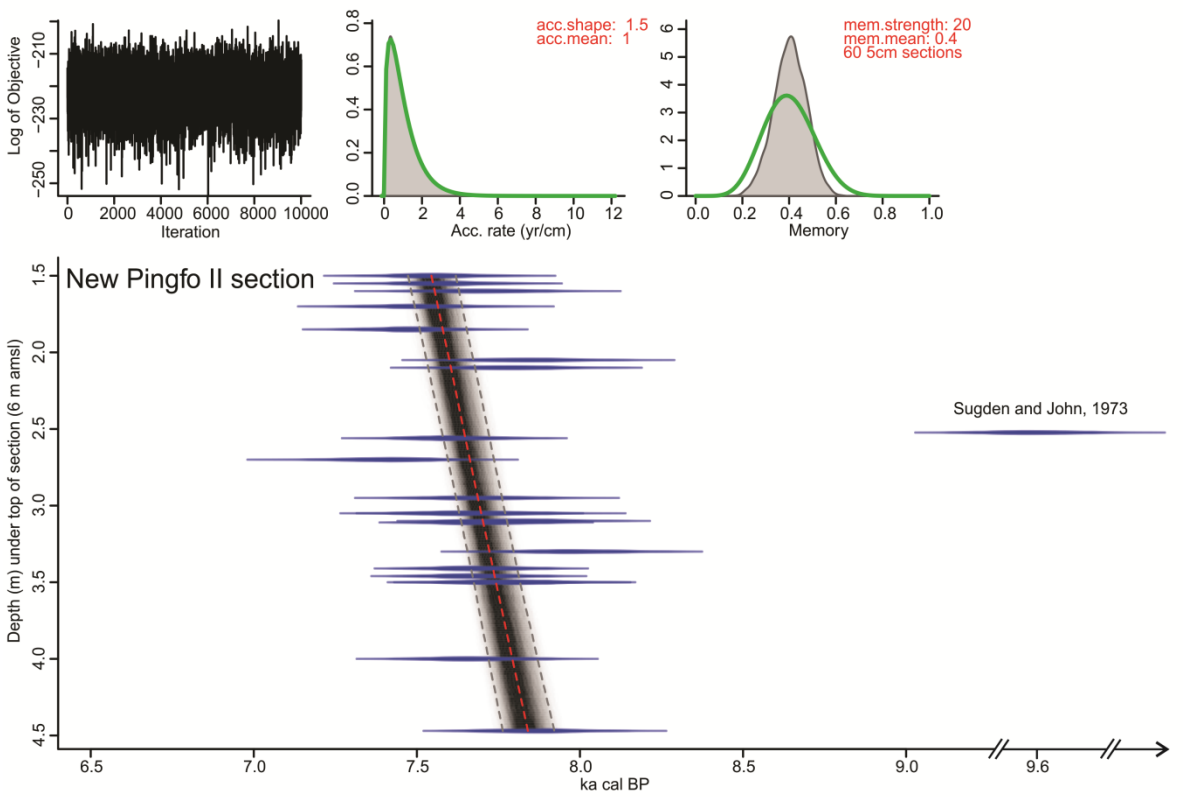

Figure 6. Bayesian age model for the new Pingfo II section with our ages clustering between 7.8 and 7.5 ka cal BP, compared to the much older age reported by Sugden and John (1973).

the deglaciation in the region. At Byers Peninsula, Livingston Island, SSI (Fig. 1B), radiocarbon data from lake sediments suggest that the onshore glacier retreat started there between 8.3 and 7.5 ka cal BP (Oliva et al., 2016b).

According to our age model and stratigraphy, the Fourcade glacier re-advanced after 7.5 ka cal BP. This re-advance can be tentatively correlated with a rise of the relative sea level curve for the SSI at 7.2-7.0 ka cal BP (Watcham et al., 2011). This rise is related to a pause on the post-LGM glacier retreat and still-stand during deglaciation (Watcham et al., 2011). Furthermore, surface exposure ages of moraine boulders on Hurd Peninsula, Livingston Island, suggest a glacier advance at c. 7.0 ka BP (Hall, 2009; pers. comm. Brenda Hall, 2015). By contrast, proxies of terrestrial and marine records from the northwestern AP indicate extensive glacial melt, open waters without sea-ice in Maxwell Bay and warm conditions similar to the present at about 7.0 ka BP (Milliken et al., 2009; Watcham et al., 2011; Mulvaney et al., 2012; Peck et al., 2015; Roberts et al., 2017). Thus, although we propose a glacier re-advance on the SSI at about 7.0 ka cal BP, it still has an unclear climate connection and could be related to changes in glacier stability due to precipitation, regional glacio-isostatic adjustment and/or sea-level variations.

Mid-Holocene

The degree of development of periglacial patterned ground landforms could be used to get a relative minimum age for the exposure of the geomorphological Unit 2 after the proposed glacier re-advance during the early Holocene in Potter Peninsula. Jeong (2006) attempted to date the deglaciation on KGI by radiocarbon dating on remnants of mosses and lichens in sorted polygons. They found that the diameter of sorted vegetated polygons is directly related to their age, with the biggest polygon (3.23 m) being the oldest (4710 ± 40 ^{14}C years BP; 5.4 ± 0.1 ka cal BP). We measured sorted polygons and circles of the geomorphological Unit 2 are up to ~2.5 m in diameter and thus, tentatively 2.6 ka old. However, ages derived from stone sorted circles have limitations as an indicator of deglaciation ages (Jeong, 2006).

On the SSI, the glaciers reached their present limits around 6 ka BP (Mäusbacher et al., 1989; Watcham et al., 2011; Ó Cofaigh et al., 2014). From 4.5 to 2.8 ka cal BP, studies based on lake sediments propose a phase of significant warming, with glaciers situated landward of their present limits and formation of peat banks (Björck et al., 1991a, 1991b). By contrast, investigations in marine sediment cores suggest decreasing sea surface temperatures and sea-ice cover increasing in Maxwell Bay between c. 5.9 and 2.6 ka cal BP, without evidence of glacier re-advance (Milliken et al., 2009). Lake sediment deposition continued. Based on relationships with adjacent moraines and on varve counting, respectively, Birkenmajer (1998) and del Valle et al. (2004) propose a minimum age of 0.5 ka for Rudy Lake in Unit 2.

In summary, the vegetated glacial deposits of Unit 2 seem to have roughly a mid-Holocene maximum age, based on the development of patterned ground landforms, lake sediment formation and regional paleoenvironmental correlations.

Late Holocene

The results of our geomorphological mapping campaign showed that vegetated protalus lobes of Units 2 and 4 are located between 30 and 60 m amsl. Several protalus lobes on the SSI are dated through cross-cutting relationships with raised beaches and linked to the last glacier re-advance (i.e. 0.8-0.3 ka old, Serrano and López-Martínez, 2000). Protalus lobes are landforms which move down-slope throughout frost creep, associated with deglaciation and transition from a glacial to a periglacial environment on the SSI (Serrano and López-Martínez, 2000). The protalus lobes on Potter Peninsula are approximately 200 m below the present-day ELA in the study area, indicating very different environmental conditions during their formation. Furthermore, as elsewhere in periglacial settings (Kääb, 2007), the vegetation cover on the protalus lobe next to Carlini Station together with the absence of a basal talus at its foot could point to the inactivity of the landform due to a more humid and warmer climate conditions.

The onshore glacier retreat of the last ~60 years revealed a till sequence with remnants of mosses at its base, which we dated at 1.8 and 1.7 ka cal BP. This sequence shows colonization of mosses, and indicates that at 1.8-1.7 ka cal BP, the glacier was at its 1950s or even at its current position, or further landward (see the relative position of the section in Fig. 3B). Afterwards, the mosses were overrun by a glacier re-advance, and became embedded in the till (Fig. 7). Thus, the ice extended further seaward than today after 1.7 ka cal BP, and the mosses may represent warmer temperatures prior to the re-advance. In Potter Cove, off-shore geomorphological studies reveal that the outermost marine moraine complex M1 (Fig. 1C) represents the latest preserved maximum position of the Fourcade Glacier, likely between 2.6 and 1.7/1.6 ka cal BP (Simms et al., 2011; Wölfl et al., 2016). Furthermore, marine sediment cores and the position of the submerged moraine complexes M2 and M3 indicate that the Fourcade Glacier was located inside the inner cove between 0.5 and 0.1 ka cal BP (Fig. 1C) (Majewski et al., 2012; Wölfl et al., 2016; Munoz and Wellner, 2018). In contrast, at Barton Peninsula and Byers Peninsula, Livingston Island, radiocarbon dating on basal lake sediments and exposure dates from bedrock outcrops, suggest that no major glacier advances occurred in the last 2.4 ka cal BP (Seong et al., 2008; Oliva et al. 2016a and b). Warm and humid climatic conditions on KGI are supposed for the time period between c. 1.4 and 1.1 ka cal BP based on sedimentological and geochemical data from a marine massive diamicton (Yoon et al., 2004). Other marine and terrestrial records on KGI indicate still warmer temperatures between 1.4 and 0.55 ka cal BP and a cooler period between 0.55 and 0.05 ka cal BP, tentatively linked to the northern hemisphere Medieval Warm Period and the Little Ice Age, respectively (Hall, 2007; Hass et al., 2010; Monien et al., 2011; Angiel and Dąbski, 2012; Majewski et al., 2012). Simms et al. (2012), based on the direct comparison of radiocarbon ages and dates obtained by means of optical stimulated luminescence concluded that the last glacier re-advance took place between 0.45 and 0.25 ka cal BP (Yoon et al., 2004; Yoo et al., 2009).

Summarizing, around 1.8/1.7 ka cal BP, a climatic optimum was reached and its final phase may be indicated by a glacier re-advance probably between 0.5 and 0.1 ka cal BP. Subsequently, the inner Potter Cove was occupied by the Fourcade Glacier, while onshore protalus lobes formed and the Warszawa Icefield bulldozed the mosses into glacier till.

Raised beaches as indicators of Holocene glacial oscillations

As elsewhere on the SSI, the distribution of raised marine beaches at certain altitudes provides minimum ages for the last coastal deglaciation (Hall, 2003). Coastal gravel deposits at 6 m amsl and below overlie till and volcanic bedrock at the west and north coast of Potter Peninsula. These coastal gravel deposits have maximum ages of 0.65 ka cal BP (Curl, 1980; Lindhorst and Schutter, 2014;

Heredia Barión et al., in review). At Potter Peninsula, they post-date the last glacial re-advance (Sugden and John, 1973; Clapperton and Sugden, 1988).

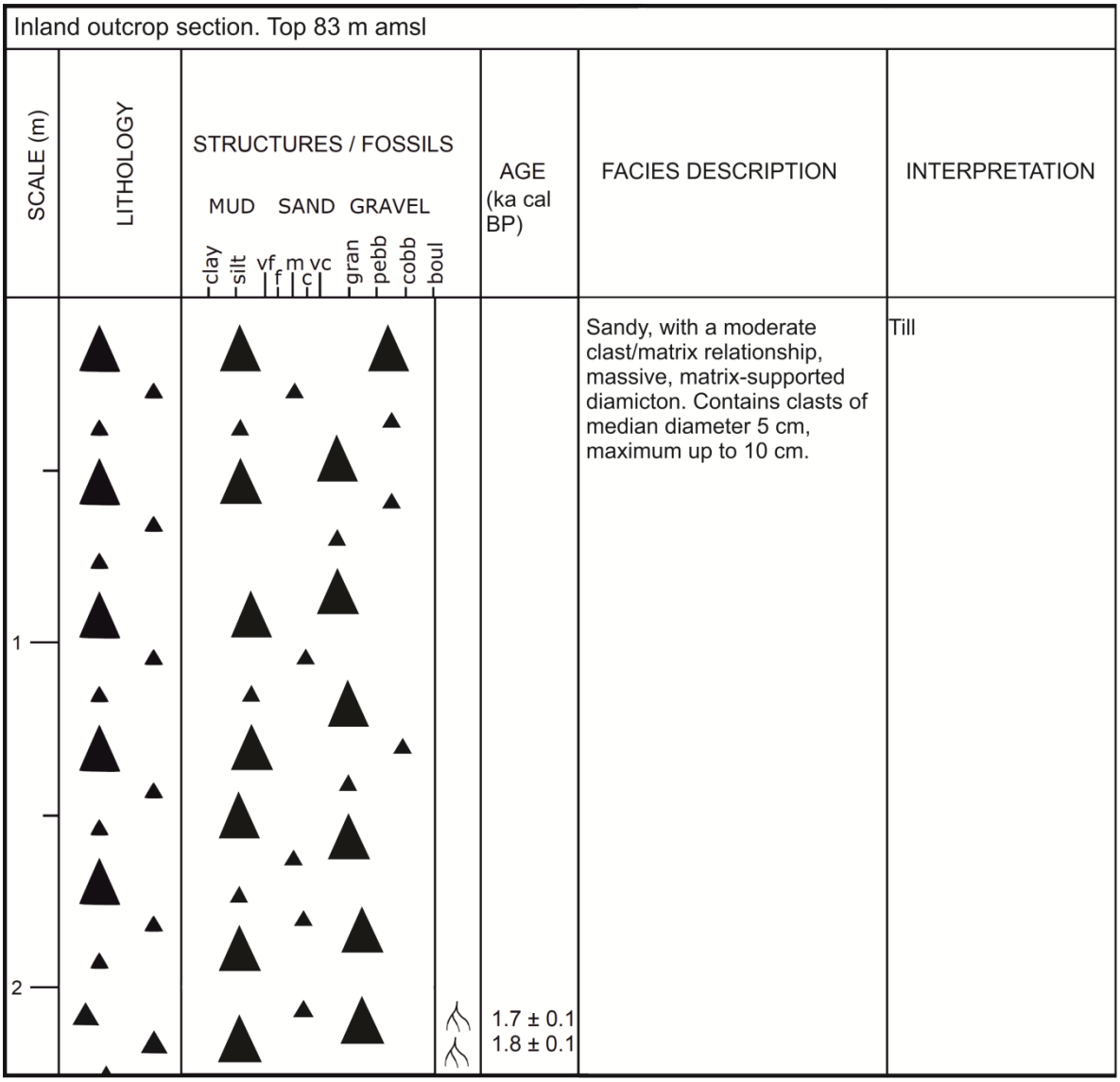

Figure 7. Stratigraphic profile of studied inland glacial deposits deposits (see Fig. 2 and location 2 in Fig. 3). For legend see Fig. 5.

Raised beaches in the south of the peninsula at an elevation of up to 7.3 m amsl are dated at 1.9 ka cal BP (Lindhorst and Schutter, 2014). Here, the highest beach sediments overlie volcanic bedrock and till (Lindhorst and Schutter, 2014). At Stranger Point, the highest raised beach at c. 12 m amsl is dated at 4.3 ka cal BP and overlies glacier sediments (Lindhorst and Schutter, 2014). Furthermore, raised coastal sediments at 14.4-17.1 m amsl dated at 5.5-5.4 ka cal BP give a minimum age for beach formation and thus for the onset of the deglaciation of Stranger Point (del Valle et al., 2002). Additionally, the Stranger Point moraine system of the

geomorphological Unit 3 cross-cuts raised beaches at 6 m amsl, suggesting a maximum age of 0.65 ka cal BP for a glacial re-advance which covered this location.

Taking everything into account, it is likely that during the Holocene the glacier limit advanced towards the outer cove several times (Fig. 8), while occupying a bigger proportion of the peninsula compared to today.

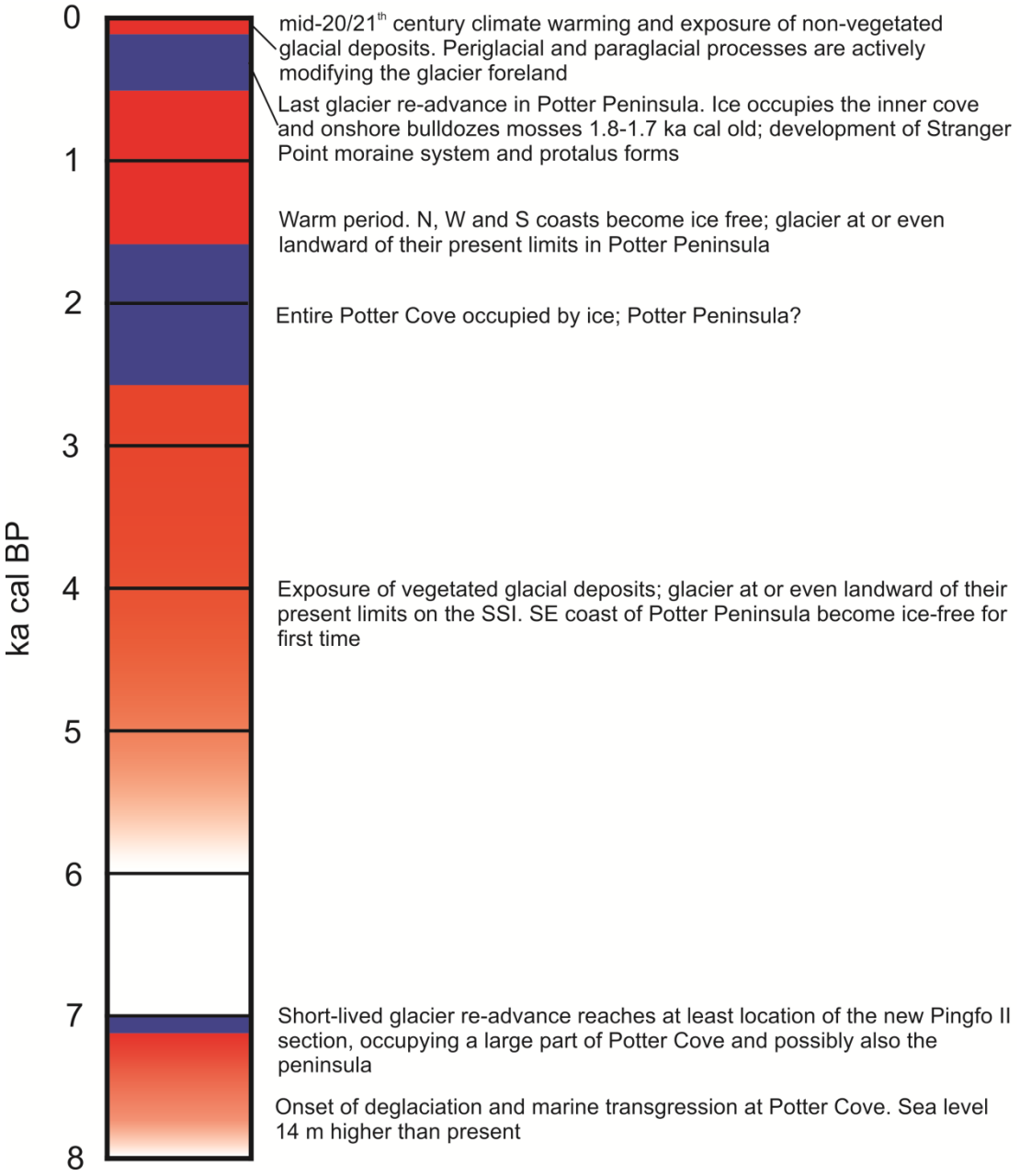

Figure 8. Chronology of glacier fluctuations and geomorphological development at Potter Peninsula and Potter Cove. Reddish tones indicate warm periods, whereas bluish tones indicate cold phases.

Present-day deglaciation and active geomorphological processes

Judging from the simultaneous retreat of the present land-terminating glaciers, there is strong evidence that glacier retreat on KGI was initiated by the increasing air temperatures along the AP of the last decades (Braun and Gossmann, 2002). Deglaciation also has exposed new onshore ice-free areas on Potter Peninsula, which are subject to intense sediment reworking and redistribution characteristic of paraglacial modifications of glacier forelands (Ballantyne, 2002). Moreover, periglacial/frost action and mass-movement are the most widely processes distributed on Potter Peninsula, particularly on the geomorphological Unit 1. Freeze-thaw weathering shatters unconsolidated sediments and boulders on moraines and other glacial deposits, but also is especially effective at bedrock outcrops of bedrock plateaus of Unit 4. Rapid mass-movements like rockfalls transfer the sedimentary products of the periglacial processes down-slope, creating talus accumulation at the foot of bedrock plateaus and of Three Brothers Hill (Unit 4).

Cryoturbation forms sorted circles and polygons in gentle slope areas above 50 m amsl on Potter Peninsula, particularly in areas where surficial sediments are saturated with water. This may be explained by a permafrost table which inhibits water draining away and being absorbed into the soil (Davies et al., 2013). On the other hand, cryoturbation creates stone stripes on inclined surfaces. Furthermore, in combination with gelifluction and frost-creep, stone stripes may result in gelifluction lobes, like those located at the foot of the bedrock plateaus of Unit 4. However, lobes do not point to the presence of permafrost in the rock slopes since gelifluction and frost-creep are linked to seasonal frost (Matsuoka, 2001).

The Stranger Point moraine system is being actively degraded by mudflows, solifluction and thermokarst processes as in similar settings of the SSI (López-Martínez et al., 2012; Oliva and Ruíz-Fernández, 2017). Thermokarst is probably related to the existence of permafrost or ice-cores, since we found them in moraines on Potter Peninsula (Fig. 4A). Ice-cored moraines are ice-marginal landforms that comprise a discrete body of glacier ice buried underneath sediment (Lukas, 2011). John and Sugden (1971) and Sugden and John (1973) mapped ice-cored moraines next to the glacier limit. Hochschild (1995) also report that all the glacial deposits on Potter Peninsula are ice-cored.

Fluvial processes are acting intensively next to the glacier front on Potter Peninsula (Fig. 2, Unit 1; Fig. 4E). They are cutting the recently exposed moraine, providing a large portion of suspended sediment load to Potter Cove and also forming alluvial fans and deltas which prograde towards the cove. Moreover, the suspended sediment input to the cove significantly changes physical and chemical properties of the cove (Jerosch et al., 2018), e.g. salinity, turbidity, light transmission and trace metals (Henkel et al., 2013), but also impacts the biological communities living there (Quartino et al., 2013; Pasotti et al., 2015a, 2015b; Sahade et al., 2015; Falk et al., 2018).

6. CONCLUSIONS

Our study contributes to a deeper understanding of the Holocene glacial geology of Potter Peninsula. We applied geomorphological mapping and stratigraphic surveys of newly ice-free areas and performed AMS radiocarbon dating. We were able to re-evaluate and improve the onset of the deglaciation on Potter Peninsula. We propose a new minimum age of 7.8 ka cal BP instead of an earlier accepted age of 9.5 ka cal BP, based on our more detailed chronology and deeper excavation of the new Pingfo II profile. We further propose a glacier re-advance after 7.5 ka cal BP, likely between 7.2 and 7.0 ka cal BP, reaching the mouth of Potter Cove. It is likely linked with a glacier re-advance or still-stand documented elsewhere on SSI at about 7 ka cal BP. Nevertheless, climatic conditions associated with these glacial re-advances remain unclear. Following the re-advance, during the mid-Holocene, the glacier front retreated to a position similar to the present one. As result of the glacier re-advance, modern vegetated glacial deposits were formed. At 1.8-1.7 ka cal BP, a climatic optimum was reached with similar glacier limits compared to 6 decades ago or even as today. This warm period ended with the last glacier re-advance between 0.5 and 0.1 ka cal BP. Integrating, these findings suggest that glaciers repeatedly occupied Potter Cove and also the peninsula throughout the Holocene. They further indicate that the present state of reduced ice in the study area is not unprecedented. Besides, the Holocene glacial history of Potter Peninsula has been more variable than previously known, having implications for calibrating local and regional ice sheet models. With regard to the last decades, our data indicate that deglaciation exposed the glacier foreland to periglacial, mass wasting and glaciofluvial processes which are degrading glacial deposits and moraines.

7. ACKNOWLEDGEMENTS

We acknowledge funding by Centro de Investigaciones en Ciencias de la Tierra (CONICET), the Dirección Nacional del Antártico/ Instituto Antártico Argentino (DNA/IAA) in the framework of the Project PICTA, 2011 – 0102, IAA "Geomorfología y Geología Glaciar del Archipiélago James Ross e Islas Shetland del Sur, Sector Norte de la Península Antártica" and support by the Alfred Wegener Institute (AWI) research program Polar regions and Coasts in a changing Earth System (PACES II). PHB, GK and JAS were funded as well by IMCONet (FP7 IRSES, action no. 318718). Special thanks go to the crews of the Argentine research station "Carlini" and the adjoined German Dallmann-Labor (AWI) during the 2014 and 2015 field seasons for their cordial hospitality and invaluable logistical support. Fieldwork assistance by M. Barrionuevo, M. Makeschin and M. Argota is highly appreciated. We also thank S. Wiebe and R. Fröhlking, for their support with textural analyses and C. Schott, A. Toltz, M. Medina and E. Schnabel for sample processing, mineralogy determination and noble gas analysis for ^{3}He exposure dating.

SUPPLEMENTAL MATERIAL TO CHAPTER 3: HOLOCENE GLACIAL DYNAMICS AND GEOMORPHOLOGY OF POTTER PENINSULA, KING GEORGE ISLAND (NW ANTARCTIC PENINSULA).

Heredia Barión, P. A., Strelin, J. A., Spiegel, C., Wacker, L., Niedermann, S., Kuhn, G.

Textural analyses

We took 13 samples along the stratigraphic profile from the new Pingfo II section (Supplemental Figure S1). For every sample, we used dry sieving to separate the fraction larger than 2 mm. The rest of the sample was put in an ultrasonic bath for 10 seconds. Afterwards, we used a reciprocating shaker and left the sample there overnight. Then, we used wet sieving to separate the fraction <0.063 mm (silt and clay size). The larger fraction was dried in an oven at 50ºC. Once dried, we used dry sieving to separate sands (>1mm, >0.5 mm, >0.25 mm, >0.125 mm and >0.063 mm). The silt and clay fraction was transferred to a sedimentation cylinder and 1 L of distilled water was added. Using Stoke´s Law, we separated fine and coarse silt from clays with the pipette method. To concentrate the clay afterwards we used a centrifuge. The silt and clay fractions were dried again in an oven at 40ºC.
The results are shown in Supplemental Table S1.

Reservoir correction for radiocarbon age calibration

Local reservoir corrections (ΔR) for marine samples as reported for the SSI are in a broad range of about 700 to 1300 years (e.g. Curl, 1980; Björck et al., 1991c; Gordon and Harkness, 1992; Berkman and Forman, 1996; Milliken et al., 2009; Hall et al., 2010; Hass et al., 2010; Watcham et al., 2011). Hall et al. (2010), based on paired radiocarbon and uranium–thorium dates of Antarctic solitary corals, proposed a ΔR of 791 ± 121 a. This local reservoir age is further supported by results of Simms et al. (2012) who used OSL of cobble surfaces to investigate the depositional age of beach ridges on KGI. Due to the verification with two independent dating methods, the local reservoir correction proposed by Hall et al. (2010) was used in this study.

^{3}He surface-exposure dating

We chose to measure cosmogenic 3He in basaltic boulders on the Three Brothers Hill moraine system because this nuclide accumulates in pyroxene and olivine crystals, which are present as phenocrysts in Potter Peninsula basalts. The basalts of the peninsula have been K-Ar dated at 49 ± 1 to 42 ± 1 Ma (cf. Smellie et al., 1984). Cosmogenic 3He is stable, and therefore accumulates within a rock, recording the total time of exposure to cosmic rays that it has experienced.

We used four samples of 1 kg weight each from basaltic boulders (Supplemental Figure S2; see Supplemental Table S2 A for dimensions of erratics). Some of them showed striated surfaces, such as 01- and 05-Potter.

The exposures ages were calculated using the CRONUScalc calculator (Version 2.0; Marrero et al., 2016) with the time-dependent Lal (1991)/Stone (2000) scaling

model (Lm) for altitude at Antarctic pressure conditions and the primary calibration data set for ^{3}He in pyroxene (Borchers et al., 2016), which yields a long term sea-level high latitude (SLHL) scaled production rate of 122 ± 13 at g^{-1} yr^{-1} (Borchers et al., 2016). External age uncertainties in Supplemental Table S2 include production rate uncertainties. Using other scaling models (eg. Lifton-Sato-Dunai, Lifton et al., 2014), the exposure ages change by up to c. 6%. We report both internal and external uncertainties, but following Balco et al. (2008) we use external uncertainties because we compare the obtained exposure ages with calibrated AMS radiocarbon ages from the excavated sedimentary sequences on the peninsula and other radiocarbon and cosmogenic exposure ages at the SSI.

Sample (depth, m)	height (m amsl)	Facies	Gravel	VC Sand >1 mm	C Sand >0,5 mm	M Sand>0,25 mm	F Sand>0,125 mm	VF Sand>0,063 mm	Silt	Clay
0.35	5.65	6	22.5	9.4	9.1	10.5	11.2	5.0	18.5	13.8
1.05	4.90	5	14.5	17.4	18.2	21.4	19.5	4.3	3.6	1.2
1.35	4.65	Contact 5-4	0.2	0.6	2.2	26.5	61.1	5.5	1.4	2.5
1.50	4.50	4	0.2	0.1	0.4	16.4	65.0	11.3	2.7	3.9
1.65	4.35	4	2.0	0.5	1.8	14.5	54.8	16.4	7.5	2.5
1.85	4.15	Contact 4-3	0.0	0.1	0.5	25.0	66.2	5.3	2.2	0.7
1.90	4.10	3	3.2	1.0	2.1	10.5	47.9	19.2	13.6	2.5
2.17	3.83	3	1.8	0.5	0.7	4.2	44.8	27.8	14.7	5.5
2.37	3.63	3	0.4	0.1	0.2	2.1	48.5	35.4	10.6	2.8
2.62	3.38	3	5.9	0.5	0.7	3.8	39.2	30.2	15.9	3.8
2.87	3.13	3	0.4	0.1	0.3	1.2	31.9	42.1	20.9	3.0
2.97	3.03	1	0.1	0.2	0.8	4.7	56.7	28.1	8.2	1.2
3.15	2.85	1	0.4	0.3	1.1	5.8	57.7	20.6	12.3	1.9

Table S1. Results of textural analyses in samples from the new Pingfo II section.

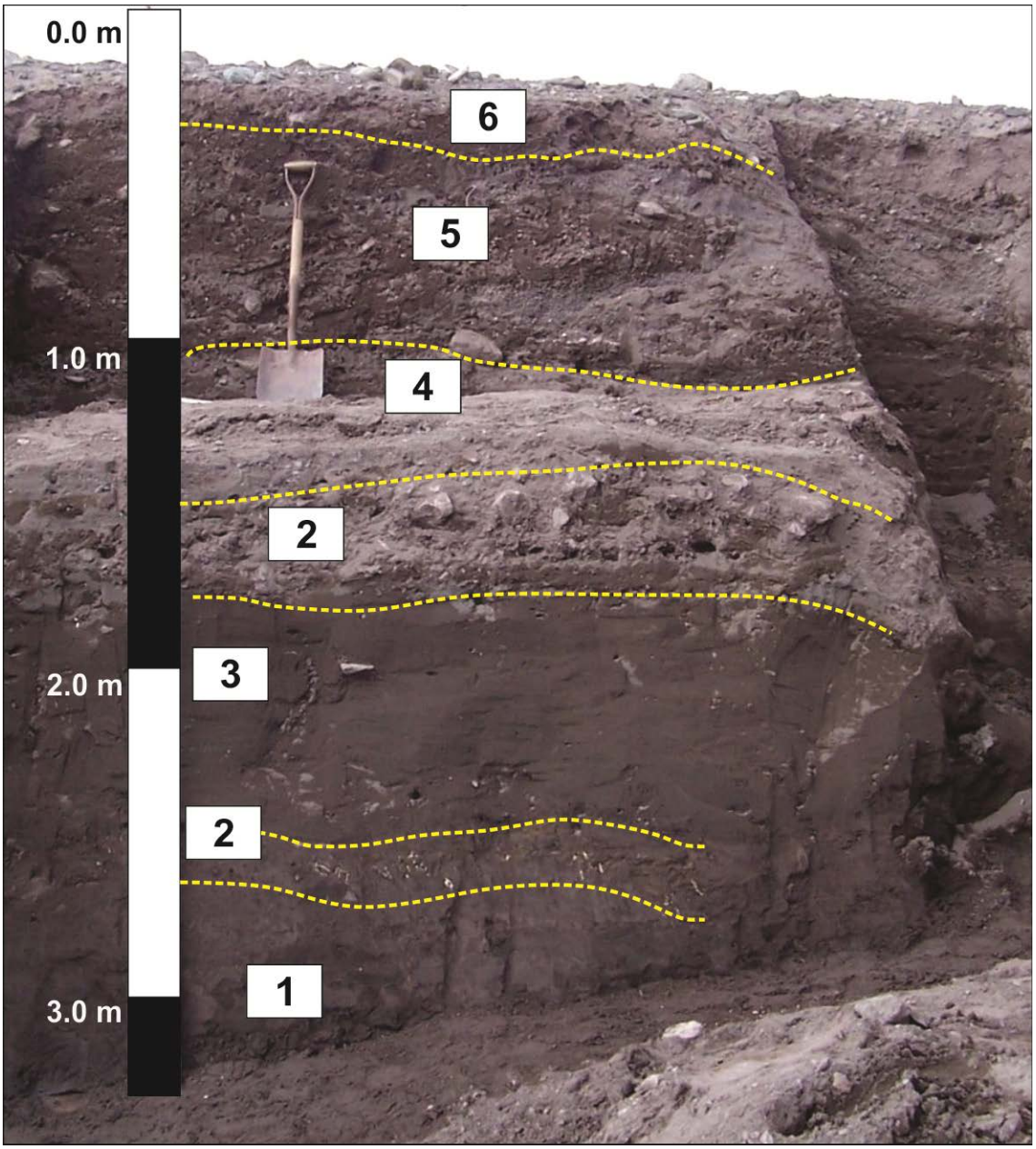

Figure S1. Field picture of the new Pingfo II outcrop excavation. Six different sedimentary facies were interpreted (Facies 1 to 6; please see main text and Fig. 5). A great amount of organic remains of bivalves Laternula sp, seaweed, and penguin bones are widely disseminated was accumulated in the stratigraphic column. In the whole exposure it is clear how the glacier approach (gravity flows, ice rafted blocks) and finally override the marine and glaciofluvial deposits, deforming the last. View is toward east-northeast.

Sampling

With the support of a GPS Trimble Pathfinder ProXH, we performed differential GPS surveys of the locations of erratic boulders sampled for exposure dating. Its accuracy is better than 10 cm in all axes. As geodetic reference, we used the landmark DALL 66019M002 (S62°14′16.335″/W58°39′52.364″/ ellipsoidal height 39.376 m) located on the Argentine Carlini base, just a couple of hundred meters away from the sampled erratics. All coordinates refer to the UTM system and are based on the WGS84 ellipsoid (zone 21E).

We collected five samples using a hammer and chisel to take the upper few centimeters of exposed surfaces, dipping less than 10º. The sample 01-Potter, a cobble sitting on top of a morainic crest facing Three Brothers Hill, was taken entirely for analyses of the whole sample (see Supplemental Table S2 a and Supplemental Figure S2). This sample exhibited a striated, more weathered upper surface, suggesting that it was preserved in situ. The boulder shapes, sizes and positions of the other samples also suggest that a recent turnover is very unlikely. Furthermore we measured the topographic shielding of each sample with a clinometer and compass. Preserved morainic crests as well as glacial erratics in good conditions are rare in the Three Brothers Hill moraine system, since the moraines are heavily degraded into debris flows and also covered by talus rock accumulations. Therefore, we also took into account the presence of those landforms to minimize the effect of post-depositional movements by sampling erratics firmly embedded on the moraine.

Sample processing

To confirm the mineralogy and rock type of the samples, we made thin sections at CICTERRA, Córdoba, Argentina. The thin section analysis showed olivine and clinopyroxene phenocrysts, which represented 5-10 % of the total sample mass, with a modal grain size of ca. 200-500 µm.

To process the samples, we used standard physical rock preparation, using a jaw crusher, sieves (125 µm-1000 µm) and Frantz magnetic separation up to 1.5 A at Bremen University, Germany. We used as a first step a low amperage (ca. 0.10-0.20 A) to get magnetic grains separated from the olivine and pyroxene. The olivine and pyroxene represented the non-magnetic fraction. We mainly used a slope on the machine of up to 24°. After that, we ran the non-magnetic fraction again, this time using 0.20-0.30 A. This left the nonmagnetic fraction with concentrated olivine and pyroxene, plus any other non-magnetic fractions. If those included feldspars, we ran the non-magnetic fraction again, this time using 1.5 A. The pyroxene and olivine went to the magnetic side, the feldspar to the non-magnetic. Using di-iodomethane (DIM, ρ = 3.3 g cm^{-3}) we concentrated the olivines and pyroxenes further. If the olivine and pyroxene concentrate had matrix still attached, even after magnetic or heavy-liquid separation, we treated them with dilute 5% HNO_3 to clean them. This was done in a bottle or beaker, in an ultrasonic bath, for c. 30 minutes. We weighed the masses before and after, to keep track of

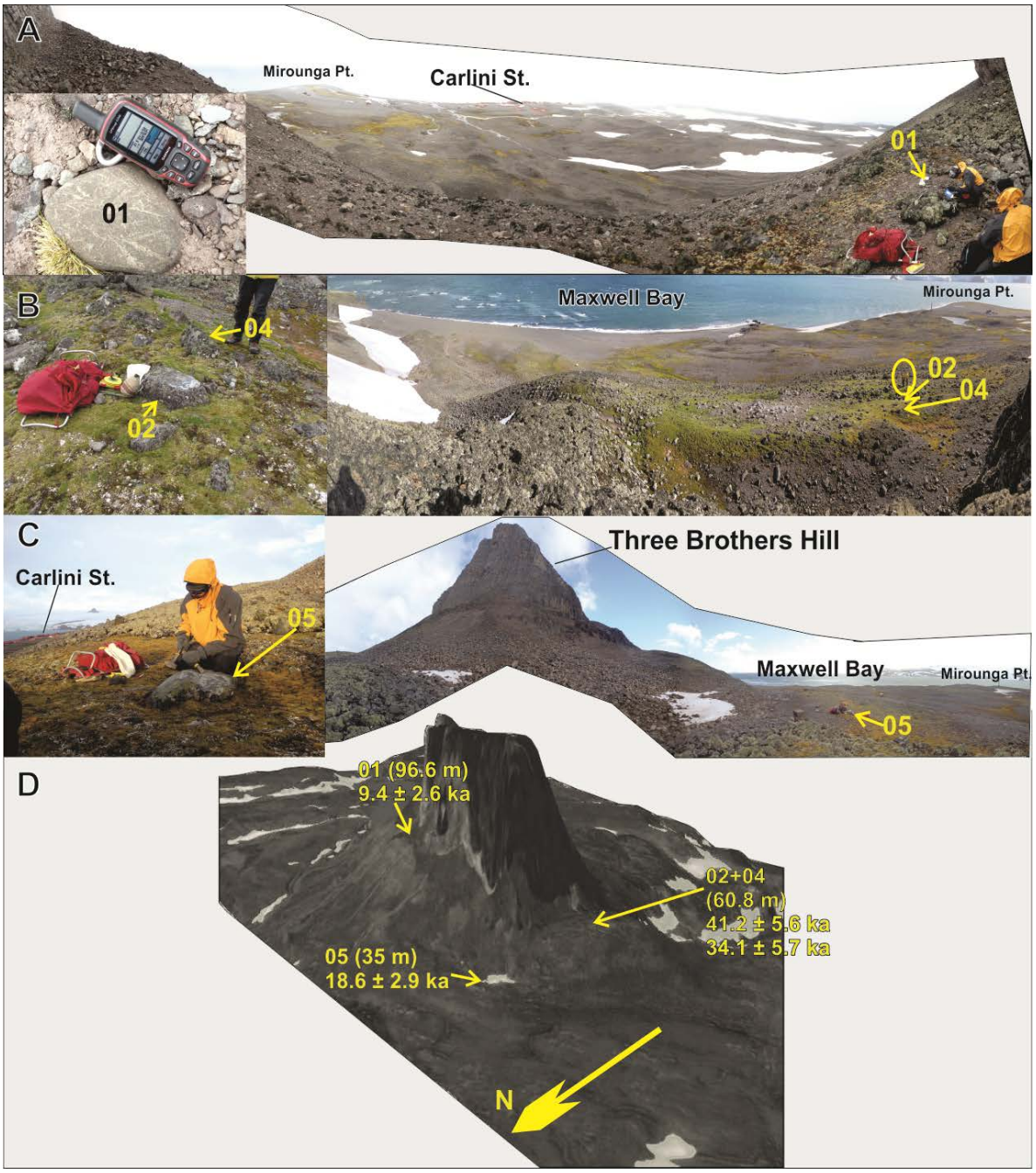

Figure S2. Field pictures of the dated glacial erratic samples on marginal moraines around Three Brothers Hill. A) Sample 01-Potter; B) Samples 02- and 04-Potter; C) Sample 05-Potter; D) Digital Elevation Model of Three Brothers Hill showing the positions of all samples with their ^{3}He exposure ages.

how much mass was lost. We obtained pure pyroxene ± olivine separates for each sample. Those samples were examined under a binocular microscope and back-picked for purity. Unfortunately, of the five samples, the mass of the separate of one sample was too small. Consequently, just four samples were further analyzed.

^{3}He preparation, methods and analysis

The remaining steps of sample analyses were performed at the noble gas laboratory of GFZ Potsdam, Germany. Pyroxene separates were squeezed between two hard-metal plates in an ultrahigh vacuum crusher in an attempt to determine the trapped $^{3}He/^{4}He$. After crushing, pulverized samples were sieved to >100 µm before heating in order to minimize the contribution of atmospheric He irreversibly adsorbed to the grains (Protin et al., 2016). They were subsequently wrapped in Al foil and loaded to the sample carrousel above the resistance-heated extraction furnace, which was baked at 100°C for one week. Noble gases were extracted in two heating steps at 900 and 1750°C (with an initial 600°C step for sample 02-Potter), purified in two Ti sponge and foil getters and two SAES (ZrAl) getters, and measured in a Helix SFT mass spectrometer using procedures similar to those reported by Niedermann et al. (1997). ^{4}He blank values were (2-10) $\times$ 10^{-12} cm^3 STP for crushing extractions, (4-5) $\times$ 10^{-12} cm^3 STP for 600 and 900°C heating steps and (18-40) $\times$ 10^{-12} cm^3 STP for 1750°C steps. He concentrations were calculated by peak-height comparison with our in-house noble gas standard, an artificial mixture of the five noble gases in nitrogen with a $^{3}He/^{4}He$ ratio of (21.66 ± 0.24) $\times$ 10^{-6} (Blard et al., 2015). Two aliquots of the CRONUS-P pyroxene standard material were measured alongside the samples and gave ^{3}He concentrations of 4.86 ± 0.10 $\times$ 10^{9} and 4.79 ± 0.10 $\times$ 10^{9} at g^{-1}, which agree within 2σ uncertainties with the global mean value of 5.02 ± 0.12 $\times$ 10^{9} at g^{-1} (Blard et al., 2015).

Calculations of exposure ages and results

We used a rock density of 2.7 g cm^{-3} and no erosion was considered in the age calculations because we did not find clear evidence on the surfaces sampled and the lithologies are not prone to substantial erosion. We also did not consider shielding by snow accumulation on the boulders. Snow accumulates up to 10 cm in Potter Peninsula, being normally between 2 and 5 cm on the top of hummocky areas (Winkler, 2000). However, winds blow off accumulated snow on the top of hummocks, so it is preserved for no longer than 50 days per year (Wunderle et al., 1998; Winkler, 2000). Moreover, rainfall occurring both in summer and winter periods, also contributes to only a short period of snow cover (Falk and Sala, 2015). We assume also past snow accumulation on the Peninsula is insignificant on top of morainic crests of the Three Brothers Hill moraine system in terms of long-term integrated exposure history.

To calculate ^{3}He exposure ages, the ^{3}He concentrations specifically produced by cosmic ray irradiation (3Hecosmo) must be determined. Ideally, He in phenocrysts is a mixture of only magmatic and cosmogenic components. If so, the

concentration of cosmogenic ^{3}He is calculated using the following equation (Niedermann, 2002):

$$^3He_{cosmo} = {}^4He_{heat} \times (^3He/^4He_{heat} - {}^3He/^4He_{crush})$$

$^4He_{heat}$ is the ^{4}He concentration and $^3He/^4He_{heat}$ the isotope ratio determined during stepwise heating, while $^3He/^4He_{crush}$ is the isotope ratio determined by crushing the mineral separates in vacuo. The latter method selectively releases gases trapped in fluid and melt inclusions. In contrast, heating also releases gases from the crystal lattice, such as cosmogenic He. The cosmogenic component is thus calculated by subtracting trapped ^{3}He from the total ^{3}He that is released by heating of the sample powders in vacuo. However, in our samples $^3He/^4He_{crush}$ ratios were systematically higher than $^3He/^4He_{heat}$, so exposure ages calculated according to the equation above are negative. This is because in old basalts such as those analyzed here, radiogenic 4He produced by decay of U and Th (either in the phenocrysts or implanted form the basalt matrix; Williams et al., 2005) and ^{3}He generated by the thermal neutron capture reaction $^6Li(n, \alpha)^3H \rightarrow {}^3He$ (Dunai et al., 2007) may be present as well. Indeed, the $^3He/^4He_{crush}$ values were lower than expected for typical magmatic He (Table SM 2), indicating that radiogenic He dominates over magmatic He and is even extracted by crushing. Therefore, instead of using $^3He/^4He_{crush}$ in the equation above, we assumed that magmatic He is negligible and thus non-cosmogenic He is essentially represented by radiogenic He with a typical $^3He/^4He$ ratio of 0.028×10^{-6} (0.02 Ra, where Ra is the atmospheric $^3He/^4He$ ratio). To be conservative, a 100% uncertainty was assigned to that value. Because of the dominance of radiogenic He, which prevented a determination of the magmatic $^3He/^4He$ ratio as some radiogenic He was even released by crushing, a mere correction for radiogenic ^{4}He based on U and Th contents (Blard and Farley, 2008) is not feasible for these samples.

The resulting surface exposure ages range between 9.4 ± 2.6 and 41.2 ± 5.6 ka (see Supplemental Figure S2, Supplemental Table S2 b and c). Unfortunately, the obtained exposure ages for the Three Brothers Hill moraine system are few and very scattered, and have external uncertainties up to ~16%, and even 28% for sample 01-Potter (Supplemental Table S2 b and c). The age scatter and large error bars may be related to 1) the unfavorable ratio cosmogenic He/radiogenic He, 2) together with the poorly known $^3He/^4He$ ratio of the non-cosmogenic component and 3) the possibility of previous exposure and inherited cosmogenic helium.

Sample ID	Sample type	Latitude (ºS)	Longitude (ºW)	Coordinates UTM -21 x	Coordinates UTM -21 y	Elevation (m amsl) (1)	Dimensions l x w x h (m) (2)	Thickness (cm)	Topographic shielding correction (3)
01-Potter	Cobble	62.2430	58.6715	413154	3097633	96.6	0.15 x 0.25 x 0.06	5.6	0.887
02-Potter	Boulder	62.2435	58.6767	412887	3097567	60.8	0.90 x 0.50 x 0.30	1.7	0.970
04-Potter	Boulder	62.2435	58.6766	412887	3097567	60.9	1.00 x 0.45 x 0.35	2.2	0.970
05-Potter	Boulder	62.2420	58.6758	412927	3097729	35.0	0.70 x 0.70 x 0.30	1.3	0.974

Table SM II A. Information of samples collected around Three Brothers Hill, Potter Peninsula, KGI.

(1) Altitudes were measured with a Differential GPS Trimble Pathfinder ProXH. Accuracy of 10 cm in all axes.
(2) The height (h) of the sample means cm above moraine surface.
(3) Calculated using the online geometric shielding calculator v1.1 (http://hess.ess.washington.edu/math/general/skyline_input.php; Balco et al., 2008)

Sample ID	Weight (g) (1)	Weight (g) (2)	$^4He_{heat}$ (10^{-8}) (3)	$^3He/^4He_{crush}$ (10^{-6})	$^3He/^4He_{heat}$ (10^{-6}) (3)	$^3He_{cosmo}$ (10^6) (4)	Exposure age (ka) (5)	Internal uncertainty (ka)	External uncertainty (ka)
01-Potter	0.827	0.526	45.8 ± 1.6	0.97 ± 0.12	0.129 ± 0.008	1.25 ± 0.32	9.4	2.4	2.6
02-Potter	0.509	0.282	76.4 ± 1.8	0.47 ± 0.03	0.318 ± 0.015	5.96 ± 0.48	41.2	3.3	5.6
04-Potter	0.511	0.426	78.3 ± 2.7	0.44 ± 0.06	0.261 ± 0.015	4.91 ± 0.62	34.1	4.3	5.7
05-Potter	0.985	0.656	38.6 ±1.3	1.62 ± 0.26	0.283 ± 0.016	2.64 ± 0.29	18.6	2.0	2.9

Table SM II B. Results of He measurements at GFZ Potsdam in pyroxene ± olivines separates from the samples collected around Three Brothers Hill, Potter Peninsula, KGI. ^4He concentrations are in units of cm^3 STP/g, ^3He cocentrations in atoms/g; all error limits are 2σ . Erosion rate of 0 and rock density of 2.7 g/cm^3 was assumed.

(1) 99% of weight of the separates was pyroxenes. The rest is composed of olivine grains.
(2) Weight of the samples used for steapwise heating extraction.
(3) Sum of all heating steps. See C for individual heating step data.
(4) Calculated from $^3He_{cosmo}=^4He_{heat}$ x ($^3He/^4He_{heat}$ - $^3He/^4He_{rad}$), assuming $^3He/^4He_{rad}$ = (0.028 ± 0.028) x10^{-6}. See text for explanation of calculation method.
(5) Obtained using the online calculator CRONUScalc v2.0 (http://cronus.cosmogenicnuclides.rocks/2.0/; Marrero et al., 2016), using the primary calibration data set for ^3He in pyroxene (Borchers et al., 2016) and the time-dependent Lal (1991)/Stone (2000) scaling model (Lm). Used SLHL scaled production rate of 122 ± 13 at/g/yr (Borchers et al., 2016).

Sample ID	TºC	$^4He_{heat}$ (10^{-8})	$^3He/^4He_{heat}$ (10^{-6})	$^3He_{cosmo}$ (10^6)	Total $^4He_{heat}$ (10^{-8})	Total $^3He/^4He_{heat}$ (10^{-6})	Total $^3He_{cosmo}$ (10^6)
01-Potter	900	39.9 ± 1.6	0.106 ± 0.008	0.84 ± 0.31			
	1750	5.93 ± 0.24	0.288 ± 0.034	0.41 ± 0.07	45.8 ± 1.6	0.129 ± 0.008	1.25 ± 0.32
02-Potter	600	30.9 ± 1.2	0.195 ± 0.016	1.39 ± 0.27			
	900	29.9 ± 1.2	0.385 ± 0.028	2.87 ± 0.34			
	1750	15.62 ± 0.63	0.433 ± 0.038	1.70 ± 0.21	76.4 ± 1.8	0.318 ± 0.015	5.96 ± 0.48
04-Potter	900	67.6 ± 2.7	0.244 ± 0.016	3.93 ± 0.60			
	1750	10.71 ± 0.43	0.367 ± 0.036	0.98 ± 0.14	78.3 ± 2.7	0.261 ± 0.015	4.91 ± 0.62
05-Potter	900	29.9 ± 1.2	0.215 ± 0.016	1.50 ± 0.26			
	1750	8.72 ± 0.35	0.515 ± 0.041	1.14 ± 0.12	38.6 ±1.3	0.283 ± 0.016	2.64 ± 0.29

Table SM II C. Values of each heating step. The total $^3He_{cosmo}$ concentrations have been calculated by summing the ^3He excesses from all heating steps.

Table S2. A) Information of samples collected around Three Brothers Hill, Potter Peninsula, KGI. B) Results of He measurements at GFZ Potsdam in pyroxene ± olivine separates from the samples collected around Three Brothers Hill. 4He concentrations are in units of cm^3 STP g^{-1}, ^3He concentrations in atoms g^{-1}; all error limits are 2σ. Erosion rate of 0 and rock density of 2.7 g cm^{-3} was assumed. C) Values of each heating step. The total $^3He_{cosmo}$ concentrations have been calculated by summing the ^3He excesses from all heating steps.

CHAPTER 4: MID–LATE HOLOCENE DEGLACIATION OF NORTHERN FILDES PENINSULA, KING GEORGE ISLAND, NW ANTARCTIC PENINSULA

Pablo Heredia Barión[1,2,3*], Stephen J. Roberts[4], Cornelia Spiegel[2], Steven A. Binnie[5], Lukas Wacker[6], Joanna Davies[7], Imogen Gabriel[8], Viv Jones[7], Simon Blockley[8], Emma Pearson[9], Steve Juggins[9], Louise Foster[4,9], Gerhard Kuhn[1]

[1]Alfred Wegener Institute, Helmholtz Center for Polar and Marine Research, Geosciences Division, Am Alten Hafen 26, 27568 Bremerhaven, Germany; [2]University of Bremen, Department of Geosciences, Klagenfurterstr. 2–4, 28359 Bremen, Germany; [3]Centro de Investigaciones en Ciencias de la Tierra (CONICET-UNC), Vélez Sársfield 1611, X5016GCA, Córdoba, Argentina; [4] British Antarctic Survey (BAS), Natural Environmental Research Council (NERC), High Cross, Madingley Road, Cambridge CB3 0ET, UK; [5] Institute for Geology und Mineralogy, University of Cologne, Zuelpicher Str. 49b, Cologne D-50674, Germany; [6] ETH Zürich, Laboratory of Ion Beam Physics, Schafmattstrasse 20, CH-8093 Zürich, Switzerland; ; [7] Dept. of Geography, University College London, Pearson Building, Gower St, Kings Cross, London WC1E 6BT; [8] Dept. of Geography, Royal Holloway, University of London, Egham, Surrey, TW20 OEX; [9] School of Geography, Politics and Sociology, Newcastle University, Newcastle-upon-Tyne, NE1 7RU, UK

ABSTRACT

The extent and timing of mid–late Holocene glacier advances on the northern Antarctic Peninsula has been long debated, with some studies suggesting rapid deglaciation and uplift following a significant late Holocene increase in ice thickness and extent. Here, we use a combined chronological, geomorphological and palaeolimnological approach to constrain mid–late Holocene glacial readvance(s) of the Bellingshausen Ice Cap on the ice-free Fildes Peninsula, South Shetland Islands, NW Antarctic Peninsula. Results show that the northern Fildes Peninsula was deglaciated close to present-day limits by c. 7,000 years ago, with the BIC receding landward of its present limit by c. 1,900 years ago. Overall, we find no evidence of extensive mid Holocene glacier advance on Fildes Peninsula. Instead, the maximum glacier readvance in the last 7,000 years occurred after 1,300 years ago, but was highly-restricted, only emplacing marine sediments and moss fragments into the moraines on its eastern flank. Our findings show limited additional ice-load changes on Fildes Peninsula during the late Holocene, with implications for glacio-isostatic adjustment models.

1. INTRODUCTION

Better resolved glacio-isostatic adjustment (GIA) models are needed to examine the impact of future Antarctic Peninsula ice-melt on rates of regional-global sea-

level change (Lindow et al., 2014). Such models rely on well-dated geomorphological features and lake records from a limited number of ice-free areas in Antarctica such as Fildes Peninsula in the south-west of King George Island (KGI) to test their performance (Fig. 1) (Watcham et al., 2011).

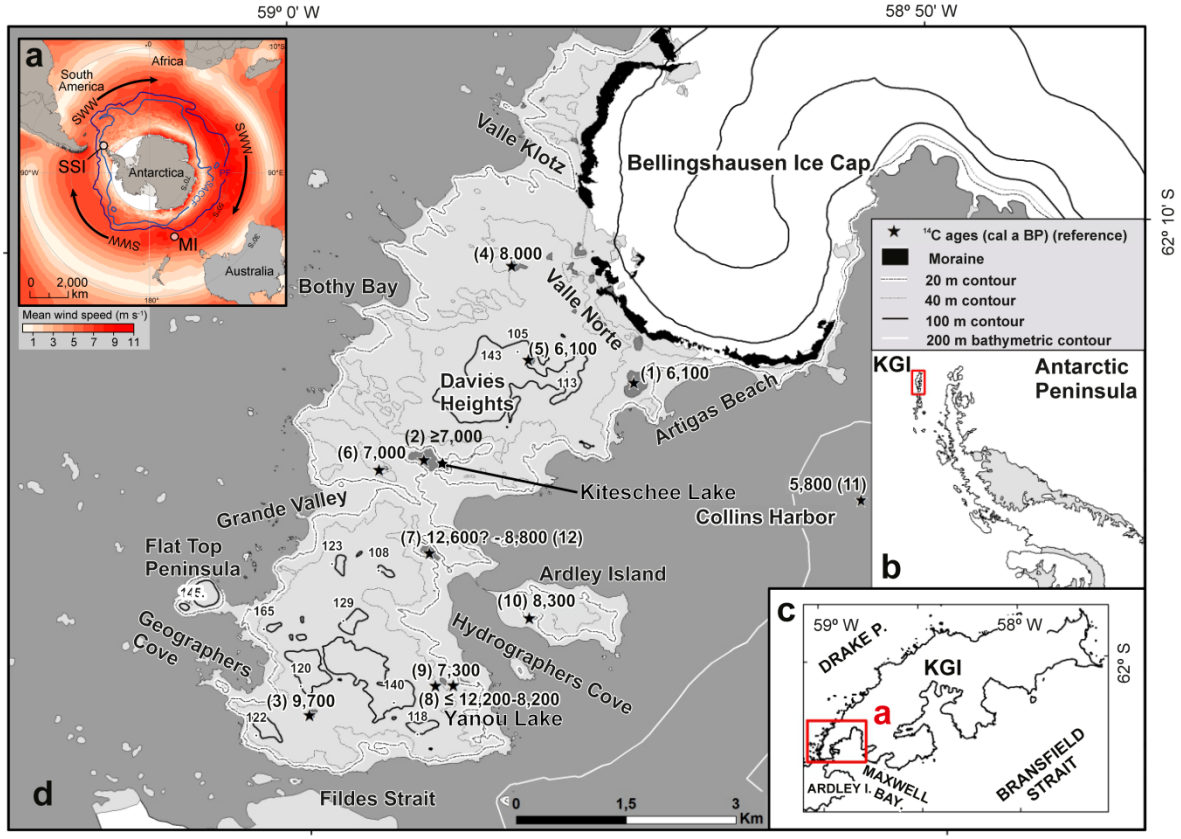

Figure 1. Geographic location of the study area. a. Location of the South Shetland Islands (SSI), currently south of the core Southern Hemisphere westerly Wind (SWW) belt. MI is Macquarie Island, located inside the core SWW belt. b. Location of King George Island (KGI), South Shetland Islands on the northwestern Antarctic Peninsula. c. KGI is framed by the Drake Passage and the Bransfield Strait. Box marks the position of Fildes Peninsula. d. Map of Fildes Peninsula showing minimum ages (cal a BP) for the onset of lake and off-shore sedimentation. Dates are numbered as follows: (1) Tiefersee Lake, (2) Kiteschee Lake, and (3) Jurasee Lake, all Mäusbacher et al. (1989); (4) Mondsee Lake (Schmidt et al., 1990); (5) Hochlandsee Lake (Mäusbacher, 1991); (6) Hotel Lake (Tatur et al., 1999); (7) and (12) Long Lake (Yoon et al., 2006; Watcham et al., 2011); (8) Yanou Lake (Watcham et al., 2011; Roberts et al., 2017); (9) Gaoshan Lake (Watcham et al., 2011); (10) Ardley Lake (Watcham et al., 2011; Roberts et al., 2017); (11) Marine core JPC-17 (Simms et al., 2011). Contour lines are from Antarctic Digital Database (http://www.add.scar.org/home/add7), bathymetry from GEBCO (Weatherall et al. 2015) and heights from Servicio Geográfico Militar de Uruguay (1997).

The mid–late Holocene ice-unloading history of the northern Antarctic Peninsula region and South Shetland Islands has long been debated. New field data can help refine GIA models of post-Last Glacial Maximum (LGM) and Holocene deglaciation. Some GIA models infer no significant changes in ice thickness and minimal ice unloading during the late Holocene compared to the early Holocene(

Watcham et al., 2011), in contrast to others that invoke a thinner lithosphere and more viscous upper mantle to infer recent ice load change (Simms et al., 2012; Simms et al., 2018). Meanwhile, field-based relative sea level reconstructions, determined primarily from radiocarbon dating of remains found in raised beaches, support rapid deglaciation following a significant increase in ice thickness and/or extent during the late Holocene (Watcham et al., 2011; Simms et al., 2012).

The onset and progression of deglaciation on the northern part of Fildes Peninsula has so far been determined from basal ages of lake sediments overlying coarse grained sediments and diamicton deposits (Fig. 1). Here, we use a combined geomorphological, chronological, and palaeolimnological approach to improve the mid–late Holocene deglaciation history of the c. 1250 km^2 Bellingshausen Ice Cap (BIC)(Simões et al., 1999), also known as the Collins Ice Cap. We undertook the first terrestrial cosmogenic nuclide exposure age dating study of glacially-transported erratics deposited on the glacier foreland of northern Fildes Peninsula. We also present new Accelerated Mass Spectrometry (AMS)-radiocarbon dates from macrofossils and shells embedded in the foreland moraine sequences, and a multi-proxy investigation of late Holocene palaeoenvironmental change from a new Kiteschee Lake sediment record (Fig. 1). Finally, we will compare our new data sets and discuss them in the context of the mid-late Holocene (de)glaciation of the Fildes Peninsula.

Cosmogenic exposure dating is a powerful chronological tool for reconstructing glacier and ice sheet extent and thickness. It has not been widely applied on King George Island, South Shetland Islands, mainly because quartz-rich (mainly granitic) bedrock and erratics required for Berylium-10 (^{10}Be) isotope analysis are largely absent from the basaltic-andesitic volcanic-arc environment of the South Shetland Islands. Elsewhere in the Antarctic Peninsula region, where granitic erratics are more prevalent, ^{10}Be exposure dating has proved successful in establishing the timing and rate of deglaciation from Last Glacial Maximum limits (Johnson et al., 2012; Davies et al., 2017; Johnson et al., 2017). Such dating is particularly useful in areas with few sedimentary deposits, insufficient organic material for radiocarbon dating or where large marine reservoir effects prevent accurate radiocarbon dating (Seong et al., 2008; Balco and Schaefer, 2013; Glasser et al., 2014; Ó Cofaigh et al., 2014).

Focusing on the northern part of Fildes Peninsula and the eastern flank of the present-day BIC foreland, our aims were to improve dating constraints on Holocene changes of the extent of the BIC on Fildes Peninsula and test whether post-LGM retreat was a continuous process or interrupted by one or more glacial readvances during the mid–late Holocene.

For this, we first obtained ^{10}Be exposure ages from the limited number granitic erratics, remnants of BIC retreat following the LGM. These erratics were most likely transported from the Peninsula area at the LGM when the South Shetland Islands and Antarctic Peninsula ice sheets coalesced. Second, we radiocarbon dated terrestrial and marine macrofossils embedded in moraines of the BIC foreland and undertook detailed multi-proxy analyses on a new lake sediment record from Kiteschee Lake (62° 11'36.55''S, 58° 57'59.93''W). This lake is located in the eastern-central region of the Fildes Peninsula c. 550 m from the east coast at 15 m above present sea level (henceforth, m a.p.s.l.) and approximately 2.6 km from the margin of the BIC (Fig. 1). It was used to test whether any late Holocene BIC readvance(s) had a significant impact on the central foreland area of Fildes Peninsula. In summary, our new combined datasets showed that no significant mid–late Holocene glacier readvance occurred on Fildes Peninsula after c. 7,000 years ago, despite a sustained late Holocene climate downturn from c. 2,000 years until c. 1970 CE, allowing further refinement of the post-LGM deglaciation and GIA models for the South Shetland Islands.

2. REGIONAL SETTING & STUDY AREA

The South Shetland Islands consist of 11 major islands, located c. 160 km north of the western Antarctic Peninsula and south of the Polar Front and the core Southern Hemisphere Westerly wind belt (Fig. 1), in one of the fastest warming locations globally (Vaughan et al., 2003; Meredith and King, 2005) (Fig. 1b). Forming a c. 230 km long, 35 km wide active volcanic-arc, the islands have milder and more humid maritime climate than the Antarctic continent. The elevated island interiors are characterized by numerous ice caps and permanent snowfields (Monien et al., 2011), whereas the coastal fringes are one of the most extensive ice-free regions in Antarctica (Fig. 1).

King George Island, the largest of the South Shetland Islands, is approximately 79 km long by up to 27 km wide and has been subdivided into three tectonic regions: the Fildes Block (Fildes Peninsula), Barton Horst (Barton and Weaver Peninsulas) and the Warszawa Block (Potter Peninsula) (Watcham et al., 2011; Smellie et al., 1984). With 38 km^2 Fildes Peninsula is the largest ice-free area on the South Shetland Islands. The Fildes Peninsula is composed of andesitic and basaltic lavas, with some interbedded terrestrial sediments, including shales and conglomerates (Smellie et al., 1984). The previously glaciated BIC foreland consists of raised marine platforms, which are formed by basic volcanic rocks of Late Cretaceous to Paleogene-age (John and Sugden, 1971; Smellie et al., 1984). The platforms reach altitudes of up to 180 m a.p.s.l. (John and Sugden, 1971) (Fig. 1). The Fildes Strait separates the Fildes Peninsula from Nelson Island, with Maxwell Bay to the east, and the open waters of the Drake Passage on its west coast (Fig. 1c). The eastern coastline is indented with coves, while the western coasts is characterized by shear sea cliffs and stacks (Hall, 2003).

The BIC occupies the northern half of Fildes Peninsula and is bounded by prominent moraines, referred to as Shetland I (Hall, 2007). A prominent marine platform of pre-Holocene age at c. 40-35 m a.p.s.l. on northwestern Fildes Peninsula, is over 7 km long and 1 km wide (John and Sugden, 1971). This feature is flat to gently undulating, seaward sloping with a limited number of granite erratics on its surface (Hall, 2003; Barsch and Mäusbacher, 1986). We surveyed and classified all of the limited number of large (>50 cm diameter) boulders on the NW glacial foreland and sampled granitic erratics most suited for ^{10}Be cosmogenic surface exposure dating analysis, following standard protocols (Gosse and Philips, 1986).

Basal lacustrine sedimentary sequences in mid-southern part of Fildes Peninsula have been dated to c. 10,000 cal a BP (e.g., Jurasee Lake; Mäusbacher et al., 1989) and were formed in over-deepened glacial basins. Several former marine embayments with basal sediment ages of c. 12,000 cal a BP (Watcham et al., 2011) were transformed into freshwater (isolation) basins when the rate of isostatic uplift outpaced the declining rate of sea level rise during the early Holocene (Watcham et al., 2011)(Fig. 1). Radiocarbon ages obtained from marine-terrestrial transition sediments and raised beaches have been used to reconstruct past changes in local RSL at several sites across the South Shetland Islands. These indicate that the thickest part of the South Shetland Islands ice cap was probably centred on the now ice-free area of Fildes Peninsula during the LGM. The South Shetland Islands ice cap could have been independent from the Antarctic Peninsula Ice Sheet, possibly during the LGM, but more likely at some point during the Lateglacial–Interglacial transition (c. 15,000–12,000 cal a BP) (John and Sugden, 1971; Fretwell et al., 2010; Watcham et al., 2011; Ó Cofaigh et al., 2014).

A well-defined Holocene high-stand of 18-15 m a.p.s.l. occurred on Fildes Peninsula between c. 8,000–7,000 years ago (Watcham et al., 2011). Marine sediments at the base of a previous record from Kiteschee Lake (Mäusbacher et al., 1989), show that the central area of Fildes Peninsula was below sea-level until c. 7,000–6,000 years ago (Mäusbacher et al., 1989). On one hand, to investigate the impact of late Holocene (de)glaciation in the central Fildes area, we analysed the post 6,000 year terrestrial sediments preserved in a new short core retrieved from a shallower part of Kiteschee Lake. On the other hand, the Davies Heights (>100 m a.s.l.) is a previously glaciated part of the former raised marine platform in the mid-central area of Fildes Peninsula. The Davies Heights is located close to Kiteschee Lake, supplying meltwater directly into the eastern end of the lake (Fig. 1).

3. METHODS

3.1 Mapping

The moraines adjacent to the BIC were mapped from field observations combined with the interpretation of satellite images (DigitalGlobe, Catalogue ID: 1030010020C0C900; Google Earth, 2006 and 2011). Contour lines are derived from the Antarctic Digital Database with elevation data obtained from the map of Servicio Geográfico Militar de Uruguay (1997).

3.2 Cosmogenic exposure dating

We used cosmogenic isotope analysis to produce exposure ages for erratic boulders remnants of glacial retreat (Balco, 2011; Glasser et al., 2014). The cosmogenic isotope concentration in a rock is proportional to the length of time that it has been exposed on, or close to the earth's surface (Balco, 2011). The production rate (amount of cosmogenic isotopes produced each year per gram of the relevant mineral) of cosmogenic isotopes varies both spatially and in time, typically due principally to atmospheric depth and magnetic field effects (Lifton, 2016). For cosmogenic isotope dating, ^{10}Be is most commonly used as it has the best determined production rate and can be measured at low concentrations (Balco, 2011).

We sampled three granitic erratics boulders as remnants of glacial retreat from the ~40–35 m a.p.s.l. high NW marine platform with a hammer and chisel to remove the upper few centimetres of sub-horizontal exposed surfaces (Fig. 3). We assume that the rock surface has been completely shielded until its first exposure by glacial retreat. The shapes, sizes and positions of the sampled boulders suggest recent overturning is very unlikely and the sampled erratics showed no signs of erosion (Table 1). We measured the skyline of each sample with a clinometer and compass for topographic shielding, determined using the online geometric shielding calculator, v. 1.1 (Balco et al., 2008). We minimized the possibility of burial by snow by sampling at well-exposed localities with flat and snow-free ground and collected samples from positions away from slopes or cliffs to minimize the probability of post-depositional movement. With the support of a GPS Trimble Pathfinder ProXH we performed differential GPS (dGPS) surveys of the locations of erratic boulders sampled for exposure dating. As geodetic reference, we used the landmark DALL 66019M002 (S62°14′16.335″, W58°39′52.364″, ellipsoidal height 39.376 m) located on the Argentine Carlini base, c. 17 km away from the sampled erratics. Post-processed uncertainties for the samples were less than 0.1 m in the altitudinal as well as in the horizontal. All coordinates are based on the WGS84 ellipsoid.

The exposures ages were calculated using CRONUS-Earth online calculator version 3 (http://hess.ess.washington.edu/math/v3/v3_age_in.html; see Balco et al. 2008). As is normal in the Antarctic Peninsula region, we used the Antarctic ("Ant")

pressure flag and the scaling scheme “LSDn” (Lifton et al., 2014). We employed the scaling model “LSDn” because it is physically based, scaling neutrons, protons and muons independently (Johnson et al., 2017). For sites in Antarctica, using the LSDn scaling yields smaller systematic biases compared with the scaling scheme “Lm” (Lal, 1991; Stone, 2000; Balco et al., 2008; Johnson et al., 2017). No snow cover or erosion correction was applied following the assumptions given by in the region (Johnson et al., 2012; Lindow et al., 2014; Glasser et al., 2014; Ó Cofaigh et al., 2014; Johnson et al., 2017). We applied a quartz density of 2.7 g cm^{-3} for the samples. Since production rates vary globally, Table 1 provides ^{10}Be ages calculated using the mid-latitude southern hemisphere New Zealand (Putnam et al., 2010) and Patagonian calibration dataset (Kaplan et al., 2011) for reference and completeness, since these are relatively proximal sites to Antarctica. There is a difference of up to c. 3% between the ages when calculated using these different production rates. We report both internal and external uncertainties, but following Balco et al. (2008) we use external uncertainties because we compare the obtained exposure ages with calibrated AMS radiocarbon calibrated ages located up to several km away. Further details on ^{10}Be preparation and analysis are provided in Supplementary Note 1.

3.3 Radiocarbon dating

Radiocarbon ages from moraines were obtained by Accelerated Mass Spectrometry (AMS) dating of marine mollusc shells, terrestrial mosses embedded in moraine sediments, and aquatic moss and sediments in the Kiteschee Lake record (Table 2). To reduce the risk of contamination with modern material, all samples for radiocarbon dating were taken from fresh and previously cleaned outcrop or sediment cores, packed in zip-lock plastic bags and stored at 4ºC. Sample preparation for samples was undertaken at the Alfred Wegener Institute Helmholtz Centre for Polar and Marine Research and the British Antarctic Survey. Sample measurements and corrections for $^{13}C/^{12}C$ ratio and calculation of Conventional Radiocarbon Ages were undertaken by ETH Zürich and Beta Analytical Inc., USA. Age depth models were constructed following the procedure in Roberts et al. (2017)(see Supplementary Note 2 for details).

Modern local marine reservoir effect (MRE) correction for radiocarbon dated samples from the South Shetland Islands cover a broad range of about 700 to 1,300 years (Curl, 1980; Björck et al., 1991c; Gordon and Harkness, 1992; Berkman and Forman, 1996; Milliken et al., 2009; Hall et al., 2010; Hass et al., 2010; Watcham et al., 2011). We applied a local MRE correction of $\Delta R=791\pm121$ yr proposed by Hall et al. (2010) to marine samples in this study due to the verification with two independent dating methods (paired radiocarbon and uranium–thorium dates of Antarctic solitary corals). A similarly ‘small’ local marine reservoir correction, within error ranges, is supported by other studies (Simms et al., 2012; e.g., OSL of cobble surfaces on King George Island to investigate the depositional age of beach ridges), and has been used extensively across the South

Shetland Islands (Watcham et al., 2011; unpublished radiocarbon ages from present-day seawater around the South Shetland Islands; Julia Wellner, pers. comm.). Calibration of conventional radiocarbon ages was done using the software Calib (v7.0.4, Stuiver and Reimer, 1993) and the calibration curve Marine13 (Reimer et al. 2013) and SHCal13 for Southern Hemisphere (Hogg et al. 2013) for marine and moss samples respectively.

3.4 Multi-proxy analyses

To reconstruct past environmental change in mid-southern BIC foreland of Fildes Peninsula, we undertook multi-proxy analyses (diatom, grain size, geochemical and sedimentological analysis) on two overlapping Russian cores (27.5 cm and 51 cm long) from the shallower part Kiteschee Lake (Supplementary Fig. 1, 2; Supplementary Note 2). The lithogenic element Titanium (Ti) was used to normalise micro-XRF scan data (Supplementary Fig. 3b) as it provides an unambiguous indictor of allochthonous inputs from the catchment. Normalisation accounts for minor variations in the organic content of the record, which are generally low (<6% LOI550, approximately <1% C_{org})(Roberts et al., 2017).

A chronology for the Kiteschee Lake sediment record was established using six AMS radiocarbon ages, including fine strands of the aquatic moss *Drepanocladus longifolius (Mitt.) Paris* sp. currently living in Kiteschee Lake (and other Fildes Peninsula lakes) hand-picked from the uppermost 1 cm of the record. Unlike other lakes on Fildes Peninsula (Watcham et al 2011, Roberts et al., 2017), we did not find visible moss layers further downcore. Therefore, we sampled the most organic-rich bulk sediments at regular intervals (determined from ultra-high resolution incoherent/coherent (inc./coh.) micro-XRF and LOI-550 °C datasets). Measured radiocarbon ages from samples shown in Supplementary Table 2 were calibrated using the SH13 calibration curves (Hogg et al., 2013). At 1-2 cm thick, the airfall tephra components in the new Kiteschee record are approximately the same thickness as prominent airfall tephra layers in other Fildes lake records (Watcham et al., 2011; Roberts et al., 2017). The absence of extensive post-eruption reworking of ash found in most lake records from King George Island (Watcham et al., 2011; Roberts et al., 2017) meant the Kiteschee Lake record provided a clearer and more well-defined sequence of volcanic events than other records. Following shard counting, shard specific major element geochemistry for the two most prominent tephra layers at 33 cm and 59 cm depth was undertaken by electron probe microanalysis (EPMA) following established procedures (Blockley et al. 2005; Roberts et al., 2017)(see Supplementary Note 2 for details).

Age-depth modelling was undertaken using BACON v.2.2 (Bayesian) age-depth modelling software by inputting uncalibrated conventional radiocarbon age data in R following procedures in Roberts et al. (2017)(Supplementary Table 1)(Blaauw et al., 2010 and 2011). We ran age initial age depth model (KITE-M9, Supplementary

Fig. 7a) based on six measured radiocarbon ages to obtain age estimates for the prominent tephra deposits (Supplementary Fig. 4-7). We then constructed a 'most-likely' age-depth model (KITE-M10; Supplementary Fig. 7a), which included three correlation ages for three of the most prominent tephra layers. These ages were determined from radiocarbon dating of aquatic mosses above tephra deposits in Yanou Lake, a well-dated record from Fildes Peninsula (Watcham et al., 2011). We in tend to explore the implications of the Kiteschee Lake record tephra geochemistry for a regional tephrochronology of the northern Antarctic Peninsula in a forthcoming paper.

Diatom smear-slide screening tests revealed that samples between 77-47 cm depth had very low diatom concentrations. Therefore, we focussed diatom counting on the uppermost 47 cm of the record, at 1 cm intervals between 1 and 32 cm, at 2 cm intervals for 32-47 cm depth. Sediment samples were treated with H_2O_2 (30%) and HCl (50%), heated in a 120°C water bath for 24 hours to remove organic material, washed, then mounted on slides in Naphrax (Batterbee et al., 2001), using a calibrated microsphere solution to determine diatom abundance and concentrations. At least 300 diatom valves were counted and identified using a Zeiss Axiostar-plus microscope under oil at 1000x magnification. Species were identified according to Sterken et al. (2015) and those with >2% abundance were plotted. Cluster analysis was undertaken using TWINSPAN to classify diatom fossil assemblages, defining five classes by cut-off levels 0%, 2%, 5%, 10% and 20%. Downcore diatom zone boundaries were identified using CONISS (Hellingers distance) with broken stick cluster analysis performed in R using packages Rioja (Juggins, 2014) and Vegan (Dixon, 2003)(Supplementary Figure 9). Similar cluster analysis was applied to the micro-XRF 1 mm (5-point moving average) Total Scatter Normalised (TSN) percentage data to provide an initial estimate of sedimentary unit boundary locations.

Multivariate analysis was undertaken to explore the trends and assemblage changes in diatom communities and potential diatom responses to changes in core geochemistry. A Detrended Correspondence Analysis (DCA) was initially performed to identify whether unimodal or linear models were suitable for further analysis (ter Braak, 2002; ter Braak and Prentice, 1998). The DCA showed that the gradient length is short, i.e., <2 standard deviation units, meaning linear methods (PCA, RDA) of data analysis were more appropriate (ter Braak, 2002). To reduce the score and bias of the most abundant species that could mask the effect of less abundant species, a square root function was used. For multivariate analysis, all diatom and geochemical variables were $\log_{10}$ transformed. The relationships between the diatom assemblages and environmental variables were explored further using RDA (Supplementary Figure 10). The significance ($p<0.05$) of each environmental variable was assessed with forward selection using an unrestricted Monte Carlo Permutation Test. Diatom compositional turnover (β-diversity) was estimated down-core using Detrended Canonical Correspondence Analysis (DCCA) for the most abundant diatoms (>2%). Log transformations were applied

prior to statistical analysis, performed using CANOCO 5.0.for Windows (Jones and Juggins, 1995). To infer changes in chlorophyll-a, we applied the diatom-chlorophyll-a training set developed for the Antarctic Peninsula using data from 61 lakes (Jones and Juggins, 1995). Diatom-based transfer functions were applied in C2 (Juggins, 2007) using simple weighted averaging (WA) and weighted partial least squares (WA- PLS) algorithms (Birks, 1998). The WA-Inverse transfer function was chosen to reconstruct chlorophyll-a as the Root Mean Square Error (RMSE) and average bias were low and displayed a strong relationship (R^2) between measured and diatom-inferred chlorophyll-a.

4 RESULTS

Our three cosmogenic surface exposure ages from erratic granitic boulders on the NW marine platform give a mean exposure age and one standard deviation of 6,580 ± 60 years, based on the global production rate calibration dataset (Ww) (Table 1, Fig. 2, 3a, b). The relatively small standard deviation estimated from the three ages is a favorable indicator of low analytical uncertainties, but omits any systematic bias in the age related to, for example, production rate. Instead, we adopt the more conservative value of 6,580 ± 530 years for the age range, which uses the same 8% relative uncertainty for our estimate of the mean exposure age as is derived by the online calculator for the individual external age estimates. However, the close agreement of the three exposure ages does imply that they have negligible pre-exposure histories and that they were exposed simultaneously on the NW foreland during a period of (potentially) rapid mid-Holocene glacier retreat.

In total, we obtained 26 new radiocarbon ages from 10 samples obtained from the Shetland I moraines and its associated glaciofluvial and marine sediments and six new radiocarbon ages from a 77 cm long, c. 7,600 year old sedimentary core record from Kiteschee Lake (Fig. 1, Table 2, Supplementary Note 2). Shells embedded in marine sandy to silty sediments reworked into the Shetland I moraines, returned infinite radiocarbon ages, implying significant reworking of older glaciomarine deposits by the BIC. Shells reworked into till have median calibrated ages of between 6,400 and 5,600 cal a BP (Table 2) and were broadly coeval with cosmogenic exposure ages of the glacial erratics. Moss fragments in glaciofluvial and glacial sediments were significantly younger, however, with ages between 1,900 and 1,300 cal a BP (Fig. 2, 3c, d; Table 2), suggesting emplacement by a limited late Holocene glacier readvance.

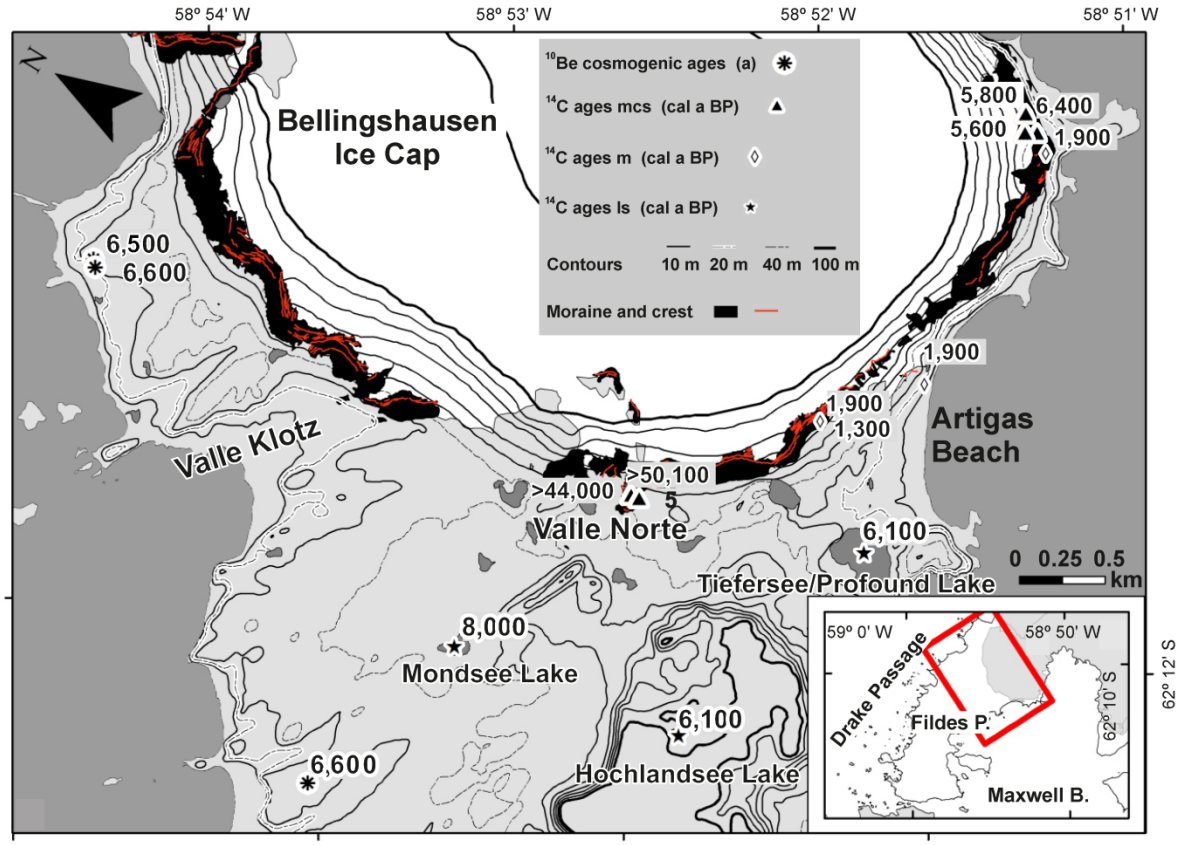

Figure 2. Map showing the position of calibrated cosmogenic ^{10}Be exposure ages of sampled erratics and calibrated radiocarbon ages of organic remains in the Shetland I moraine. Inset map shows the area where the study sites are located (red box) and minimum ages of the onset of lake sedimentation (stars); mcs = marine carbonate shells, m= mosses, ls = lake sediments.

In accordance with other lake records from the mid and southern Fildes Peninsula foreland, the continuous and finely-laminated nature of the Kiteschee Lake sediment record shows that the mid-southern BIC foreland has not been overridden by glaciers in the last c. 7,600 years (weighted mean basal modelled age (KITE-M10); 7,360–7,900 cal a BP min.–max. 95% confidence age range; 7,580 cal a BP median age; (Supplementary Fig. 7b; Supplementary Note 2)). Average 95% confidence age-depth model uncertainties are 770 years, with a minimum of 10 years at 0 cm and maximum of 1,080 years at 21 cm. A single bulk age obtained from immediately below a fine grey glaciofluvial deposit (20-12.1 cm depth in Supplementary Fig 2a) at 21 cm has a calibrated age of 10,550±60 cal a BP and significantly depleted δ13C value of -32.6 ppm most likely reflect late Holocene (glacial) reworking of old (marine?) carbon in sediments deposited in or around the Davis Heights area during the early Holocene (post-LGM) deglaciation of the BIC foreland. All other calibrated radiocarbon ages were in chronological order and straightforward to model (Supplementary Fig. 7b)

High-resolution sedimentological (0.5 cm intervals) and micro-XRF (μ-XRF) scanning geochemical analysis; 200 μm contiguous) revealed several prominent visible ash layers, some of which define the boundaries between different sedimentary units (Supplementary Fig 2a). Downcore changes in (K/Ti) and (Ca/Ti) (Supplementary Fig. 3a and b) mirror one another and changes in sand content. Alignment of these parameters along the first Principal Component Analysis (PCA) axis indicates changes in these ratios are driven by minerogenic catchment inputs and tephra deposition (Supplementary Fig. 3a and b).

Sediments between 77–60 cm, have a weighted mean modelled age range of 7,600–5,500 cal a BP (rounded to the nearest 50 years to account for calibration and age-depth modelling errors). They are composed of poorly sorted olive-brown silt with three prominent fine black ash layers (most likely T7; Roberts et al., 2017, Supplementary Fig 1; Supplementary Figs. 3–10; Supplementary Note 2). Following the deposition of the T5 tephra c. 5,500-5,000 cal a BP (Roberts et al., 2017), there is a distinct change to a light orange-brown silty-clay at 58.3 cm downcore (Supplementary Figures 2a and 9). Tephra layers aside, the most prominent lithological change in the record occurred at c. 20 cm depth (c. 1,950 cal a BP), with the deposition of a light grey clayey-mud sediments containing sand-rich layers (20-12 cm depth; 1,950–1,450 cal a BP; Supplementary Figures 2a and 9). These sediments were overlain by a unit of olive-brown silt between 12-5 cm (1,400 – -20 cal a BP), and capped by living aquatic moss in the uppermost 5 cm, which returned a post-bomb age (>1950 CE, most likely 2010 CE) at 0–1 cm depth (Supplementary Figure 2a and b; Supplementary Table 1).

Since the early Holocene isolation history of Kiteschee Lake is well-established (Mäusbacher et al., 1989), we focused on analysing high-resolution diatom compositional changes in the mid-late Holocene (uppermost 47 cm) part of our new record where diatom preservation was sufficient for meaningful environmental interpretation (Supplementary Figs. 2 and 9). Diatoms were poorly preserved below c. 47 cm depth and almost completely absent at the base of the record. All sedimentary units younger than c. 6,000 cal a BP (c. 63 cm) should contain terrestrial diatoms as Kiteschee Lake is situated at c. 15 m a.s.l. and would have been higher than reconstructed relative sea level from that time onwards (Mäusbacher, 1991). Although a clear shift in geochemistry exists at c. 60 cm depth (Supplementary Fig. 3b), we found no clear biological evidence of (glacio)marine sedimentation and the $\delta^{13}C$ value from 73.5–74.5 cm depth remains consistent with freshwater sedimentation.

Sample ID	AMS ID	Longitude	Latitude	Altitude (m a.p.s.l.)	Boulder dimension (L x W x H) (m)	Sample thickness (cm)	^{10}Be concentration (atoms g-1)	^{10}Be concentration 1σ (atoms g^{-1})	^{10}Be age (yr) (Ww) ± 1σ int (ext) error	^{10}Be age (yr) (Pt) ± 1σ ext. error	^{10}Be age (yr) (Kp) ± 1σ ext. error
Fildes1	s08808	58° 57' 45.97" W	62° 10' 2.34" S	43	2.65 x 2.10 x 1.98	1.4	37.1 x 10^3	1.9 x 10^3	6630 ± 340 (520)	6640 ± 350	6830 ± 660
Fildes2	s08809	58° 55' 35.96" W	62° 08' 43.65" S	40	0.87 x 0.71 x 0.35	1.2	36.4 x 10^3	2.0 x 10^3	6510 ± 350 (520)	6530 ± 370	6710 ± 660
Fildes3	s08810	58° 55' 37.18" W	62° 08' 43.97" S	39	0.74 x 0.62 x 0.26	1.2	36.9 x 10^3	2.2 x 10^3	6610 ± 390 (550)	6630 ± 400	6810 ± 680

Table 1. Cosmogenic surface exposure dating results. We used an erosion rate of 0 cm yr^{-1}, the AMS standard flag 07KNSTD, an "Ant" elevation pressure flag and a density of 2.7 g cm^{-2}. A shielding correction of 0.9999 was applied to all samples as the value is the same for all. Calculations of ^{10}Be exposure ages using the global (Ww) “LSDn” scaling (Lifton et al., 2014), the New Zealand-Macaulay (Pt)(Putnam et al., 2010) and the Patagonia calibration dataset (KP) (Kaplan et al., 2011). Calculated ages have been rounded to the nearest 10 years; int: Internal error; ext: External error.

Sample ID	Lab ID	**Longitude Latitude**	Alt. (m amsl)	Material	$\delta^{13}C$ (‰)	Conventional ^{14}C age (yr)	Median Calibrated age ± 95% conf. range	Context and facies dated	Comments
ART-01A-2015	Beta - 441405	58° 53' 58.34" W 62° 10' 46.20" S	72	Moss	-22.6	1980 ± 30	1890 ± 60	Moss in glaciofluvial sediments	Maximum age of glacial advance
ART-01B-2015	Beta - 441406				-22.4	1950 ± 30	1860 ± 70		
ART-01A-2015 bis	Beta - 441407				-19.6	1920 ± 30	1820 ± 80		
ART-01B-2015 bis	Beta - 441408				-16.8	1940 ± 30	1850 ± 70		
ART-03A-2015	Beta - 441409	58° 53' 58.34" W 62° 10' 46.20" S	72	Moss	-22.7	1380 ± 30	1270 ± 20	Moss in glacifluvial sediments, overlying ART 01-2015	Maximum age of glacial advance
ART-03B-2015	Beta - 441410				-20.5	1380 ± 30	1270 ± 20		
ART-08-arriba-A-2015	Beta - 441411	58° 51' 43.94" W 62° 10' 54.52" S	16	Moss	-17.9	2030 ± 30	1950 ± 60	Moss above till	Maximum age of glacial advance
ART-08-arriba-B-2015	Beta - 441412				-24.5	2050 ± 30	1960 ± 70		
ART-08-abajo-A-2015	Beta - 441413	58° 51' 43.94" W 62° 10' 54.52" S	16	Moss	-20.9	1870 ± 30	1770 ± 70	Moss in till	Maximum age of glacial advance
ART-08-abajo-B-2015	Beta - 441414				-28.6	1900 ± 30	1790 ± 60		
ARTIGAS-1-A	Beta - 441415	58° 53' 22.15" W 62° 10' 56.07" S	7	Moss	-20.5	2050 ± 30	1960 ± 70	Moss in till, overlying 6-7 m amsl raised beach level	Maximum age of glacial advance
ARTIGAS-2-A	Beta - 441417				-21.9	2010 ± 30	1930 ± 70		
ARTIGAS-2-B	Beta - 441418				-23.7	1980 ± 30	1890 ± 60		
ART-07A-2015	ETH-69688	58° 51' 39.45" W 62° 10' 51.73" S	18	Shell	-0.9	7045 ± 85	6710 ± 360	Shells in fine sediments	Maximum age of glacial advance
ART-07B-2015	ETH-69689				4.0	6590 ± 70	6210 ± 300		
ART-07C-2015	ETH-69690				0.0	6730 ± 75	6360 ± 330		
ART-09A-2015	ETH-69691	58° 51' 40.66" W 62° 10' 50.59" S	27	Shell	-2.2	6265 ± 75	5850 ± 310	Shells in till	Maximum age of glacial advance
ART-09B-2015	ETH-69692				3.4	5895 ± 70	5450 ± 350		
ART-10A-2015	ETH-69693	58° 51' 34.88" W 62° 10' 49.04" S	28	Shell	0.9	6235 ± 70	5820 ± 310	Shells in till	Maximum age of glacial advance
ART-10B-2015	ETH-69694				-1.2	5925 ± 70	5480 ± 340		
ART-10C-2015	ETH-69695				-2.8	6520 ± 75	6130 ± 310		
ART-04A-2015	ETH-69684	58° 54' 59.09" W ° 10' 23.69" S	42	Shell	-1.4	>44,300		Shell in fine sandy and silty sediments.	In thrust-up marine sediments
ART-04B-2015	ETH-69685				2.8	>43,700			
ART-05A-2015	ETH-69686	58° 54' 59.05" W 62° 10' 24.55" S	42	Shell	2.8	>48,500		Shell in fine sandy and silty sediments.	In thrust-up marine sediments
ART-05B-2015	ETH-69687					>51,700			

KITE(M)_0–0.5 cm	Beta - 501582	62° 11'36.55''S	15	Aq. Moss	-27.4	Post-bomb pMC=101±0.4	-60±1 or -7±1	Aquatic moss: *Drepanocladus longifolius*	Sample living when core was taken in 2011 CE
KITE_9–10 cm	Beta - 504801	58° 57'59.93''W		Bulk sed.	-23.9	1,600±30	1,450±80	Bulk orange-brown silt	Post-glaciogenic sediment unit transition age
KITE_20–21 cm	Beta - 497408			Bulk sed.	-32.6	9,380±30	10,550±130	Bulk 'glacial' grey silt-clay	Influenced by old carbon
KITE_36.5–37 cm	Beta - 501584			Bulk sed.	-18.0	1,860±30	1,760±100	Bulk orange-brown silt	AMS-Micro-sample due to low carbon content
KITE_45.5–46 cm	Beta - 501585			Bulk sed.	-17.7	3,350±30	3,530±90	Bulk orange-brown silt	AMS-Micro-sample due to low carbon content
KITE_73.5–74.5 cm	Beta - 498331			Bulk sed.	-18.0	6,410±30	7,420±120	Bulk orange-brown silt	δ^{13}C values consistent with terrestrial sediments

Table 2. Radiocarbon ages from the eastern Shetland I Moraine and Kiteschee Lake record. Calibration of radiocarbon ages was undertaken using Calib 7.0.4 (Stuiver and Reimer, 1993) and OXCAL v. 4.3 (Bronk Ramsey and Lee, 2013)(Kiteschee Lake data) (see Supplementary Table 1 for details). The calibration curve Marine13 (Reimer et al., 2013) was used for marine shells, with a local reservoir effect of ΔR=791±121 years (Hall et al., 2010). Terrestrial and aquatic moss (Aq. moss) and bulk sediment sample radiocarbon ages were calibrated using SHCal13 (Hogg et al., 2013). Dating replicates were used to assess dating and interpretation accuracy. Calibrated ages have been rounded to the nearest 10 years. Elevation data (Alt. m amsl - above mean sea level) were taken with a Garmin handheld GPS map 62stc, with a minimum precision ±2 m, but up to 10 m (latitude, longitude) and a z-axis precision of 10–20 m (altitude). Data were checked against known altitudinal data from Fildes Peninsula and the KGI-DEM.

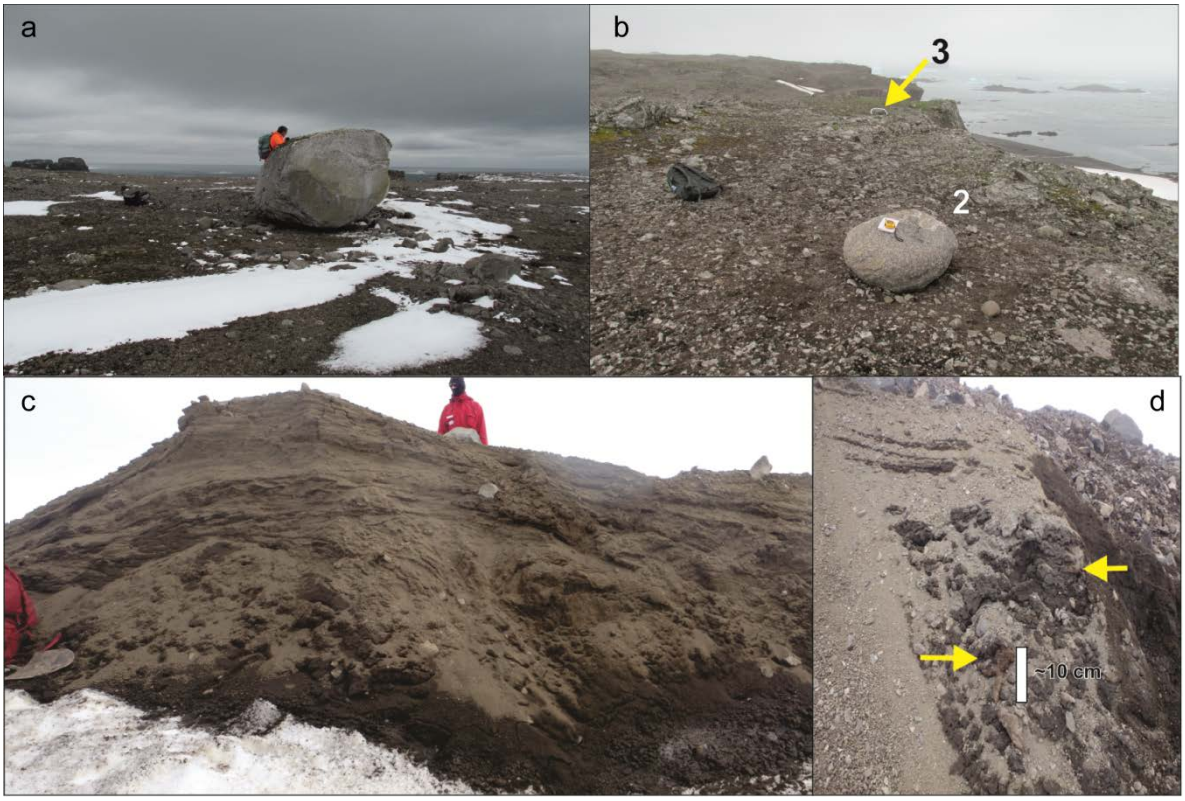

Figure 3. Field photographs showing the erratics sampled on the NW marine platform for terrestrial cosmogenic nuclide exposure age dating and terrestrial sediments preserved within the Shetland I moraine. a. Fildes 1 and b. Fildes 2 and 3 boulders sampled for cosmogenic analysis. Boulder dimensions and locations are in Table 1. c. Radiocarbon dating samples ART-01 and ART-03 embedded in moraine sediments as described in Table 2.

Distinguishing unequivocal climate signals from diatom assemblages in lake sediments can be complex since diatoms usually respond to changes in water chemistry rather than temperature. Nevertheless, deglaciation and warming can have a significant impact on catchment processes affecting nutrient supply to lakes and diatom compositional turnover (β-diversity). The proximity of the Fildes Peninsula to the still-active Deception Island volcano (c. 115 km) means it is vulnerable to the potentially devastating effects of tephra deposition on diatom communities (Roberts et al., 2017). While large volumes of tephra can lead to deterioration in light conditions and an increased suspension load, some studies have found that minor volcanic ash deposition can lead to increased diatom concentrations as silica becomes more bio-available (Lotter et al., 1995; Telford et al., 2004).

Redundancy analysis (RDA), using key geochemical variables associated with tephra, showed that tephra deposition did not have a significant impact on the diatom community composition in the Kiteschee Lake record (p=0.596)

(Supplementary Figs. 9, 10; Supplementary Note 2). While certain species respond to climate variability (e.g. changing wind speed, temperature and precipitation), the overall community structure response in Kiteschee Lake was more directly related to ice expansion, increased (glacial) erosion and associated increases in turbidity. Hence, changes in the diatom accumulation rate, reconstructed chlorophyll-a, variations in key indicator species were used to examine the impact of (climate-driven) glacier readvances in the mid-southern BIC foreland.

The uppermost 47 cm of the record was divided into five ecologically-distinct zones using cluster analysis (see Supplementary Note 2 for details). The most prominent change in diatom community composition occurred in Diatom Zone 3 (2,700–2,060 cal a BP; 33.5–22 cm) where a distinct peak in aerophilic diatoms species (e.g., *Diatomella balfouriana*, *Achnanthes exigua* and *Gomphonema* sp., usually found on littoral mosses) corresponded with increased diatom β-diversity, and an increasing Detrended Canonical Correspondence Analysis (DCCA) score (1.6 times greater than the std dev.) (Fig. 4d; Supplementary Note 2; Supplementary Fig. 9). This is broadly indicative of reduced turbidity and warmer climatic conditions, possibly with reduced lake-ice seasonality on Fildes Peninsula and the northern Peninsula at this time (Roberts et al., 2017) (Figure 4).

The subsequent decline in aerophilic and littoral diatom species, coupled with the concurrent increases in species associated with more turbid conditions (e.g. *Stauriserella pinnata*) and lower DCCA scores at the start of Diatom Zone 4 (2,060–1,510 cal a BP; 22-13 cm) corresponded with the transition to a glaciogenic sedimentary environment in the lake (Fig. 4d; Supplementary Figs. 8 and 9) A reduction in biomarker reconstructed mean summer air temperatures in nearby Yanou Lake Fildes Peninsula also occurred at this time (Roberts et al., 2017) (Figure 4e). These changes coincide with the late Holocene readvance of the BIC, as indicated by our radiocarbon data from the moraine close to the BIC.

The clear increase in diatom accumulation rate from c. 2,700 cal a BP (compared to previous record mean) is likely linked to the increased accumulation rate between c. 2,800 and 1,400 cal a BP (Supplementary Figure 8). Elevated mass accumulation rates and increased sand deposition within the glacigenic unit (1,950–1,450 cal a BP) are indicative of increased (glacial) erosion and meltwater input from a nearby source after c. 2,000 cal a BP (Supplementary Figures 3a, 8; Supplementary Note 2). As our cosmogenic and radiocarbon data indicate very limited readvance of the BIC during the late Holocene, we conclude that the most likely source of glaciogenic sediment into Kiteschee Lake is from increased melt from a small glacier that had formed on the Davies Heights, located immediately north of Kiteschee Lake (Fig. 1).

5. DISCUSSION

5.1 Mid Holocene deglaciation

Previously published lake sediment records show that the terrestrial deglaciation of the southern-mid part of Fildes Peninsula extends to c. 12,000–9,000 cal a BP (Mäusbacher et al., 1989; Watcham et al., 2011) (Fig. 1). After 7,000 cal a BP, the BIC retreated northwards from central Fildes Peninsula, and the Davies Heights area (Fig. 1, 5). Combined, our new evidence and existing data suggests that the process of mid Holocene deglaciation started in the flat platform areas in the north-west BIC foreland region of Fildes Peninsula following a still-stand at c. 7,000 cal a BP (Watcham et al., 2011). Recession then progressed towards the higher elevation areas in the eastern sector located above the equilibrium line altitude and zones located in depressions next to the former ice limit and sea-level (Fig. 5). This rapid ice retreat and thinning during the mid-Holocene triggered the increased rate of isostatic uplift and falling RSL (cf. Watcham et al. 2011).

Our new cosmogenic exposure ages show that the NW edge of the marine platform was ice-free by 6,580 ± 530 years ago (Fig. 4c, Table 1). These ages are consistent with the onset of deglaciation at 8,000 ± 500 cal a BP in nearby Mondsee Lake, located at an altitude of 45 m a.p.s.l. on the NW platform and c. 1,500 m away from the present glacier margin (Schmidt et al., 1990). By 6,100 ± 400 cal a BP, Tiefersee Lake and Hochlandsee Lake, at c. 800 and 1500 m from the present-day ice cap, also became ice free (Mäusbacher et al., 1989; Mäusbacher, 1991). By 6,000 cal a BP, the glacier front occupied the inner bay of Collins Harbour in Maxwell Bay (Mäusbacher et al., 1989; Tatur et al., 1999; Yoon et al., 2006; Milliken et al., 2009; Watcham et al., 2011; Simms et al., 2011; Chu et al., 2017) (Fig. 1, 5), while the BIC had retreated to within its present-day limits, driven by persistently warmer mid–Holocene atmospheric temperatures across the Peninsula region between 8,200 to 5,900 cal a BP (Mulvaney et al., 2012; Roberts et al., 2017)(Fig. 4i). This warm phase coincided with reduced sea-ice and warmer-than-Holocene-average sea-surface temperatures recorded in marine sediments records from Maxwell Bay and the Palmer Deep (Milliken et al., 2009; Etourneau et al., 2013) as well as broadly warmer conditions across the Southern Hemisphere (Marcott et al., 2013) (Fig. 4j).

A second phase of warmer-than-Holocene average atmospheric temperatures also existed on the Western Peninsula and the South Shetland Islands between c. 4,500–2,800 cal a BP (Sun et al., 2005; Roberts et al., 2017). At this time, glaciers across the Antarctic Peninsula retreated landward of their present limits and large areas of peat banks formed (Björck et al., 1991a and b; Hall, 2007; Bentley et al., 2009). Although sea surface temperatures decreased and sea-ice cover increased in Maxwell Bay between c. 5,900 and 2,600 cal a BP (Fig. 4f-i), there is no evidence of a significant glacier readvance or glaciogenic sediment deposition in any lakes on Fildes Peninsula at this time (Milliken et al., 2009; Watcham et al., 2011; Roberts et al., 2017). Indeed, prolonged summer sea-ice still occupied the

inner Collins Harbour of Maxwell Bay until at least c. 1,700 cal a BP (Simms et al., 2011), implying that that sea-ice could have been trapped by more intense, poleward-shifted, Southern Hemisphere westerly winds over the South Shetland Islands at this time (Watcham et al., 2011; Saunders et al., 2018) (Fig. 4b, f).

5.2 Late Holocene Neoglaciation

Lake, marine and fluvial sediments immediately in front of the present-day BIC limits were thought to have been bulldozed into their current positions by the BIC glacier re-advancing after 650 cal a BP, in what was the most extensive phase of glacier readvance of the last 3,500 years (Hall, 2007). Raised beaches levels (<10 m a.p.s.l.) were previously thought to be contemporaneous with the last glacier readvance on King George Island, c. 450–250 cal a BP, during a post-Medieval Climate Anomaly cold phase (Sugden and John, 1973; Simms et al., 2012)(broadly equivalent in timing to the Northern Hemisphere Little Ice Age). Our new radiocarbon ages of c. 1,900 cal a BP from moss fragments incorporated into a small moraine on top of a raised beach at 7–6 m a.p.s.l. on Artigas Beach indicate that glacial re-advance could have also taken place earlier, after the formation of this beach level (Fig. 2; Table 2).

Holocene raised beaches up to c. 16 m a.p.s.l. in the Artigas Beach area, which possibly extend under the BIC (John and Sugden, 1971; Fretwell et al., 2010), may have survived relatively unmodified beneath the ice cap or the ice extent was less advanced at the time of their formation (Hall, 2007; Fretwell et al., 2010). Marine sediments with bivalve shells reworked into till are located at the extreme east of the Shetland I moraines (Fig. 2; Table 2). These shells have ages between 6,400 and 5,600 cal a BP and must have been located close to the former sea-level of c. 15 m a.p.s.l. at that time (Watcham et al., 2011). Our new data show that the BIC also readvanced in this area during the late Holocene, but by only tens of metres relative to its present position. Hall (2007) came to a similar conclusion for the Shetland I moraines at Valle Norte and Valle Klotz (Figs. 1,2), with maximum ages for a glacier readvance at c. 650 and c. 1,000 cal a BP (Fig. 4c). There, the ice advanced in form of lobes, which spread out into ice-marginal depressions, forming several small thrust moraines which are located c. 300 m away from the prominent moraine ridges dated in this study.

Our new chronological data also enable us to more precisely constrain the initial formation of the Shetland I moraine from Valle Norte towards its eastern extension (Fig. 2), where moraines are still ice-cored and in contact with the ice. We found moraine crests several meters above the ice-level in this area similar to those found in Valle Norte (Hall, 2007) that post-date c. 1,300 cal a BP, the age of our youngest sample. Combined, our new cosmogenic and radiocarbon data from the moraines mean the eastern part of the BIC was landward of its present limit, with mosses colonizing its foreland until at least 1,300 cal a BP. The timing of the

glacier readvance coincides with a shift to more sustained colder conditions and the most significant change point in the Yanou Lake palaeotemperature record (Roberts et al., 2017) (Supplementary Fig. 11, Supplementary Note 3). More generally, the timing of BIC late Holocene readvance is consistent with the more general downturn in climatic conditions from c., 2,000 years onwards across the Antarctic Peninsula (Mulvaney et al., 2012), the Southern Hemisphere (Marcott et al., 2013) and globally (Mann et al., 2009) (Fig. 4c).

Multi-proxy data from the Kiteschee Lake sediment record revealed a shift to a more glaciogenic and turbid lake environment between c. 1,950–1,450 cal a BP. However, the lack of evidence for a more substantial late Holocene BIC readvance covering Kiteschee Lake, c. 2.6 km from its active ice-front suggests that the post-1,300 cal a BP readvance was somewhat restricted in extent. Instead, we link the deposition of glaciogenic sediments in Kiteschee Lake at this time to meltwater input from a localized and independent ice cap that formed on the elevated Davies Heights area (Fig. 5) (Supplementary Note 2). The Davies Heights is currently unglaciated, but is close to the equilibrium line altitude for the South Shetland Islands and could have sustained a more permanent ice-cover with a relatively minor downshift in temperatures (Fig. 4a–e, 5c).

The most extensive readvance of the BIC mid-late Holocene occurred between 1,300-600 cal a BP, broadly synchronous with the Mediaeval Climate Anomaly (MCA; 1,200-800 cal a BP) as defined in Bentley et al. (2009) as Medieval Warm Period (MWP); c. 800-1400 CE defined globally in Lamb (1965) and Mann et al. (2009) (Fig. 4d, e, Supplementary Fig. 12). Most Southern Hemisphere proxy records from between 30-60 °S (Marcott et al., 2013) (Fig. 4j) compilation exhibit warming during the MCA, but nearly all are north of 60 °S. Although new change point analysis of the Yanou Lake palaeotemperature data (Roberts et al., 2017) shows an upward trend between 1,300-800 cal a BP (Fig. 4e; Supplementary Fig. 11b), more stringent sequential Mann-Kendall trend change analysis, with a correction for serial autocorrelation included, suggested there is no significant change in the downward temperature trend since c. 2,900 cal a BP (Supplementary Fig. 13). While sea surface temperature records from the western Peninsula indicate MCA-warming (Etourneau et al. 2013), marine sediment records show no change in sea-ice conditions in Maxwell Bay or Potter Cove at this time (Hass et al., 2010; Monien et al., 2011). There is also no evidence for significant upturn in climate during the MCA in the James Ross Island ice core record, the only other quantitative atmospheric palaeotemperature record from the northern Peninsula region (Fig 4i; Supplementary Fig. 12).

Ultimately, the climate of the South Shetland Islands seems to be controlled by changes in Holocene insolation and its position relative to the Polar Front where the Southern Hemisphere westerly winds and the polar cell converge (Bentley et al., 2009; Lamy et al., 2010; Varma et al., 2012) (Fig. 4). We link late Holocene

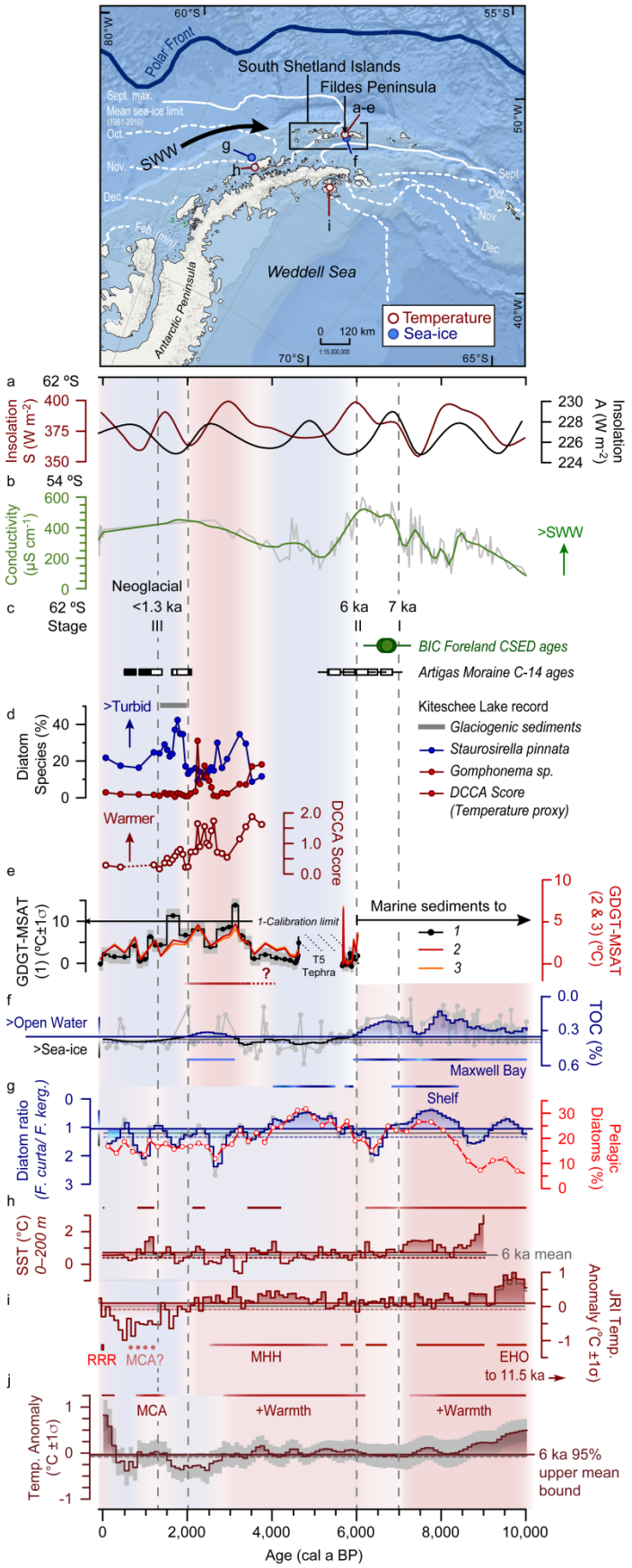
60°S
55°S
80°W
60°W
40°W
70°S
65°S
Polar Front
South Shetland Islands
Fildes Peninsula
a-e
Sept. max.
Mean sea-ice limit
(1981-2010)
Oct.
Nov.
Dec.
Feb
min.
SWW
g
h
i
f
Sept.
Oct.
Nov.
Dec.
Weddell Sea
Antarctic Peninsula
Temperature
Sea-ice
0 120 km
1:15,000,000
a
62 °S
Insolation S (W m-2)
400
375
350
230
228
226
224
Insolation A (W m-2)
b
54 °S
Conductivity (µS cm-1)
600
400
200
0
>SWW
Neoglacial
c
62 °S
Stage
<1.3 ka
III
6 ka
II
7 ka
I
BIC Foreland CSED ages
Artigas Moraine C-14 ages
d
Diatom Species (%)
40
20
0
>Turbid
Warmer
2.0
1.0
0.0
DCCA Score
Kiteschee Lake record
Glaciogenic sediments
Staurosirella pinnata
Gomphonema sp.
DCCA Score
(Temperature proxy)
e
GDGT-MSAT (1) (°C±1σ)
10
0
1-Calibration limit
T5
Tephra
?
Marine sediments to
1
2
3
10
5
0
GDGT-MSAT (2 & 3) (°C)
f
>Open Water
>Sea-ice
0.0
0.3
0.6
TOC (%)
Maxwell Bay
g
Diatom ratio (F. curta/ F. kerg.)
0
1
2
3
Shelf
30
20
10
0
Pelagic Diatoms (%)
h
SST (°C) 0–200 m
2
0
6 ka mean
i
1
0
-1
JRI Temp. Anomaly (°C ±1σ)
RRR
MCA?
MHH
EHO
to 11.5 ka
j
Temp. Anomaly (°C ±1σ)
1
0
-1
MCA
+Warmth
+Warmth
6 ka 95%
upper mean
bound
0
2,000
4,000
6,000
8,000
10,000
Age (cal a BP)

Figure 4. Summary of cosmogenic and radiocarbon ages from boulders and moraines of the BIC foreland compared with key results from the Kiteschee Lake record and climate and sea-ice reconstructions from theSouth Shetland Islands,Antarctic Peninsula and Southern Ocean. Location map of records: a. Mean summer (red line) and mean annual insolation (black line) received at 62°S (Laskar et al., 2004). Plotted insolation are 500-year annual mean at 62ºS. b. Diatom-inferred conductivity record from Macquarie Island at 54°S, a proxy for changes in Southern Ocean and Southern Hemisphere westerly wind (SWW) strength during the mid–late Holocene (Saunders et al., 2018). c. Summary of exposure ages (green circles) and radiocarbon chronological data (white squares) from the BIC foreland boulders and moraines (this study). Black squares are from Hall (2007). BIC re-advance Stages I–III are as shown in Figure 5. d. Key indicator species for more turbid conditions (*Staurosirella pinnata* sp. and DCCA Axis 1) and more aerophilic conditions (possibly warmer, more ice-free) (increased *Gomphonema* sp.) and). e. Yanou Lake GDGT-MSAT (mean summer annual temperature) reconstructions showing a summary comparison of three different calibrations: 1 after Foster et al. (2016), 2 and 3 are new data produced in this study (see Methods and Supplementary Note 3 for details). f. Maxwell Bay TOC (total organic carbon) derived sea-ice record (Milliken et al., 2009). g. Anvers Shelf diatom-based sea-ice reconstruction. Measured data, shown in grey in d. and in e., were smoothed using polynomial negative exponential regression (thick lines), producing similar results to locally-weighted smoothing (LOESS first order polynomial) (not shown). h. Palmer Deep 0–200 m SST record (Etourneau et al., 2013). i. James Ross Island (JRI) Ice core (Mulvaney et al., 2012) and warm phases on the Antarctic Peninsula(as defined in Bentley et al. 2009; MCA: Medieval Climate Anomaly cold phase; RRR: Recent Rapid Warming). j. the Southern Hemisphere 90–30° S temperature data stack (Marcott et al., 2013).

glacial re-advances and the shift to 'Neoglacial' conditions on the South Shetland Islands after c. 2,000 cal a BP (and across the northern AP) to reductions in summer/annual insolation coupled with a shift to more intense Southern Hemisphere westerly winds in the Southern Ocean, as identified in the increased turbidity in the Kiteschee Lake record (Fig. 4d) and some South America and sub-Antarctic records (Garreaud, 2007; Moy et al., 2008; Moreno et al., 2014; Charman et al., 2018; Moreno et al., 2018; Saunders et al., 2018) (Fig. 4a, b). Stronger, and possibly more poleward-shifted Southern Hemisphere westerly winds most likely reflect the millennial-scale expression of decadal-centennial changes in the Southern Annular Mode (Charman et al., 2018) leading to more precipitation-laden storm fronts passing over the South Shetland Islands and increased ice accumulation on the BIC. It is possible that atmospheric warming north of 60 °S could be linked to increased precipitation associated with strengthening (and possibly poleward shifts) of the core Southern Hemisphere westerly wind belt during the MCA (Marcott et al., 2013). Combined, these factors help to drive the late Holocene readvance of the BIC on the Fildes Peninsula between 1,300 and c. 650 cal a BP (Hall, 2007). The BIC was, therefore, highly-sensitive to even the relatively minor variations in temperature and Southern Hemisphere westerly winds intensity during the late Holocene.

Notably, we also found no evidence for a significant shift to a 'warming' trend at c. 500–600 years ago in the Fildes Peninsula lake records that has been identified in the James Ross Island ice core and the Beak Island lake records from the eastern Antarctic Peninsula (Milliken et al., 2009; Hass et al., 2010; Sterken et al., 2012)(Supplementary Fig. 12) and in compilations of climate records from the

Southern Hemisphere (e.g., Marcott et al., 2013; Fig. 4j). While this might relate to the low accumulation rates and temporal resolution of these records, it could also reflect the spatially heterogenous influence of oceanographic and orographic controls on climate across the northern and western Antarctic Peninsula (Milliken et al., 2009; i.e., dipole) (Fig. 4).

The generally colder, 'Neoglacial', conditions persisted on Fildes Peninsula through the Southern Hemisphere 'Little Ice Age' 650-80 cal a BP (SH-LIA: c. 1300–1870 CE, defined as the period when a majority of Southern Hemisphere records exhibit 'extreme cold' (Neukom et al., 2014); Supplementary Figs. 12 and 13). The absence of a significant readvance of the BIC during the SH-LIA is probably related to cooling north of 60 °S and an equatorward shift in the core Southern Hemisphere westerly wind belt. In mid-late C20th, the mode of sedimentation in the lake shifted dramatically to one dominated by aquatic moss (Supplementary Fig. 9). We link this final shift to a moss-dominated environment to the Recent Rapid Warming (RRR) (as defined by Bentley et al. 2009) (Fig. 4i). A thriving aquatic moss community still exists at the sediment-water interface (Supplementary Fig. 9).

In terms of glacio-isostatic adjustment (GIA), the late Holocene readvance of the BIC is consistent with the more restricted late Holocene ice-loading scenario of the Whitehouse-GIA model for the South Shetland Islands (Watcham et al., 2011). Other GIA models (Simms et al., 2012) require more substantial 'Neoglacial' ice-loading, but are well-supported by field data (Watcham et al., 2011), and this may be evidence for late Holocene ice-load change elsewhere on the South Shetland Islands. GIA model parameters for the South Shetland Islands crustal block (e.g., lithospheric thickness, mantle viscosity) might need to be re-evaluated in light of two recent studies (Roberts et al., 2017; Antoniades et al., 2018) which highlighted the possibility of at least one highly explosive eruption (Volcanic Explosivity Index, VEI>6) from the Deception Island volcano between 6,000-3,000 cal a BP. Data from Fildes Peninsula lacustrine records suggest several eruptions from Deception Island were significantly larger than those of the last 1,000 years (Roberts et al., 2017). Deglaciation and glacio-isostatic uplift of South Shetland Island block would have created significant crustal stress on the underlying magma chamber, causing localized changes in mantle viscosity, which could have influenced rates of glacio-isostatic uplift during the mid-late Holocene. Moreover, the (non-glacial) isostatic uplift effect of unloading a significant mass of lithosphere in explosive eruption from the SSI crustal block in mid to late Holocene is unknown.

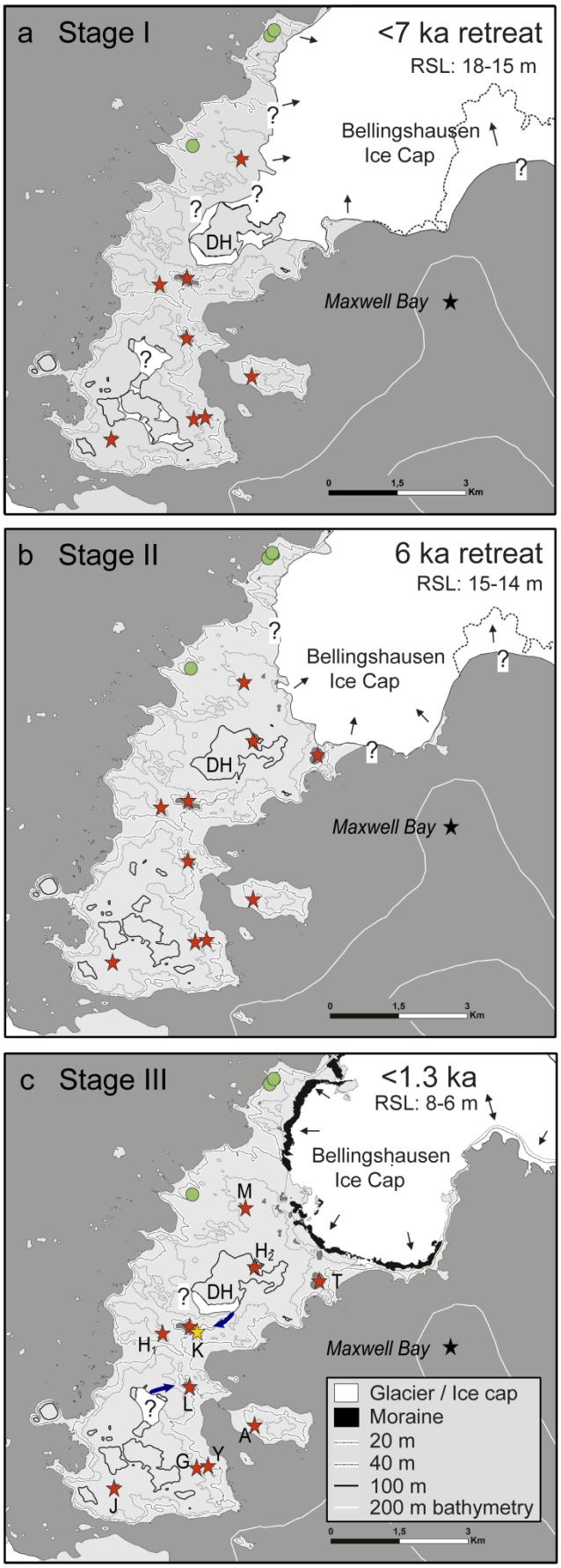
a Stage I
<7 ka retreat
RSL: 18-15 m
Bellingshausen
Ice Cap
DH
Maxwell Bay
0 1,5 3 Km
b Stage II
6 ka retreat
RSL: 15-14 m
Bellingshausen
Ice Cap
DH
Maxwell Bay
0 1,5 3 Km
c Stage III
<1.3 ka
RSL: 8-6 m
Bellingshausen
Ice Cap
M
H2
T
DH
H1
K
L
A
G
Y
J
Maxwell Bay
Glacier / Ice cap
Moraine
20 m
40 m
100 m
200 m bathymetry
0 1,5 3 Km

Figure 5. Schematic reconstruction of mid–late Holocene glacier extent on Fildes Peninsula and deglaciation of the study area based on a compilation of new dates in this study and published data. Panels correspond to the key stages of deglaciation changes in climate/sea-ice at a. Stage I (<7 ka), b. Stage II (6 ka) and c. Stage III (1.3 ka) shown in Figure 4. Arrows in a. and b. indicate glacier retreat, while the arrows in c. represent glacier readvance. Green circles show the location of the erratics sampled for cosmogenic ^{10}Be exposure dating. The orange star is the location of the new Kiteschee Lake record, while red stars represent the location of published lake data and basal (deglaciation) ages mentioned in the text. The black star is the location of the Maxwell Bay marine records (Milliken et al., 2009; Simms et al., 2011). Question marks on the maps indicate uncertain locations of the glacier fronts. Note the relative sea level elevation of the coastlines in each panel.

To summarise, we reconstructed the mid–late Holocene deglaciation history of northern Fildes Peninsula using a combination of: (i) cosmogenic exposure ages from glacial erratics on the foreland of the Bellingshausen Ice Cap; (ii) radiocarbon analysis of (a) macrofossils and marine remains found in moraines formed by the most significant glacial readvance during the late Holocene and (b) of cored sediments from the Kiteschee Lake: (iii) multi-proxy analyses (diatoms, grain size, geochemical and sedimentological analysis) of the lake sediments. We found no evidence for a mid–Holocene glacier advance in the northern glacier foreland of Fildes Peninsula area. Our new evidence, combined with previously published data suggests that late Holocene glacial readvances were restricted and close to present limits, with localized minor ice build-up on topographic highs on the Fildes Peninsula. In conclusion, readvances of the Bellingshausen Ice Cap beyond its present position on the Fildes Peninsula have been minimal during the last 7,000 years.

6. CONCLUSIONS

We propose the following sequence of events for the mid–late Holocene deglaciation and glacier re-advances on the Fildes Peninsula:

1) As a result of the early Holocene warming, the north-western marine platform at c. 40–35 m a.p.s.l. became ice-free after 7,000 cal a BP, and ice cap configuration similar to the present day existed on Fildes Peninsula by c. 6,000 cal a BP.
2) The presence of mosses embedded in till of the Shetland I moraine suggest that the BIC extended landward of its present position on its eastern flank c.1,900–1,300 cal a BP, before the onset of regional 'Neoglacial' conditions.
3) Sometime after 1,300 cal a BP, a minor glacier readvance translocated mosses and mid Holocene marine sediments into the moraines surrounding the present-day BIC, consistent with 'Neoglacial' conditions, which continued in Kiteschee Lake until the mid C20th.
4) Recovery from the 'Neoglacial' cooling is characterised in Kiteschee and other lakes on Fildes Peninsula by the re-colonisation of thick aquatic moss at the lake sediment-water interface. This occurred from the mid–late C20th onwards (modelled age of c. 1970 CE) driven by late C20th warming of the Antarctic Peninsula.

5) The restricted late Holocene readvance of the BIC is consistent with a more restricted late Holocene ice-loading scenario implied by the Whitehouse GIA model for the South Shetland Islands. Other GIA models require more substantial 'Neoglacial' ice-loading and are well-supported by field data, suggesting greater ice-loading elsewhere on the South Shetland Islands crustal block during the late Holocene.

ACKNOWLEDGEMENTS

We acknowledge funding by CONICET, the DNA/IAA in the framework of the Project PICTA, 2011 – 0102, IAA "Geomorfología y Geología Glaciar del Archipiélago James Ross e Islas Shetland del Sur, Sector Norte de la Península Antártica" granted to Jorge Strelin and support by the Alfred Wegener Institute (AWI), Helmholtz Centre PACES II (Polar Regions and Coasts in the changing Earth System). P.H.B, S.J.R, E.P. and G.K were funded by IMCONet (FP7 IRSES, action no. 319718) and a NERC/BAS-AFI Grant. Special thanks to the crews of the Uruguayan research station "Artigas", the Russian Bellingshausen Station and Argentine research station "Carlini" and the adjoined German Dallmann-Labor (AWI) during the 2011 and 2015 field seasons for their cordial hospitality and invaluable logistical support. Fieldwork assistance by Magnus Makeschin, Bulat Mavlyudov, Eliseo Flores and Marco Petit and technical assistance from Anke Toltz and Ruben Rosenkranz for samples processing assistance for ^{10}Be exposure dating was greatly appreciated.

SUPPLEMENTAL MATERIAL TO CHAPTER 4: MID-LATE HOLOCENE DEGLACIATION OF NORTHERN FILDES PENINSULA, KING GEORGE ISLAND, NW ANTARCTIC PENINSULA

Pablo Heredia Barión, Stephen J. Roberts, Cornelia Spiegel, Steven A. Binnie, Lukas Wacker, Joanna Davis, Imogen Gabriel, Viv Jones, Simon Blockley, Emma Pearson, Steve Juggins, Louise Foster, Gerhard Kuhn

Supplementary Note 1: Processing for ^{10}Be exposure dating

Purified quartz separates were prepared from the rock samples at Bremen University cosmogenic nuclide laboratory. We used standard physical rock preparation, using a jaw crusher, sieves (125 µm–1000 µm) and Frantz magnetic separation up to 1.5 A. We further cleared the non-magnetic fraction of unwanted phases such as feldspar and carbonates through chemical purification with a 30% HCl + 0.03% H_2O_2 leaching. The resulting, almost pure quartz and feldspar sample was further cleaned of meteoric beryllium by 3 steps of weak 2% HNO_3 + 2% HF leaching. We weighed the mass before and after, to keep track of how much mass had been lost.

Separation of beryllium from the quartz separates was carried out at the Institute for Geology und Mineralogy, University of Cologne, Germany. Quartz purity was determined prior to dissolution by ICP-OES. The samples were spiked with ~300 micrograms of commercially available Be carrier (Scharlab, 1000 microgram/l Berylium ICP standard solution, batch number 14569501). After digestion in HF acid, remaining insoluble fluoride salts were heated several times in the presence of aqua regia and aliquot of the sample was taken for an ICP-OES measurement before the sample underwent column separation using the single-step column procedure (Binnie et al., 2015). The separated $Be(OH)_2$ was co-precipitated alongside Ag (Stone et al., 2004) with a respective mass ratio of around 1:5, before being pressed into Cu targets for measurement on Cologne AMS, Institute of Nuclear Physics, University of Cologne (Dewald et al., 2013). ^{10}Be/^{9}Be AMS measurements were normalised to the standards of Nishiizumi using the nominal values reported in Nishiizumi et al. (2007). A blank was prepared in tandem with the samples and ^{10}Be concentrations are reported following subtraction of the ^{10}Be atoms measured in the blank. Though sample concentrations are relatively low the maximum blank subtraction was <6%. Analytical uncertainties for the ^{10}Be concentrations were derived by summing in quadrature the uncertainty in the mass of Be added during sample processing (estimated to be 1% at 1 sigma) and the AMS measurement uncertainties of both the samples and blank.

Supplementary Note 2: Kiteschee Lake sediment core record

Located at c. 15 m above present sea level (henceforth, m a.p.s.l.), Kiteschee Lake is approximately 430 m x 220 m and has a surface area of 0.09 km^2. During the Austral winter it is covered by 50 cm thick lake-ice, while in late spring and summer (November-March) it is usually permanently ice free (Martinez-Macchiavello et al., 1996). Multi-proxy analyses (diatom, grain size, geochemical and sedimentological

analysis) were used to reconstruct past environmental change in Kiteschee Lake record. Since the early Holocene isolation history of Kiteschee Lake is well-established (Mäusbacher et al., 1989), we undertook high-resolution analysis of diatoms in the late Holocene part of a new composite (70 cm long) c. 7,000-year old record where diatoms were best-preserved.

Radiocarbon dating of Antarctic lake sediments from high latitudes is often problematic due to prolonged ice cover, low terrestrial and aquatic biological production and slow rates of organic matter (OM) decomposition (Wolfe et al., 2004). Bulk glaciolacustrine/glaciofluvial sediments have produced 'reliable' ages in some lake records from Fildes Peninsula, often overlapping with paired macrofossil ages and tephra-based chronologies from well-dated terrestrial and marine records (Roberts et al., 2017). Dried sediment samples radiocarbon dated by Beta Analytic, Miami. Following procedures described in detail in Roberts et al. (2017). We also used the visible tephra deposits and their well-constrained aquatic moss ages from Ardley and Yanou records (radiocarbon-dated and age-depth modelled) that have been linked with thicker ash layers in the James Ross ice (JRI) core record (Mulvaney et al., 2012) (modelled ages) (Supplementary Table 2).

Distinguishing clear climate and deglaciation signals from lake sediments can also be complicated. The proximity of Fildes Peninsula to Deception Island makes it vulnerable to tephra input, which can have a significant impact on lake ecosystems. Volcanic activity can increase lake sedimentation rates, grain size and influence ecosystem function through deterioration in light conditions and high suspension load. While these can all have a negative impact on some diatom species abundance, tephra is rich in silica and some species have been shown to flourish following deposition of tephra in lakes on the South Shetland Islands (e.g., Björck et al., 1993).

Summary Methods: To assess potential key drivers of ecological change to deglaciation, glacier readvance and climate, and applied a diatom-based transfer function to reconstruct past chlorophyll-a and derives diatom and XRF trends using Principal Component Analysis (PCA). Sediment core scanning (GEOTEK and ITRAX µ-XRF) procedures used are as described in Roberts et al. (2017) and Davies et al. (2015). In summary, µ-XRF analysis was performed at contiguous 0.02 cm (200 µm) intervals. Whole core gamma (bulk) wet density (5 mm aperture gamma ray attenuation sensor), magnetic susceptibility (Bartington Instruments MS2E point sensor, 10 second count time) and P-wave amplitude and velocity were measured with GEOTEK core logger using standard calibration procedures. Grain size was measured organic- (LOI550 °C) and carbonate-free (5% HCl) sediments using a Malvern laser particle counter, which detects particles between 0.01-2000 µm. As diatom abundance was high throughout the core, we examined the impact of diatoms on grain size distributions using four sediment samples from 6 cm, 13 cm, 20 cm and 33.5 cm, using sodium hydroxide. Results showed minimal difference in grain size distribution, insufficient to undertake the process for all samples. Calgon was added to the sample to reduce aggregation before being diluted. Grain size data was analysed using GRADISTAT (Blott and Pye,

2011). Stratigraphic diagrams of %LOI (Loss-on-ignition), wet-sediment micro-XRF (X-ray fluorescence) geochemistry and grain size were created in C2 1.7.7 and analysed using the R package Rioja (Juggins, 2007; Juggins, 2014). Other data analysis and plotting was undertaken in Sigmaplot and Analyseries.

A chronology for the Kiteschee Lake sediment record was established using six AMS radiocarbon (^{14}C) ages from, in order of preference: 1) moss macrofossil layers (consisting of hand-picked fine strands of the aquatic moss *Drepanocladus longifolius (Mitt.) Paris* sp. currently living in Kiteschee Lake (and other Fildes Peninsula lakes). Unlike some other lakes on Fildes Peninsula (Roberts et al., 2017), we did not find visible moss layers further downcore. Therefore, we sampled the most organic-rich bulk sediments (determined from incoherent/coherent (inc./coh.) micro-XRF and LOI data) at regular intervals. Measured radiocarbon ages from samples shown in Supplementary Table 2 were calibrated using the SH13 calibration curves (Hogg et al., 2013). Age-depth models were generated using BACON v2.2 Bayesian age-depth modelling techniques (Blaauw, 2010; Blaauw and Christen, 2011) used are as outlined in Roberts et al. (2017). Shard specific major element geochemistry for the most prominent tephra layers was undertaken by electron probe microanalysis (EPMA) following procedures in Roberts et al. (2017) and Blockley et al. (2005).

Diatom Analysis: Samples were taken at 1 cm intervals between 1 and 32 cm, at 2 cm intervals to 47 cm depth. Samples between 47–77 cm depth were screened from smear slides to determine the presence/absence of marine or brackish diatom species. Sediment samples were treated with H_2O_2 (30%) and HCl (50%), heated in a 120◦C water bath for 24 hours to remove organic material, washed, then mounted on slides in Naphrax (Battarbee et al., 2001). To determine diatom concentrations, which are needed to infer primary productivity, 1 ml of 8.20 x 10^5 spheres per ml DVB microsphere suspension was added per 1 ml of diatom solution. At least 300 diatom valves were counted and identified using a Zeiss Aciostar-plus microscope under oil at 1000x magnification. Species were identified according to Sterken et al. (2015). To avoid double counting specimens, only valves that were >50% intact were counted and valves that could not be identified (due to the orientation or obscuration) were noted. Species which had >2% abundance were plotted and zones identified.

Cluster analysis was undertaken using TWINSPAN to classify diatom fossil assemblages, defining five classes by cut-off levels 0%, 2%, 5%, 10% and 20%. Multivariate analysis was undertaken to explore the trends and assemblage changes in diatom communities and potential diatom responses to changes in core geochemistry. A Detrended Correspondence Analysis (DCA) was initially performed to identify whether unimodal or linear models were suitable for further analysis (Ter Braak and Smilauer, 2002). The DCA showed that the gradient length is short, i.e., <2 standard deviation units, meaning linear methods (PCA, RDA) of data analysis were more appropriate (Ter Braak and Prentice, 1998). To reduce the score and bias of the most abundant species that could mask the effect of less abundant species, a square root function was used. For multivariate analysis, all

diatom and geochemical variables were log_{10} transformed. The relationships between the diatom assemblages and environmental variables were explored further using RDA (Supplementary Figure 10). The significance ($p<0.05$) of each environmental variable was assessed with forward selection using an unrestricted Monte Carlo Permutation Test. Diatom compositional turnover (β-diversity) is estimated down-core using Detrended Canonical Correspondence Analysis (DCCA) for the most abundant diatoms (>2%). Log transformations were applied prior to statistical analysis. Ordinations were performed using CANOCO 5.0.for Windows (Ter Braak and Smilauer, 2002).

To reconstruct changes in chlorophyll-a, we applied the diatom-chlorophyll-a training set developed for the Antarctic Peninsula using data from 61 lakes (Jones and Juggins, 1995). Diatom-based transfer functions were applied in C2 (Juggins, 2007) using simple weighted averaging (WA) and weighted partial least squares (WA- PLS) algorithms (Birks, 1998). The WA-Inverse transfer function was chosen to reconstruct chlorophyll-a as the RMSE and average bias were low and displayed a strong relationship (R^2) between measured and diatom-inferred chlorophyll-a.

***Summary Results and Interpretations*:** The two overlapping cores were aligned using magnetic susceptibility data to construct a composite core profile (Supplementary Figure 1, 2). Several visible tephra layers were readily apparent in the Kiteschee record (Supplementary Figure 2). Their position was straightforward to determine using geochemical micro-XRF scanning (Ti, Ca, incoherent/coherent scattering ratio) and manual-counting (Supplementary Figure 2, 3, 4).

Lithology: The base of the core (77-60cm) is composed of olive-brown silt with several fine black ash layers (T6 and T7), with elevated MS values (Supplementary Figure 2). From 57cm upwards, following the deposition of the T5 tephra, there is a distinct change to lighter orange-brown sediments composed of silt-clay material. Tephra layers are interspersed between 54 and 18 cm depth, within a brown silt-clay matrix (Supplementary Figure 2). The main lithological change in the core occurred at c. 20-11 cm depth, where an orange-brown silt-dominated lithofacies unit is overlain by a light grey clayey-mud lithofacies unit containing some sand-rich layers. This is overlain by a unit of olive-brown silt between 11 and 5 cm, capped by living aquatic moss, which present in the uppermost 5 cm and returned a post-bomb (>1950 CE) age of 2010 CE (Supplementary Figure 2b, Supplementary Table 1).

Organic matter content is generally very low (<5 % LOI550) and relatively stable throughout the record (Supplementary Figure 3). Grain size analysis of the core indicates that its sediment is dominated by counter-opposing silt and sand components, with consistently low clay content (~3–10%) (Supplementary Figure 3a). The silt (sand) component gradually increases to 61% (decreases to 20%), peaking at 35 cm, before declining (increasing) gradually to 23 cm (2,120±500 cal a BP). Silt (sand) content remains stable from 23 cm upwards, but has four sharp peaks (troughs), at 20, 16, 15, 13 cm depth (1,950, 1,700, 1,640, 1,510 cal a BP).

Silt content gradually increases and sand content decreases towards the top of the core.

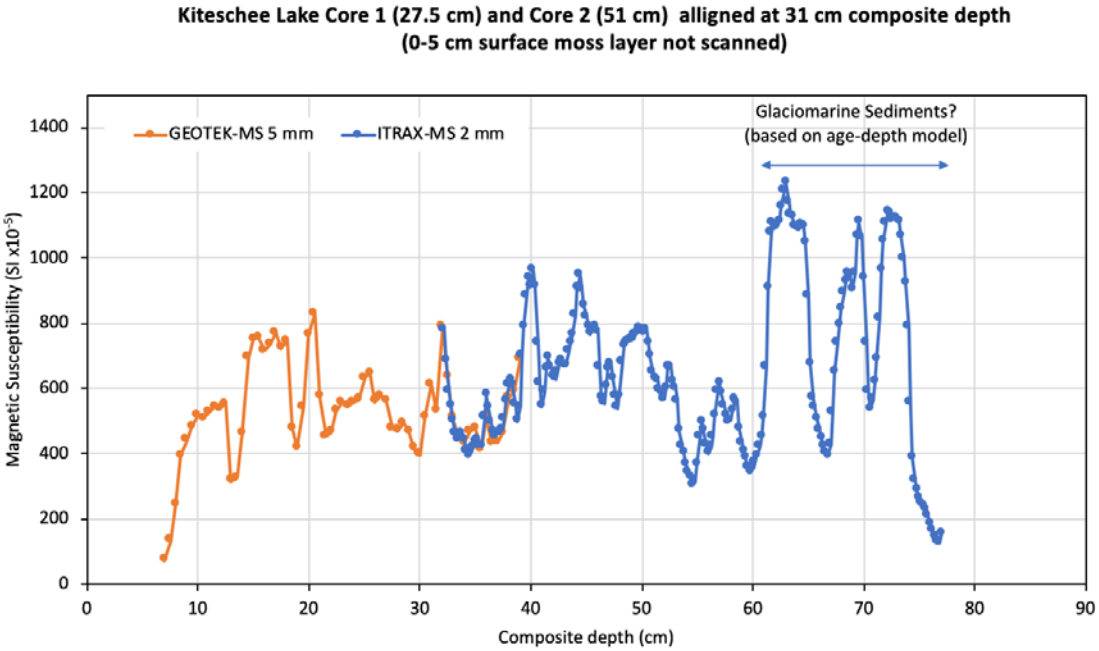

Supplementary Figure 1 Magnetic susceptibility data used to align Kiteschee Lake sediment cores into the composite core shown in Supplementary Figure 2a.

The lithogenic element Titanium (Ti) was used for normalisation of wet sediment XRF scan data, as it provides an unambiguous indictor of allochthonous inputs from the catchment and accounts for varying organic content in the sample (Cohen, 2003; Davies et al., 2015). Changes in log K/Ti and log Ca/Ti mirror one another, with noticeable decline and sharp troughs between 24 and 19 cm (2,170 and 1,890 cal a BP). The geochemistry appears to reflect changes in particle size, while PCA axis 1 follows changes in the sand component of the core (Supplementary Figure 3b). This is likely to be driven by material input from the catchment as well as tephra layers.

a.

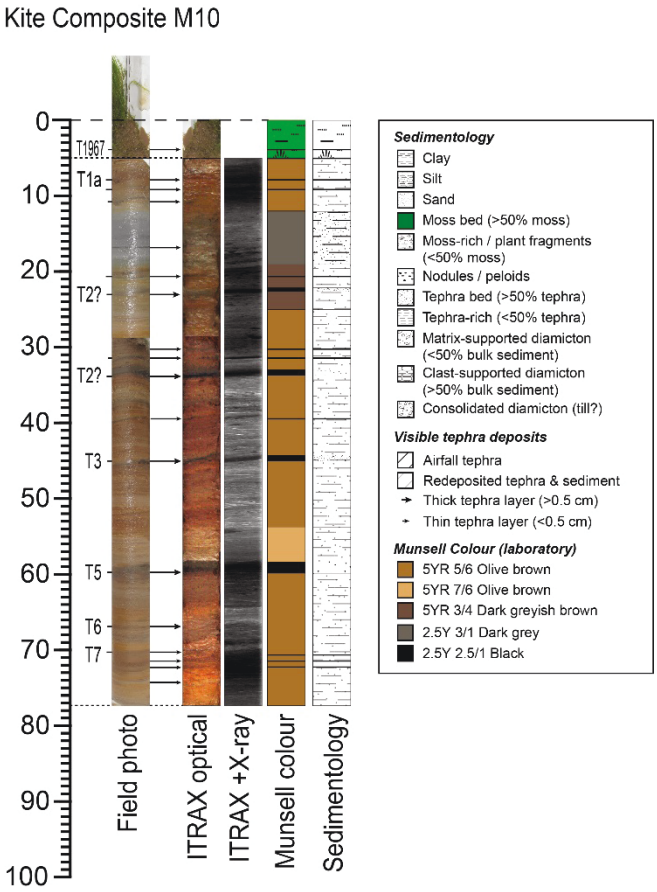

b.

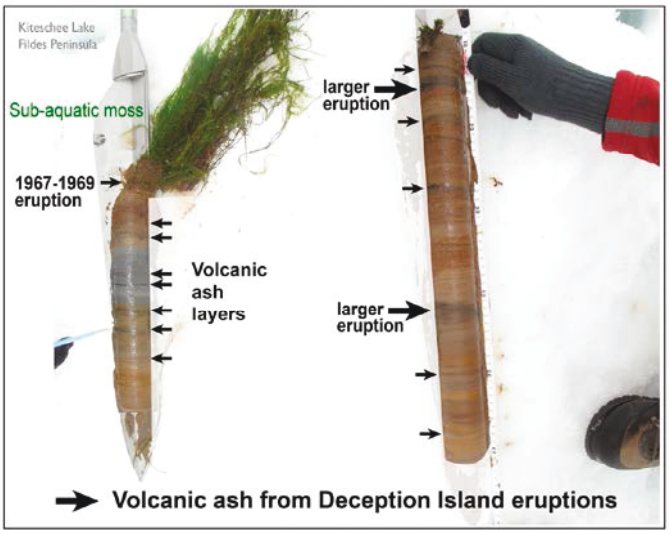

Supplementary Figure 2 a. Summary sedimentology of the 77 cm long Kiteschee Lake composite core. T1–7 represent the main visible ash layers identified in Fildes Peninsula lake sediment cores (Roberts et al., 2017). **b.** Field photograph showing the development of thick living aquatic moss at the sediment-water interface at the bottom of Kiteschee Lake and tephra layers visible in both Russian cores (photograph taken in November 2011 CE)

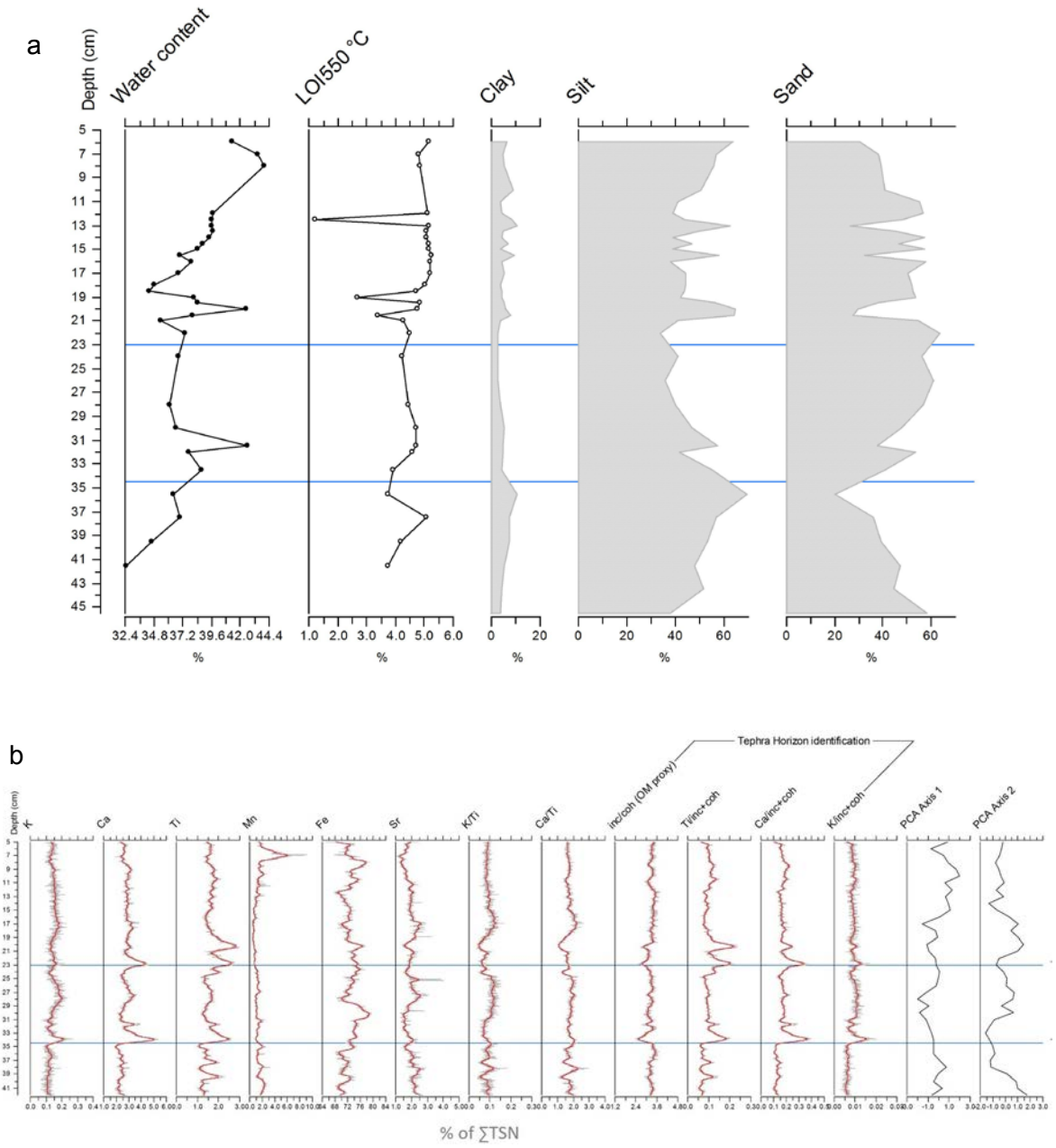

Supplementary Figure 3 Down-core changes in: **a.** Water content, LOI 550 ^{o}C (organic matter), grain size and **b.** Geochemical elements and PCA axes values from multivariate analysis. Blue lines are unmatched tephra deposits of uncertain age. TSN is the Total Scatter (incoherent + coherent scatter, inc.+coh.) Normalised ratio sum as defined in Roberts et al. (2017). Elemental data were normalised to TSN to account for changes in water content and organic matter and are expressed as a percentage to assess closed-sum effects in the XRF dataset.

Chronology: The radiocarbon age of obtained from the 'glaciogenic' lithofacies unit contained old carbon from reworked from early Holocene deglaciation deposits. All other bulk sediment ages from organic-richer sediments, which all have low OM values of <5% carbon, are in chronological order. Tephra deposits were assigned as shown in Supplementary Figure 4, based on count data shown KITE-M9 age-depth model and tephra geochemistry as described below (Supplementary Figure 4, 5, 6, 7). We explore the implications of its tephra geochemistry for a regional tephrochronology of the northern AP further in a forthcoming paper.

Age-depth modelling was undertaken using BACON v.2.2 (Bayesian) age-depth modelling software by inputting uncalibrated conventional radiocarbon age data in R (Supplementary Table 1) (Blockley et al., 2005; Blaauw, 2010) following procedures in Roberts et al. (2017). All 'as measured' (uncalibrated) conventional radiocarbon age data were inputted in age-depth model runs Kite-M9 and Kite-M10 (model run number is indicated by the KITE-M_n suffix) (Supplementary Figure 2). Prior settings for the KITE age-depth models runs were: acc.shape = 1.5, acc.mean = 100 a cm^{-1}, mem.strength = 20, mem.mean = 0.1, segment thickness = 5 cm. We also investigated the effect of varying the starting mean accumulation rate setting using three different acc. mean settings of 10, 20 and 50 a cm^{-1}, but retained 100 a cm^{-1} as this produced the best fit to measured data and to minimise the mean core errors.

To obtain initial age estimates for the tephra layers, we ran age depth modelling process without tephra ages included (KITE-M9 model run shown in Figure 5a). All ages and years are rounded to the nearest 10 years in data tables and to the nearest 100 years in the text to account for calibration and modelling errors. Interpolated modelled ages quoted in the text were derived from the 'best-fit' age of the BACON age depth model. Weighted mean modelled ages were used, with minimum to maximum 95% confidence age ranges shown in square brackets. It was necessary to calculate ages for some proxy data at resolution higher than dating errors allow (e.g., sub-cm resolution scanning data) to enable plot proxy data against time.

The most prominent ash layer in the Kiteschee Lake record shown by shard count and incoherent/coherent scatter ratio data is at 62–56 cm depth. This contains an exclusively rhyolitic (explosive) layer at 58 cm depth whose major element glass shard-specific geochemistry could not be matched to the shard geochemistry of Holocene rhyolitic-tephra producing eruptions from South America (Supplementary Figure 4). Instead, its composition is most similar to the rhyolitic component of the early–mid Holocene Deception Island eruption T7 (Supplementary Figure 7) or possibly the early Holocene/pre-Holocene 'Megascopic' (caldera-forming?) eruption (Moreton and Smellie, 1998; Roberts et al., 2017). The overall bi-modal geochemical composition of the 62-56 cm ash layer suggests it could have evolved from Deception Island (basalt-andesitic) magma by interaction with seawater, possibly during a two-stage explosive eruption event (Supplementary Figure 5, 6).

Based on M9 age model, this ash layer has a 95% confidence age range which overlaps with the well-defined aquatic moss-based radiocarbon for the T5 eruption event at c. 5,500-5,000 cal a BP in the Yanou Lake record (Roberts et al., 2017). Re-running the Kiteschee Lake M10 age-depth model produced a 95% confidence age of between 5,790 and 4,960 cal a BP for 62–56 cm depth in the Kiteschee Lake record. Other tephra layers were assigned using the nomenclature used in Roberts et al. (2017) as shown in Supplementary Figure 4b. Ages used in this study for these layers are shown in Supplementary Table 2 and are derived from Supplementary Table 3 of Roberts et al. (2017) and references therein.

Antoniades et al. (2018) suggested that the caldera-forming eruption of the Deception Island volcano occurred between 4-3.5 ka, equivalent to the T3 or T4 eruption. While evidence of a large eruption (or series of eruptions), exists between c. 4-3 ka in all Fildes Peninsula lake records, including our new Kiteschee Lake, tephra deposits for these eruptions are not as prominent as the T5 event. The most prominent ash caldera-forming eruption tephra deposit in one of the Byers Peninsula lake records was similarly dated to c. 5.5 ka (Antoniades et al., 2018). Two radiocarbon ages from above and below the approximately 30 cm of reworked ash generated by seismic gravity flows are essentially identical. Bulk ages of c. 10-11 ka from reworked sediment in the gravity flow deposit are equivalent in magnitude to the Kiteschee Lake age offset in the glacigenic facies. As a result of these ages, the whole record was considered unreliable due to the unknown and variable influence of old carbon. Nevertheless, all other ages are in sequence, with no apparently large offsets close to the surface. The c. 4-3.5 ka eruption age in most of the other cores from Byers Peninsula in Antoniades et al. (2018) is based on radiocarbon dating of moss layers from above the eruption event. This constrains when the lake ecosystem had recovered sufficiently for moss recolonization rather than the age of the eruption event. Ages below the reworked/seismically-influenced ash deposits on Byers Peninsula are somewhat ambiguous. The pre-eruption sediments are dated to c. 4 ka in at one record but are potentially as old as 7 ka in others. Similarly, the age of the T4 eruption in Yanou Lake remains uncertain as there is no organic material to date due to the continued influence of post 5ka eruption reworking and allochthonous input of catchment material (Roberts et al., 2017)

Despite a clear shift in geochemistry at c. 60 cm depth (Supplementary Figure 1), a complicating factor is that the new Kiteschee Lake sediment record does not contain any clear biological evidence of (glacio)marine sedimentation that should be present in deposits >6,000 years old. Diatoms were poorly preserved from c. 47 cm depth downwards and almost completely absent from the base the record. The $\delta^{13}C$ value of the near basal age obtained from 73.5–74.5 cm depth is consistent with sediments that contain only terrestrial diatom species. Nevertheless, all sedimentary units younger than c. 6,000 cal a BP contain terrestrial diatoms. As Kiteschee Lake is situated at c. 15 m a.s.l., it would have been higher than reconstructed relative sea level at from time onwards (Mäusbacher et al., 1989; Watcham et al., 2011).

KITE rangefinder ages		Core	Strat		IRMS d13C		Radiocarbon age	SH13 Calibrated Ages (OXCAL 95.4%) (cal a BP)			
BETA	Core ID_core depth	depth	Depth	Material dated & pretreatment		pMC (%)	(C-14 a BP)	from	to	Mean ± 1σ	Median
501582	KITE2.1M_0-0.5 cm	0-0.5	0.25	Aquatic moss: *Drepanocladus longifolius* sp.	-27.4	101 ± 0.4	-	after 2010		-60 ± 1	-60
								-6	-8	-7 ± 1	-7
504801	KITE2.1_4.5 cm	9-10	9.5	Bulk orange-brown sediment: acid washes	-23.9	81.9 ± 0.3	1600 ± 30	1530	1380	1450 ± 40	1450
497408	KITE2.1_16-17cm	16-17	21.5	Bulk 'glacial' grey sediment: acid washes	-32.6	31.1 ± 0.1	9380 ± 30	10670	10420	10550 ± 60	10550
501584	KITE1.1_7.5-8 cm	7.5-8	36.25	Bulk orange-brown sediment: acid washes	-18.0	79.3 ± 0.3	1860 ± 30	1830	1630	1760 ± 50	1760
501585	KITE1.1_17-18 cm	17-18	45.75	Bulk orange-brown sediment: acid washes	-17.7	65.9 ± 0.3	3350 ± 30	3630	3450	3530 ± 50	3530
498331	KITE1.1_45-46 cm	45-46	74	Bulk orange-brown sediment: acid washes	-18.0	45 ± 0.2	6410 ± 30	7420	7180	7310 ± 50	7300

Supplementary Table 1 *Radiocarbon age and* calibration data for the Kiteschee Lake record. OXCAL v. 3.299 using the SHCal13 Southern Hemisphere atmosphere dataset (see Table 2 for references). Absolute percentage of modern carbon (pMC) data were corrected according to $^{13}C/^{12}C$ isotopic ratios from measured pMC, where a "modern" pMC value is defined as 100% (1950 CE). Post-bomb (>1950 CE) samples were corrected according to $^{13}C/^{12}C$ isotopic ratios from measured pMC, where the 'present day' pMC value is defined as 107.5% (2010 CE), and calibrated using the SHCal13 SH Zone 1-2 Bomb curve using CALIBomb (Reimer and Reimer, 2004; Hua et al., 2013).

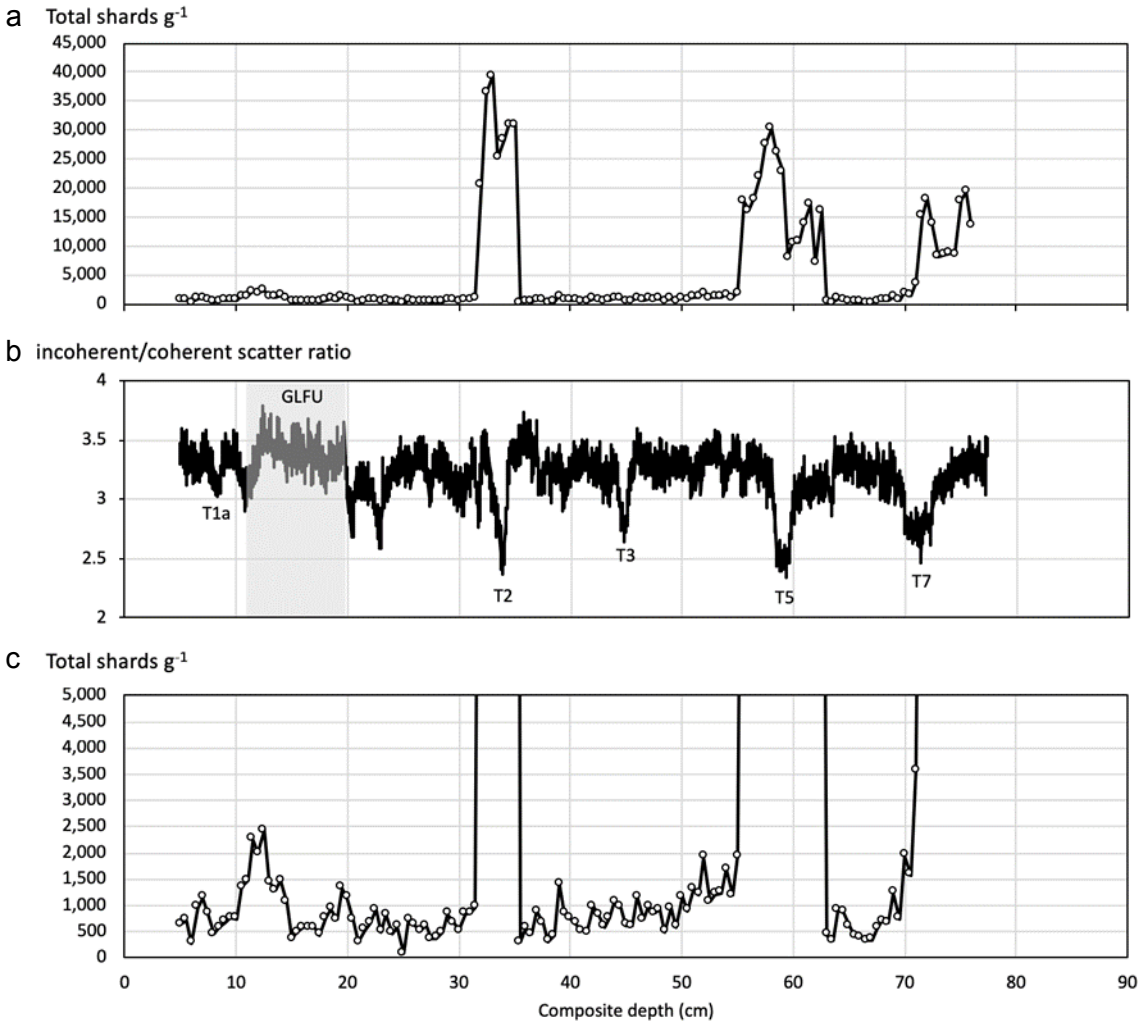

Supplementary Figure 4 a. Summary tephra shard count data undertaken at 0.5 cm intervals for the 77 cm long Kiteschee Lake composite core compared to **b.** The incoherent/coherent ratio µ-XRF data measured contiguously at 200 µm intervals. The inc./coh. ratio is widely used as a proxy for changes in organic content and airfall tephra should, in theory, have zero organic content. Hence, inc./coh. minima should provide the most precise position of the tephra deposition in the Kiteschee Lake record. c. Total shard counts between 0–5,000 shards per gram to demonstrating the near-continuous nature of background tephra deposition in the Kiteschee Lake core.

Supplementary Figure 5 (overpage) a., b. Summary lithostratigraphic log, total shard count, magnetic susceptibility, inc./coh., Fe/inc.+coh., Ti/inc.+coh. and Ca/inc.+coh. profiles for the Kiteschee Lake record. In a., the purple stars indicate peaks in tephra, while glass shards separated and analysed by electron probe microanalysis (EPMA) for samples marked by red stars. The black star at 61 cm could be an early-eruption phase also responsible for the 58-59 cm peak (red star). The most prominent visible tephra layers identified in the field are marked in the stratigraphic log by black lines. No data is available for the moss layer (0-5 cm).

a

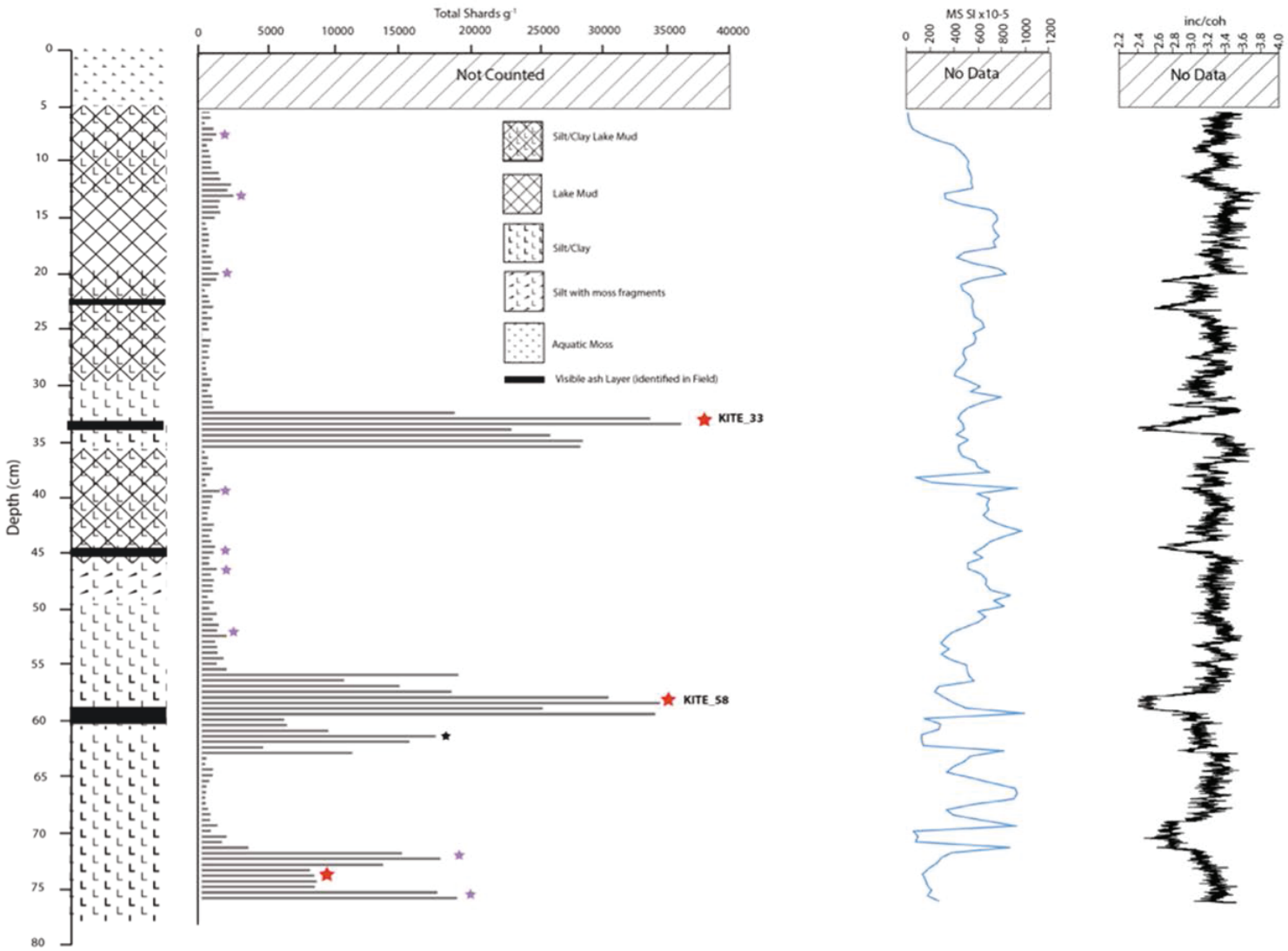
Total Shards g-1
0
5000
10000
15000
20000
25000
30000
35000
40000
Not Counted
MS SI x10-5
0
200
400
600
800
1000
1200
No Data
inc/coh
2.2
2.4
2.6
2.8
3.0
3.2
3.4
3.6
3.8
4.0
No Data
Depth (cm)
0
5
10
15
20
25
30
35
40
45
50
55
60
65
70
75
80
Silt/Clay Lake Mud
Lake Mud
Silt/Clay
Silt with moss fragments
Aquatic Moss
Visible ash Layer (identified in Field)
KITE_33
KITE_58

b

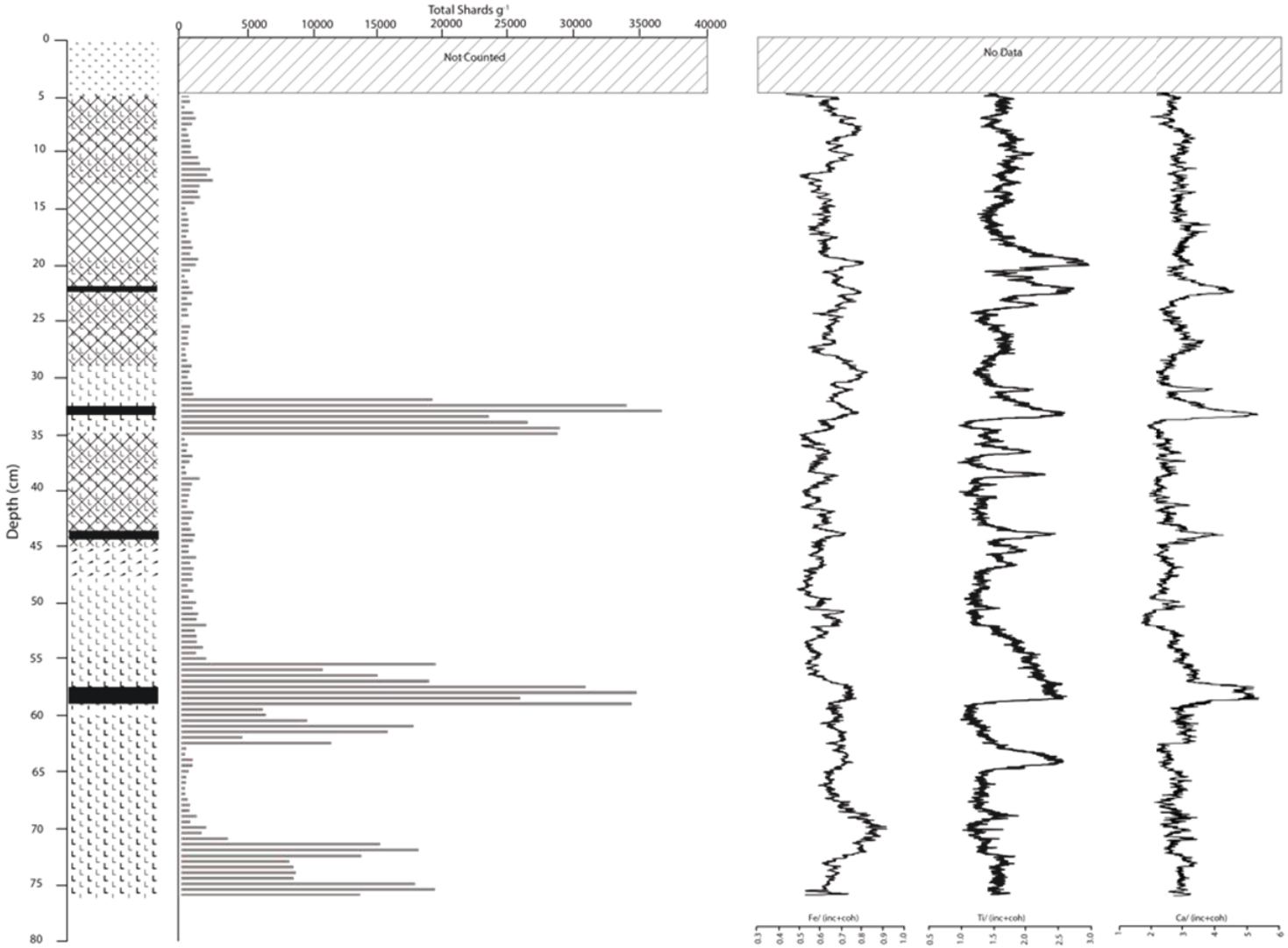
Total Shards g-1
0
5000
10000
15000
20000
25000
30000
35000
40000
Not Counted
No Data
Depth (cm)
0
5
10
15
20
25
30
35
40
45
50
55
60
65
70
75
80
Fe/ (inc+coh)
Ti/ (inc+coh)
Ca/ (inc+coh)

.

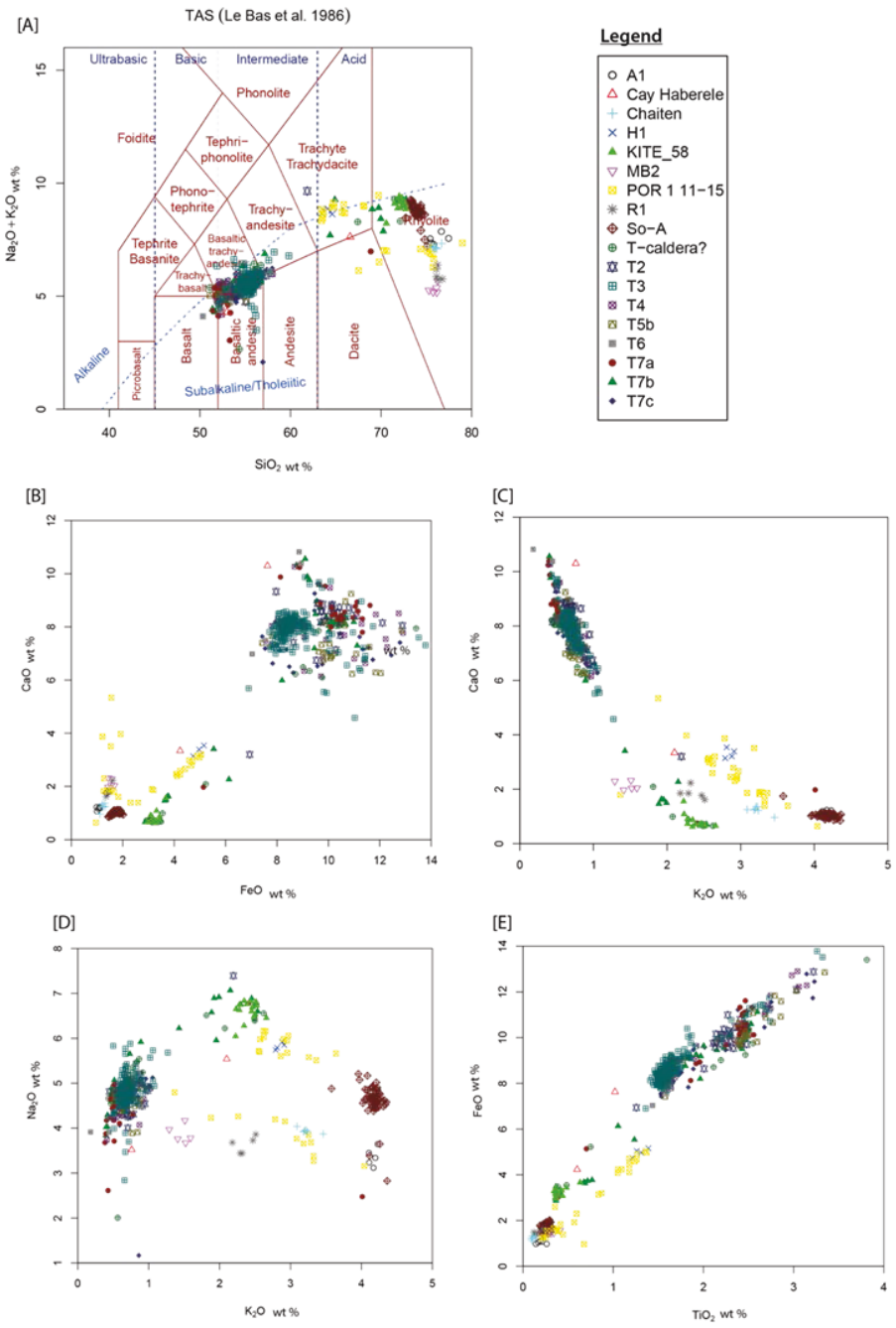

Supplementary Figure 6 a. Total-Alkali-Silica (TAS) plot (Le Bas et al., 1986) and key element bi-plots **b.** and **c.** CaO/FeO, **d.** Na_2O/K_2O, **e.** FeO/TiO_2 of glass shards from the exclusively rhyolitic tephra layer KITE_58 at 58 cm in the Kiteschee Lake record (green triangles) compared to similarly-analysed glass shard geochemical data from Holocene-age rhyolite-forming eruptions from South America (A1, Cay Haberele, Chaiten, H1, MB2, PO1 11-15, R1, So-A) compiled by Fontijn et al. (2014) and Deception Island (T-caldera, T2, T3, T4, T5b, T6, T7a-c) compiled and defined in Roberts et al. (2017).

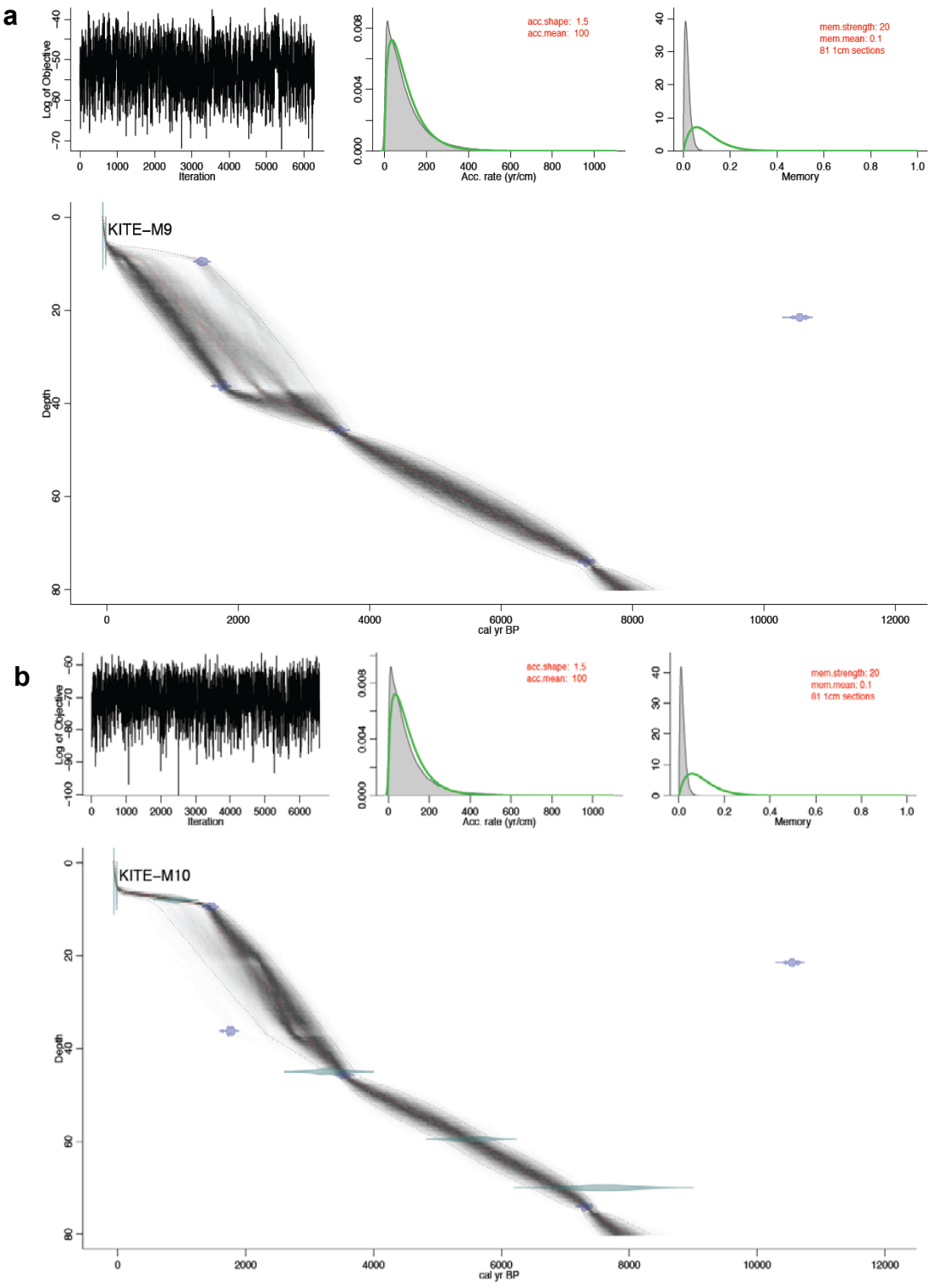

Supplementary Figure 7 Age-depth models used to construct a chronology for the Kiteschee Lake record. **a.** KITE-M9 run with radiocarbon age data only. **b.** KITE-M10 run with radiocarbon and M9 ages for key tephra layers T1b, T3, T5 and T7 as defined in Roberts et al. (2017). In b., the light blue probability ranges represent the most likely published tephra ages.

C-14 Lab. ID	C-14 input age *Calibrated age	Age error	Depth (cm)
501582	-60	1	0.25
T1967	**17***	**3**	**5**
T1a	**910***	**100**	**8**
504801	1600	30	9.5
497408	9380	30	21.5
501584	1860	30	36.25
T3	**3300***	**200**	**45**
501585	3350	30	45.75
T5	**5530***	**200**	**59.5**
T7	**7600***	**400**	**70**
498331	6410	30	74

Supplementary Table 2 Data input for KITE-M10 age-depth model showing calibrated ages for tephra layers from Roberts et al. (2017) included.

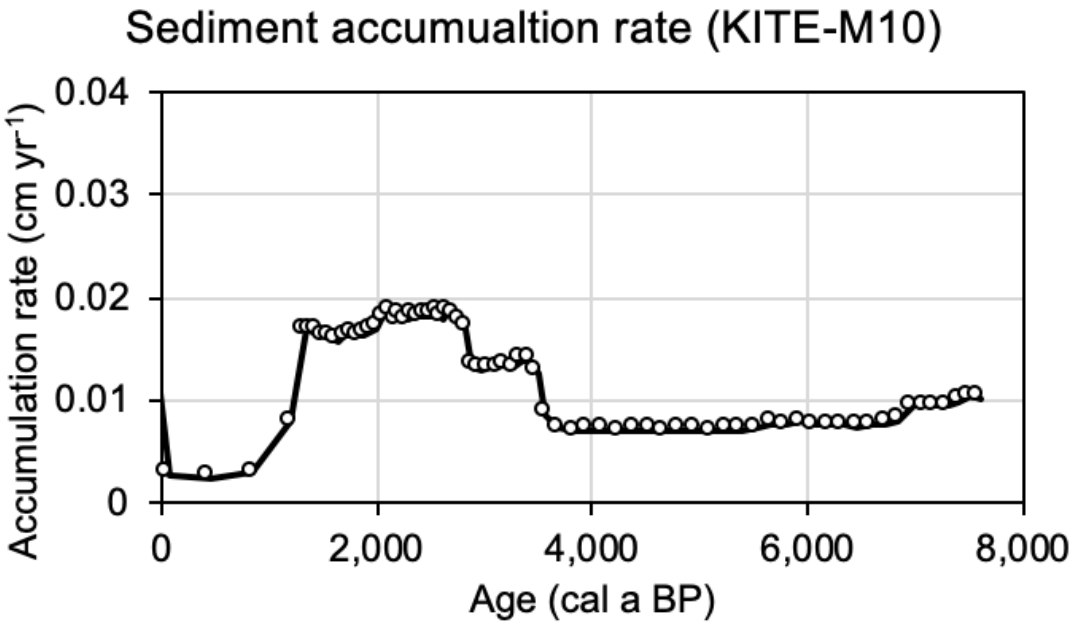

Supplementary Figure 8 Changes in sediment accumulation rate in the Kiteschee Lake record, based on age-depth model KITE-M10. The highest sedimentation rates correspond to the locally-warmest part of the late Holocene in the nearby Yanou Lake GDGT temperature record from c. 3,500 cal a BP and the subsequent downturn into the 'Neoglacial' at c. 2,000 cal a BP until c. 1,400 cal a BP.

Diatoms: We examined the diatom composition of the uppermost 47 cm of the Kiteschee Lake record, focusing in detail on the uppermost 33.5 cm (Diatom Zones 1–3) where diatom preservation was sufficient high enable meaningful environmental interpretation. We used the high resolution DCCA Axis 1 and indicator species to investigate diatom response to late Holocene climate, where higher values in the DCCA Axis 1 represent warmer lake temperatures (Supplementary Figure 9).

The diatom community from 47 cm upwards (c. 3,300 cal a BP) was initially characterised by epipelic, aerophilic species associated with mosses (Zones 1–2; 41.5–33.5 cm depth), indicative of generally warmer conditions between c. 3,200 and 2,700 cal a BP and low diatom accumulation rates, and high β-diversity, suggesting (re)establishment of an increasingly diverse diatom flora following an environmental disturbance (e.g., climatic downturn or volcanic impact on the lake ecosystem). Zone 2 and 3 are characterised by a decline and then increase of epiphytic species, with distinct peaks in aerophilic species. Zone 3 culminates in a shift to episanmic species, with significant increases in the diatom accumulation rate and declining β-diversity (Supplementary Figure 9).

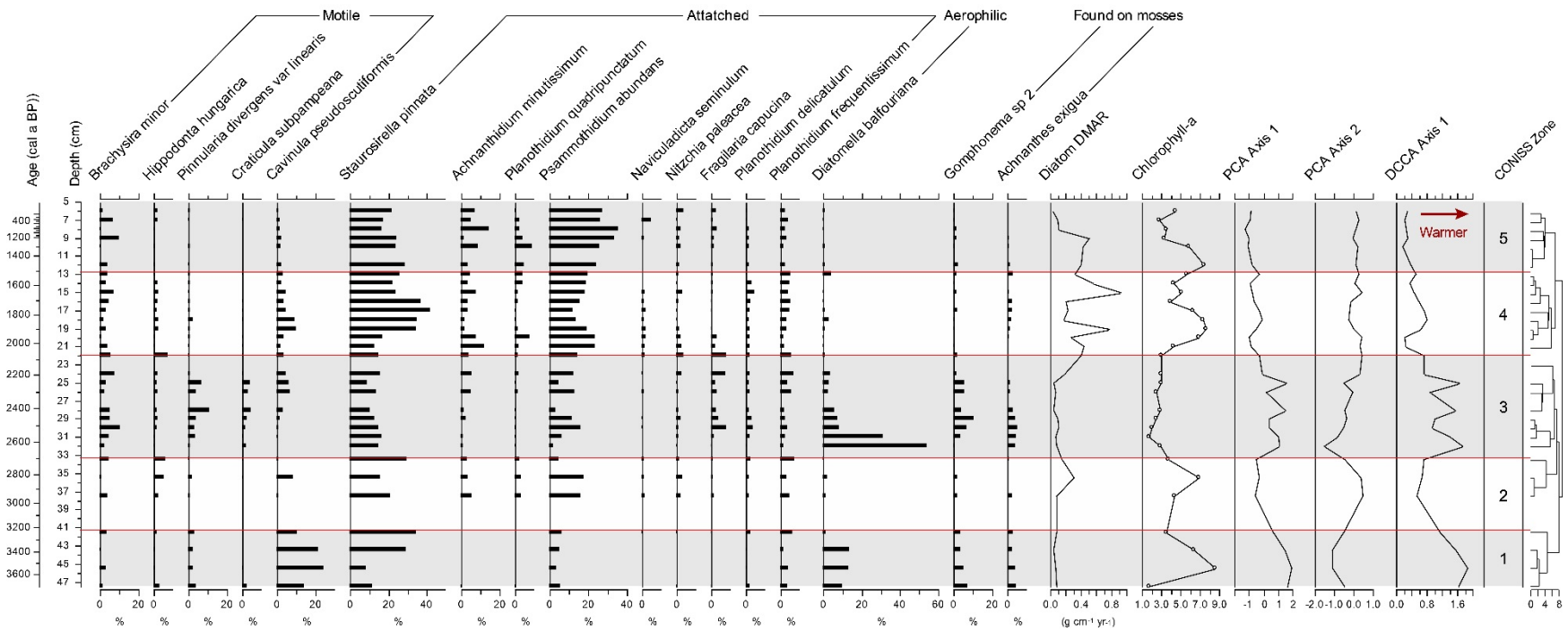

Supplementary Figure 9 Down-core variations in relative abundances (%) of the most abundant diatom species in the Kiteschee Lake record. The diatom concentration, reconstructed chlorophyll-a (from WA inverse transfer function), PCA axis 1 and 2 and DCCA Axis 1 (higher values are warmer temperatures) scores are also plotted. Five zones shaded were initially identified visually, and broadly match with CONISS cluster zones shaded in grey (sum of squares). Zone 1 = 41.5–47 cm, upper boundary weighted mean modelled BACON age (KITE-M10) of 3,230 cal a BP [min.–max. 95% confidence range: 2,870–3,520 cal a BP]; Zone 2 = 33.5–41.5 cm, 2,700 cal a BP [2,120–3,090 cal a BP]; Zone 3 = 22–33.5 cm 2,060 cal a BP [1,400–2,460 cal a BP]; Zone 4 = 13–22 cm (glaciogenic sediments), 1,510 cal a BP [850–1,850 cal a BP]; Zone 5 = 5–13 cm, weighted mean age -20 cal a BP [-33– -3 cal a BP].

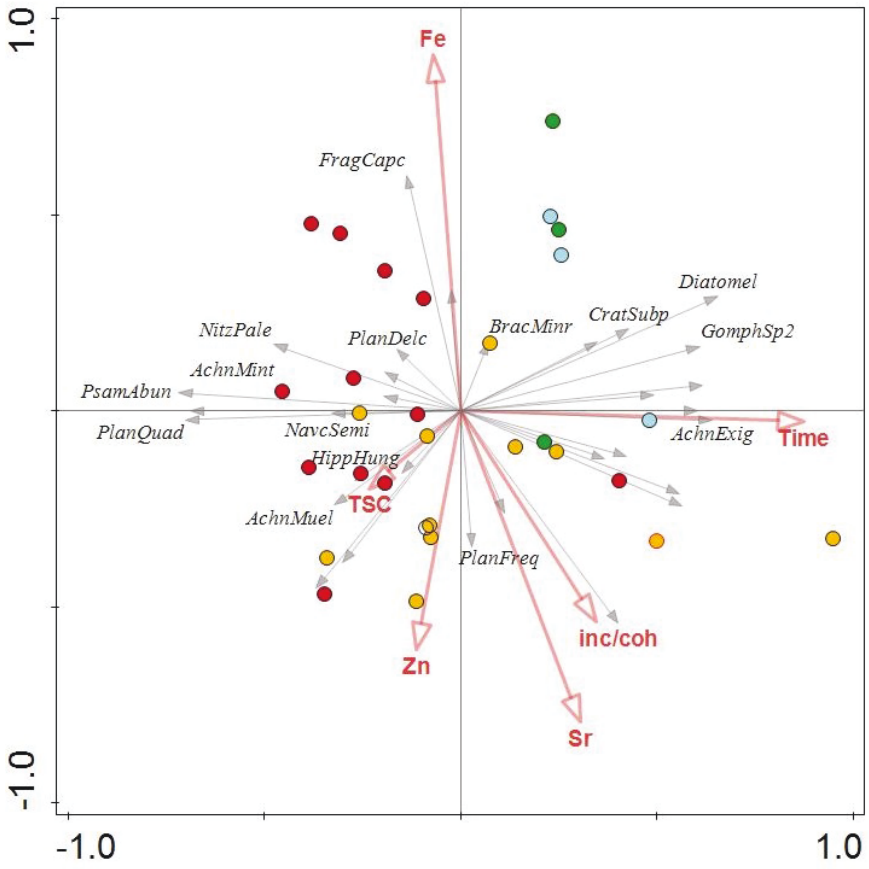

Supplementary Figure 10 RDA ordination using depth, inc./coh. (incoherent/coherent ratio, a proxy for changes in sediment organic and/or water content), Zn, Fe, Sr and Tephra shard counts (TSC) as explanatory variables (red arrows). Species are displayed (arrows) and samples (symbols) split using TWINSPAN groups. Highlighted species arrows are the most abundant (>2%).

Environmental Variable	Time	Sr	Fe	Ca	K	Ti	Inc/Coh	Zn	Clay	Sand	Silt	Tephra counts/g
Eigen value	0.2054	0.0830	0.0602	0.0356	0.0643	0.0404	0.0591	0.0565	0.0445	0.0428	0.0387	0.0270
Explained variation	20.54	8.30	6.02	3.56	6.43	4.04	5.91	5.72	4.45	4.28	3.87	2.70
p value	0.002	0.024	0.088	0.374	0.068	0.286	0.128	0.096	0.4673	0.256	0.33	0.596

Supplementary Table 3 Summary variance for geochemical, grain size and tephra variables (with p-value significance) in explaining diatom assemblage variations down-core. Significant variables ($p<0.05$) are highlighted in grey.

RDA axes	1	2	3	4
Eigenvalue	0.2670	0.7088	0.0369	0.0278
Explained variation (cumulative)	26.70	34.58	38.28	41.05
Pseudo-canonical correlation	0.8417	0.7980	0.6929	0.7682
Explained variance of species-env relationship	60.92	78.91	87.34	93.67

Supplementary Table 4 Summary of output table from RDA using environmental variables (depth, inc./coh., TSC, Fe, Sr, Zn) to determine drivers of variation in diatom assemblages.

Overall, shorter term changes in diatom communities are superimposed upon the slow and steady evolution of the lake, probably reflecting climate variations (e.g. changing wind speed, temperature and precipitation) and ice expansion and/or increased (glacial) erosion. Changes in the diatom accumulation rate, reconstructed chlorophyll-a, variations in key indicator species and grain size can therefore be used to examine the impact of (climate-driven) glacier readvances into or around the mid-southern foreland area. We interpret the climatic conditions in Diatom Zones 3–5 as follows:

Diatom Zone 3 (33.5–22 cm; weighted mean age range of 2,700–2,060 cal a BP): Late Holocene warm phase (latter part of Mid Holocene Hypsithermal (MHH) in Figure 5i as defined in Bentley et al. (2009). Although diatoms usually reflect water chemistry rather than temperature, deglaciation and warming can have a significant impact on nutrient supply to lakes and diatom compositional turnover (β-diversity) (Spaulding et al., 2010). In the Arctic, recent warming corresponds closely to a regional increase in β-diversity (DCCA axis 1) observed in high latitude lakes over the 20th century (Hobbs et al., 2010). Similarly, recent shifts in primary productivity and an increase in β-diversity have been linked to recent warming in the Marguerite Bay region, Antarctica (Hodgson et al., 2013). In Kiteschee Lake, β-diversity is highest in this zone, likely driven by the appearance of new species in higher abundances (e.g., *C. pseudoscutiformis*, *C. subpampeana* and *P. divergens var linearis*) after a prolonged warm phase (Figure 5d, Supplementary Figure 9). Although reconstructed chlorophyll-a values in this zone could reflect cooler conditions, colonisation from new benthic species suggests the establishment of productive diatom communities, more often associated with warmer climates (Björck et al., 1993; Björck et al., 1996).

Diatom Zone 4 (22–13 cm; 2,060–1,510 cal a BP):' Neoglacial' downturn: A significant decline in β-diversity (DCCA axis 1) in Kiteschee Lake is evident in Zone 4 (Supplementary Figure 9). The distinct decline in *D. balfouriana* and *Gomphonema sp.* occurred in the transitions between Zones 3 and 4, and, by c. 2,000 cal a BP, they were almost completely absent. Colder temperatures have been shown to reduce species diversity in the McMurdo Dry Valleys and increase

the abundance of dominant species (Esposito et al., 2008). The coeval decline in *A. exigua*, an epiphytic species found on mosses and indicative of humid soil (Martinez-Macchiavello et al., 1996; Van de Vijver and Beyens, 1997), possibly reflects a reduction in suitable littoral habitats in colder conditions (Sterken et al., 2008). We associate the distinct increase in *P. abundans* and *A. minutissiumum* (up to 20% and 10%) at 20 cm depth (c. 1,950 cal a BP) with low nutrient concentrations (Sterken et al., 2012). Often, these species are found in association with benthic mosses, which have an acidifying influence and have been used as indicators of low productivity and cooler 'Neoglacial' conditions in similar environments along the AP (Björck et al., 1991a; Gibson and Zale, 2006).

The notable increase in the episanmic species *S. pinnata* at 20–21 cm depth, c. 2,000 cal a BP, corresponds with the initiation of glaciogenic sediment input into the lake. This species thrives in turbid and poor-quality water, absorbing nutrients better than its competitors due to their higher surface area to volume ratio (Reynolds, 1984; Michel et al., 2006). It has also been found in recently deglaciated areas, suggesting it can colonize harsh environments (Haworth, 1976). In Kiteschee Lake, its presence is most likely indicative of particularly nutrient-poor, turbid conditions that occurred during colder 'Neoglacial' conditions. This clear change in sedimentology and species assemblage also coincides with a decline in epipelic species (*H. hungarica*, *P. divergens var linearis*, *C. subpampeana*), which favour calmer lake conditions and are typically associated with 'warmer' climatic conditions.

Diatom Zone 5.1 (13–5 cm; 1,150 cal a BP – 1969 CE): Continued Neoglacial cold phase (including SH-LIA cold phase, c. 1,300–1870 CE, with no significant MCA warming): *S. pinnata* dominate the diatom assemblage (>40%) from their peak at 17 cm depth, c. 1,760 cal a BP until the glaciogenic lithofacies unit transitions back to an orange-brown silt-dominated matrix at c. 11–9 cm depth, 1,480–1,300 cal a BP (modelled age). Sample Beta-504801 at 9–10 cm has a median calibrated age of 1,450±80 cal a BP. Overall, the lake conditions favoured 'colder' species, likely reflecting extended periods of snow, ice and lake-ice cover. Under complete ice cover, wind induced mixing of the water column cannot occur and turbulence is reduced significantly, leading to perennial in-lake stratification (Spaulding et al., 2010). The latter is reflected in the renewed appearance of fine-scale laminations of this zone. A lack of turbulence would have meant that dense-silica walled, motile diatoms could no longer remain in suspension (Wharton et al., 1993) and led to a gradual decline of this species in the Kiteschee Lake record.

The diatom-based DCCA Axis 1 profile and the Yanou Lake reconstructed GDGT-temperature (Figure 4d, e) show no significant recovery in climatic conditions until (c. 5–6 cm depth (mid-C20th), when a significant shift to an aquatic moss (*Drepanocladus longifolius* (*Mitt. Paris)* sp.) dominated environment occurred. A post-bomb radiocarbon age from the moss means that this transition occurred after c. 1950 CE (1969–70 CE from age-depth modelling KITE-M10; Supplementary

Figure 7b). We associate this shift with the Recent Rapid Warming (RRR) on the AP as defined by Bentley et al. (2009) (Supplementary Figure 2b).

Whilst the most abundant fossilised diatom species in Kiteschee Lake are well represented in the chlorophyll-a training set (89.4%), some key species (e.g., *D. balfouriana, C. pseudoscutiformis, A. muelleri*) are not present. This may result in an unreliable reconstruction, particularly in the lower zones where *D. balfouriana* dominates. Furthermore, the training set has a strong correlation between chlorophyll-a and species abundance, meaning other factors may determine the composition of benthic algae. These include light regime, substrate availability, temperature and competition from other algae (Oppenheim and Ellis-Evans, 1989; Jones and Juggins, 1995). Hence, we make no inferences about changes in chlorophyll-a in Kiteschee Lake from our diatom dataset.

Supplementary Note 3: GDGT-Temperature re-evaluation

To provide a local atmospheric climate comparison with new data in this study, we updated the Yanou Lake reconstructed glycerol dialkyl glycerol tetraethers, GDGT, biomarker-based palaeotemperature (YAN-GDGT) dataset with two new GDGT calibration outputs described below. GDGTs were extracted and analysed from Yanou Lake sediments as described in Foster et al. (2016) and Roberts et al. (2017). The YAN-GDGT dataset was previously calibrated using the Foster et al. (2016) Antarctic lake calibration (grey plot, with RMSE errors of 1.45 °C shaded grey in Figure 4e) Reconstructed GDGT temperatures reflect mean summer (December, January, February or DJF) air temperatures (MSAT) in the shallow and well-mixed open lake water environment of Yanou Lake.

Applying the original Foster et al. (2016) calibration resulted in a mean ± 1σ 6–0 ka reconstructed YAN-GDGT <10 °C dataset weighted mean MSAT value of +2.39 ± 2.67 °C [95% confidence interval: 1.52– 3.25 °C] (Bootstrapping, n=10,000, +2.38 ± 2.61 °C [1.52– 3.25 °C]; 5th/95th percentile = -0.51/+7.96 °C; weighted by Antarctic Foster et al. (2016) GDGT calibration dataset RMSE value of 1.45 °C) is higher than the modern-day observational mean summer (DJF) temperature from Bellingshausen Research Station on Fildes Peninsula of +1.09 ± 0.56 °C, but encompasses its 2σ 95% measured range of -0.03 to 2.21 °C (n=48, 1968–2015 CE) (Marshall, pers. comm.; SCAR-READER database: http://www.antarctica.ac.uk/met/READER/). For the whole YAN-GDGT dataset, two outliers greater than the whole dataset 95th percentile (<-0.33 °C and >8.61 °C) of 11.34 °C and 13.84 °C at 1,164 and 3,135 cal a BP were identified. All reconstructed GDGT temperatures were greater than the -2.2 °C minimum limit of the ANT-GDGT calibration dataset, but these two outliers are also greater than the 10.3 °C maximum limit of the Foster et al. (2016) surface-MSAT calibration dataset (solid black horizontal line in Figure 4e).

Roberts et al. (2017) provided the following environmental explanation for elevated mid-late Holocene MSAT in the Yanou Lake record: ‘At the local, small lake scale, water temperature might decouple from observed mean summer air temperature

due to factors such as the thickness and length of seasonal lake ice-cover and the volume of meltwater input, both of which suppress lake water temperatures. Conversely, since water bodies store excess heat generated during extended ice-free seasons, small and/or shallow lakes (<10 m deep) reach temperatures of 6 °C or more (e.g., Sombre Lake, Signy Island ; Ellis-Evans and Lemon, 1989).

As a follow-up to that study, we examined whether the existing GDGT lake calibrations themselves could be the cause temperature overestimates. While the Foster et al. (2016) calibration is particularly good at reproducing observational summer temperatures on Fildes Peninsula (since c. 1968 CE) and on South Georgia (since c. 190 CE), it lacks data in the c. 8–15 °C MSAT range (n=2 of 32 samples). In the Yanou Lake record, there is a significant increase the proportion of the GDGT-IIIb compound prior to c. 1,000 cal a BP (Foster et al., 2016; Roberts et al., 2017). Since the factor used to amplify this compound is large (362xGDGTIIIb), we examined whether inclusion of this compound alone could be leading to higher-than-had-been-expected reconstructed GDGT-MSAT temperatures for the mid-late Holocene. In contrast, the Pearson et al. (2011) global lake calibration, which does not contain the GDGT-IIIb compound in its calibration equation, does not reproduce observational MSAT on Fildes Peninsula or South Georgia, and has limited variability throughout the Holocene when applied to Antarctic lake records. Our initial investigation showed this was most likely due to the lack of sufficient 'cold' (i.e., <4 °C) MSAT datapoints in its calibration dataset (n=4 of 85) (Foster et al., 2016).

Since publication, we have been continually assessing and improving the ability of the Foster et al. (2016) Antarctic and the Pearson et al. (2011) Global lake GDGT calibrations produce reliable palaeotemperature data from Antarctic lake sediments. Here, we present initial findings from data-based experiments that are particularly relevant to the aims of this study.

In the first experiment, we tested whether the lack of data at key temperature points and ranges in both calibrations was leading to significant temperature overestimates in mid Holocene parts of both test records (Yanou Lake, Fildes Peninsula and Fan Lake, South Georgia). To improve both calibrations, we combined the Pearson et al. (2011) and Foster et al. (2016) calibration datasets (n=85+32) and re-ran the same set of regression analyses described in Foster et al. (2016) on the combined dataset (n=117). We compared the original regression outputs for both calibrations with outputs newly derived regression equations (Figure 11a) and then applied two new calibration regression equations based on compound used in the original calibrations to reconstruct new palaeotemperature data the Yanou Lake record.

Results show a general improvement in R^2 values. However, the original Foster et al. (2016) calibration performed poorly (R^2=0.62) compared and especially poorly at higher temperatures, possibly due to the inclusion of the large GDGTIIIb factor. After recalibration, both the new Foster et al. (2016) + Pearson et al. (2011) Antarctic + Global (A+G) regressions both obtained R^2 values >0.84, with the new

Foster et al. (2016) recalibration performing better than all other regressions (R^2=0.87) (Supplementary Figure 11b). Both new recalibrations reproduced modern-day measured MSAT at Yanou Lake (and on South Georgia) well and both produced similar mid-late Holocene reconstructed GDGT-MSAT profiles for the Yanou Lake 6-0 ka record (Supplementary Figure 11b).

Overall, our initial re-evaluation suggests that the lack of data in key parts of both the original Foster et al. (2016) and Pearson et al. (2011) calibrations are more significant issues than the inclusion of the GDGTIIIb in the Foster et al. (2016) calibration. The generally lower mid–late Holocene temperatures and reduced variability produced the new combined dataset calibrations are probably more realistic than reconstructed GDGT-MSAT of the Foster et al. (2016) calibration for Yanou Lake (Figure 11b) (cf. Roberts et al., 2018).

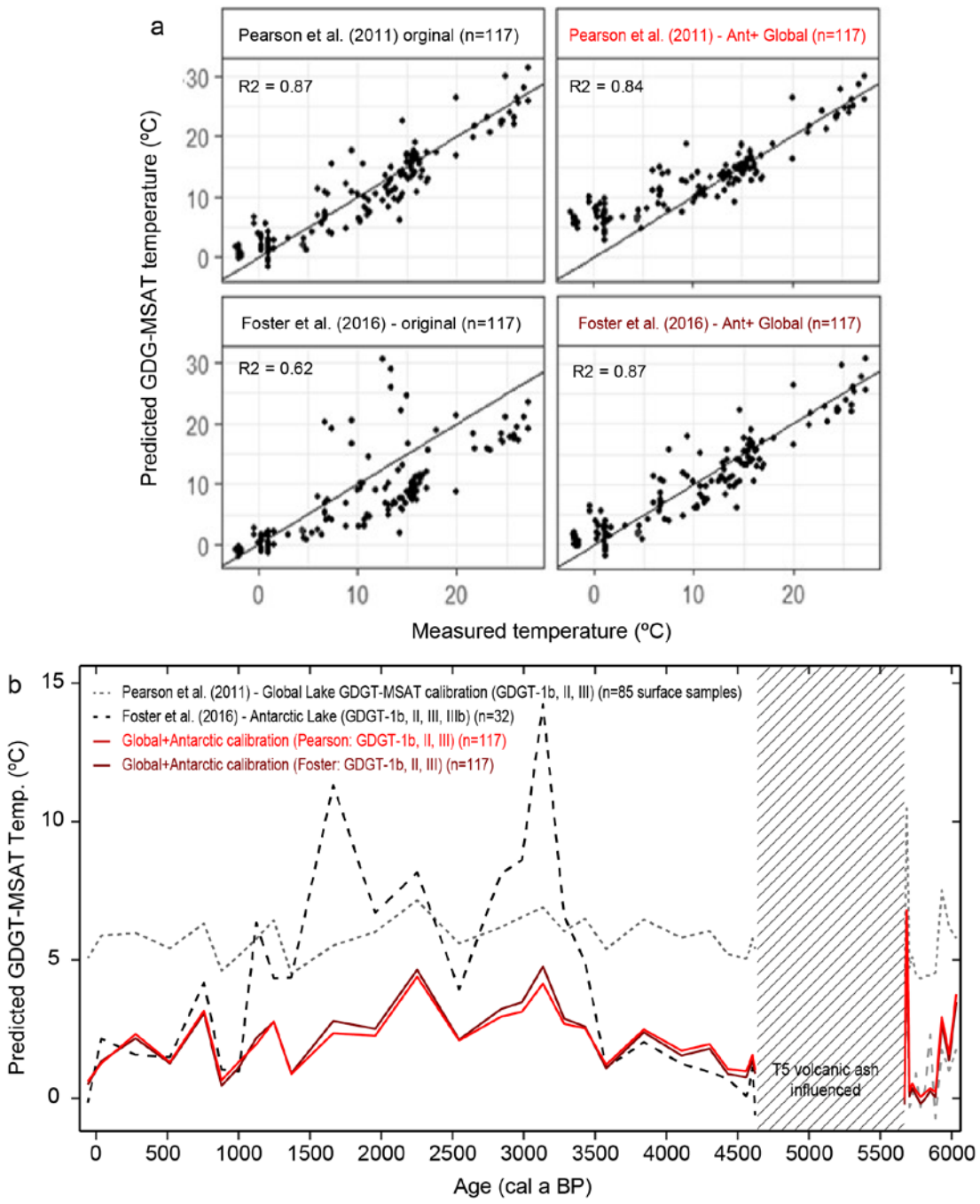

Supplementary Figure 11 a. Regression data examining the effect of combining the Foster et al. (2016) Antarctic GDGT calibration dataset with the Pearson et al. (2011) global calibration GDGT dataset and re-running the calibration. Errors are not shown for clarity but are between 1–2 °C. **b.** Comparison of the Yanou Lake Glycerol Dialkyl Glycerol Tetraether (GDGT) Mean Summer Annual Temperature (MSAT) reconstruction for the mid–late Holocene based on the Foster et al. (2016) calibration and originally presented in Hua et al. (2013) and new GDGT-MSAT reconstructions based on the new combined Antarctic + Global calibration (this study).

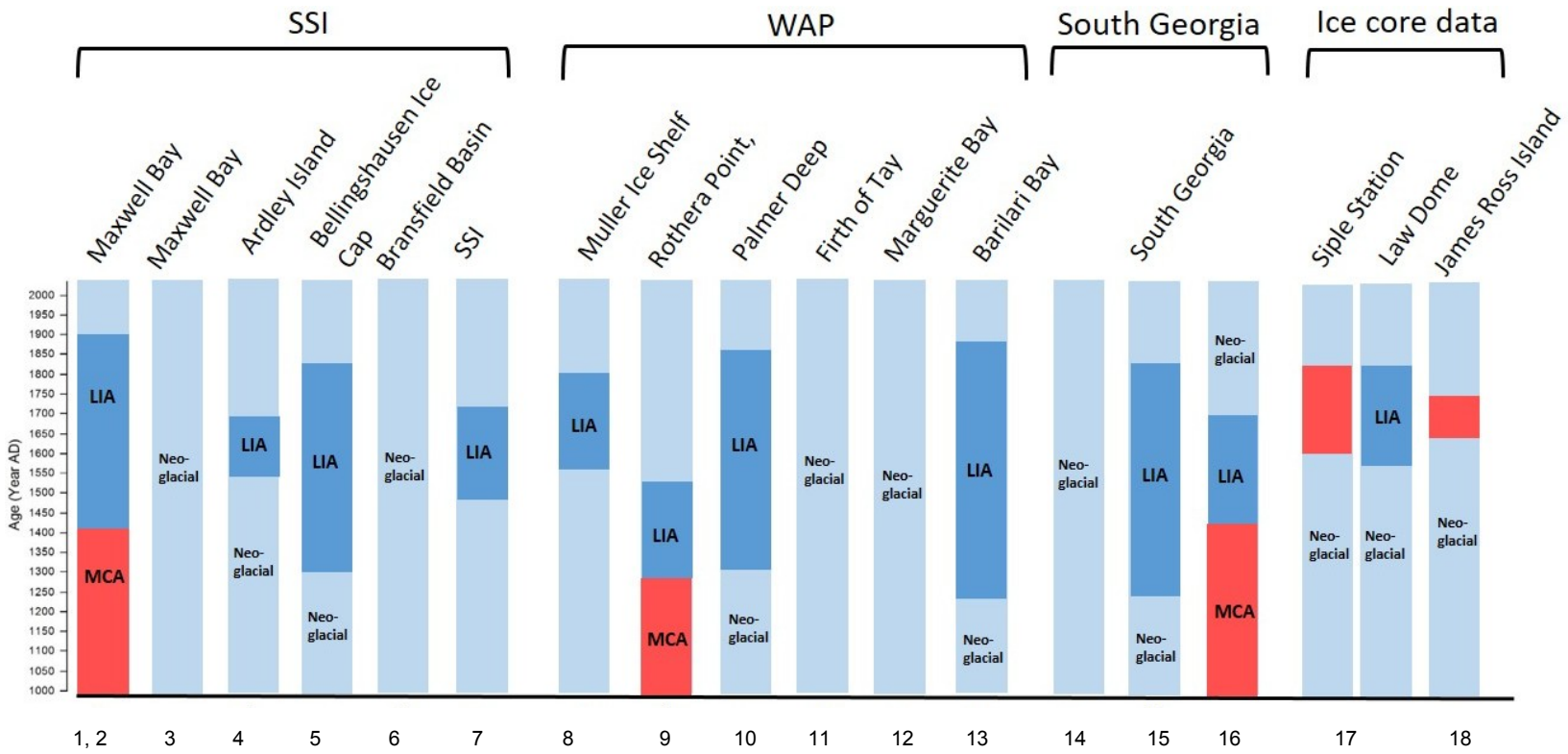

Supplementary Figure 12 Summary of climate change between 1000 and 2000 CE from selected ice core data, marine, lake and terrestrial sediments from the South Shetland Islands (SSI), Western Antarctic Peninsula (WAP), South Georgia and ice core records from Antarctica. MCA is the Medieval Climate Anomaly, LIA is the 'Little Ice Age'. Reference numbers are shown at the base. 1: Monien et al. (2011); 2: Hass et al. (2010); 3: Milliken et al. (2009); 4: Liu et al. (2005); 5: Hall (2007); 6: Heroy et al. (2008); 7: Simms et al. (2012); 8: Domack et al. (1995); 9: Guglielmin et al. (2016); 10: Domack et al. (2001); 11: Leventer et al. (1996); 12:: Hodgson et al. (2013); 13: Christ et al. (2015); 14: Bertler et a. (2011);15: Clapperton et al. (1988); 16: Mosley-Thompson et al. (1990); 17: Van der Bilt et al. (2017); 18: Mulvaney et al. (2012).

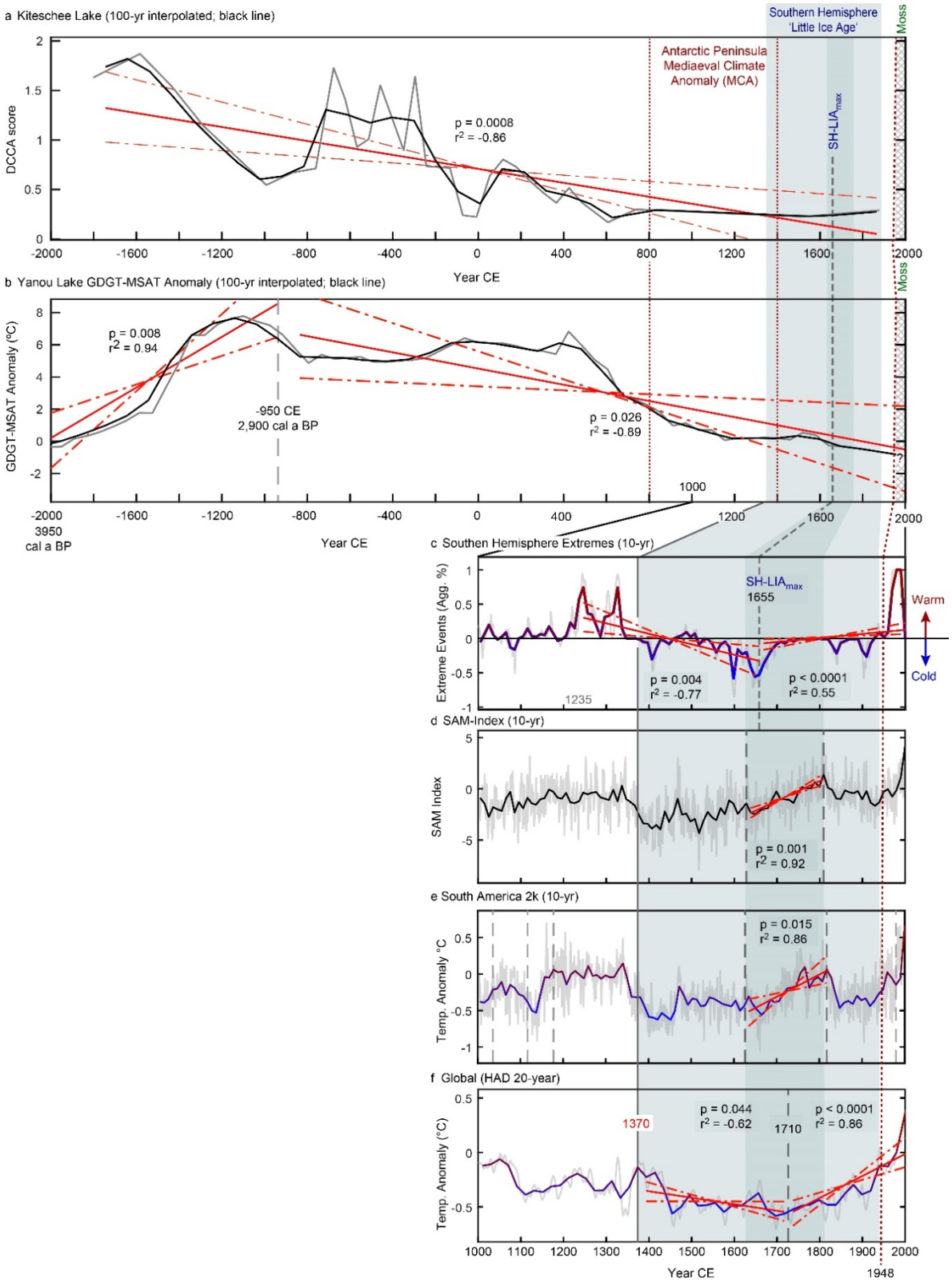

Supplementary Figure 13 caption overpage

Supplementary Figure 13 Summary results Sequential Mann-Kendall (SMKT) change in trend time series analysis with a correction applied for serial autocorrelation to the following datasets: **a.** Kiteschee Lake DCCA Axis 1 score. **b.** Yanou Lake palaeotemperature anomaly (relative to the pre-industrial 1,000-250 cal a BP mean) . **c.** Southern Hemisphere extreme events (Neukom et al., 2014) **d.** the Southern Annular Mode (SAM)-index (Abram et al., 2014 and 2016). **e.** PAGES 2k South America temperature anomaly (pre-industrial anomaly, as defined for Yanou Lake) (PAGES2k Consortium, 2013). **f.** The global HAD 20-yr temperature reconstruction (Mann et al., 2009). Only data from 4,000-0 cal a BP were included; data were interpolated into equally-spaced 100-year intervals to allow SMKT analysis to run. SMKT trend change points detected are shown as dashed grey lines with age (cal a BP). Solid red lines are linear trends that statistically significant at the $p \leq 0.05$ level, with 95% confidence intervals shown as dashed red lines.

CHAPTER 5: CONCLUSIONS AND OUTLOOK

The aim of this study was to reconstruct the post-LGM deglaciation history of on-shore ice-free areas around Maxwell Bay, King George Island, NW Antarctic Peninsula. In order to fulfill the aim of the thesis, I used an integrated approach combining cosmogenic exposure and radiocarbon dating, stratigraphy, with geomorphological mapping and GPR investigations.

I propose a new minimum age of 7.8 ka cal BP for the onset of the deglaciation in Potter Peninsula, instead of an earlier accepted age of 9.5 ka cal BP, based on a more detailed chronology and deeper excavation of the new Pingfo II profile. I further propose a glacier re-advance after 7.5 ka cal BP, likely between 7.2 and 7.0 ka cal BP, reaching the mouth of Potter Cove. It is likely linked with a glacier re-advance or still-stand documented elsewhere on South Shetland Islands at about 7 ka cal BP. Nevertheless, climatic drivers associated with these glacial re-advances remain unclear. Following the re-advance, during the mid-Holocene, the glacier front retreated to a position similar to the present one. As result of the glacier re-advance, modern vegetated glacial deposits were formed. On Fildes Peninsula, its NW ~40-35 m a.m.s.l marine platform was completely ice-free after 7.0 ka cal BP, and an ice cap configuration similar to the present day existed by c. 6.0 ka cal BP. In contrast to the findings in Potter Peninsula, I found no evidence for a mid-Holocene glacier advance on Fildes Peninsula.

At 1.8-1.7 ka cal BP in Potter Peninsula, a climatic optimum was reached with similar glacier limits compared to 6 decades ago or even as today. This warm period ended with the last glacier re-advance between 0.5 and 0.3 ka cal BP. Integrating, these findings suggest that the ice repeatedly occupied Potter Cove and also the peninsula throughout the Holocene. They further indicate that the present state of reduced ice in the study area is not unprecedented. The presence of mosses within till into the of the Shetland I moraine on Fildes Peninsula suggest that the Bellingshausen Ice Cap extended landward of its present position c.1.9-1.3 ka cal BP. Sometime after 1.3 ka cal BP, most likely between 0.5-0.1 ka cal ago, a further minor glacier readvance translocated mosses and mid-Holocene marine sediments into the moraines surrounding the present day Bellingshausen Ice Cap, coinciding with the findings in Potter Peninsula. This advance is linked to reductions in summer/annual insolation coupled with a shift to more intense Southern Hemisphere westerly winds in the Southern Ocean. Stronger, and possibly more poleward-shifted southern westerly winds produced more precipitation-laden storm fronts passing over the South Shetland Islands and thus, increased ice accumulation.

Progradation of Holocene polar gravel spits in the South Shetland Islands as exemplarily observed in the Potter Cove spit system, is bound to phases of comparable low rates of glacio isostatic uplift and a resulting stable relative sea level. The morphology of the Potter Cove spit system, with an active cliff and two terrace levels connected by a steep slope with superimposed amalgamated beach ridges, is seen to archive an abrupt increase in the rate of local glacio-isostatic uplift and an associated accelerated fall of relative sea level in a clear reaction to deglaciation after the last glacial (LIA equivalent) re-advance. Those findings introduce a concept which shows that genesis and resulting morphology of polar gravel spits could reflect past short-term changes in the rate of glacio-isostatic adjustment. Moreover, this concept also bears implications for the expected future development of similar beach systems in King George Island and elsewhere in comparable settings.

Overall, my results suggest that the Holocene glacial history of Potter Peninsula has been more variable than previously known, having implications for calibrating local and regional ice sheet models. Furthermore, the maximum mid-late Holocene (last) readvance found in Potter Peninsula and Fildes Peninsula occurred following well-defined regional 'Neoglacial' climatic downturn. In terms of glacio-isostatic adjustment, my data supports both, a more restricted ice-loading scenario for the late Holocene as suggested by most GIA models, and also other GIA models suggesting a greater ice-loading elsewhere on the South Shetland Islands during the Holocene.

Outlook

Although the results presented in this study enabled a more detailed view of the Holocene history of the northern Antarctic Peninsula, there are still open questions, leaving space for further investigations:

-The obtained dates of my pilot study with ^{3}He exposure dating on basaltic boulders in the Three Brothers Hill moraine system ridges show very scattered values, presumably due to nuclide inheritance. However, a more detailed and comprehensive chronology could unravel the age of deposition of these moraines, the oldest one preserved in Potter Peninsula.

-To ensure the age of the last glacier re-advance in the region and further possible `Neoglacials´, a comprehensive surface exposure dating of polished basaltic blocks present in moraine ridges surrounding the Warszawa Glacier in Potter Peninsula and the Bellingshausen Ice Cap in Fildes Peninsula is needed. Surface exposure dating is particularly useful in Antarctica, where few exposures with organic remains make radiocarbon dating difficult.

-More GPR studies on spit systems from South Shetland Islands could further validate the role of a last glacier re-advance in the region and the subsequent deglaciation as the main drivers of gravel spit genesis and morphology in such settings. Moreover, data about sediment supply and an analysis in terms of source-transport-sink system could establish a new sedimentary model on the genesis of polar gravel spits.

REFERENCES

Abram NJ, McGregor HV, Tierney JE, Evans MN, McKay NP, Kaufman DS, the PkC, Thirumalai K, Martrat B, Goosse H, Phipps SJ, Steig EJ, Kilbourne KH, Saenger CP, Zinke J, Leduc G, Addison JA, Mortyn PG, Seidenkrantz M-S, Sicre M-A, Selvaraj K, Filipsson HL, Neukom R, Gergis J, Curran MAJ, Gunten Lv. 2016. Early onset of industrial-era warming across the oceans and continents. Nature 536: 411. DOI: 10.1038/nature19082.

Allard J, Bertin X, Chaumillon E, Pouget F. 2008. Sand spit rhythmic development: A potential record of wave climate variations? Arçay Spit, western coast of France. Marine Geology 253: 107-131. DOI: 10.1016/j.margeo.2008.05.009.

Angiel PJ and Dąbski M. 2012. Lichenometric ages of the Little Ice Age moraines on King George Island and of the last volcanic activity on Penguin Island (West Antarctica). Geografiska Annaler: Series A, Physical Geography 94: 395-412.

Antoniades D, Giralt S, Geyer A, Álvarez-Valero AM, Pla-Rabes S, Granados I, Liu EJ, Toro M, Smellie JL, Oliva M. 2018. The timing and widespread effects of the largest Holocene volcanic eruption in Antarctica. Scientific Reports 8: 17279

Ashton AD, Nienhuis J, Ells K. 2016. On a neck, on a spit: controls on the shape of free spits. Earth Surface Dynamics 4: 193-210. DOI: 10.5194/esurf-4-193-2016.

Balco G, Stone JO, Lifton NA, Dunai TJ. 2008. A complete and easily accessible means of calculating surface exposure ages or erosion rates from 10Be and 26Al measurements. Quaternary Geochronology 3: 174-195. doi:https://doi.org/10.1016/j.quageo.2007.12.001.

Balco G. 2011. Contributions and unrealized potential contributions of cosmogenic-nuclide exposure dating to glacier chronology, 1990–2010. Quaternary Science Reviews 30: 3-27. DOI: 10.1016/j.quascirev.2010.11.003.

Balco G, Schaefer JM. 2013. Exposure-age record of Holocene ice sheet and ice shelf change in the northeast Antarctic Peninsula. Quaternary Science Reviews 59: 101-111. DOI: 10.1016/j.quascirev.2012.10.022.

Ballantyne CK. 2002. Paraglacial geomorphology. Quaternary Science Reviews 21: 1935-2017.

Bañón M, Justel A, Velázquez D, Quesada A. 2013. Regional weather survey on Byers Peninsula, Livingston Island, South Shetland Islands, Antarctica. Antarctic Science 25: 146-156. DOI: 10.1017/S0954102012001046.

Baroni C, Orombelli G. 1991. Holocene raised beaches at Terra Nova Bay, Victoria Land, Antarctica. Quaternary Research 36: 157-177. DOI: 10.1016/0033-5894(91)90023-X.

Barsch D, Mäusbacher R. 1986. New Data on the Relief Development of the South Shetland Islands, Antarctica. *Interdisciplinary Science Reviews* **11**: 211-218, DOI:10.1179/isr.1986.11.2.211.

Battarbee RW, Jones VJ, Flower RJ, Cameron NG, Bennion H, Carvalho L, Juggins S. 2001. Diatoms. In: Smol, J.P., Birks, H.J.B. & Last, W.M. (eds.) Tracking Environmental Change Using Lake Sediments, Volume 3, Terrestrial, Algal, and Siliceous Indicators. Kluwer Academic Publishers, Dordrecht; 155– 202.

Benn DI, Evans DJA. 2010. Glaciers and Glaciation. London: Hodder Education.

Bentley MJ, Hodgson DA, Smith JA, Cox NJ. 2005. Relative sea level curves for the South Shetland Islands and Marguerite Bay, Antarctic Peninsula. Quaternary Science Reviews 24: 1203-1216. DOI: 10.1016/j.quascirev.2004.10.004.

Bentley MJ, Hodgson DA, Smith JA, Cofaigh CÓ, Domack EW, Larter RD, Roberts SJ, Brachfeld S, Leventer A, Hjort C, Hillenbrand C-D, Evans J. 2009. Mechanisms of Holocene palaeoenvironmental change in the Antarctic Peninsula region. The Holocene 19: 51-69. DOI: 10.1177/0959683608096603.

Bentley MJ, Ó Cofaigh C, Anderson JB, Conway H, Davies B, Graham AGC, Hillenbrand C-D, Hodgson DA, Jamieson SSR, Larter RD, Mackintosh A, Smith JA, Verleyen E, Ackert RP, Bart PJ, Berg S, Brunstein D, Canals M, Colhoun EA, Crosta X, Dickens WA, Domack E, Dowdeswell JA, Dunbar R, Ehrmann W, Evans J, Favier V, Fink D, Fogwill CJ, Glasser NF, Gohl K, Golledge NR, Goodwin I, Gore DB, Greenwood SL, Hall BL, Hall K, Hedding DW, Hein AS, Hocking EP, Jakobsson M, Johnson JS, Jomelli V, Jones RS, Klages JP, Kristoffersen Y, Kuhn G, Leventer A, Licht K, Lilly K, Lindow J, Livingstone SJ, Massé G,

McGlone MS, McKay RM, Melles M, Miura H, Mulvaney R, Nel W, Nitsche FO, O'Brien PE, Post AL, Roberts SJ, Saunders KM, Selkirk PM, Simms AR, Spiegel C, Stolldorf TD, Sugden DE, van der Putten N, van Ommen T, Verfaillie D, Vyverman W, Wagner B, White DA, Witus AE, Zwartz D. 2014. A community-based geological reconstruction of Antarctic Ice Sheet deglaciation since the Last Glacial Maximum. Quaternary Science Reviews 100: 1-9. DOI: http://dx.doi.org/10.1016/j.quascirev.2014.06.025

Berkman PA, Forman SL. 1996. Pre-bomb radiocarbon and the reservoir correction for calcareous marine species in the Southern Ocean. Geophysical Research Letters 23: 363-366.

Bertler NAN, Mayewski PA, Carter L. 2011. Cold conditions in Antarctica during the Little Ice Age e Implications for abrupt climate change mechanisms. Earth and Planetary Science Letters 308: 41-51.

Binnie SA, Dunai TJ, Voronina E, Goral T, Heinze S, Dewald A. 2015. Separation of Be and Al for AMS using single-step column chromatography. Nuclear Instruments and Methods in Physics Research Section B: Beam Interactions with Materials and Atoms 361: 397-401. DOI: 10.1016/j.nimb.2015.03.069.

Birkenmajer K. 1998. Quaternary geology at Potter Peninsula, King George Island (South Shetland Islands, West Antarctica). Bulletin of the Polish Academy of Sciences. Earth Sciences 46: 9-20.

Björck S, Håkansson H, Zale R, Karlén W, Jönsson BL. 1991a. A late Holocene lake sediment sequence from Livingston Island, South Shetland Islands, with palaeoclimatic implications. Antarctic Science 3: 61-72. DOI: 10.1017/S095410209100010X.

Björck S, Nils Malmer, Christian Hjort, Per Sandgren, Ólafur Ingólfsson, Bo Wallén, Ronald Ian Lewis Smith, and Bodil Liedberg Jónsson. 1991b. Stratigraphic and Paleoclimatic Studies of a 5500-Year-Old Moss Bank on Elephant Island, Antarctica. Arctic and Alpine Research **23**: 361-374. DOI: 10.2307/1551679.

Björck S, Hjort, C., Ingolfsson, O., Skog, G. 1991c. Radiocarbon dates from the Antarctic Peninsula region — problems and potential. In Radiocarbon dating: recent applications and future potential, Lowe JJ (ed). Quaternary Proceedings; 55–65.

Björck S, Håkansson H, Olsson S, Barnekow L, Janssens J. 1993. Palaeoclimatic studies in South Shetland Islands, Antarctica, based on numerous stratigraphic variables in lake sediments. Journal of Paleolimnology 8: 233-272. DOI: 10.1007/bf00177858.

Björck S, Olsson S, Ellis-Evans C, Håkansson H, Humlum O, de Lirio JM. 1996. Late Holocene palaeoclimatic records from lake sediments on James Ross Island, Antarctica. Palaeogeography, Palaeoclimatology, Palaeoecology 121: 195-220. DOI: 10.1016/0031-0182(95)00086-0.

Blaauw M. 2010. Methods and code for 'classical' age-modelling of radiocarbon sequences. Quaternary Geochronology 5: 512–518.

Blaauw M, Christen JA. 2011. Flexible paleoclimate age-depth models using an autoregressive gamma process. Bayesian Anal. 6: 457-474.

Blard PH, Farley KA. 2008. The influence of radiogenic 4He on cosmogenic 3He determinations in volcanic olivine and pyroxene. Earth and Planetary Science Letters 276: 20-29.

Blard PH, Balco G, Burnard PG, Farley KA, Fenton CR, Friedrich R, Jull AJT, Niedermann S, Pik R, Schaefer JM, Scott EM, Shuster DL, Stuart FM, Stute M, Tibari B, Winckler G, Zimmermann L. 2015. An inter-laboratory comparison of cosmogenic 3He and radiogenic 4He in the CRONUS-P pyroxene standard. Quaternary Geochronology 26: 11-19. DOI: 10.1016/j.quageo.2014.08.004

Blindow N, Suckro SK, Rückamp M, Braun M, Schindler M, Breuer B, Saurer H, Simões JC, Lange MA. 2010. Geometry and thermal regime of the King George Island ice cap, Antarctica, from GPR and GPS. Annals of Glaciology 51: 103-109. DOI: 10.3189/172756410791392691.

Blockley SPE, Pyne-O'Donnell SDF, Lowe JJ, Matthews IP, Stone A, Pollard AM, Turney CSM, Molyneux EG. 2005. A new and less destructive laboratory procedure for the physical separation of distal glass tephra shards from sediments. Quaternary Science Reviews 24: 1952-1960. DOI: 10.1016/j.quascirev.2004.12.008

Blott S, Pye K. 2011. Gradistat: a grain size distribution and statistics package for the analysis of unconsolidated sediments. Earth Surface Processes and Landforms 26: 1237–1248.

Bluck BJ, Ward JD, Spaggiari R. 2001. Gravel beaches of southern Namibia. In Ecology and Geomorphology of Coastal Shingle, Randall RE, Barnes RSK, Neal A, Packham JR (eds). Westbury Academic Scientific Publishing; 56-76.

Bockheim J, Vieira G, Ramos M, López-Martínez J, Serrano E, Guglielmin M, Wilhelm K, Nieuwendam A. 2013. Climate warming and permafrost dynamics in the Antarctic Peninsula region. Global and Planetary Change 100: 215-223. DOI: 10.1016/j.gloplacha.2012.10.018.

Borchers B, Marrero S, Balco G, Caffee M, Goehring B, Lifton N, Nishiizumi K, Phillips F, Schaefer J, Stone J. 2016. Geological calibration of spallation production rates in the CRONUS-Earth project. Quaternary Geochronology 31: 188-198. DOI: 10.1016/j.quageo.2015.01.009.

Braun M, Gossmann H. 2002. Glacial Changes in the Areas of Admiralty Bay and Potter Cove, King George Island, Maritime Antarctica. In: Beyer L and Bölter M (eds) Geoecology of Antarctic Ice-Free Coastal Landscapes. Berlin, Heidelberg: Springer Berlin Heidelberg; 75-89.

Braun M, Saurer H, Vogt S, Simões JC, Goßmann H. 2001. The influence of large-scale atmospheric circulation on the surface energy balance of the King George Island ice cap. International Journal of Climatology 21: 21-36. DOI: 10.1002/joc.563.

Braun M, Saurer H, Gossmann H. 2004. Climate, energy fluxes and ablation rates on the ice cap of King George Island. Pesquisa Antártica Brasileira 4: 87-103.

Bristow C. 1995. Facies analysis in the Lower Greensand using ground-penetrating radar. Journal of the Geological Society of London 152: 591-598. DOI: 10.1144/gsjgs.152.4.0591.

Bronk Ramsey C, Lee S. 2013. Recent and Planned Developments of the Program OxCal. Radiocarbon 55: 720-730.

Bujalesky GG, Gonzalez Bonorino G. 2015. El Paramo Transgressive Gravel Spit, Tierra del Fuego, Argentina. In Sand and Gravel Spits, Randazzo G, Jackson DWT, Cooper JAG (eds). Springer International Publishing: Cham; 37-50.

Burningham H. 2015. Gravel Spit-Inlet Dynamics: Orford Spit, UK. In Sand and Gravel Spits, Randazzo G, Jackson DWT, Cooper JAG (eds). Springer International Publishing: Cham; 51-65.

Charman DJ, Roland TP, Amesbury MJ, Griffiths H, Convey P, Royles J, Hodgson DA. 2018. Spatially coherent late Holocene Antarctic Peninsula surface air temperature variability. Geology 46: 1071-1074. DOI: 10.1130/g45347.1.

Christ AJ, Domack EW, Talaia-Murray M, Elking N, Leventer A, Lavoie C, Brachfeld S, Yoo K-C, Jeong S-M, Gilbert R, Petrushak S, Wellner J, Group tL. 2015. Late Holocene glacial advance and ice shelf growth in Barilari Bay, Graham Land, west Antarctic Peninsula. GSA Bulletin 127: 297-315. DOI: 10.1130/b31035.1.

Chu Z, Sun L, Wang Y, Huang T, Zhou X. 2017. Depositional environment and climate changes during the Holocene in Grande Valley, Fildes Peninsula, King George Island, Antarctica. Antarctic Science 29: 545-554. DOI:10.1017/S095410201700030X.

Clapperton CM, Sugden DE. 1988. Holocene glacier fluctuations in South America and Antarctica. Quaternary Science Reviews 7: 185-198. DOI: 10.1016/0277-3791(88)90005-4.

Cohen AS. 2003. Paleolimnology: the history and evolution of lake systems. Oxford University Press, 757 USA: 528 pp.

Cook AJ, Fox AJ, Vaughan DG, Ferrigno JG. 2005. Retreating Glacier Fronts on the Antarctic Peninsula over the Past Half-Century. Science 308: 541-544. DOI: 10.1126/science.1104235.

Cooper JAG, Jackson DWT, Randazzo G. 2015. Introduction. In Sand and Gravel Spits, Randazzo G, Jackson DWT, Cooper JAG (eds). Springer International Publishing: Cham; vii-ix.

Curl JE. 1980. A glacial history of the South Shetland Islands, Antarctica. In Institute of Polar Studies Report No. 63. The Ohio State University; 129.

Davies BJ, Glasser NF, Carrivick JL, Hambrey MJ, Smellie JL, Nývlt D. 2013. Landscape evolution and ice-sheet behaviour in a semi-arid polar environment: James Ross Island, NE Antarctic Peninsula. Geological Society, London, Special Publications 381: 353-395. DOI: 10.1144/sp381.1.

Davies SJ, Lamb HF, Roberts SJ. 2015. MicroXRF core scanning in palaeolimnology: recent developments. In: Croudace, I.W.; Rothwell, R.G., (eds.) Micro-XRF studies of sediment cores: Applications of a non-destructive tool for the environmental sciences. Developments in Paleoenvironmental Research 17. Dordrecht, Springer; 189-226.

Davies BJ, Hambrey MJ, Glasser NF, Holt T, Rodés A, Smellie JL, Carrivick JL, Blockley SPE. 2017. Ice-dammed lateral lake and epishelf lake insights into Holocene dynamics of Marguerite Trough Ice Stream and George VI Ice Shelf, Alexander Island, Antarctic Peninsula. Quaternary Science Reviews 177: 189-219. DOI: https://doi.org/10.1016/j.quascirev.2017.10.016.

del Valle RA, Montalti D, Inbar M. 2002. Mid-Holocene macrofossil-bearing raised marine beaches at Potter Peninsula, King George Island, South Shetland Islands. Antarctic Science 14: 263–269.

del Valle RA, Tatur A, Lusky J, Gómez Izquierdo D. 2004. Cambios morfológicos recientes en lagos de la península Potter, isla 25 de Mayo, islas Shetland del Sur, Antártida. Revista de la Asociación Geológica Argentina 59: 443-450.

del Valle RA, Montalti D, Inbar M, Boaretto E. 2007. Holoceno marino en la península Potter, Isla 25 de Mayo, Antártida. Revista de la Asociación Geológica Argentina 62: 35-43.

Deregibus D, Scharf FK, Pasotti F, Ruiz Barlett E, Servetto N, Abele D. 2015. IMCONet Research Areas Map of Potter Cove, King-George Island (I. 25 de Mayo), with links to maps. PANGAEA. DOI: 10.1594/PANGAEA.853859.

Dewald A, Heinze S, Jolie J, Zilges A, Dunai T, Rethemeyer J, Melles M, Staubwasser M, Kuczewski B, Richter J, Radtke U, von Blanckenburg F, Klein M. 2013. CologneAMS, a dedicated center for accelerator mass spectrometry in Germany. Nuclear Instruments and Methods in Physics Research Section B: Beam Interactions with Materials and Atoms 294: 18-23. DOI: 10.1016/j.nimb.2012.04.030.

Dixon P. 2003. VEGAN, a package of R functions for community ecology. Journal of Vegetation Science 14: 927-930. DOI: 10.1111/j.1654-1103.2003.tb02228.x

Domack EW, Ishman SE, Stein AB, McClennen CE, Jull AJT. 1995. Late Holocene advance of the Müller Ice Shelf, Antarctic Peninsula: sedimentological, geochemical and palaeontological evidence. Antarctic Science 7: 159-170. DOI: 10.1017/S0954102095000228.

Domack E, Leventer A, Dunbar R, Taylor F, Brachfeld S, Sjunneskog C. 2001. Chronology of the Palmer Deep site, Antarctic Peninsula: a Holocene palaeo-environmental reference for the circumAntarctic. The Holocene 11: 1-9.

Dunai TJ, Stuart FM, Pik R, Burnard P, Gayer E. 2007. Production of 3He in crustal rocks by cosmogenic thermal neutrons. Earth and Planetary Science Letters 258: 228-236. DOI: https://doi.org/10.1016/j.epsl.2007.03.031.

Ellis-Evans JC, Lemon EC. 1989. Some aspects of iron cycling in maritime antarctic lakes. Hydrobiologia 172: 149–164.

Esposito RMM, Spaulding SA, McKnight DM, Van de Vijver BART, Kopalov K, Lubinski D, Hall B, Whittaker T. 2008. Inland diatoms from the McMurdo dry valleys and James Ross Island, Antarctica. Botany 86: 1378-1392.

Etourneau J, Collins LG, Willmott V, Kim JH, Barbara L, Leventer A, Schouten S, Sinninghe Damsté JS, Bianchini A, Klein V, Crosta X, Massé G. 2013. Holocene climate variations in the western Antarctic Peninsula: evidence for sea ice extent predominantly controlled by changes in insolation and ENSO variability. Clim. Past 9: 1431-1446. DOI: 10.5194/cp-9-1431-2013.

Evans OF. 1942. The Origin of Spits, Bars, and Related Structures. The Journal of Geology 50: 846-865. DOI: 10.1086/625087.

Falk U, Sala H. 2015. Winter melt conditions of the inland ice cap on King George Island, Antarctic Peninsula. Erdkunde 69: 341-363. DOI: 10.3112/erdkunde.2015.04.04.

Falk U, López DA, Silva-Busso A. 2018. Multi-year analysis of distributed glacier mass balance modelling and equilibrium line altitude on King George Island, Antarctic Peninsula. The Cryosphere 12: 1211-1232.

Fletcher III CH, Fairbridge RW, Møller JJ, Long AJ. 1993. Emergence of the Varanger Peninsula, Arctic Norway, and climate changes since deglaciation. The Holocene 3: 116-127. DOI: 10.1177/095968369300300203.

Fontijn K, Lachowycz SM, Rawson H, Pyle DM, Mather TA, Naranjo JA, Moreno-Roa H. 2014. Late Quaternary tephrostratigraphy of southern Chile and Argentina, Quaternary Science Reviews 89: 70-84.

Forbes D, Taylor R. 1987. Coarse-grained beach sedimentation under paraglacial conditions, Canadian Atlantic coast. In Glaciated coasts, FitzGerald DM, Rosen PS (eds). Academic Press: San Diego; 51-86.

Forbes DL, Orford JD, Carter RWG, Shaw J, Jennings SC. 1995. Morphodynamic evolution, self-organisation, and instability of coarse-clastic barriers on paraglacial coasts. Marine Geology 126: 63-85. DOI: 10.1016/0025-3227(95)00066-8.

Foster LC, Pearson EJ, Juggins S, Hodgson D.A, Saunders KM, Verleyen E, Roberts SJ. 2016. Development of a regional glycerol dialkyl glycerol tetraether (GDGT)–temperature calibration for Antarctic and sub-Antarctic lakes. Earth and Planetary Science Letters 433: 370–379.

Fourcade NH. 1960. Estudio geológico-petrográfico de Caleta Potter, Isla 25 de Mayo, Islas Shetland del Sur, Buenos Aires, Argentina: Instituto Antártico Argentino 8.

Fretwell PT, Hodgson DA, Watcham EP, Bentley MJ, Roberts SJ. 2010. Holocene isostatic uplift of the South Shetland Islands, Antarctic Peninsula, modelled from raised beaches. Quaternary Science Reviews 29: 1880-1893. DOI: 10.1016/j.quascirev.2010.04.006.

Garreaud, R.D. 2007. Precipitation and circulation covariability in the extratropics. Journal of Climate 20: 47894797.

Gawthorpe RL, Collier REL, Alexander J, Bridge JS, Leeder MR. 1993. Groundpenetrating radar: application to sandbody geometry and heterogeneity studies. In Characterization of fluvial and aeolian reservoirs. , North CP, Prosser DJ (eds). Geological Society of London Special Publications: London; 421–432.

Gibson JA, Zale R. 2006. Holocene development of the fauna of Lake Boeckella, northern Antarctic Peninsula. The Holocene 16: 625-634.

Glasser NF, Bennett MR. 2004. Glacial erosional landforms: origins and significance for palaeoglaciology. Progress in Physical Geography: Earth and Environment 28: 43-75.

Glasser NF, Davies BJ, Carrivick JL, Rodés A, Hambrey MJ, Smellie JL, Domack E. 2014. Ice-stream initiation, duration and thinning on James Ross Island, northern Antarctic Peninsula. Quaternary Science Reviews 86: 78-88. DOI: 10.1016/j.quascirev.2013.11.012.

González-Ferrán O, Katsui Y. 1970. Estudio integral del volcanismo cenozoico superior de las Islas Shetland del Sur, Antártida, Santiago de Chile, Chile: Servicio Científico Instituto Antártico Chileno; pp 123-174.

Goodwin BP, Mosley-Thompson E, Wilson AB, Porter SE, Sierra-Hernandez MR. 2016. Accumulation Variability in the Antarctic Peninsula: The Role of Large-Scale Atmospheric Oscillations and Their Interactions. Journal of Climate 29: 2579-2596. DOI: 10.1175/jcli-d-15-0354.1.

Gordon JE, Harkness DD. 1992. Magnitude and geographic variation of the radiocarbon content in Antarctic marine life: Implications for reservoir corrections in radiocarbon dating. Quaternary Science Reviews 11: 697-708. DOI: 10.1016/0277-3791(92)90078-M

Gosse J, Phillips F. 2001. Terrestrial in situ cosmogenic nuclides: theory and application. Quaternary Science Reviews 20: 1475-1560 DOI: 10.1016/s0277-3791(00)00171-2 (2001).

Griffith TW, Anderson JB. 1989. Climatic control of sedimentation in bays and fjords of the northern Antarctic Peninsula. Marine Geology 85: 181-204. DOI: 10.1016/0025-3227(89)90153-9.

Guglielmin M, Convey P, Malfasi F, Cannone N. 2016. Glacial fluctuations since the Medieval warm period at Rothera Point (western Antarctic Peninsula). The Holocene 26: 154-158.

Hall BL. 2003. An Overview of Late Pleistocene Glaciation in the South Shetland Islands. Antarctic Peninsula Climate Variability: Historical and Paleoenvironmental Perspectives. American Geophysical Union; 103-113.

Hall BL, Perry ER. 2004. Variations in ice rafted detritus on beaches in the South Shetland Islands: a possible climate proxy. Antarctic Science 16: 339-344. DOI: 10.1017/S0954102004002147.

Hall, BL. 2007. Late-Holocene advance of the Collins Ice Cap, King George Island, South Shetland Islands. The Holocene 17: 1253-1258. DOI:10.1177/0959683607085132.

Hall BL. 2009. Holocene glacial history of Antarctica and the sub-Antarctic islands. Quaternary Science Reviews 28: 2213-2230.

Hall BL. 2010. Holocene relative sea-level changes and ice fluctuations in the South Shetland Islands. Global and Planetary Change 74: 15-26. DOI: 10.1016/j.gloplacha.2010.07.007.

Hall BL, Henderson GM, Baroni C, Kellogg TB. 2010. Constant Holocene Southern-Ocean 14C reservoir ages and ice-shelf flow rates. Earth and Planetary Science Letters 296: 115-123. DOI: 10.1016/j.epsl.2010.04.054.

Hass HC, Kuhn G, Monien P, Brumsack H-J, Forwick M. 2010. Climate fluctuations during the past two millennia as recorded in sediments from Maxwell Bay, South Shetland Islands, West Antarctica. Geological Society, London, Special Publications 344: 243-260. DOI: 10.1144/sp344.17

Haworth EY. 1976. Two late-glacial (Late Devensian) diatom assemblage pro- files from northern Scotland. New Phytologist: 227-256.

Hayes MO, Michel J, Betenbaugh DV. 2010. The Intermittently Exposed, Coarse-Grained Gravel Beaches of Prince William Sound, Alaska: Comparison with Open-Ocean Gravel Beaches. Journal of Coastal Research 26: 4-30. DOI: 10.2112/08-1071.1.

Henkel S, Kasten S, Sala H, Busso AS, Staubwasser M. 2013. Effect of increased glacier melt on diagenetic Fe cycling in marine sediments at King George Island (Antarctica). Mineralogical Magazine - H: Goldschmidt Abstracts 2013 **77**: 1287-1287. DOI: 10.1180/minmag.2013.077.5.8.

Heredia Barión P, Lindhorst S, Schutter I, Falk U, Kuhn G. 2018. Reaction of a polar gravel-spit system to atmospheric warming and glacier retreat as reflected by morphology and internal sediment geometries (South Shetland Islands, Antarctica). Earth Surface Processes and Landforms 0. DOI: 10.1002/esp.4565

Heroy DC, Sjunneskog C, Anderson JB. 2008. Holocene climate change in the Bransfield Basin, Antarctic Peninsula: evidence from sediment and diatom analysis. Antarctic Science 20: 69-87.

Hobbs WO, Telford RJ, Birks HJB, Saros JE, Hazewinkel RR, Perren BB, Saulnier-Talbot, Wolfe AP. 2010. Quantifying recent ecological changes in remote lakes of North America and Greenland using sediment diatom assemblages. PloS One 5: p.e10026.

Hochschild V. 1995. Geomorphologische Kartierung und Untersuchung der Auftaudynamik mit ERS-1-SAR-Daten im Bereich der Antarktischen Halbinsel. Universität Bremen: Vertrieb, Universitätsbuchhandlung. Bremer Beiträge zur Geographie und Raumplanung, 28.

Hodgson DA, Roberts SJ, Smith JA, Verleyen E, Sterken M, Labarque M, Sabbe K, Vyverman W, Allen CS, Leng MJ, Bryant C. 2013. Late Quaternary environmental changes in Marguerite Bay, Antarctic Peninsula, inferred from lake sediments and raised beaches. Quaternary Science Reviews, 68: 216-236.

Hogg AG, Hua Q, Blackwell PG, Niu M, Buck CE, Guilderson TP, Heaton TJ, Palmer JG, Reimer PJ, Reimer RW, Turney CSM, Zimmerman SRH. 2013. SHCal13 Southern Hemisphere Calibration, 0–50,000 Years cal BP. Radiocarbon 55: 1889-1903. DOI: 10.2458/azu_js_rc.55.16783.

Hua Q, Barbetti M, Rakowski AZ. 2013. Atmospheric radiocarbon for the period 1950-2010. Radiocarbon 55: 1–14.

Jeong GY. 2006. Radiocarbon ages of sorted circles on King George Island, South Shetland Islands, West Antarctica. Antarctic Science 18: 265-270.

Jerosch K, Pehlke H, Monien P, Scharf F, Weber L, Kuhn G, Braun MH, Abele D. 2018. Benthic meltwater fjord habitats formed by rapid glacier recession on King George Island, Antarctica. Philosophical Transactions of the Royal Society A: Mathematical, Physical and Engineering Sciences 376: 20170178. DOI: 10.1098/rsta.2017.0178.

John BS, Sugden DE. 1971. Raised marine features and phases of glaciation in the South Shetland Islands. British Antarctic Survey Bulletin 24: 45-111.

Johnson JS, Everest JD, Leat PT, Golledge NR, Rood DH, Stuart FM. 2012. The deglacial history of NW Alexander Island, Antarctica, from surface exposure dating. Quaternary Research 77: 273-280. DOI: https://doi.org/10.1016/j.yqres.2011.11.012.

Johnson JS, Smith JA, Schaefer JM, Young NE, Goehring BM, Hillenbrand C-D, Lamp JL, Finkel RC, Gohl K. 2017. The last glaciation of Bear Peninsula, central Amundsen Sea Embayment of Antarctica: Constraints on timing and duration revealed by in situ cosmogenic 14C and 10Be dating. Quaternary Science Reviews 178: 77-88. DOI: https://doi.org/10.1016/j.quascirev.2017.11.003.

Jones VJ, Juggins S. 1995. The construction of a diatom-based chlorophyll a transfer function and its application at three lakes on Signy Island (maritime Antarctic) subject to differing degrees of nutrient enrichment. Freshwater Biology 34: 433-445.

Juggins S. 2007. C2 Version 1.5 User Guide. Software for ecological and palaeoecological data analysis and visualization. Newcastle University.

Juggins, S. 2014. Rioja: Analysis of Quaternary Science Data, R package version (0.9-3).

Kääb A. (2007) Rock glaciers and protalus forms. In: Elias S (ed) Encyclopedia of Quaternary Science. Amsterdam: Elsevier; 2236-2242.

Kaplan MR, Strelin JA, Schaefer JM, Denton GH, Finkel RC, Schwartz R, Putnam AE, Vandergoes MJ, Goehring BM, Travis SG. 2011. In-situ cosmogenic 10Be production rate at Lago Argentino, Patagonia: Implications for late-glacial climate chronology. Earth and Planetary Science Letters 309: 21-32. DOI: http://dx.doi.org/10.1016/j.epsl.2011.06.018.

Kejna M, Araźny A, Sobota I. 2013. Climatic change on King George Island in the years 1948–2011. Polish Polar Research 34: 213-235. DOI: 10.2478/popore-2013-0004.

Kennicutt MC. 2009. King George Island and SCAR Science. COMNAP meeting, 03- 06 August 2009. Punta Arenas, Chile, 1-8.

Klages JP, Kuhn G, Hillenbrand CD, Graham AGC, Smith JA, Larter RD, Gohl K. 2013. First geomorphological record and glacial history of an inter-ice stream ridge on the West Antarctic continental shelf. Quaternary Science Reviews 61: 47-61. DOI: 10.1016/j.quascirev.2012.11.007.

Kraus S and del Valle R. 2008a. Geology, tectonics and Ar− Ar ages of the magmatic dykes from Potter Peninsula (King George Island, South Shetland Islands). In: Wiencke C, Ferreyra GA, Abele D, et al. (eds) The Antarctic Ecosystem of Potter Cove, King− George Island (Isla 25 de Mayo): Synopsis of Research performed. Bremerhaven, Germany: Alfred Wegener Institut für Polar- und Meeresforschung, Helmholz Gemeinschaft, pp. 20-30.

Kraus S and del Valle R. 2008b. Geological map of Potter Peninsula (King George Island, South Shetland Islands, Antarctic Peninsula). PANGAEA.

Lal D. 1991. Cosmic ray labeling of erosion surfaces: in situ nuclide production rates and erosion models. Earth and Planetary Science Letters 104: 424-439. DOI: 10.1016/0012-821X(91)90220-C

Lamb HH. 1965. The early medieval warm epoch and its sequel. Palaeogeography, Palaeoclimatology, Palaeoecology, 1: 13-37.

Lamy F, Kilian R, Arz HW, Francois JP, Kaiser J, Prange M, Steinke T. 2010. Holocene changes in the position and intensity of the southern westerly wind belt. Nature Geoscience 3: 695-699.

Laskar J, Robutel P, Joutel F, Gastineau M, Correia ACM, Levrard B. 2004. A long-term numerical solution for the insolation quantities of the Earth. Astronomy and Astrophysics 428: 261-285.

Le Bas ML, Maitre RL, Streckeisen A, Zanettin B. 1986. IUGS Subcommission on the Systematics of Igneous Rocks. A chemical classification of volcanic rocks based on the total alkali-silica diagram', Journal of Petrology 27: 745-750.

Lemoine FG, Kenyon SC, Factor JK, Trimmer RG, Pavlis NK, Chinn DS, Cox CM, Klosko SM, Luthcke SB, Torrence MH, Wang YM, Williamson RG, Pavlis EC, Rapp RH, Olson TR. 1998. The Development of the Joint NASA GSFC and NIMA Geopotential Model EGM96. In NASA Technical Paper TP-1998-206861. NASA Goddard Space Flight Center Greenbelt, USA 584.

Leventer A, Domack EW, Ishman SE, Brachfield S, McClennen CE, Manley P. 1996. Productivity cycles of 200300 years in the Antarctic Peninsula region: understanding linkages among the sun, atmosphere, oceans, sea ice, and biota. Geological Society of America Bulletin 108: 162644.

Lifton N, Sato T, Dunai TJ. 2014. Scaling in situ cosmogenic nuclide production rates using analytical approximations to atmospheric cosmic-ray fluxes. Earth and Planetary Science Letters 386: 149-160.

Lifton N. 2016. Implications of two Holocene time-dependent geomagnetic models for cosmogenic nuclide production rate scaling. Earth and Planetary Science Letters 433: 257-268. DOI: 10.1016/j.epsl.2015.11.006.

Lim CH, Lettmann K, Wolff J-O. 2013. Numerical study on wave dynamics and wave-induced bed erosion characteristics in Potter Cove, Antarctica. Ocean Dynamics 63: 1151-1174. DOI: 10.1007/s10236-013-0651-z.
Lindhorst S, Betzler C, Hass HC. 2008. The sedimentary architecture of a Holocene barrier spit (Sylt, German Bight): Swash-bar accretion and storm erosion. Sedimentary Geology 206: 1-16. DOI: 10.1016/j.sedgeo.2008.02.008.
Lindhorst S, Schutter I. 2013. 47 ground-penetrating radar lines of Area 4 - Gravel spit system from Potter Cove, King George Island, Antarctic Peninsula. PANGAEA. DOI: 10.1594/PANGAEA.825658.
Lindhorst S, Schutter I. 2014. Polar gravel beach-ridge systems: Sedimentary architecture, genesis, and implications for climate reconstructions (South Shetland Islands/Western Antarctic Peninsula). Geomorphology 221: 187-203. DOI: 10.1016/j.geomorph.2014.06.013.
Lindow J, Castex M, Wittmann H, Johnson JS, Lisker F, Gohl K, Spiegel C. 2014. Glacial retreat in the Amundsen Sea sector, West Antarctica – first cosmogenic evidence from central Pine Island Bay and the Kohler Range. Quaternary Science Reviews 98: 166-173. DOI: https://doi.org/10.1016/j.quascirev.2014.05.010.
Liu X, Sun L, Xie Z, Yin X, Wang Y. 2005. A 1300-year record of penguin populations at Ardley Island in the Antarctic, as deduced from the geochemical data in the ornithogenic lake sediments. Arctic, Antarctic, and Alpine Research 37: 490-498.
López-Martínez J, Serrano E, Schmid T, Mink S, Linés C. 2012. Periglacial processes and landforms in the South Shetland Islands (northern Antarctic Peninsula region). Geomorphology 155–156: 62-79. DOI: 10.1016/j.geomorph.2011.12.018.
Lotter AF, Birks HJB, Zolitschka B. 1995. Late-glacial pollen and diatom changes in response to two different environmental perturbations: volcanic eruption and Younger Dryas cooling. Journal of Paleolimnology 14: 23-47.
Lukas S. 2011. Ice-Cored Moraines. In: Singh VP, Singh P and Haritashya UK (eds) Encyclopedia of Snow, Ice and Glaciers. Dordrecht: Springer Netherlands, 616-619.
Majewski W, Wellner JS, Szczuciński W, Anderson JB. 2012. Holocene oceanographic and glacial changes recorded in Maxwell Bay, West Antarctica. Marine Geology 326–328: 67-79. DOI: 10.1016/j.margeo.2012.08.009.
Mann ME, Zhang Z, Rutherford S, Bradley RS, Hughes MK, Shindell D, Ammann C, Faluvegi G, Ni F. 2009. Global Signatures and Dynamical Origins of the Little Ice Age and Medieval Climate Anomaly. Science 326: 1256-1260. DOI: 10.1126/science.1177303.
Marcott SA, Shakun JD, Clark PU, Mix AC. 2013. A reconstruction of regional and global temperature for the past 11,300 years. Science 339: 1198- 1201.
Marrero SM, Phillips FM, Borchers B, Lifton N, Aumer R, Balco G. 2016. Cosmogenic nuclide systematics and the CRONUScalc program. Quaternary Geochronology 31: 160-187. DOI: 10.1016/j.quageo.2015.09.005.
Marshall GJ, Orr A, Lipzig NPMv, King JC. 2006. The Impact of a Changing Southern Hemisphere Annular Mode on Antarctic Peninsula Summer Temperatures. Journal of Climate 19: 5388-5404. DOI: 10.1175/jcli3844.1.
Martinez-Macchiavello JC, Tatur A, Servant-Vildary S, Del Valle R. 1996. Holocene environmental change in a marine–estuarine sediment sequence, King George Island, South Shetland Islands. Antarctic Science 8: 313–322.
Mason OK. 2010. Beach Ridge Geomorphology at Cape Grinnell, northern Greenland: A Less Icy Arctic in the Mid-Holocene. Geografisk Tidsskrift-Danish Journal of Geography 110: 337-355. DOI: 10.1080/00167223.2010.10669515.
Matsuoka N. 2001. Solifluction rates, processes and landforms: a global review. Earth-Science Reviews 55: 107-134.
Mäusbacher R, Müller J and Schmidt R. 1989. Evolution of postglacial sedimentation in Antarctic lakes (King George Island). Zeitschrift für Geomorphologie 33: 219–234.
Maüsbacher R. 1991. Die jungquartare Relief- und Klimageschichte im Bereich der Fildeshalbinsel Süd-Shetland Inseln, Antarktis, Heidelberg.
Mäusbacher R, Müller J, Schmidt R. 1989. Evolution of postglacial sedimentation in Antarctic lakes (King George Island). Zeitschrift für Geomorphologie 33: 219–234.

Meredith MP, King JC. 2005. Rapid climate change in the ocean west of the Antarctic Peninsula during the second half of the 20th century. Geophysical Research Letters 32: 1-5. DOI: 10.1029/2005GL024042.

Michalchuk BR, Anderson JB, Wellner JS, Manley PL, Majewski W, Bohaty S. 2009. Holocene climate and glacial history of the northeastern Antarctic Peninsula: the marine sedimentary record from a long SHALDRIL core. Quaternary Science Reviews 28: 3049-3065.

Michel TJ, Saros JE, Interlandi SJ, Wolfe AP. 2006. Resource require- ments of four freshwater diatom taxa determined by in situ growth bioassays using natural populations from alpine lakes. Hydrobiologia 568: 235-243.

Milliken KT, Anderson JB, Wellner JS, Bohaty SM, Manley PL. 2009. High-resolution Holocene climate record from Maxwell Bay, South Shetland Islands, Antarctica. Geological Society of America Bulletin 121: 1711-1725. DOI: 10.1130/b26478.1.

Mitchum RM, Vail PR, Sangree JB. 1977. Stratigraphic interpretation of seismic reflection patterns in depositional sequences. In Seismic stratigraphy —Applications to hydrocarbon exploration., Payton CE (ed). American Association of Petroleum Geologists Memoir 16; 117–133.

Møller JJ, Yevzerov VY, Kolka VV, Corner GD. 2002. Holocene raised-beach ridges and sea-ice-pushed boulders on the Kola Peninsula, northwest Russia: indicators of climatic change. The Holocene 12: 169-176. DOI: doi:10.1191/0959683602hl532rp.

Monien P, Schnetger B, Brumsack HJ, Hass HC, Kuhn G. 2011. A geochemical record of late Holocene palaeoenvironmental changes at King George Island (maritime Antarctica). Antarctic Science 23: 255-267.

Montes-Hugo M, Doney SC, Ducklow HW, Fraser W, Martinson D, Stammerjohn SE, Schofield O. 2009. Recent Changes in Phytoplankton Communities Associated with Rapid Regional Climate Change Along the Western Antarctic Peninsula. Science 323: 1470-1473. DOI: 10.1126/science.1164533.

Moreno PI, Vilanova I, Villa-Martínez R, Garreaud RD, Rojas M, De Pol-Holz R. 2014. Southern Annular Mode-like changes in southwestern Patagonia at centennial timescales over the last three millennia. Nature Communications 5: 4375.

Moreno PI, Vilanova I, Villa-Martínez R, Dunbar RB, Mucciarone DA, Kaplan MR, Garreaud RD, Rojas M, Moy CM, De Pol-Holz R, Lambert F. 2018. Onset and Evolution of Southern Annular Mode-Like Changes at Centennial Timescale. Scientific Reports 8: 3458.

Moreton SG, Smellie JL, 1998. Identification and correlation of distal tephra layers in deep-sea sediment cores, Scotia Sea, Antarctica. Annuals of Glaciology 27: 285–289.

Mosley-Thompson E, Thompson LG, Grootes PM, Gundestrup N. 1990. Little ice age (neoglacial) paleoenvironmental conditions at Siple Station, Antarctica. Annals of Glaciology 14: 199-204.

Moy CM, Dunbar RB, Moreno PI, Francois J-P, Villa-Martínez R, Mucciarone DM, Guilderson TP, Garreaud RD. 2008. Isotopic evidence for hydrologic change related to the westerlies in SW Patagonia, Chile, during the last millennium. Quaternary Science Reviews 27: 1335-1349. DOI: 10.1016/j.quascirev.2008.03.006

Mulvaney R, Abram NJ, Hindmarsh RCA, Arrowsmith C, Fleet L, Triest J, Sime LC, Alemany O, Foord S. 2012. Recent Antarctic Peninsula warming relative to Holocene climate and ice-shelf history. Nature 489: 141-144. DOI: http://www.nature.com/nature/journal/v489/n7414/abs/nature11391.html#supplementary-information.

Munoz YP, Wellner JS. 2018. Seafloor geomorphology of western Antarctic Peninsula bays: a signature of ice flow behaviour. The Cryosphere 12: 205-225.

Navarro FJ, Jonsell UY, Corcuera MI, Martín-Español A. 2013. Decelerated mass loss of Hurd and Johnsons Glaciers, Livingston Island, Antarctic Peninsula. Journal of Glaciology 59: 115-128. DOI: 10.3189/2013JoG12J144.

Neukom R, Gergis J, Karoly DJ, Wanner H, Curran M, Elbert J, Gonzalez-Rouco F, Linsley BK, Moy AD, Mundo I, Raible CC, Steig EJ, van Ommen T, Vance T, Villalba R, Zinke J, Frank D. 2014. Inter-hemispheric temperature variability over the past millennium. Nature Climate Change 4: 362-367.

Niedermann S, Bach W, Erzinger J. 1997. Noble gas evidence for a lower mantle component in MORBs from the southern East Pacific Rise: Decoupling of helium and neon isotope systematics. Geochimica et Cosmochimica Acta 61: 2697-2715.
Niedermann S. 2002. Cosmic-Ray-Produced Noble Gases in Terrestrial Rocks: Dating Tools for Surface Processes. Reviews in Mineralogy and Geochemistry 47: 731-784.
Nielsen LH, Johannessen PN. 2009. Facies architecture and depositional processes of the Holocene–Recent accretionary forced regressive Skagen spit system, Denmark. Sedimentology 56: 935-968. DOI: 10.1111/j.1365-3091.2008.01007.x.
Nielsen L, Bendixen M, Kroon A, Hede MU, Clemmensen LB, Weβling R, Elberling B. 2017. Sea-level proxies in Holocene raised beach ridge deposits (Greenland) revealed by ground-penetrating radar. Scientific Reports 7: 1-8. DOI: 10.1038/srep46460.
Nishiizumi K, Imamura M, Caffee MW, Southon JR, Finkel RC, McAninch J. 2007. Absolute calibration of 10Be AMS standards. Nuclear Instruments and Methods in Physics Research Section B: Beam Interactions with Materials and Atoms 258: 403-413. DOI: 10.1016/j.nimb.2007.01.297.
Ó Cofaigh C, Davies BJ, Livingstone SJ, Smith JA, Johnson JS, Hocking EP, Hodgson DA, Anderson JB, Bentley MJ, Canals M, Domack E, Dowdeswell JA, Evans J, Glasser NF, Hillenbrand C-D, Larter RD, Roberts SJ, Simms AR. 2014. Reconstruction of ice-sheet changes in the Antarctic Peninsula since the Last Glacial Maximum. Quaternary Science Reviews 100: 87-110. DOI: 10.1016/j.quascirev.2014.06.023.
Oliva M, Antoniades D, Giralt S, Granados I, Pla Rabes S, Toro M, Sanjurjo J. 2016a. La deglaciación de las áreas libres de hielo de las islas Shetland del Sur (Antártida). Ejemplos de Byers (Livingston) y Barton (King George). Cuaternario y Geomorfología: 14. DOI: 10.17735/cyg.v30i1-2.48665.
Oliva M, Antoniades D, Giralt S, Granados I, Pla-Rabes S, Toro M, Liu EJ, Sanjurjo J, Vieira G. 2016b. The Holocene deglaciation of the Byers Peninsula (Livingston Island, Antarctica) based on the dating of lake sedimentary records. Geomorphology 261: 89-102. DOI: http://dx.doi.org/10.1016/j.geomorph.2016.02.029.
Oliva M, Navarro F, Hrbáček F, Hernández A, Nývlt D, Pereira P, Ruiz-Fernández J, Trigo R. 2017. Recent regional climate cooling on the Antarctic Peninsula and associated impacts on the cryosphere. Science of The Total Environment 580: 210-223. DOI: https://doi.org/10.1016/j.scitotenv.2016.12.030.
Oliva M, Ruiz-Fernández J. 2017. Geomorphological processes and frozen ground conditions in Elephant Point (Livingston Island, South Shetland Islands, Antarctica). Geomorphology 293: 368-379.
Oppenheim DR, Ellis-Evans JC. 1989. Depth-related changes in benthic diatom assemblages of a maritime Antarctic lake. Polar Biology 9: 525432.
Orford JD, Forbes DL, Jennings SC. 2002. Organisational controls, typologies and time scales of paraglacial gravel-dominated coastal systems. Geomorphology 48: 51-85. DOI: 10.1016/S0169-555X(02)00175-7.
Osmanoğlu B, Braun M, Hock R, Navarro FJ. 2013. Surface velocity and ice discharge of the ice cap on King George Island, Antarctica. Annals of Glaciology 54: 111-119. DOI: 10.3189/2013AoG63A517.
Otvos EG. 2012. Coastal barriers — Nomenclature, processes, and classification issues. Geomorphology 139: 39-52. DOI: 10.1016/j.geomorph.2011.10.037.
PAGES 2k Consortium. 2013. Continental-scale temperature variability during the past two millennia. Nature Geoscience 6: 339.
Pallàs R, James T, Sàbat F, Vilaplana J, Grant D, Ricci C. 1997. Holocene uplift in the South Shetland Islands: evaluation of tectonics and glacio-isostasy. In The Antarctic region: geological evolution and processes, Ricci C (ed). Terra Antarctica Publication, Siena, Italy; 861-868.
Pasotti F, Manini E, Giovannelli D, Wölfl A-C, Monien D, Verleyen E, Braeckman U, Abele D, Vanreusel A. 2015a. Antarctic shallow water benthos in an area of recent rapid glacier retreat. Marine Ecology 36: 716-733. DOI: 10.1111/maec.12179.

Pasotti F, Saravia LA, De Troch M, Tarantelli MS, Sahade R, Vanreusel A. 2015b. Benthic Trophic Interactions in an Antarctic Shallow Water Ecosystem Affected by Recent Glacier Retreat. PLoS ONE 10: e0141742. DOI: 10.1371/journal.pone.0141742.

Pearson EJ, Juggins S, Talbot HM, Weckstrm J, Rosn P, Ryves DB, Roberts SJ, Schmidt R. 2011. A lacustrine GDGT-temperature cali- bration from the Scandinavian Arctic to Antarctic: renewed potential for the application of GDGT-paleothermometry in lakes. Geochimica et Cosmochimica Acta 75: 6225-6238.

Peck VL, Allen CS, Kender S, McClymont EL, Hodgson DA. 2015. Oceanographic variability on the West Antarctic Peninsula during the Holocene and the influence of upper circumpolar deep water. Quaternary Science Reviews 119: 54-65. DOI: 10.1016/j.quascirev.2015.04.002.

Putnam AE, Schaefer JM, Barrell DJA, Vandergoes M, Denton GH, Kaplan MR, Finkel RC, Schwartz R, Goehring BM, Kelley SE. 2010. In situ cosmogenic 10Be production-rate calibration from the Southern Alps, New Zealand. Quaternary Geochronology 5: 392-409. DOI: 10.1016/j.quageo.2009.12.001.

Protin M, Blard P-H, Marrocchi Y, Mathon F. 2016. Irreversible adsorption of atmospheric helium on olivine: A lobster pot analogy. Geochimica et Cosmochimica Acta 179: 76-88. DOI: 10.1016/j.gca.2016.01.032.

Quartino ML, Deregibus D, Campana GL, Latorre GEJ, Momo FR. 2013. Evidence of macroalgal colonization on newly ice-free areas following glacial retreat in Potter Cove (South Shetland Islands), Antarctica. PLoS ONE 8: e58223.

Reimer RW, Reimer PJ. 2004. CALIBomb - calibration of post-bomb C-14 data (www.calib.org).

Reimer PJ, Bard E, Bayliss A, Beck JW, Blackwell PG, Ramsey CB, Buck CE, Cheng H, Edwards RL, Friedrich M, Grootes PM, Guilderson TP, Haflidason H, Hajdas I, Hatté C, Heaton TJ, Hoffmann DL, Hogg AG, Hughen KA, Kaiser KF, Kromer B, Manning SW, Niu M, Reimer RW, Richards DA, Scott EM, Southon JR, Staff RA, Turney CSM, van der Plicht J. 2013. IntCal13 and Marine13 Radiocarbon Age Calibration Curves 0–50,000 Years cal BP. Radiocarbon 55: 1869-1887. DOI: 10.2458/azu_js_rc.55.16947.

Reynolds CS. 1984. The Ecology of Freshwater Phytoplankton. Cambridge University Press, New York.

Roberts SJ, Hodgson DA, Sterken M, Whitehouse PL, Verleyen E, Vyverman W, Sabbe K, Balbo A, Bentley MJ, Moreton SG. 2011. Geological constraints on glacio-isostatic adjustment models of relative sea-level change during deglaciation of Prince Gustav Channel, Antarctic Peninsula. Quaternary Science Reviews 30: 3603-3617. DOI: 10.1016/j.quascirev.2011.09.009.

Roberts SJ, Monien P, Foster LC, Loftfield J, Hocking EP, Schnetger B, Pearson EJ, Juggins S, Fretwell P, Ireland L, Ochyra R, Haworth AR, Allen CS, Moreton SG, Davies SJ, Brumsack H-J, Bentley MJ, Hodgson DA. 2017. Past penguin colony responses to explosive volcanism on the Antarctic Peninsula. Nature Communications 8: 14914. DOI: 10.1038/ncomms14914.

Rückamp M, Braun M, Suckro S, Blindow N. 2011. Observed glacial changes on the King George Island ice cap, Antarctica, in the last decade. Global and Planetary Change 79: 99-109. DOI: 10.1016/j.gloplacha.2011.06.009.

Rülke A, Dietrich R, Capra A, Cisak J, Dongchen E, Eiken T, Fox A, Hothem LD, Johnston G, Malaimani EC, Matveev AJ, Milinevsky G, Schenke H-W, Shibuya K, Sjöberg LE, Zakrajsek A, Fritsche M, Groh A, Knöfel C, Scheinert M. 2015. The Antarctic Regional GPS Network Densification: Status and Results. In IAG 150 Years: Proceedings of the IAG Scientific Assembly in Postdam, Germany, 2013, Rizos C, Willis P (eds). Springer International Publishing: Cham; 133-139.

Sahade R, Lagger C, Torre L, Momo F, Monien P, Schloss I, Barnes DKA, Servetto N, Tarantelli S, Tatián M, Zamboni N, Abele D. 2015. Climate change and glacier retreat drive shifts in an Antarctic benthic ecosystem. Science Advances 1. DOI: 10.1126/sciadv.1500050.

Sánchez-Lugo A, Morice C, Berrisford P, Argüez A. 2018. Global surface tempetatures. In State of the Climate in 2017. Bulletin of the American Meteorological Society 99 (8), Blunden J, Arndt DS, Hartfield G (eds); 11-13.

Santana E, Dumont JF. 2007. Granulometry of pebble beach ridges in Fort William Point, Greenwich Island, Antarcitic Peninsular; a possible result from Holocene climate

fluctuations. Antarctica: A keystone in changing world-Online proceeding of the 10th ISAES. USGS Open File Report. Short Research Paper 027 1047: 1-4.
Saunders KM, Roberts SJ, Perren B, Butz C, Sime L, Davies S, Van Nieuwenhuyze W, Grosjean M, Hodgson DA. 2018. Holocene dynamics of the Southern Hemisphere westerly winds and possible links to CO2 outgassing. Nature Geoscience 11: 650-655. DOI: 10.1038/s41561-018-0186-5.
Schloss IR, Abele D, Moreau S, Demers S, Bers AV, González O, Ferreyra GA. 2012. Response of phytoplankton dynamics to 19-year (1991–2009) climate trends in Potter Cove (Antarctica). Journal of Marine Systems 92: 53-66. DOI: 10.1016/j.jmarsys.2011.10.006.
Schloss IR, Wasilowska A, Dumont D, Almandoz GO, Hernando MP, Michaud-Tremblay CA, Saravia L, Rzepecki M, Monien P, Monien D, Kopczyńska EE, Bers AV, Ferreyra GA. 2014. On the phytoplankton bloom in coastal waters of southern King George Island (Antarctica) in January 2010: An exceptional feature? Limnology and Oceanography 59: 195-210. DOI: 10.4319/lo.2014.59.1.0195.
Schmidt R, Mäusbacher R, Müller J. 1990. Holocene diatom flora and stratigraphy from sediment cores of two Antarctic lakes (King George Island). Journal of Paleolimnology 3: 55-74. DOI:10.1007/bf00209300.
Schoene T, Pohl M, Zakrajsek AF, Schenke H-W. 1998. Tide Gauge Measurements - A Contribution for the Long Term Monitoring of the Sea Level. In The Potter Cove coastal ecosystem, Antarctica, Berichte zur Polarforschung, Wiencke C, Ferreyra G, Arntz W, Rinaldi C (eds). Alfred Wegener Institute for Polar and Marine Research: Bremerhaven, Germany; 12-14.
Seong YB, Owen LA, Lim HS, Yoon HI, Kim Y, Lee YI, Caffee MW. 2008. Rate of late Quaternary ice-cap thinning on King George Island, South Shetland Islands, West Antarctica defined by cosmogenic 36Cl surface exposure dating. Boreas 38: 207-213. DOI: 10.1111/j.1502-3885.2008.00069.x.
Serrano E, López-Martínez J. 2000. Rock glaciers in the South Shetland Islands, Western Antarctica. Geomorphology 35: 145-162.
Servicio Geográfico Militar de Uruguay. 1997. Instituto Antártico Uruguayo, Uruguay.
Simkins LM, Simms AR, Dewitt R. 2015. Assessing the link between coastal morphology, wave energy and sea ice throughout the Holocene from Antarctic raised beaches. Journal of Quaternary Science 30: 335-348. DOI: 10.1002/jqs.2782.
Simms AR, Milliken KT, Anderson JB, Wellner JS. 2011. The marine record of deglaciation of the South Shetland Islands, Antarctica since the Last Glacial Maximum. Quaternary Science Reviews 30: 1583-1601. DOI: 10.1016/j.quascirev.2011.03.018.
Simms AR, Ivins ER, DeWitt R, Kouremenos P, Simkins LM. 2012. Timing of the most recent Neoglacial advance and retreat in the South Shetland Islands, Antarctic Peninsula: insights from raised beaches and Holocene uplift rates. Quaternary Science Reviews 47: 41-55. DOI: 10.1016/j.quascirev.2012.05.013.
Simms AR, Whitehouse PL, Simkins LM, Nield G, DeWitt R, Bentley MJ. 2018. Late Holocene relative sea levels near Palmer Station, northern Antarctic Peninsula, strongly controlled by late Holocene ice-mass changes. Quaternary Science Reviews 199: 49-59. DOI: https://doi.org/10.1016/j.quascirev.2018.09.017
Smellie JL, Pankhurst R, Thomson MRA, Davies RES. 1984. The geology of the South Shetland Islands: VI. Stratigraphy, geochemistry and evolution. Cambridge, British Antarctic Survey; 85pp. British Antarctic Survey Scientific Reports, 87.
SMN: Meteorological observations at Carlini base. AMS, Argentina, Buenos Aires, http://www.smn.gov.ar, date: 01.01.2016.
Spada G, Bamber JL, Hurkmans RTWL. 2013. The gravitationally consistent sea-level fingerprint of future terrestrial ice loss. Geophysical Research Letters 40: 482-486.
Spaulding SA, Van B, De Vijver D.A.H, McKnight DM, Verleyen E, Stanish L. 2010. Diatoms as indicators of environ- mental change in Antarctic and subantarctic freshwaters. The Diatoms: applications for the environmental and earth sciences; p.267.
Stammerjohn SE, Martinson DG, Smith RC, Yuan X, Rind D. 2008. Trends in Antarctic annual sea ice retreat and advance and their relation to El Niño–Southern Oscillation and Southern

Annular Mode variability. Journal of Geophysical Research: Oceans 113: 1-20. DOI: 10.1029/2007JC004269.
Steig EJ, Schneider DP, Rutherford SD, Mann ME, Comiso JC, Shindell DT. 2009. Warming of the Antarctic ice-sheet surface since the 1957 International Geophysical Year. Nature 457: 459. DOI: 10.1038/nature07669.
Sterken M, Verleyen E, Sabbe K, Terryn G, Charlet F, Bertrand S, Bos X, Fagel N, De Batist M, Vyverman W. 2008. Late Quaternary climatic changes in southern Chile, as recorded in a diatom sequence of Lago Puyehue (40 40 S). Journal of Paleolimnology 39: 219-235.
Sterken M, Roberts SJ, Hodgson DA, Vyverman W, Balbo AL, Sabbe K, Moreton SG, Verleyen E. 2012. Holocene glacial and climate history of Prince Gustav Channel, northeastern Antarctic Peninsula. Quaternary Science Reviews 31: 93-111.
Sterken M, Verleyen E, Jones VJ, Hodgson DA, Vyverman W, Sabbe K, Van de Vijver B. 2015. An illustrated and annotated checklist of freshwater diatoms (Bacillariophyta) from Livingston, Signy and Beak Island (Maritime Antarctic Region). Plant Ecology and Evolution 148: 431-455.
St-Hilaire-Gravel D, Bell TJ, Forbes DL. 2010. Raised Gravel Beaches as Proxy Indicators of Past Sea-Ice and Wave Conditions, Lowther Island, Canadian Arctic Archipelago. Arctic 63: 213-226.
St-Hilaire-Gravel D, Forbes DL, Bell T. 2012. Multitemporal Analysis of a Gravel-Dominated Coastline in the Central Canadian Arctic Archipelago. Journal of Coastal Research: 421-441. DOI: 10.2112/jcoastres-d-11-00020.1.
St-Hilaire-Gravel D, Forbes DL, Bell T. 2015. Evolution and morphodynamics of a prograded beach-ridge foreland, northern baffin island, canadian arctic archipelago. Geografiska Annaler: Series A, Physical Geography 97: 615-631.
Stone JO. 2000. Air pressure and cosmogenic isotope production. Journal of Geophysical Research: Solid Earth 105: 23753-23759. DOI:10.1029/2000JB900181.
Stone J, Fifield K, Beer J, Vonmoos M, Obrist C, Grajcar M, Kubik P, Muscheler R, Finkel R, Caffee M. 2004. Co-precipitated silver–metal oxide aggregates for accelerator mass spectrometry of 10Be and 26Al. Nuclear Instruments and Methods in Physics Research Section B: Beam Interactions with Materials and Atoms 223-224: 272-277. DOI: htt10.1016/j.nimb.2004.04.055.
Strelin JA, Heredia Barión P, Martini MA, Kaplan M, Kuhn G. 2014. The age of the first Holocene marine transgression in Potter Cove, Isla 25 de Mayo (King George Island), South Shetland Islands. In Actas del XIX Congreso Geológico Argentino, Martino RD, Lira R, Guereschi A, Baldo E, Franzese J, Krohling D, Manassero M, Ortega G, Pinotti L (eds). Asociación Geológica Argentina: Córdoba, Argentina; T1-51.
Strzelecki MC, Long AJ, Lloyd JM. 2015. Post-Little Ice Age Development of a High Arctic Paraglacial Beach Complex. Permafrost and Periglacial Processes 28: 4-17. DOI: 10.1002/ppp.1879.
Strzelecki MC, Long AJ, Lloyd JM, Małecki J, Zagórski P, Pawłowski Ł, Jaskólski MW. 2018. The role of rapid glacier retreat and landscape transformation in controlling the post-Little Ice Age evolution of paraglacial coasts in central Spitsbergen (Billefjorden, Svalbard). Land Degradation and Development 29: 1962-1978. DOI: 10.1002/ldr.2923.
Stuiver M, Reimer PJ. 1993. Extended 14C Data Base and Revised CALIB 3.0 14C Age Calibration Program. Radiocarbon 35: 215-230. DOI: 10.1017/S0033822200013904.
Sugden DE, John BS. 1973. The ages of glacier fluctuations in the South Shetland Islands, Antarctica. In Palaeoecology of Africa, the Surrounding Islands and Antarctica, van Zinderen; Bakker EM (eds). Balkema, Cape Town; 141-159.
Sun LG, Liu XD, Yin XB, Xie ZQ, Zhao JL. 2005. Sediments in palaeo-notches: potential proxy records for palaeoclimatic changes in Antarctica. Palaeogeography, Palaeoclimatology, Palaeoecology 218: 175-193. DOI: https://doi.org/10.1016/j.palaeo.2004.12.009
Tamura, T. 2012. Beach ridges and prograded beach deposits as palaeoenvironment records. Earth-Science Reviews 114: 279-297. DOI: 10.1016/j.earscirev.2012.06.004.
Tatur A, Martinez-Macchiavello JC, Niegodzisz J, del Valle R. 1999. A record of Holocene environmental changes in sediment core of Hotel Lake, King George Island, Antarctica. Polish Polar Studies 26 Polar Symposium.

Telford RJ, Barker P, Metcalfe S, Newton A. 2004. Lacustrine responses to tephra deposition: examples from Mexico. Quaternary Science Reviews 23: 2337-2353 (2004).
Ter Braak CJ, Prentice IC. 1998. A theory of gradient analysis. In Advances in ecological research18. Academic Press; 271-317).
Ter Braak CJ, Smilauer P. 2002. CANOCO reference manual and CanoDraw for Windows user's guide: software for canonical community ordination (version 4.5). www. canoco.com.
Thomas ER, Marshall GJ, McConnell JR. 2008. A doubling in snow accumulation in the western Antarctic Peninsula since 1850. Geophysical Research Letters 35: L01706.
Toro M, Granados I, Pla S, Giralt S, Antoniades D, Galán L, Cortizas AM, Lim HS, Appleby PG. 2013. Chronostratigraphy of the sedimentary record of Limnopolar Lake, Byers Peninsula, Livingston Island, Antarctica. Antarctic Science 25: 198-212. DOI: 10.1017/S0954102012000788.
Tucker, M.E. 1996. Sedimentary rocks in the field. John Wiley & Sons, England, 153 p.
Turner J, Colwell SR, Marshall GJ, Lachlan-Cope TA, Carleton AM, Jones PD, Lagun V, Reid PA, Iagovkina S. 2004. The SCAR READER Project: Toward a High-Quality Database of Mean Antarctic Meteorological Observations. Journal of Climate 17: 2890-2898. DOI: 10.1175/1520-0442(2004)017<2890:tsrpta>2.0.co;2.
Turner J, Lachlan-Cope T, Colwell S, Marshall GJ. 2005. A positive trend in western Antarctic Peninsula precipitation over the last 50 years reflecting regional and Antarctic-wide atmospheric circulation changes. Annals of Glaciology 41: 85-91.
Van de Vijver B, Beyens L. 1997. The epiphytic diatom flora of mosses from Stromness Bay area, South Georgia. Polar Biology 17: 492-501.
van den Broeke MR. 2000. The semi-annual oscillation and Antarctic Climate. Part 4: A note on sea ice cover in the Amundsen and Bellingshausen Seas. International Journal of Climatology 20: 455– 462.
van der Bilt WG, Bakke J, Werner JP, Paasche Ø, Rosqvist G, Vatle S.S. 2017. Late Holocene glacier reconstruction reveals retreat behind present limits and two stage Little Ice Age on sub-Antarctic South Georgia. Journal of Quaternary Science 32: 888-901. DOI:10.1002/jqs.2937.
Varma V, Prange M, Merkel U, Kleinen T, Lohmann G, Pfeiffer M, Renssen H, Wagner A, Wagner S, Schulz M. 2012. Holocene evolution of the Southern Hemisphere westerly winds in transient simulations with global climate models. Climate of the Past 8: 391-402.
Vaughan DG, Marshall GJ, Connolley WM, Parkinson C, Mulvaney R, Hodgson DA, King JC, Pudsey CJ, Turner J. 2003. Recent Rapid Regional Climate Warming on the Antarctic Peninsula. Climatic Change 60: 243-274. DOI: 10.1023/a:1026021217991
Vaughan DG. 2006. Recent Trends in Melting Conditions on the Antarctic Peninsula and Their Implications for Ice-sheet Mass Balance and Sea Level. Arctic, Antarctic, and Alpine Research 38: 147-152. DOI: 10.1657/1523-0430(2006)038[0147:RTIMCO]2.0.CO;2.
Vaughan DG, Comiso JC, Allison I, Carrasco J, Kaser G, Kwok R, Mote P, Murray T, Paul F, Ren J, Rignot E, Solomina O, Steffen K, Zhang T. 2013. Observations: Cryosphere. In Climate Change 2013: The Physical Science Basis. Contribution of Working Group I to the Fifth Assessment Report of the Intergovernmental Panel on Climate Change, Stocker TF, Qin D, Plattner G-K, Tignor M, Allen SK, Boschung J, Nauels A, Xia Y, Bex V, Midgley PM (eds). Cambridge University Press: Cambridge, United Kingdom and New York, NY, USA; 317–382.
Watcham EP. 2010. Late Quaternary relative sea level change in the South Shetland Islands, Antarctica. Doctoral thesis. Durham; 317.
Watcham EP, Bentley MJ, Hodgson DA, Roberts SJ, Fretwell PT, Lloyd JM, Larter RD, Whitehouse PL, Leng MJ, Monien P, Moreton SG. 2011. A new Holocene relative sea level curve for the South Shetland Islands, Antarctica. Quaternary Science Reviews 30: 3152-3170. DOI: 10.1016/j.quascirev.2011.07.021.
Weatherall P, Marks KM, Jakobsson M, Schmitt T, Tani S, Arndt JE, Rovere M, Chayes D, Ferrini V, Wigley R. 2015. A new digital bathymetric model of the world's oceans. Earth and Space Science 2: 331-345. DOI: doi:10.1002/2015EA000107.
Wharton RA Jr, McKay CP, Clow G D, Andersen D T. 1993. Perennial ice covers and their influence on antarctic lake ecosystems. In W. J. Green and E. I. Friedmann (eds), Physical and

Biogeochemical Processes in Lakes, Antarctic Research Series, American Geophysical Union, Washington, D.C: 5370.
Whitehouse PL, Bentley MJ, Le Brocq AM. 2012. A deglacial model for Antarctica: geological constraints and glaciological modelling as a basis for a new model of Antarctic glacial isostatic adjustment. Quaternary Science Reviews 32: 1-24. DOI: 10.1016/j.quascirev.2011.11.016.
Williams AJ, Stuart FM, Day SJ, Phillips WM. 2005. Using pyroxene microphenocrysts to determine cosmogenic 3He concentrations in old volcanic rocks: an example of landscape development in central Gran Canaria. Quaternary Science Reviews 24: 211-222. DOI: https://doi.org/10.1016/j.quascirev.2004.07.004.
Winkler JB. 2000. Die Rolle der Schneebedeckung für die Kryptogamen-Vegetation in der maritimen Antarktis (Potter-Halbinsel, King George Island) = The role of snowcover on the cryptogamic vegetation in the maritime Antarctic (Potter Peninsula, King George Island). Bremerhaven: Alfred Wegener Institute for Polar and Marine Research.
Wölfl A-C, Wittenberg N, Feldens P, Hass HC, Betzler C, Kuhn G. 2016. Submarine landforms related to glacier retreat in a shallow Antarctic fjord. Antarctic Science 28: 475-486. DOI: 10.1017/S0954102016000262.
Wunderle S, Saurer H, Grossmann H. 1998. Meteorological Conditions and Snow Cover Dymanics on the Potter Peninsula, King George Island, Antarctica. Das Künstenökossystem der Potter Cove, Antarktics. Eine Synopsis der Forschungsarbeiten im Rahmen der argentinish-deutshen Kooperation in Dallmann Labour und an der Jubany–Station (1991-1997). Berichte zur Polarforschung 299: 15-27.
Yoo K-C, Yoon HI, Kim J-K, Khim B-K. 2009. Sedimentological, geochemical and palaeontological evidence for a neoglacial cold event during the late Holocene in the continental shelf of the northern South Shetland Islands, West Antarctica. Polar Research 28: 177-192. DOI: 10.1111/j.1751-8369.2009.00109.x.
Yoon HI, Woo Han M, Park B-K, Oh J-K, Soon-Keun C. 1997. Glaciomarine sedimentation and palaeo-glacial setting of Maxwell Bay and its tributary embayment, Marian Cove, South Shetland Islands, West Antarctica. Marine Geology 140: 265-282. DOI: 10.1016/S0025-3227(97)00028-5.
Yoon HI, Yoo K-C, Park B-K, Kim Y, Khim B-K, Kang C-Y. 2004. The origin of massive diamicton in Marian and Potter coves, King George Island, West Antarctica. Geosciences Journal 8: 1-10. DOI: 10.1007/bf02910274
Yoon H-I, Khim B-K, Lee K, Park Y-H, Yoo K-C. 2006. Reconstruction of postglacial paleoproductivity in Long Lake, King George Island, West Antarctica. Polish Polar Research 7: 189-206.
Zervas D, Nichols GJ, Hall R, Smyth HR, Lüthje C, Murtagh F. 2009. SedLog: A shareware program for drawing graphic logs and log data manipulation. Computers & Geosciences 35: 2151-2159. DOI: https://doi.org/10.1016/j.cageo.2009.02.009.